



HAL
open science

Galactic archaeology of the Milky Way disc with the Gaia space mission

Pablo Santos-Peral

► **To cite this version:**

Pablo Santos-Peral. Galactic archaeology of the Milky Way disc with the Gaia space mission. Galactic Astrophysics [astro-ph.GA]. Université Côte d'Azur, 2021. English. NNT : 2021COAZ4001 . tel-03288463

HAL Id: tel-03288463

<https://theses.hal.science/tel-03288463>

Submitted on 16 Jul 2021

HAL is a multi-disciplinary open access archive for the deposit and dissemination of scientific research documents, whether they are published or not. The documents may come from teaching and research institutions in France or abroad, or from public or private research centers.

L'archive ouverte pluridisciplinaire **HAL**, est destinée au dépôt et à la diffusion de documents scientifiques de niveau recherche, publiés ou non, émanant des établissements d'enseignement et de recherche français ou étrangers, des laboratoires publics ou privés.



THÈSE DE DOCTORAT

Archéologie galactique du disque de la Voie
Lactée avec la mission spatiale Gaia

Pablo SANTOS-PERAL

Laboratoire J-L. Lagrange – Observatoire de la Côte d'Azur

**Présentée en vue de l'obtention
du grade de docteur en**
Sciences de la Planète et de l'Univers
de l'Université Côte d'Azur

Dirigée par : Alejandra Recio-Blanco

Soutenue le : 18 février 2021

Devant le jury, composé de :

Vardan Adibekyan, Chercheur, Institut d'Astrophysique
et Sciences de l'Espace de Porto

Francesca Matteucci, Professeur, Université de Trieste

Alejandra Recio-Blanco, Astronome, OCA

Nils Ryde, Professeur, Université de Lund

Caroline Soubiran, Directrice de Recherche,
Université de Bordeaux – CNRS



Archéologie galactique du disque de la Voie Lactée avec la mission spatiale Gaia

Jury:

Présidente du jury et examinateur:

Mme. Caroline Soubiran, Directrice de Recherche, Université de Bordeaux - CNRS

Rapporteurs:

Mme. Francesca Matteuci, Professeur, Université de Trieste

M. Nils Ryde, Professeur, Université de Lund

Examineurs:

M. Vardan Adibekyan, Chercheur, Institut d'Astrophysique et Sciences de l'Espace de Porto

“Sans déconner.”

Chef Khaled, philosophe Français

(Toulon, quelque siècle)

Résumé

L'Archéologie Galactique a pour objectif de révéler l'histoire de la Voie Lactée grâce à l'analyse de différentes propriétés stellaires: des abondances chimiques, de la cinématique, de la dynamique et de l'âge. En particulier, l'abondance d'éléments α (e.g. O, Mg, Si, S, Ca, Ti) par rapport au fer ($[\alpha/\text{Fe}]$) est une importante signature fossile pour tracer l'évolution chimique des populations du disque Galactique, i.e. les disques épais et mince. Le but de cette thèse est d'explorer les différentes contraintes relatives à la détermination précise d'abondances à partir des spectres stellaires observés et, en utilisant les données astrométriques de grand précision de la mission spatiale *Gaia*, analyser les propriétés chimico-dynamique du disque Galactique (e.g. gradients radiaux de abondance, rôle de la migration stellaire, relations âge-abondance) pour inférer la formation et évolution de la Voie Lactée.

L'algorithme employé a été la procédure automatique d'estimation d'abondances GAUGUIN, qui fait partie d'analyse du RVS (Spectromètre de Vitesse Radiale) de la mission *Gaia*. En premier lieu, nous avons déterminé les abondances de $[\text{Mg}/\text{Fe}]$ pour 2210 étoiles observés dans le voisinage solaire par le spectrographe HARPS ESO (haute résolution spectrale: $R \sim 115000$), et paramétrées par le Projet AMBRE (température effective, gravité de surface, métallicité globale $[\text{M}/\text{H}]$, abondance $[\alpha/\text{Fe}]$, et vitesse radiale). Il a été trouvé que la définition de continuum pour normaliser les spectres observés est responsable de la majeure fraction d'incertitude dans l'estimation d'abondances pour les spectres d'étoiles riches en métaux. On montre une méthode qui améliore notablement la précision, et que nous permet d'observer une tendance décroissante de la abondance de $[\text{Mg}/\text{Fe}]$ même à métallicités supérieures à la solaire ($[\text{M}/\text{H}] > 0$), à résoudre partiellement les divergences entre le plateau observé dans la littérature, et la majeure pente prédite par les modèles d'évolution chimique de la Galaxie.

Nous avons utilisé ces nouvelles mesures de $[\text{Mg}/\text{Fe}]$ pour interpréter la formation et l'évolution du disque Galactique. À cet effet, nous avons estimé des âges précises et des paramètres orbitaux pour 366 étoiles de la 'main sequence turn-off' (MSTO), en utilisant des isochrones PARSEC, ainsi que des données astrométriques et photométriques de *Gaia* DR2. Nous constatons un gradient plus escarpé de $[\text{Mg}/\text{Fe}]$, par rapport aux valeurs de la littérature, qui est un résultat direct de la amélioration des estimations d'abondances pour les étoiles riches en métaux. De plus, une dispersion significative des âges stellaires a été trouvé pour chaque valeur de $[\text{Mg}/\text{Fe}]$, et aussi une claire corrélation de la dispersion d'abondances de $[\text{Mg}/\text{Fe}]$ avec la métallicité pour un âge fixe. Tandis que pour $[\text{M}/\text{H}] \leq -0.2$, une claire tendance âge-métallicité et âge- $[\text{Mg}/\text{Fe}]$ est observée, des étoiles plus riches montrent des âges entre 3 jusqu'à 12 Gyr, en décrivant une tendance plate dans les relations $[\text{M}/\text{H}]$ -age et $[\text{Mg}/\text{Fe}]$ -age. De plus, nous trouvons une fraction significative d'étoiles ayant migré radialement dans le disque galactique, dont la distribution d'âges est très dispersée.

Enfin, les résultats ont montré l'apparition d'une deuxième séquence chimique dans le disque extérieur, il y a 10-12 Gyr. Ces étoiles sont moins riches en métaux que la population stellaire coexistante dans les parts intérieures du disque, et montrent des valeurs inférieurs de $[\text{Mg}/\text{Fe}]$ que les étoiles plus anciennes avec la même métallicité, en produisant une discontinuité chimique. Au vu de ces résultats, ils privilégient une formation rapide d'un disque primitif qui s'est développée dans les régions internes, suivie d'une accrétion de gaz pauvre en métaux, probablement lié à l'accrétion d'un satellite riche en gaz, qui a pu avoir déclenché la formation du disque mince.

Mots clés: Voie Lactée, Archéologie galactique. Étoiles: abondances. Méthodes: spectroscopie, procédure automatique. Galaxie: disque, évolution.

Abstract

Galactic archaeology aims at unveiling the history of the Milky Way by analysing different stellar properties: chemical abundances, kinematics, dynamics and ages. In particular, the abundance of α -elements (e.g. O, Mg, Si, S, Ca, Ti) with respect to iron ($[\alpha/\text{Fe}]$) is an important fossil signature to trace the chemical evolution of the Galactic disc's populations, i.e. the thin and the thick disc. The goal of this thesis is to explore the main issues concerning the determination of high-precision abundances from observed spectral data and, by using the high-quality astrometric data provided by the *Gaia* space mission, analyse the chemodynamical properties of the Galactic disc (e.g. radial abundance gradients, role of stellar migration, age-abundance relations) in order to infer the formation and evolution of the Milky Way.

The implemented algorithm was the automated abundance estimation procedure GAUGUIN, which is integrated into the RVS (Radial Velocity Spectrometer) DPAC analysis pipeline of the *Gaia* mission. We first applied our method to derive $[\text{Mg}/\text{Fe}]$ abundances for 2210 solar neighbourhood stars observed by the HARPS ESO spectrograph (high spectral resolution: $R \sim 115000$), and parametrised by the AMBRE Project (effective temperature, surface gravity, overall metallicity $[\text{M}/\text{H}]$, $[\alpha/\text{Fe}]$ abundance, and radial velocity). We found that the definition of continuum to normalise the observed spectra is responsible for the largest fraction of the uncertainty in the abundance estimate for the metal-rich stellar spectra. We show a methodology that significantly improve the abundance estimate precision, and allows to observe a decreasing trend in the $[\text{Mg}/\text{Fe}]$ abundance even at supersolar metallicities ($[\text{M}/\text{H}] > 0$), partly solving the apparent discrepancies between the observed flat trend in the literature, and the steeper slope predicted by Galactic chemical evolution models.

We used these new $[\text{Mg}/\text{Fe}]$ abundance measurements to interpret the Galactic disc formation and evolution. To this purpose, we estimated ages and orbital properties for 366 main sequence turn-off (MSTO) stars, using PARSEC isochrones, together with astrometric and photometric values from *Gaia* DR2. We observe a steeper $[\text{Mg}/\text{Fe}]$ gradient, compared to literature values, which is a direct result of the improvement of the abundance estimates in the metal-rich regime. Moreover, we find a significant spread of stellar ages at any given $[\text{Mg}/\text{Fe}]$ value, and observe a clear correlated dispersion of the $[\text{Mg}/\text{Fe}]$ abundance with the metallicity at a given age. While for $[\text{M}/\text{H}] \leq -0.2$, a clear age-metallicity and age- $[\text{Mg}/\text{Fe}]$ trends are observed, more metal-rich stars display ages from 3 up to 12 Gyr, describing an almost flat trend in the $[\text{M}/\text{H}]$ -age and $[\text{Mg}/\text{Fe}]$ -age relations. In addition, we found a significant fraction of radial migrated stars in the Galactic disc, for a wide range of stellar ages.

Finally, we observe the appearance of a second chemical sequence at the outer disc, 10-12 Gyr ago. These stars are more metal-poor with respect to the coexisting stellar population in the inner parts of the disc, and show lower $[\text{Mg}/\text{Fe}]$ abundances than prior disc stars of the same metallicity, leading to a chemical discontinuity. Our data favour the rapid formation of an early disc that settled in the inner regions, followed by the accretion of metal-poor gas, probably related to a major accretion event from a gas-rich satellite merger, that may have triggered the formation of the thin disc population.

Keywords: Milky Way, Galactic archaeology. Stars: abundances. Methods: spectroscopy, automatic procedure. Galaxy: disc, evolution.

Resumen

La Arqueología Galáctica tiene como objetivo revelar la historia de la Vía Láctea a través del análisis de diferentes propiedades estelares: abundancias químicas, cinemática, dinámica y edad. En particular, la abundancia de elementos α (e.g. O, Mg, Si, S, Ca, Ti), con respecto al hierro ($[\alpha/\text{Fe}]$), es un importante rastro fósil para trazar la evolución química de las componentes del disco Galáctico, i.e. el disco delgado y el disco grueso. El objetivo de esta tesis es explorar las diferentes limitaciones relativas a la determinación precisa de abundancias a partir de espectros estelares observados y, usando los excelentes datos astrométricos de la misión espacial *Gaia*, analizar las propiedades químico-dinámicas del disco Galáctico (e.g. gradientes radiales de abundancia, papel de la migración estelar, relaciones edad-abundancia) para inferir la formación y evolución de la Vía Láctea.

El algoritmo empleado ha sido el método automático de estimación de abundancias GAUGUIN, que forma parte de la interfaz de análisis del RVS (Espectrómetro de Velocidad Radial) de la misión *Gaia*. En primer lugar, aplicamos nuestro método para obtener abundancias de $[\text{Mg}/\text{Fe}]$ para 2210 estrellas de la vecindad solar, observadas por el espectrógrafo HARPS ESO (alta resolución espectral: $R \sim 115000$), y parametrizadas por el Proyecto AMBRE (temperatura efectiva, gravedad superficial, metalicidad global $[\text{M}/\text{H}]$, abundancia $[\alpha/\text{Fe}]$, y velocidad radial). Encontramos que la definición de continuo en la normalización de espectros observados es responsable de la mayor fracción de incertidumbre en la estimación de abundancias de las estrellas ricas en metales. Mostramos una metodología que mejora significativamente la precisión, y que nos permite observar una tendencia decreciente en la abundancia de $[\text{Mg}/\text{Fe}]$ incluso a metalicidades superiores a la solar ($[\text{M}/\text{H}] > 0$), resolviendo así parcialmente las aparentes discrepancias entre la tendencia plana observada en la literatura, y la mayor pendiente prevista por modelos de evolución química de la Galaxia.

Posteriormente, hemos usado estas nuevas medidas de $[\text{Mg}/\text{Fe}]$ para interpretar la formación y evolución del disco Galáctico. Para ello, hemos estimado edades y parámetros orbitales de 366 estrellas de la ‘main sequence turn-off’ (MSTO), usando isocronas PARSEC, junto con datos astrométricos y fotométricos de *Gaia* DR2. Observamos un gradiente más empinado de $[\text{Mg}/\text{Fe}]$, en comparación con valores de la literatura, que es un resultado directo de la mejora en las estimaciones de abundancia para las estrellas ricas en metales. Además, encontramos una amplitud significativa de edades estelares para cada valor de $[\text{Mg}/\text{Fe}]$, y observamos una clara correlación en la dispersión de $[\text{Mg}/\text{Fe}]$ con la metalicidad a una edad dada. Mientras que para $[\text{M}/\text{H}] \leq -0.2$, una clara tendencia edad-metalicidad y edad- $[\text{Mg}/\text{Fe}]$ es observada, estrellas más metálicas muestran edades desde 3 hasta 12 Gyr, describiendo una curva plana en las relaciones $[\text{M}/\text{H}]$ -age y $[\text{Mg}/\text{Fe}]$ -age. Por otra parte, encontramos una fracción significativa de estrellas que han migrado radialmente en el disco galáctico, presentando un amplio rango de edades.

Finalmente, observamos la aparición de una segunda secuencia química en las partes externas del disco, hace 10-12 Gyr. Estas estrellas son más pobres en metales que la población estelar coexistente en las partes internas del disco, y muestran menores abundancias de $[\text{Mg}/\text{Fe}]$ que las estrellas más antiguas con la misma metalicidad, produciendo así una discontinuidad química. Nuestros datos privilegian una rápida formación de un disco primitivo que se asentó en las regiones interiores, seguido de una acreción de gas externo pobre en metales, probablemente vinculado con la acreción de una galaxia satélite rica en gas, que pudo haber desencadenado la formación del disco delgado.

Palabras clave: Vía Láctea, Arqueología galáctica. Estrellas: abundancias. Métodos: espectroscopía, procedimiento automático. Galaxia: disco, evolución.

Remerciements

Il a fait plus de 8 ans que j'ai entré pour la première fois à la Faculté de Physique de l'Université Complutense de Madrid, accompagné de mes parents et un premier plat de tortilla espagnole dans la cantine. Ainsi, il a commencé la meilleure époque de ma vie: en connaissant et cohabitant avec des gens exceptionnel, où la tortilla est devenue la bière, en apprenant de la physique (le juste nécessaire) et au-delà (le beaucoup et nécessaire). Je comprend ce manuscrit de thèse en tant que pointe d'orgue generale (pas finale) à toute cette période, soyant ces dernières 3 années le projet personnel et scientifique plus complet et merveilleux que j'ai veçu jusqu'à présent. Je vous promets que je ne l'oublierai jamais, et je ne peux qu'être vraiment remercié à:

- En premier lieu, à **ma famille**. À mes chers parents et frère, avec lesquelles j'ai partagé tout depuis toujours. Grace à eux, j'ai hérité des valeurs, façon de travailler et de penser, et la nature d'affronter les choses. Avec la bonne humeur en avant et pour emblème. Je peux pas vous aimer plus. Et à **mes grands-parents**, qui sont la greine qui a réussi sa vieque contre toute attente et, ensemble mes parents, m'ont permis de toujours choisir l'option que j'ai souhaitée faire, avec un effort et une éthique que je ne laisserai de admirer et apprendre chaque jour. Je suis chanceux. Vous êtes mes véritables héros.

- Dans une catégorie especial on trouve M^{lle} **Paula Iriarte Pestaña**. Mon pilier fondamental. Elle est la raison/motif/cause de tout dans ma vie. C'est impossible de verbaliser et te montrer combien je t'aime est l'importante que tu es pour moi chaque jour, et impossible de savoir où je serais s'il n'est pas grâce à toi. Je profit de la vie parce que je sais que tu es toujours là, en faisant-moi heureux. Ma plus grande satisfaction est avoir pu parcourir et vivre cette expérience avec toi. Prépare-toi bien: je reviens! Je t'aime beaucoup, ma niçoise.

- À ma merveilleuse directrice de thèse, **Alejandra Recio Blanco**, qui je considère une collègue et amie. Alejandra, tu ne peut pas avoir une idée du nombre de fois que j'ai réfléchi à la chance que j'ai eu pour être ton étudiant de doctorat. Tu me samble une personne extraordinaire: brillant sur le plan professionnel et très sympathique et amusante sur le plan personnel. Il a été un véritable plaisir te voir travailler et partager ces années avec toi. Depuis le premier jour, je me sense avec toute la confiance et très confortable dans la vie à l'Observatoire. D'ailleurs, je voudrais te remercier pour tout le soutien, le courage, l'aide et l'état d'esprit reçu de ta part durant tout ce temps.

De la même façon, merci à **Patrick de Laverny** pour son bon charisme et son sens de l'humour tout le temps. Et pour les délicieux barbecues, meh bien sûr eh!! J'espère honnêtement que tu sois capable de gagner à tennis un jour, l'espoir est le dernier chose à perdre. Une étreinte spéciale à **Pablo et Naia**, qui ont un avenir sans limites.

- Les rapporteurs et les examinateurs de ma thèse: **Nils Ryde, Francesca Matteucci, Caroline Soubiran et Vardan Adibekyan**. Je remercie pour l'honneur qu'ils m'ont fait de corriger mon manuscrit de thèse, et le précieux temps qu'ils m'ont consacré pour assister à ma soutenance.

- À l'entière brillante équipe d'Archéologie Galactique de l'OCA: **Georges Kordopatis, Mathias Schultheis, Vanessa Hill et Christophe Ordenovic**. Pour leur soutien et très bon accueil au group. Et surtout pour la grande combinaison de sens de l'humour avec des intéressants discussions scientifiques sur lesquelles je n'ai pas cessé d'apprendre.

- Une mention spéciale à ma grande collègue galicienne de fatigues, **Emma Fernández Alvar**. L'union fait la force pour survivre à la bureaucratie française, à la langue française, à la idiosyncrasie française et... à les Français (en general ;)). La vie dans l'Observatoire n'aurait pas été la même sans la partager avec toi. Merci de tout coeur, Emma, pour ton soutien et avoir profité de Nice ensemble.

- À **Alisson Michel y Jolanta Jzupa**, pour leur vitalité et bonne humeur que bien réjouissaient la vie dans le couloir, dans la montagne, à Cannes, et je suis sûre que à Vienne aussi en ce moment même.

- Un très grand merci à la super équipe de la cantine de l'Observatoire: **Khaled, Karima et Dominique**. Il sont les véritables responsables d'avancement de la recherche scientifique à Nice. Cette thèse je la dois à eux, au meilleur moment du jour. Ainsi j'ai fait des amis, j'ai grossi, et j'ai connu la situation sociale-économique-politique de France de première main du sage Khaled, dont son vocabulaire et sa connaissance font partie de ce manuscrit scientifique... ("*de mes couilles*"). Ils me manquèrent partout où j'aille.

- À un autre galicienne, **Olga Suárez**, du service éducatif, pour me donner l'opportunité de prendre part à la *Journée de la Science* et en un couple des cours pratiques d'astronomie à des élèves du lycée.

- À mon copain de bureau cette dernière année, **Pedro Alonso Palicio**, qui m'a enseigné à m'en sentir chanceux que les formalités administratives ne soient pas à la ULL.

- À tous et toutes mes bons amis de thèse: **Nastya, Edouard, Brynna, Ximena, Álvaro, Umberto, Angela, Michael Buhlmann, Max, Nico, He, Nacho, Camille, Marco, Chiara, Cosmin, Tobias, Gabriele, Annelore, Adrien, João, Vincent, Elena, Vitalii**. Je veux souligner à les grands **Francesco Cipriano et Govind Nandakumar**, pour ces matches compétitifs de ping-pong au début de la thèse que me réjouissent le jour, et que m'ont fait sentir comme à la maison.

- Je suis très remercie à ma superviseur du CIEMAT, **Mercedes Molla**, de qui je garde le contact depuis le projet du fin de master. Elle m'a aidé et recommandé plus que nécessaire pour que je puisse être là. Merci bien aussi à les chercheurs astrophysiques de la Université Complutense de Madrid, **África Castillo Morales et Armando Gil de Paz**. Leur dévouement et vocation n'ont pas des limites, et leurs opinions favorables m'ont donné le dernier coup de pouce pour commencer cette aventure à Nice.

- Je ne veux pas oublier de mes collègues astrophysiques du máster: **Daniel Morcuende, Mario Chamorro, Ángela García Argumánez, Carlos Cifuentes, José Cano, Juan Carbajo et Paloma López**. Camarades de souffrance et de travail, ainsi comme de jouissance et déconnexion.

-Pour finir, je n'ai pas des mots de remerciement suffisantes à la chance d'avoir joui (et continuer à profiter) d'un groupe de gens spectaculaire qui ont fait de l'université les meilleures années de ma vie. La physique est seulement le contexte, j'aurais étudié quelque autre chose si je savais que eux aussi. Merci pour tout, cabrones: **Diego Moral, Daniel San Julián, David Rubira, Micaela Rodríguez, Jordi Sabater, Manolo Sánchez, Pedro Rodríguez, Drago Lehn, Leire Posilio, Alberto Madrigal, et Rafael 'Fotón Virtual' Priego**.

Agradecimientos

Hace más de 8 años pisé por primera vez la facultad de físicas de la Universidad Complutense de Madrid, acompañado por mis padres y un primer pincho de tortilla de la cafetería. Así comenzaron los mejores años de mi vida: conociendo y conviviendo con gente excepcional, en los que los pinchos de tortilla pasaron a ser tercios de cerveza, aprendiendo física (lo justo y necesario) y más allá de ella (lo mucho y necesario). Entiendo este manuscrito de tesis como broche general (que no final) de todo este período, siendo estos tres últimos años el proyecto personal y científico más completo y maravilloso que he vivido hasta ahora. Prometo no olvidarlo jamás, y no puedo más que estar sinceramente agradecido a:

- En primer lugar, a **mi familia**. A **mis queridos padres y hermano**, con los que he compartido todo desde siempre y de quién he heredado mis valores, mi forma de trabajar y de pensar, y mi carácter para afrontar las cosas. Con el buen humor por delante y por bandera. No os puedo querer más. Y a **mis abuelos**, que son la semilla que salió adelante contra todo pronóstico y, junto a mis padres, permitirme la opción de elegir siempre lo que he querido hacer, con una ética y esfuerzo que no dejaré de admirar y de aprender cada día. Soy un afortunado. Sois mis verdaderos héroes.

- En una categoría especial se encuentra M^{lle} **Paula Iriarte Pestaña**. Mi pilar. Ella es la razón/motivo/causa de todo en mi vida. Es imposible verbalizar y demostrarte todo lo que te quiero y lo importante que eres para mi cada día, e imposible saber dónde estaría y cómo sería si no fuera gracias a ti. Disfruto en esta vida porque sé que siempre estás ahí, haciéndome feliz. Mi mayor satisfacción es haber recorrido y vivido contigo toda esta experiencia. ¡Prepárate que vuelvo! Te quiero mucho, Nizarda.

- A mi maravillosa directora de tesis, **Alejandra Recio Blanco**, a la cuál considero compañera y amiga. No te haces una idea de las veces qué he pensado en la suerte que he tenido por ser estudiante tuyo de doctorado. Me pareces una persona espectacular: brillante en lo profesional y muy “maja” (~ simpática, traducción madrileño-gallego ;)) y divertida en lo personal. Ha sido una gozada verte trabajar y compartir estos años contigo. Desde el primer día me he sentido con toda la confianza y muy cómodo en la vida del observatorio. También te quiero agradecer todo el apoyo y ánimo recibido por tu parte durante todo este tiempo.

De la misma manera, gracias a **Patrick de Laverny** por su buen trato y sentido del humor todo el tiempo, y por las ricas barbacoas, por supuesto! Espero que algún día ganes al tenis, la esperanza es lo último que se pierde. Un abrazo muy especial a **Pablo y Naia**, cuyo futuro no tiene límites.

-Gracias a los 'rapporteurs' y examinadores de la tesis: **Nils Ryde, Francesca Matteucci, Caroline Soubiran y Vardan Adibekyan**. Les estoy muy agradecido por el honor que me supone que corrijan la memoria de mi tesis, y el preciado tiempo que han dedicado para asistir y formar parte de la defensa.

- Al brillante equipo de Arqueología Galáctica del OCA: **Georges Kordopatis, Mathias Schultheis, Vanessa Hill y Christophe Ordenovic**. Por su gran apoyo y acogida al grupo, y su combinación de buen humor con interesantes discusiones científicas de las que he aprendido sin cesar.

- Una mención especial a mi gran compañera gallega de fatigas, **Emma Fernández Alvar**. La unión hace la fuerza para sobrevivir a la burocracia francesa, al idioma francés, a la idiosincrasia

francesa y... a los franceses (en general ;)). La vida en el observatorio no hubiera sido la misma sin compartirla contigo. Gracias de verdad por este tiempo, Emma, por tu apoyo y haber disfrutado de Niza juntos.

- A **Alisson Michel y Jolanta Jzupa**, por su vitalidad y buen humor que tanto alegraron la vida en el pasillo, en la montaña, en Cannes, y estoy seguro de que ahora mismo en Viena.

- Gracias al gran equipo de la cantina: **Khaled, Karima y Dominique**. Ellos son las personas más importantes del observatorio, los responsables del avance de la investigación científica en Niza. Mi tesis se la debo a ellos, a la mejor hora del día. Así he hecho amigos, engordado, y aprendido la situación social-económico-política de Francia de la mano del sabio Khaled, cuyo extenso vocabulario y conocimiento forma parte de este manuscrito científico... (“*de mes couilles*”). Los echaré de menos allá donde vaya.

- A una gallega más, **Olga Suárez**, del servicio educativo, por darme la oportunidad de participar en la *Journée de la Science* y en un par de clases prácticas de astronomía a alumnos de instituto.

- A mi compañero de despacho el último año, **Pedro Alonso Palicio**, que me enseñó a sentirme afortunado de que los trámites de la tesis no fueran en la ULL.

- A todos mis buenos amigos de tesis: **Nastya, Edouard, Brynna, Ximena, Álvaro, Umberto, Angela, Michael Buhlmann, Max, Nico, He, Nacho, Camille, Chiara, Cosmin, Tobias, Gabriele, Annelore, Adrien, João, Vincent, Elena, Vitalii**. Y quiero destacar a los grandes **Francesco Cipriano y Govind Nandakumar**, por aquellos partidos competitivos de ping-pong al comienzo de la tesis que me alegraban el día, y que me hicieron sentir como en casa.

- Muchas gracias a mi tutora del CIEMAT, **Mercedes Molla**, cuyo contacto conservo desde el proyecto de fin de máster y me ha ayudado y recomendado más de lo necesario para que yo esté aquí. Gracias también a los astrofísicos de la Universidad Complutense, **África Castillo Morales y Armando Gil de Paz**, cuya dedicación y vocación no tienen límites, y sus opiniones y valoraciones me dieron el último empujón a emprender esta aventura en Niza.

- No me quiero olvidar de mis compañeros astrofísicos del máster: **Daniel Morcuende, Mario Chamorro, Ángela García Argumánez, Carlos Cifuentes, José Cano, Juan Carbajo y Paloma López**. Compañeros de sufrimiento y trabajo, pero también de disfrute y desconexión.

-Para terminar, no tengo palabras de agradecimiento suficientes a la suerte de haber disfrutado (y seguir disfrutando) de un grupo de gente espectacular que han hecho de la universidad los mejores años de mi vida. La física sólo es el contexto, hubiera estudiado cualquier cosa si supiera que ellos también. Gracias por todo, cabrones: **Diego Moral, Daniel San Julián, David Rubira, Micaela Rodríguez, Jordi Sabater, Manolo Sánchez, Pedro Rodríguez, Drago Lehn, Leire Posilio, Alberto Madrigal, y Rafael ‘Fotón Virtual’ Priego**.

Contents

1	Introduction	1
1.1	Our Galaxy: an overview of the Milky Way	1
1.1.1	Observing the sky: growth of knowledge from ancient times	2
1.1.2	Formation and evolution of galaxies: the Λ CDM model	4
1.1.3	Structure of the Milky Way: stellar components	6
1.2	Galactic archaeology	9
1.2.1	Chemical abundances as tracers of the star's history	10
1.2.2	Stellar kinematics	13
1.2.3	Stellar age dating	14
1.3	The Gaia mission	17
1.4	Galactic spectroscopic surveys	21
1.4.1	The AMBRE Project	23
1.5	Chemical evolution of the Galactic disc	24
1.5.1	Models vs. Observations	24
1.5.2	Radial abundance gradients & radial migration	26
1.5.3	Gaia mission impact on Milky Way disc studies	26
1.6	Goals of this thesis	27
2	Determination of chemical abundances from stellar atmospheres	29
2.1	Spectral continuum and line formation	30
2.1.1	Parameter dependence	32
2.2	Automated abundance analysis	35
2.2.1	Measurement of equivalent widths	35
2.2.2	Spectrum synthesis	37
2.3	Automatic parametrisation algorithms	37
2.3.1	Optimisation methods	38
2.3.2	Projection methods	38
2.3.3	Classification methods	39
2.4	Challenges for high-precise and accurate abundance measurements	39
3	Automated normalisation and abundance estimation procedures	42
3.1	Normalisation procedure	42
3.2	The GAUGUIN automated abundance estimation algorithm	43
3.3	Synthetic spectra grid	44
3.4	Line list	45
3.5	Sensitivity to spectral resolution and signal-to-noise	47
4	Observational data sample	50
4.1	The AMBRE:HARPS spectra	50
4.2	Gaia DR2: photometry, astrometry and distances	52

5	Optimisation of the automatic normalisation procedure: influence on the magnesium abundances in the Galactic disc	54
5.1	Analysed local normalisation intervals	55
5.2	Sensitivity to spectral line-broadening	55
5.3	Continuum placement optimisation for different lines and stellar types	58
5.3.1	Non-saturated lines	58
5.3.2	Strong saturated lines	58
5.3.3	Mg abundances line-to-line scatter	63
5.4	Disentangling the low- and high-[Mg/Fe] sequences in the disc	65
5.5	Summary	68
6	Determination of stellar ages and orbital properties	70
6.1	Estimation of ages	70
6.2	Determination of orbital properties	72
7	Solar neighbourhood chemodynamical constraints on Galactic disc evolution	74
7.1	Radial chemical trends and stellar migration	75
7.1.1	Definition of the thin disc	75
7.1.2	Present-day chemical abundance gradients	76
7.1.3	Radial migration	80
7.2	Age-abundance relations	84
7.2.1	[Mg/Fe] abundance as a chemical clock	84
7.2.2	Temporal evolution in the [Mg/Fe]-[M/H] plane	87
7.2.3	Trends with stellar age: relation to radius	89
7.3	Formation and evolution history of the Galactic disc	91
7.4	Summary	94
8	Conclusions and future works	97
8.1	High-precision estimation of chemical abundances	98
8.2	From surveys to models: Galactic disc formation scenarios	100
8.3	Future works: perspectives in Galactic archaeology	101
A	Publications	104
	Bibliography	105

Chapter 1

Introduction

Contents

1.1 Our Galaxy: an overview of the Milky Way	1
1.1.1 Observing the sky: growth of knowledge from ancient times	2
1.1.2 Formation and evolution of galaxies: the Λ CDM model	4
1.1.3 Structure of the Milky Way: stellar components	6
1.2 Galactic archaeology	9
1.2.1 Chemical abundances as tracers of the star's history	10
1.2.2 Stellar kinematics	13
1.2.3 Stellar age dating	14
1.3 The Gaia mission	17
1.4 Galactic spectroscopic surveys	21
1.4.1 The AMBRE Project	23
1.5 Chemical evolution of the Galactic disc	24
1.5.1 Models vs. Observations	24
1.5.2 Radial abundance gradients & radial migration	26
1.5.3 Gaia mission impact on Milky Way disc studies	26
1.6 Goals of this thesis	27

1.1 Our Galaxy: an overview of the Milky Way

In literary terms, the origin of the Milky Way can be found in the Greek mythology. According to the legend, Zeus, cheating on his wife Hera, secretly took the shape of Alcmena's husband and had a son with her: Heracles. Since Heracles was born mortal, he should be feeded from Hera's breasts in order to achieve his immortality. To this purpose, while Hera was deeply asleep during the night, Heracles was placed to get the divine milk. Hera suddenly awakened, and sharply pushed Heracles away. The milk continued flowing out, spraying all around the Universe, illuminating it, and giving form to the Milky Way. Based on that, the term 'Milky Way' comes from latin *Via Lactea*, and also the term 'galaxy' has its etymological origin from the greek word for milk: *gala, galaktos*.

In scientific terms, the ‘real’ origin, nature, and properties of our Galaxy have been sources of debates, concerns, and hunger of knowledge since the most ancient civilisations looked up to the sky questioning everything. At the present time, few questions have been answered but there are plenty of them yet to be discovered.

1.1.1 Observing the sky: growth of knowledge from ancient times

Astronomy could be considered as the oldest of the sciences. Astronomy has evolved from being an applied science in ancient times (the observation of the cyclic movements of the Sun, Moon, and stars, leads to the development of calendars, the implementation of agriculture epochs, and the domain of orientations), to a pure and theoretical science, playing a significant role on the scientific revolution in the 17th century, and driving the birth of modern physics.

The birth of modern astronomy can be placed in Greece, where mathematics were imposed on the development of ideas and models, and precise observations were assumed to be indispensables to test and corroborate the approaching models. The philosopher Democritus of Abdera (460-370 B.C) described the Milky Way as a large collection of stars that were too weak and joint to be seen individually. Already at that early epochs, Hipparchus (194-120 B.C.), the first great astronomic observer in the ancient history, made the first precise catalogue with positions and brightness of 850 stars¹, and placed the Earth out of the centre of the Universe.

The flame of astronomy was kept during Middle Ages by the Islamic culture: by the translation of ancient texts, important mathematics contributions, and precise observations and stellar catalogues. The Persian astronomer Abd Al-Rahman Al Sufi (903-986 A.D.) documented for the first time the observations of the Large Magellanic Cloud (LMC) and the Andromeda (M31) galaxies (*Book of Fixed Stars*, 964). The Magellanic Clouds, later discovered as satellite galaxies of the Milky Way, were announced in the sky of the Southern Hemisphere by Fernando de Magallanaes and Juan Sebastián Elcano during their circumnavigation around the globe in 1520.

The genuine astronomic revolution started with Galileo Galilei (1564-1642), father of the observational astronomy, who pointed at the sky with a telescope for the first time, and directly observed in 1610 that the Milky Way was constituted by an infinite number of stars. At the end of the 17th century, Isaac Newton (1643-1727) opened a new era in the understanding of the cosmos by the publication of the three laws of motion and the universal theory of gravity (*Principia*, 1687): the complexity of the Universe was based on few principles of physics that also govern the motion of the bodies in the Earth. Astronomy had turned into astrophysics.

In 1755, the German philosopher Immanuel Kant (1724-1804) proposed that the Milky Way was an ensemble of Solar systems, with a global structure similar to our Solar system itself: a flat plane, with the stars rotating around a centre describing elliptical orbits similar to the planets around the Sun (Johannes Kepler, *Astronomia Nova*, 1609). From a philosophical point of view, Kant affirmed that a logical framework would consist of the existence of others ‘island-universe’, like the Milky Way, whose stars cannot be distinguish from our position and, therefore, they seem to be visible ‘nebulae’. At the end of the 18th century, in 1785, Caroline Herschel (1750-1848) and his brother William (1738-1822) made the first map of the Galaxy by counting the number of stars for 683 different regions in the sky, and placed the Sun in the Galactic centre. In addition, they catalogued around 2500 nebulae with an impressive precision. One century later, a similar exploration was carried out by Jacobus Kapteyn (1851-1922) in 1906, over 206 areas in the sky. Kapteyn reported that the disc of Milky Way was thick (3 kpc²), with a radius of 8 kpc, and the Sun was in the centre.

¹Hipparchus introduced the system of apparent magnitudes to catalogue the brightness of stars that it is currently used in modern astrophysics.

²1pc = 3.26 light years = 3.09 x 10¹⁶m.

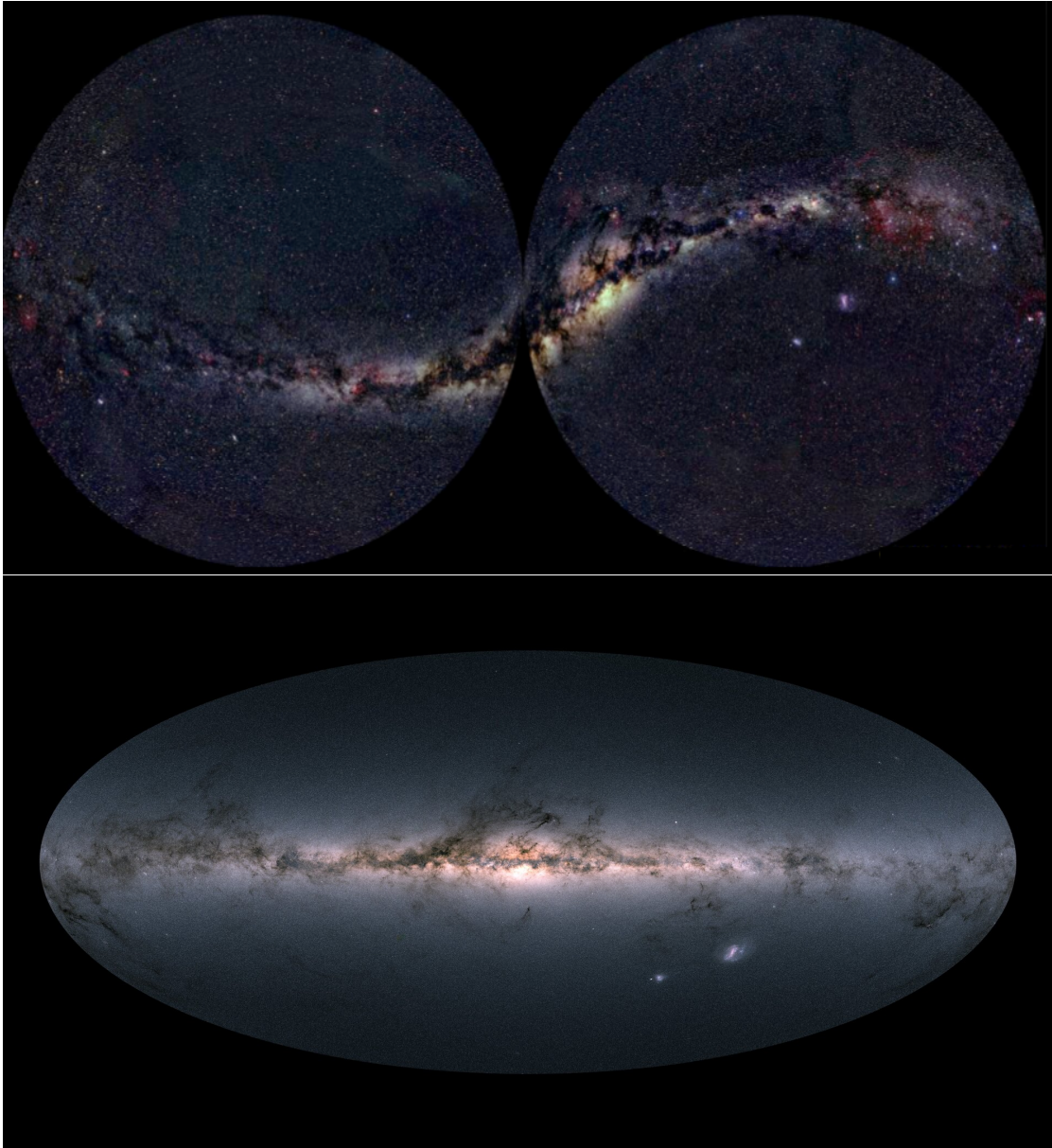


FIGURE 1.1: View of the Milky Way. **Top:** projected on the celestial sphere (Source: Axel Mellinger, 2000; <https://www.milkywaysky.com>). **Bottom:** in Galactic coordinates (Source: ESA).

Between the 19th and 20th centuries, with the developments of physics and new astronomical instrumentation, a variety of catalogues of stars and large diffuse objects ('nebulae') were performed by different independent observers and campaigns. Some of them, and their correspondent nomenclature, are currently used: the Messier Catalogue in 1774 by Charles Messier (1730-1817), the General Catalogue GC by John Herschel (1792-1891), and its followed extension to the New General Catalogue NGC, first, and the Index Catalogue IC, later, both by J.L.E. Dreyer (1852-1926).

At the early 20th century, a fundamental discussion about the size and nature of the Milky way, and the possible extragalactic nature of the observed diffuse spirals nebulae, constituted a turning point in Galactic astrophysics.

In 1920, Harlow Shapley (1885-1972) and Herber Curtis (1872-1942) leded 'The Great Debate', which took place in the National Academy of Sciences of USA with Albert Einstein as a remarkable spectator. On the one hand, Shapley measured the distances of Cepheids stars (variables) using the period-luminosity relation found by Henrietta S. Leavitt (Leavitt, 1908, analysis of 1777 variable stars in the Magellanic Clouds), and found that stellar globular clusters were rotating around a different gravitational centre, far from the Sun location. He affirmed that our Galaxy was larger than it was previously thought (diameter ~ 100 kpc), with the Sun out of the centre, and the spirals nebulae consisted of gaseous nearby objects. He finally claimed that the Universe was our Galaxy itself. On the other hand, Curtis asserted that the Galaxy had a size ten times smaller (diameter < 10 kpc), where the Sun was placed in the centre, and the spirals nebulae were long-distant objects (from 150 to 3000 kpc away), and consisted on rotational systems similar to the Milky Way. Therefore, the Universe had to be composed of a high number of different galaxies. In 1924, Edwin Hubble (1889-1953) clarified the extragalactic nature of the spirals nebulae after finding a Cepheid star in the Andromeda 'nebula' ('identical' in properties to the presented ones by Shapley), and measured a 300 kpc distance (well-known today: ~ 750 -800 kpc). To the press, Shapley was the 'winner' of the debate (he guessed the position of the Sun and the size of the Milky Way) but, with the present-day scientific knowledge, Curtis succeed in the answer of the most relevant questions: the nature of the spirals nebulae, the model of the Universe, and the idea of galaxies.

From that moment up to the present time, the knowledge about the Milky Way and the extragalactic structures has undergone an unstoppable development. Fig. 1.1 shows some of the most recent and clear observations of our Galaxy, the Milky Way. A state-of-the-art knowledge in the Galactic formation and evolution scenarios will be described and explored throughout this manuscript.

1.1.2 Formation and evolution of galaxies: the Λ CDM model

How did our galaxy form? What is its place, and ours, in the cosmic evolution? Modern astrophysics has revealed that the origins of our planet, our Sun and the Milky Way are intricately tied to the nature of the early Universe and the laws of physics.

Modern sophisticated observations of the far-field Universe have shown that the Milky Way is just one more galaxy among millions of them (with different shapes: ellipticals, spirals, dwarf galaxies) that constitute the Universe. The development of a standard model of cosmological structure formation, the Λ CDM (Λ Cold Dark Matter), has been extremely useful in explaining the large-scale matter and galaxy distribution, providing a framework of how galaxies form and evolve (see e.g. reviews by Springel et al., 2006, Frenk & White, 2012). The Λ CDM model predicts a flat universe in accelerated expansion (the cosmological constant, Λ , represents the dark energy influence in the acceleration), with densities (Ω_M, Ω_Λ) $\sim (0.3, 0.7)$ (see e.g. Spergel et al., 2007), where Ω_Λ is referred to the dark energy and Ω_M to the total matter (from which baryonic matter only corresponds to a small fraction: $\Omega_B \sim 0.04$).

In the Λ CDM model, nonlinear processes transformed the near-uniform universe that emerged from the Big Bang into the highly structured world that we observe today. In other words, density fluctuations in the dark matter leded to the presence of inhomogeneities and the growth of gravitational instabilities. Each instability could be considered as an isolated system (the seeds of the structure formation), decoupled from the Universe expansion. Those overdensities described an spherical collapse forming a dark matter halo. The final dark matter distribution is the result from the reached dynamical equilibrium among the different local overdensities inside the halo during the collapse ('violent relaxation', Lynden-Bell, 1967, Schneider, 2015). Thus, the galaxies are hierarchically formed inside the dark matter haloes, through the accretion of dark

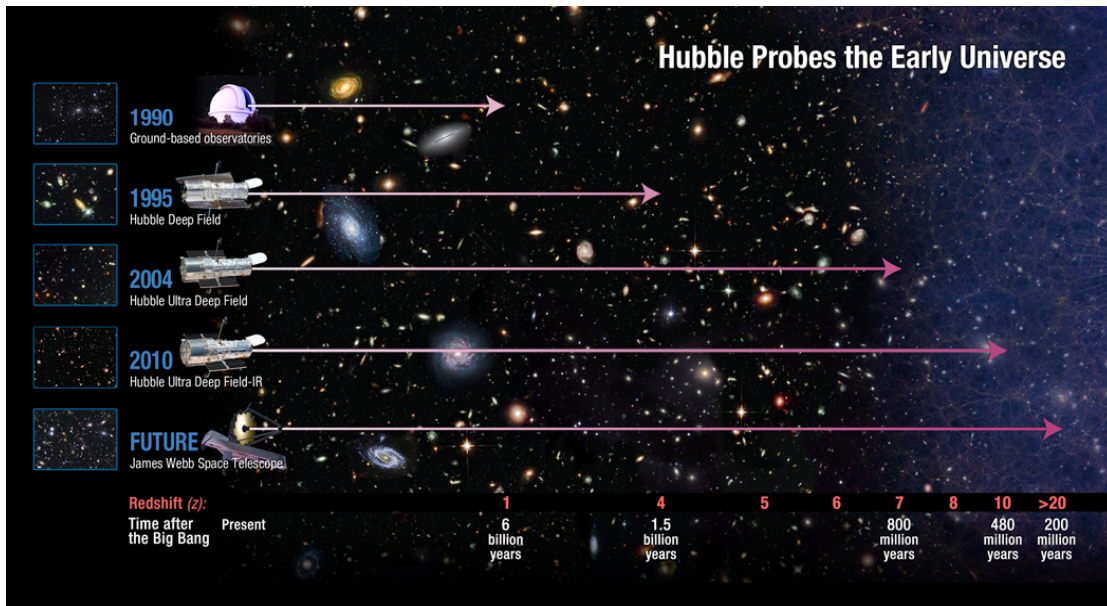


FIGURE 1.2: Illustration of the development of the observational facilities during the last decades to observe the far-field Universe, in the framework of the Hubble and James Webb Space Telescopes (Source: NASA, ESA, and A. Feild (STScI)).

matter substructures (White & Rees, 1978). The baryonic matter (in a gaseous configuration) is accrued in the described process, and it will form the visible structures of the Universe: the gas cooled and collapsed to the central regions, building a rotationally supported gaseous disc (Mo et al., 2010, Helmi, 2020) and forming the first stars (so-called Pop III, Abel et al., 2002) through the collapse of gas clouds.

The major development in observational facilities during the last century has allowed to observe the far-field Universe in increasingly detailed (see Fig. 1.2). The further we observe, the more we approach to the early Universe, from which the light is reaching us at the present day³. As a consequence, the Λ CDM model has been supported by strong observational evidences: the Hubble’s law⁴ of the expansion of the Universe (Hubble, 1929), the measured chemical abundances of light elements produced in the first three minutes after the Big Bang by a rapid nucleosynthesis of the primordial hydrogen (deuterium, D, helium isotopes, ^3He , ^4He , and lithium, ^7Li), and the measured cosmic background radiation, CMB⁵. The CMB was firstly measured by Penzias & Wilson (1965) and more precisely by recent space missions as COBE (COsmic Background Explorer, Mather et al., 1990), WMAP (Wilkinson Microwave Anisotropy Probe, Spergel et al., 2007), and PLANCK (Planck Collaboration et al., 2016). The latest measured values of cosmological parameters by PLANCK were: $H_0 = 67.81 \pm 0.92$, $\Omega_\Lambda = 0.692 \pm 0.012$, and $\Omega_M = 0.308 \pm 0.012$ (see Table 4 in Planck Collaboration et al., 2016).

In addition, the detailed examination of our Galaxy offers a near-field small-scale cosmological approach. The described Λ CDM cosmology, on smaller scales, has still difficulties on reproducing the physical properties of galaxies like the Milky Way (e.g. Scannapieco et al., 2012). In particular, the extremely complex physics of baryons is still unreliably simulated. Baryon physics implies highly non-linear processes that are presently introduced in the galaxy evolution models via parametrised heuristic algorithms. For instance, the lack of a complete theory for

³The speed of light is finite: $c = 299792.458 \text{ km s}^{-1}$.

⁴ $v = H_0 \cdot D$; where v is velocity due to the expansion and D the distance of the galaxy with respect to the observer (galaxies are moving away faster the further they are). Hubble measured the distance by the luminosity of variable Cepheids stars.

⁵Relic radiation from an early stage of the universe when first atoms started to form, with a temperature of 2.73 K and extremely isotropic (anisotropies of an order of magnitud 10^{-5}).

the formation of stars forces to use empirical relations between the cold gas and the star formation rate (SFR⁶, Schmidt, 1959). Additionally, among other issues, the Λ CDM model predicts a higher number of low-luminosity galaxies (White & Rees, 1978, Frenk & White, 2012), and, for instance, it predicts a larger number of satellite galaxies for the Milky Way (‘missing satellite problem’, Klypin et al., 1999, Strigari et al., 2007, Bullock et al., 2010). The theoretical models require calibration with well-studied (nearby) test cases, and the Galactic Archaeology approach (see Sect. 1.2) offers a unique opportunity to provide such constraints.

Today, the observational evidences of interaction between the Milky Way and its satellites are multiple (e.g. Ibata et al., 1994, Antoja et al., 2018, Laporte et al., 2019, Helmi, 2020). This affects our galaxy dynamics, star formation history, morphology, structure, and chemical enrichment. Translated into Kant’s terms, the galaxies are not ‘island-universes’. The high frequency of these encounters (from observations and simulations) supports the hierarchical Galactic formation model, where the galaxy is formed by mergers of smaller galaxies that provide gas to the formation and evolution of the disc.

1.1.3 Structure of the Milky Way: stellar components

From a morphological point of view, the Milky Way is defined as a spiral disc galaxy with a central bar (SBbc-type galaxy in Hubble’s morphological classification, later extended by Vaucouleurs, 1959). The Milky Way is constituted by $\sim 10^{11-12}$ stars, with a total stellar mass of $\sim 10^{11} M_{\odot}$ ⁷ (see e.g. Sparke & Gallagher, 2006), distributed in several structural components with different retained signatures of their formation process: a bulge with a bar, the disc (thin and thick components), and the halo. The current diagram of the Milky Way is shown in Fig. 1.3, similar to other observed nearby spiral galaxies (e.g. Andromeda M31). The components are physically distinct, showing differences in their stellar ages, chemical abundance distributions, dynamics and spatial locations.

The stellar halo

The stellar halo is the most extended structure, considered as an spheroidal component (although the tidal streams of the Sgr dwarf galaxy suggest that the halo is triaxial, Law et al., 2009), with a radius of ~ 100 kpc (Sirko et al., 2004), and a stellar mass around $1.3 \times 10^9 M_{\odot}$ (Deason et al., 2019) immersed in a larger dark matter halo of $10^{12} M_{\odot}$ (Binney & Tremaine, 2008). The stellar halo population is mainly composed by old stars ($\gtrsim 10$ Gyr, Tolstoy et al., 2009) with very low metallicities⁸ (average $\langle [\text{Fe}/\text{H}] \rangle = -1.2$ dex, Conroy et al., 2019), describing very eccentric⁹ orbits far from the Galactic plane, and with zero rotation speed around the Galactic centre (no angular momentum), being mostly kinematically supported by random motions.

In the halo, the stellar population density is low, and many of the found stellar systems (e.g. field stars, globular clusters, dwarf galaxies, stellar streams) seem to have been accreted by the Galaxy through satellite interactions (in agreement with Λ CDM model predictions, described

⁶SFR: star formation rate. It corresponds to the stellar mass formed in a certain period of time (M_{\odot}/yr), being a measurement of the rhythm of star formation.

⁷ M_{\odot} : solar mass = 2×10^{30} kg.

⁸A metal is any chemical element heavier than helium (He) (i.e. all except hydrogen (H) and He). The notation for the global stellar metallicity can be expressed by $[\text{M}/\text{H}]$ (considering all the metal lines as M) or $[\text{Fe}/\text{H}]$ (iron lines are the most numerous ones in the optical).

The chemical abundance is always expressed with respect to the Sun in a logarithmic scale: e.g. $[\text{Fe}/\text{H}] = \log \left[\frac{N(\text{Fe})}{N(\text{H})} \right]_{\star} - \log \left[\frac{N(\text{Fe})}{N(\text{H})} \right]_{\odot}$, where $N(X)$ is the density of the number of atoms for the element X.

⁹The eccentricity of an orbit can be estimated as $\sqrt{1 - b^2/a^2}$, where a is the length of the semi-major axis and b the length of the semi-minor axis. It presents values from 0 (circular orbit) to 1 (parabola).

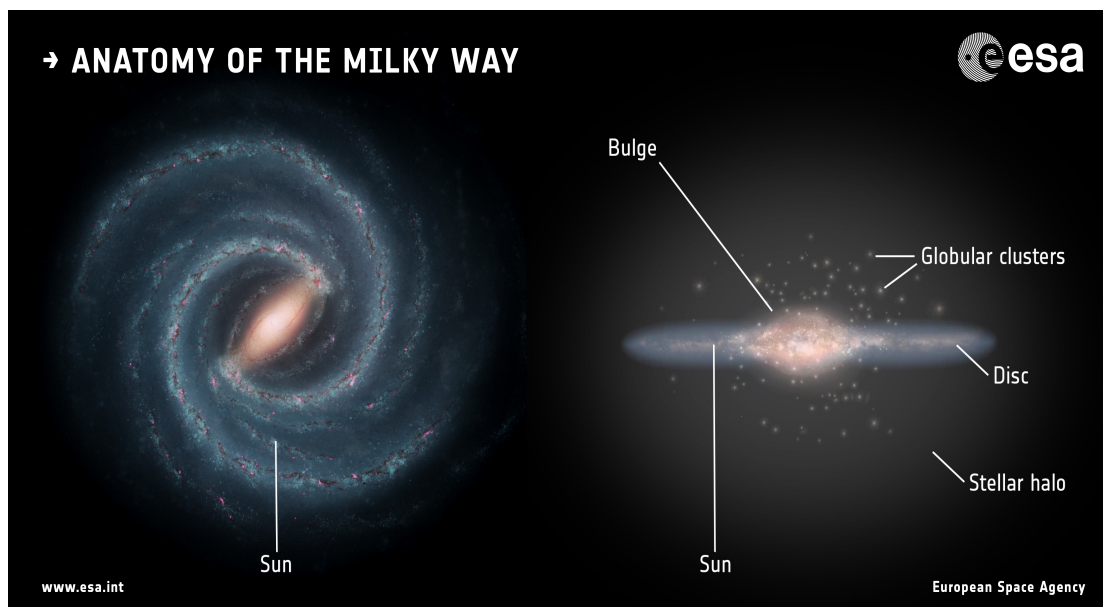


FIGURE 1.3: Illustrative view of the different stellar structures of the Milky Way.

in previous Sect. 1.1.2). Therefore, the metal-poor halo of the Milky Way is a very interesting field for galaxy formation studies, constituted by some of the first formed Galactic objects, and where globular clusters seem to be remnants of early satellite galaxies, which experienced an independent chemical evolution (Freeman & Bland-Hawthorn, 2002, Bland-Hawthorn et al., 2014). These systems would have deposited their dark matter and their stars into the Galactic disc. The pioneer analysis of Searle & Zinn (1978) on halo globular clusters pointed towards two possible different halo populations: an inner halo that may have formed *in-situ* during the dissipative collapse (monolithic model by Eggen et al., 1962), and an outer halo population accreted from satellite galaxies. More recently, Carollo et al. (2007) distinguished two separated halo populations using data from the Sloan Digital Sky Survey (SDSS, York et al., 2000): an inner halo formed *in-situ* with an averaged $\langle [\text{Fe}/\text{H}] \rangle = -1.6$ dex, and an outer accreted halo more metal-poor $\langle [\text{Fe}/\text{H}] \rangle = -2.2$ dex. However, the definition of the dual nature of the halo is still under debate, since several studies have found an important fraction of *ex-situ* stars populating the inner halo (e.g. Helmi et al., 2018). Therefore, the inner/outer distinction may correspond to a simple variation of properties with distance. The accreted stellar system candidates have shown lower $[\alpha/\text{Fe}]$ ¹⁰ abundances and different kinematics with respect to the *in-situ* stars (Nissen & Schuster, 2010, Fernández-Alvar et al., 2018). Some observed accreted stellar streams in the halo are the Sagittarius stream (Ibata et al., 1994) or the Helmi stream (Helmi et al., 1999).

The Galactic disc(s)

The Galactic disc is the most massive stellar component, which comprises the 75% of the total stellar mass of the Galaxy ($6 \times 10^{10} M_{\odot}$, Sofue et al., 2009, Bland-Hawthorn & Gerhard, 2016). The stars, gas and dust of the disc are supported by a rotation pattern around the Galactic centre on fairly circular orbits. The Galactic disc structure can be decomposed into two different substructures well differentiated in stellar age, kinematics and chemical abundances: the thin and the thick disc (firstly identified by Yoshii, 1982, Gilmore & Reid, 1983).

¹⁰ α -elements are the result of the stellar fusion reactions that convert helium into heavier elements (see Chapter 1.2.1): carbon (C), oxygen (O), neon (Ne), magnesium (Mg), silicium (Si), sulfur (S), argon (Ar), calcium (Ca), and titanium (Ti).

Generally, with respect to the thin disc, the thick disc component comprises relatively old, metal-poor and $[\alpha/\text{Fe}]$ -enhanced stars (Fuhrmann et al., 1997, Soubiran & Girard, 2005, Adibekyan et al., 2011, 2012, 2013, Recio-Blanco et al., 2014, Haywood et al., 2013, Bensby et al., 2014, Hayden et al., 2015, 2017, Palla et al., 2020) that move in Galactic orbits with a larger scale height and longer scale length¹¹ (Robin et al., 1996, Ojha, 2001, Jurić et al., 2008, Kordopatis et al., 2011b, Katz et al., 2011). The exponential thin disc has a vertical scale height of about 300 pc and a radial scale length of 2.8 kpc (Ojha, 2001), while the thick disc present a vertical scale around 750 pc and a radial scale length about 3.5 kpc (Robin et al., 1996, Ojha, 2001, Kordopatis et al., 2011b). The Sun is currently located in the thin disc, with a Galactocentric distance of $R \sim 8.0$ kpc and a height of $z \sim 30$ pc (Eisenhauer et al., 2003).

The Galactic thin disc hosts the spiral arms, which consists of prominent regions with stars, gas clouds and dust, where most of the star formation processes take place in the Galaxy. They seem to have been forming stars at least for the last 10 Gyr with metallicities from $[\text{Fe}/\text{H}] \sim -0.7$ to $+0.3$ (Adibekyan et al., 2011, Fuhrmann, 2011, Haywood et al., 2013, Hayden et al., 2017, Helmi, 2020). However, the thick disc stellar population appears to be older than about 10 Gyr, with similarities in age and abundance ranges with globular clusters ($[\text{Fe}/\text{H}] \sim -2.2$ to -0.5 , Freeman & Bland-Hawthorn, 2002). This behaviour suggests that the thick disc stellar population could have been formed on a short timescale before the epoch of the thin disc formation (Haywood et al., 2013, Kordopatis et al., 2015a, Fuhrmann et al., 2017, Silva Aguirre et al., 2018, Delgado Mena et al., 2019, Grisoni et al., 2019, Palla et al., 2020). In addition, thin disc stars are more rotationally supported than the thick disc ones, showing different kinematics (Soubiran, 1993, Bensby et al., 2003, 2005, Reddy et al., 2006, Soubiran et al., 2008). The circular velocity of thin disc stars at the solar radius is known as the velocity of the *Local Standard of Rest* (LSR), and its value is $V_{\text{LSR}} \approx 220 \text{ km s}^{-1}$ (Kerr & Lynden-Bell, 1986, McMillan & Binney, 2010). The stellar interactions with spiral arms or giant molecular clouds can perturb their orbits and increase the velocity dispersion (Sellwood & Binney, 2002) and, therefore, the thin disc present a delay with respect the LSR (so-called *lag*) of about $\sim 10\text{-}15 \text{ km s}^{-1}$, while the thick disc is kinematically hotter and present a lower rotation speed, lagging the thin-disc rotation by $\sim 50 \text{ km s}^{-1}$ (Edvardsson et al., 1993, Soubiran et al., 2003, Bensby & Feltzing, 2006).

Furthermore, the $[\alpha/\text{Fe}]$ vs. $[\text{M}/\text{H}]$ plane provides some hints about how the disc stellar populations have evolved, showing two separated chemical sequences. The observed thick disc population has been reported to be $[\alpha/\text{Fe}]$ -enhanced relative to the thin disc for most metallicities, unveiling distinct chemical evolution histories in both disc components (e.g. Soubiran & Girard, 2005, Adibekyan et al., 2012, Recio-Blanco et al., 2014, Fuhrmann et al., 2017). The chemical evolution scenario of the Milky Way will be described in detail in Section 1.5, and it is one of the main goals of this thesis.

Bulge

The spheroidal part of the Galaxy also comprises the bulge (see the complete review by Barbuy et al., 2018), which is the most centrally concentrated component (radius ~ 3 kpc, Binney et al., 1997), more voluminous than the disc (scale height $h = 0.5$ kpc), and with a stellar mass around $1.6 \times 10^{10} M_{\odot}$ (Gerhard, 2006). In particular, the bulge has a triaxial structure (Law et al., 2009): with a symmetric stellar distribution with respect to the Galactic plane ($z = 0$) but not with respect to the galactic longitude, being brighter and thicker towards positive longitudes ($l > 0$). The stars present eccentric orbits (some retrogrades) without following the rotation pattern of the disc, being able to recover far distances with respect to the Galactic plane. Furthermore, the Galactic bulge is dominated by stellar populations older than 10 Gyr (Feltzing

¹¹The scale height (length) is defined as the vertical (radial) distance z (R) for which the density has decreased by a factor of $1/e \sim 0.37$ with respect to the density at $z=0$ ($R=0$).

& Gilmore, 2000, Zoccali et al., 2003) that show a bimodal metallicity distribution between $-1.0 \lesssim [\text{Fe}/\text{H}] \lesssim 0.5$ dex, with peaks at $[\text{Fe}/\text{H}] \sim -0.5$ and $[\text{Fe}/\text{H}] \sim +0.3$ (Zoccali et al., 2008, Bensby et al., 2013, Nandakumar et al., 2018). In addition, they appear to be $[\alpha/\text{Fe}]$ -enhanced, similar to the local thick disc component ($[\alpha/\text{Fe}] \sim +0.3$ dex, e.g. Meléndez et al., 2008, Ryde et al., 2009, 2010, Jönsson et al., 2017, Thorsbro et al., 2020).

The bulge is currently described as a superposition of two components: a “classical” bulge (old metal-poor population, supported by random motions of stars, and probably formed via mergers in an initial dissipative collapse, Eggen et al., 1962), and an X-shaped boxy/peanut bulge (metal-rich stars showing a cylindrical rotation pattern, formed primarily via disk/bar dynamical instabilities, Hill et al., 2011, Rojas-Arriagada et al., 2017, Matteucci et al., 2019). The global velocity dispersion is higher than in the disc, showing a similar value to the halo component ($\sim 120 \text{ km s}^{-1}$, Howard et al., 2008). The presence of an X-shaped bulge with cylindrical rotation (i.e. the rotational velocity is constant with height above the galactic plane) reveals the existence of a central bar (Howard et al., 2009, Wegg & Gerhard, 2013, Zoccali et al., 2014). Recent works suggested the presence of a long bar with an angle of $\sim 25^\circ$ with respect to the line-of-sight¹² (e.g. Wegg et al., 2015). The bar has been reported to host a high density of stars, more metal-rich compared to the rest of the bulge (Hill et al., 2011), and to drive radial migration of matter in the Galaxy (stars, gas, and dust).

In the inner parts of the bulge, where it is extremely difficult to observe due to the high interstellar extinction provoked by the presence of dust, a very intense radio source has been measured, along with some orbits from the high number density of stars around this particular region: the center of the Galaxy, Sgr A*. This region have a stellar mass of $4 \times 10^6 M_\odot$ in a small radius $\sim 0.001 \text{ pc}$ (Ghez et al., 2008), which constitute an indirect evidence of the presence of a supermassive black hole (SMBH). In addition, there are direct observations of matter accretion by the black hole, emitting X-rays radiation (Baganoff et al., 2003).

The bulge formation is not an essential element of the formation processes of disc galaxies (more luminous disc galaxies have bulges, but many of the fainter ones do not). Based on the mentioned properties, the $[\alpha/\text{Fe}]$ enrichment of the bulge stars in the Milky Way could have come from the rapid star formation and chemical evolution that took place in the inner disc before different instabilities had time to act (Freeman & Bland-Hawthorn, 2002, Bland-Hawthorn et al., 2014).

1.2 Galactic archaeology

Galactic archaeology (term adopted from the influential review by Freeman & Bland-Hawthorn, 2002) aims at unveiling the history of the Milky Way by analysing stars, just as the history of life was deduced from examining rocks. Stars record the past in their ages, chemical compositions, kinematics (velocity space) and dynamics (orbital properties). In particular, because of low-mass stars have long lifetimes, they can provide unprecedented detailed constraints on the early phases of galaxy formation, back to redshifts greater than two (a look-back time of 10 billion years).

As a consequence, a deep insight into the formation and evolution of the Milky Way demands precise chemical abundances, ages, and astrometric¹³ information from the different stellar populations in the Galaxy.

¹²Angular separation between the major axis of the bar and the Sun-Galactic Center direction.

¹³Astrometry: branch of the astronomy that involves precise measurements of the positions and movements of the stars or other celestial bodies.

1.2.1 Chemical abundances as tracers of the star’s history

The stellar chemical “tagging” approach consists of the measurement of chemical abundances in the photosphere of the stars. This approach relies on the fact that the stellar upper atmospheres, particularly from main-sequence FGK-type stars, provide fossil evidence of the available metals of the interstellar medium (ISM) at the time of its formation (Freeman & Bland-Hawthorn, 2002). The basis is that stars are known to contribute to the chemical enrichment of the ISM through matter release during their evolution (e.g. stellar winds, supernova explosions). Therefore, the next generation of stars will be formed from the enriched gas, retaining in their atmospheres a fossil record of that environment. For a given isolated stellar population system, those stars with lower metallicity values will have been formed earlier than those more metal-rich. As a consequence, chemical tagging contains lots of information about the chemical evolution history of the Milky Way.

In order to properly analyse the Galactic star formation history (SFH) and evolution, a theory of stellar nucleosynthesis of chemical elements is required (Burbidge et al., 1957), along with a detailed description of the enrichment processes: amount of gas transformed into stars in a certain timescale (SFR), the initial mass distribution function (IMF) of the formed stars in a single star formation burst from a certain amount of gas, the different productions of elements (yields) for stars at different masses and timescales ranges, or the gas evolution in the Galaxy (e.g. migration, infall, or outflows).

Stellar nucleosynthesis

The origin of chemical elements lies in the interior of the stars during their lifetimes, produced via thermonuclear reactions. The stars are formed from the collapse of cold ($T < 100$ K) and high-density (10^{3-4} cm⁻³) molecular clouds and dust, which are mainly constituted by hydrogen and helium (produced in the Big Bang: 75 % H and 25 % He). The fragmentation of the cloud give birth of a group of stars with different masses and near-homogeneous chemical element composition. From that moment, the evolution of every star consists on a continuous battle between its gravity (that tends to collapse the star) and its internal pressure (that tries to expand it).

Once the stars are settled, the thermonuclear reactions starts in their cores by transforming hydrogen into helium. This first evolution phase, so-called the Main Sequence (MS), covers the 90% of the stars’ lifetime. The time spent in the MS directly depends on the stellar mass: the more massive stars evolve faster, burning the hydrogen more efficiently in their cores. Then, when the hydrogen is depleted, the core of helium contracts, increasing the temperature of the outer layers of the star. At that time, the star leaves the MS to enter into the sub-giant evolution phase. During this new phase, the fusion of hydrogen is located in a shell around the helium’s core, where, at the same time, the fusion of helium evolves producing carbon (C) and oxygen (O). From now on, the subsequent evolution of the star will depend on the stellar mass.

On the one hand, low-mass stars ($M_{\star} \lesssim 8 M_{\odot}$) develop a degenerated C-O core, and evolve in the asymptotic giant branch (AGB). During this phase, the star is thermally unstable, releasing the external layers to the ISM through different thermal pulses, and leaving an inert core mainly constituted by carbon and oxygen: a white dwarf (WD). In the case that the white dwarf is part of a binary system, it could accret material from the outer layers of its companion due to pair-instabilities. When the dwarf stellar mass exceeds $1.4 M_{\odot}$ (Chandrasekhar mass limit), the internal pressure cannot support the gravity forces, which provoke a collapse of the stellar structure, and the subsequent explosion as a type Ia supernova (SNe Ia; Whelan & Iben, 1973, Han & Podsiadlowski, 2004). The clock to the explosion is given by the lifetime of the stellar

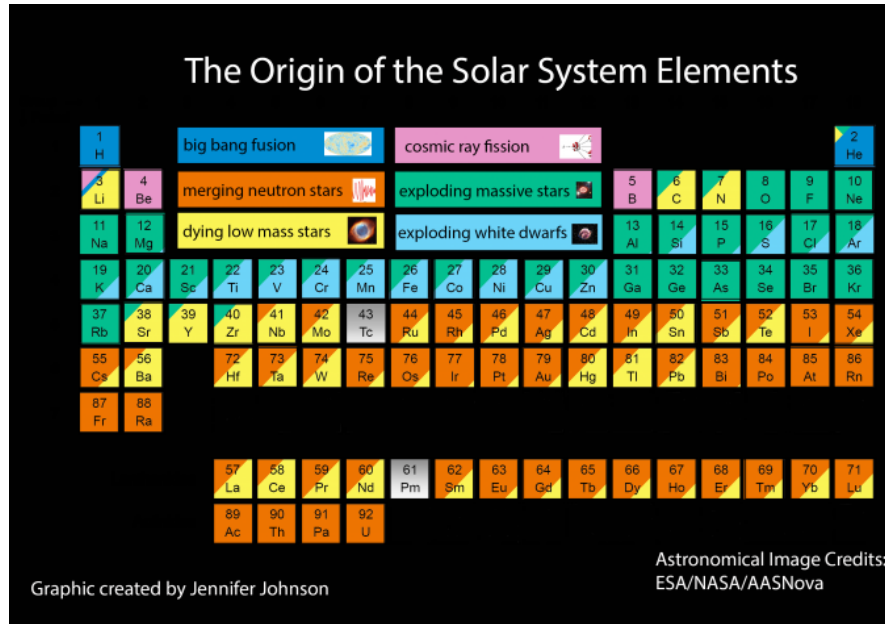


FIGURE 1.4: Origin of the chemical elements in the Universe.

companion ($\sim 10^{8-9}$ years, [Matteucci & Recchi, 2001](#)). This phenomenon releases a significant amount of Fe-peak elements (e.g. chromium, cobalt, nickel) to the ISM, being the main source of iron in the Universe (see blue coloured elements in Fig. 1.4).

On the other hand, a cascade of consecutive core collapses and expansions take place in the interior of more massive stars ($M_* > 8 M_\odot$) during the giant (or supergiant) phase. This leads to a chain of nucleosynthesis processes, developing an internal structure with different elements fusing at different layers: carbon, neon, oxygen, silicon, and iron. At the end of their lives, the star presents an internal layer structure (so-called ‘onion-skin’). The nucleosynthesis of more and more massive elements finally consumes the energy of the star, stopping the thermonuclear reactions, being the iron (Fe) the heaviest possible synthesised element inside a star. When the production of elements finishes, the star is not able to support its own weight, and the outer layers collapse towards the core, exploding as a type II supernova (SNe II). The generated shockwave releases to the ISM all the formed elements during its evolution (see green coloured elements in Fig. 1.4). They mainly produce α -elements and some Fe-peak elements, in shorter timescales than SNe Ia ($< 10^7$ years; e.g. [Tinsley, 1979](#)).

Stars more massive than $40 M_\odot$ will also end up as core-collapse SNe (known as Type Ib/c SNe). They mainly release α -elements as oxygen, magnesium or calcium, and are linked to gamma-ray bursts (GRB). As they are formed from rare, very massive stars, the rate of SNe Ib and Ic occurrence is much lower than the SNe II.

Chemical enrichment timescales in the Galaxy

As described in Sect. 1.1.2, the formation and evolution of stars and galaxies share the same time framework (from the Big Bang event, ~ 13.8 Gyr ago (e.g. [Bennett et al., 2003](#)), up to the present day). As a consequence, the timescale of the nucleosynthesis processes during the stars’ lifetimes provides an extraordinary cosmological clock.

In particular, the abundance of α -elements, relative to iron ($[\alpha/\text{Fe}]$), is an important fossil signature in Galactic archaeology to trace the chemical evolution of disc stellar populations.

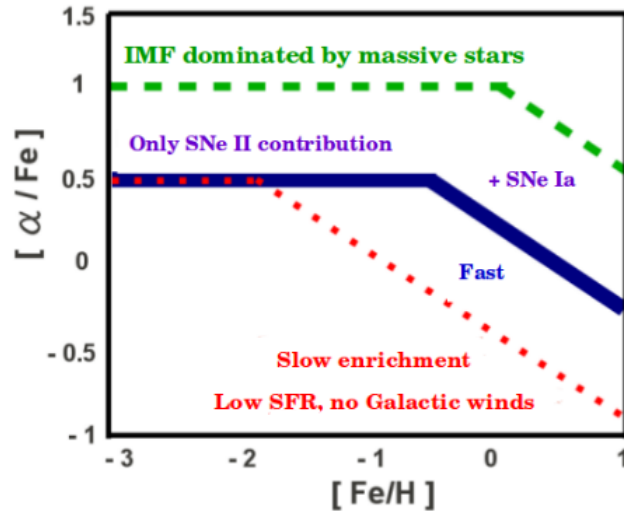


FIGURE 1.5: Chemical enrichment of α -elements for different star formation regions. The dashed green curve illustrates a region with an initial mass function (IMF) dominated by massive stars, i.e. mainly producing α -elements. The thick blue curve shows a region with a star formation rate (SFR) more significant than the one represented by red squares, which comprises the galactic winds expelling the gas to the interstellar medium (ISM). Increased initial mass function (IMF) and star formation rate (SFR) affect the trend in the directions indicated. The knee in the diagram is thought to be due to the onset of type Ia supernovae (SN Ia). (Source: Kordopatis, 2011, Wyse & Gilmore, 1993).

The behaviour of α -elements is well explained by the time-delay model paradigm (Matteucci & Greggio, 1986, Matteucci, 2012), which interprets the present time delay of the iron production from SNe Ia in comparison with the faster α -elements production from core-collapse supernovae SNe II of more massive stars. Concretely, the amount of Fe-peak elements released by SNe Ia is estimated to be three times larger than SNe II (Matteucci & Greggio, 1986, Timmes et al., 1995, Iwamoto et al., 1999). Figure 1.5 schematically illustrates the predicted chemical evolution of the $[\alpha/\text{Fe}]$ abundance as a function of the global metallicity (i.e. \sim iron abundance estimate $[\text{Fe}/\text{H}]$). The SNe II rapidly enrich the ISM ($< 10^7$ years), reproducing a flat trend at low metallicities, until the appearance of the SNe Ia explosions (at least 10^{8-9} years), which contribute to the $[\alpha/\text{Fe}]$ abundance decline in the ISM.

The position of the reported knee will depend on the star formation history and the environment of the analysed Galaxy or any other stellar system. The first application of the time-delay model to galaxies with different star formation histories can be found in Matteucci & Brocato (1990). For instance, an active SFR or a system that keep most of the their gas attached (no Galactic winds or outflows), will present the knee at higher metallicity regimes (i.e. more contribution of massive stars; Schmidt, 1959, Matteucci & Franco, 1989). Moreover, since the ratio $[\alpha/\text{Fe}]$ abundance depends on the stellar mass, the more massive the IMF (e.g. Salpeter, 1955, Kroupa et al., 1993), the higher the described ‘plateau’ in the $[\alpha/\text{Fe}]-[\text{M}/\text{H}]$ plane.

As a consequence, high-precision chemical abundances are crucial to improve our understanding of the chemodynamical properties present in the Galaxy. With the help of a dynamical model and the ages of the stars, it might be possible to find their original site of formation, their cluster membership, or identify discrete substructures from the chemical abundance space (Freeman & Bland-Hawthorn, 2002, Hogg et al., 2016). In addition, accurate and precise abundances of large samples of stars are highly required to constrain chemical evolution models in order to properly reproduce the variety of physical processes taking place inside stars, and their relation with

stellar masses and lifetimes. However, deriving precise abundance estimations from metal-rich stars is still challenging for analysis procedures, as it will be further discussed throughout this manuscript.

1.2.2 Stellar kinematics

As it was already introduced in Sect. 1.1.3, the different major stellar components in the Galaxy retains different kinematical and dynamical information, where the stars show different orbital properties (e.g. eccentricity, rotation pattern speed, angular momentum). To separate different stellar populations by their kinematics, the space velocity components (U,V,W)¹⁴ are generally computed with respect to the LSR. However, kinematic signatures can be modified or completely erased with time through the secular evolution of the Galaxy (e.g. migration, tidal forces from satellite encounters, dynamic perturbations with spiral arms).

In the framework of the Λ CDM model (Sect. 1.1.2), the galaxies are formed following an hierarchical evolution model, that is, by accretion of smaller systems which can be considered as building blocks. In this way, when a satellite is caught by the Galactic gravitational potential, it will deposit stellar debris on the host galaxy at every pericentric passage, forming stellar streams. This disrupted material can be identified in the velocity space. For instance, based on purely kinematic analysis over metal-poor stars in the Milky Way halo, Helmi et al. (1999) found two stellar streams from the same satellite progenitor. Moreover, recent analysis have revealed that the Galaxy is out of equilibrium, finding evidence that the Galactic disc can be strongly perturbed by external interactions with satellite galaxies (Antoja et al., 2018, Laporte et al., 2019). In line with this findings, Helmi et al. (2018) and Belokurov et al. (2018) found clear kinematical and spatial signatures of a major accretion event by a massive satellite approximately 10 Gyr ago, so-called *Gaia*-Enceladus/Sausage.

Furthermore, in order to distinguish the different Milky Way components from an observed stellar sample, a pure kinematical approach can be performed by using Toomre diagrams. Figure 1.6 illustrates two application examples: for the selection of thick disc-halo stars (left panel; Nissen & Schuster, 2010), and a local identification of thin-thick disc stars in the solar neighbourhood (right panel; Bensby et al., 2005). In a Toomre diagram, the V_{LSR} component represents the stellar angular momentum and has an asymmetric distribution with a negative mean. The U and W components have more or less symmetric distributions about zero mean, so their combination is a measure of the orbital energy (Bland-Hawthorn et al., 2014). For instance, Nissen & Schuster (2010) assume Gaussian velocity distributions with canonical dispersions and asymmetric drifts for the thin, thick disc, and halo populations. Then, for a given star, the relative likelihoods can be computed to identify to which stellar component they belong. For instance, stars with $V_{\text{total}} > 180 \text{ km s}^{-1}$ generally have a high probability of belonging to the halo population (Venn et al., 2004). On the other hand, if it is assumed a non-Gaussian velocity distribution for the thick disc, with an extended tail toward high velocities (Schönrich & Binney, 2009), then the high- α stars with $180 < V_{\text{total}} < 210 \text{ km s}^{-1}$ might belong to the thick-disc population.

The computation of the stellar orbits demands an accurate and precise measurements of radial velocities, proper motions and distances. I will describe in the following Sect. 1.3 how the European Space Agency (ESA) *Gaia* mission has revolutionised the field with an unprecedented precision in the Milky Way. Additionally, both internal (e.g. bar or spiral arms) and external (e.g. satellites) dynamical interactions in the Galaxy can lead to sub-structures with similar kinematical information (e.g. UVW, eccentricities). As a consequence, the combination of

¹⁴Velocity space (km s^{-1}) is defined by coordinates U: positive toward the Galactic center, V: positive in the direction of Galactic rotation, and W: positive toward the North Galactic Pole.

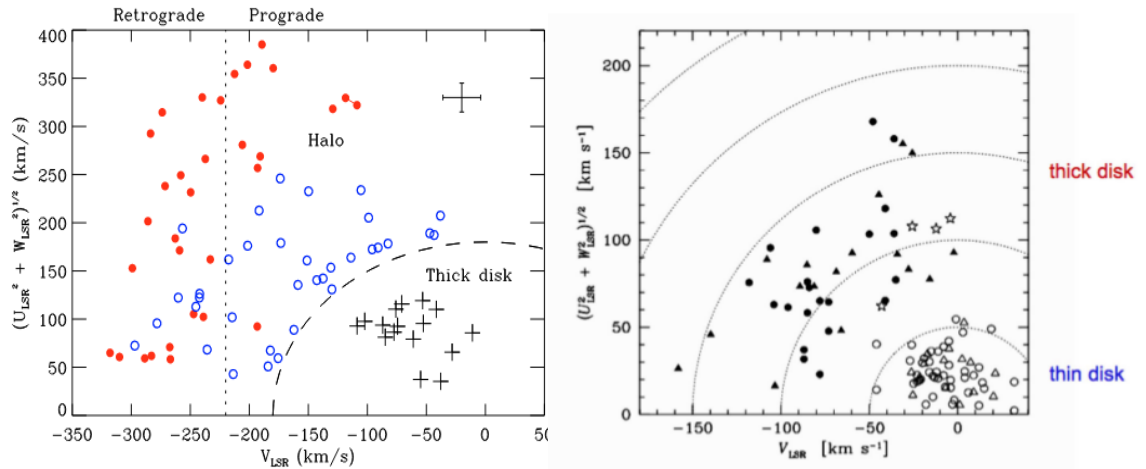


FIGURE 1.6: **Left:** Toomre diagram for halo and thick-disk stars. Stars with halo kinematics have been divided into high-alpha stars shown with open blue circles and low-alpha stars shown with filled red circles. Stars with thick-disk kinematics are shown with crosses. Only stars with $[\text{Fe}/\text{H}] > -1.4$ are included. The long-dashed line corresponds to $V_{\text{total}} = 180 \text{ km s}^{-1}$ and the dotted line separates stars moving in retrograde orbits from stars with prograde orbits. (Source: [Nissen & Schuster, 2010](#)). **Right:** Toomre diagram for the thick and thin disc stars are marked by filled and open symbols, respectively. (Source: [Bensby et al., 2005](#)).

stellar kinematics and chemical abundances looks crucial to disentangle the *in-situ* with respect to the *ex-situ* (accreted) stellar populations in the Galaxy.

1.2.3 Stellar age dating

Ideally, the best way to date the sequence of events that led to the formation of the different components of the Galaxy, and their subsequent evolution, would be through the measurement of accurate stellar ages. However, individual reliable estimates of stellar ages are constrained to a certain reduced stellar type samples (see e.g. complete review by [Soderblom, 2010](#)), being still difficult to measure without leading to high uncertainties in the Galactic evolution. For that reason, the chemical abundance ratio of two elements, produced by two different nucleosynthesis processes, are a widespread indirect technique to obtain a timescale estimate (as previously introduced in Sect. 1.2.1). The most important direct methods for deriving individual stellar ages are described hereunder:

Isochrone fitting methods

Isochrone¹⁵ fitting methods have been widely used for determining individual stellar ages. The method consists in a comparison of the absolute stellar luminosity L ¹⁶ (or magnitude M ¹⁷) and the effective temperature T_{eff} ¹⁸ (or color) with theoretical isochrones that are derived from stellar evolution models. When the metallicity $[\text{Fe}/\text{H}]$ is known, the regions on the Hertzsprung-Russel diagram where L and T_{eff} depend on the age can give a precise estimate, that is, for main sequence turn-off (MSTO) stars and the sub-giant branch (see Fig. 1.7). For other stellar populations, a complex overlap of different isochrones leads to multi-valued age estimates. In

¹⁵Theoretical lines that link stars with the same age and different masses.

¹⁶A measure of the total amount of energy radiated by a star per second.

¹⁷Apparent magnitude (m): measure of the brightness of a star observed from the Earth.

Absolute magnitude (M): measure of the intrinsic brightness, apparent magnitude from a distance of 10 pc.

¹⁸Temperature at the upper stellar atmosphere (photosphere), that corresponds to a blackbody emitting energy from its surface like a star: $\text{Flux} = \sigma T_{\text{eff}}^4$, where σ is Stefan-Boltzmann constant ($\sigma = 5.67 \times 10^{-5} \text{ erg cm}^{-2} \text{ s}^{-1} \text{ K}^{-4}$).

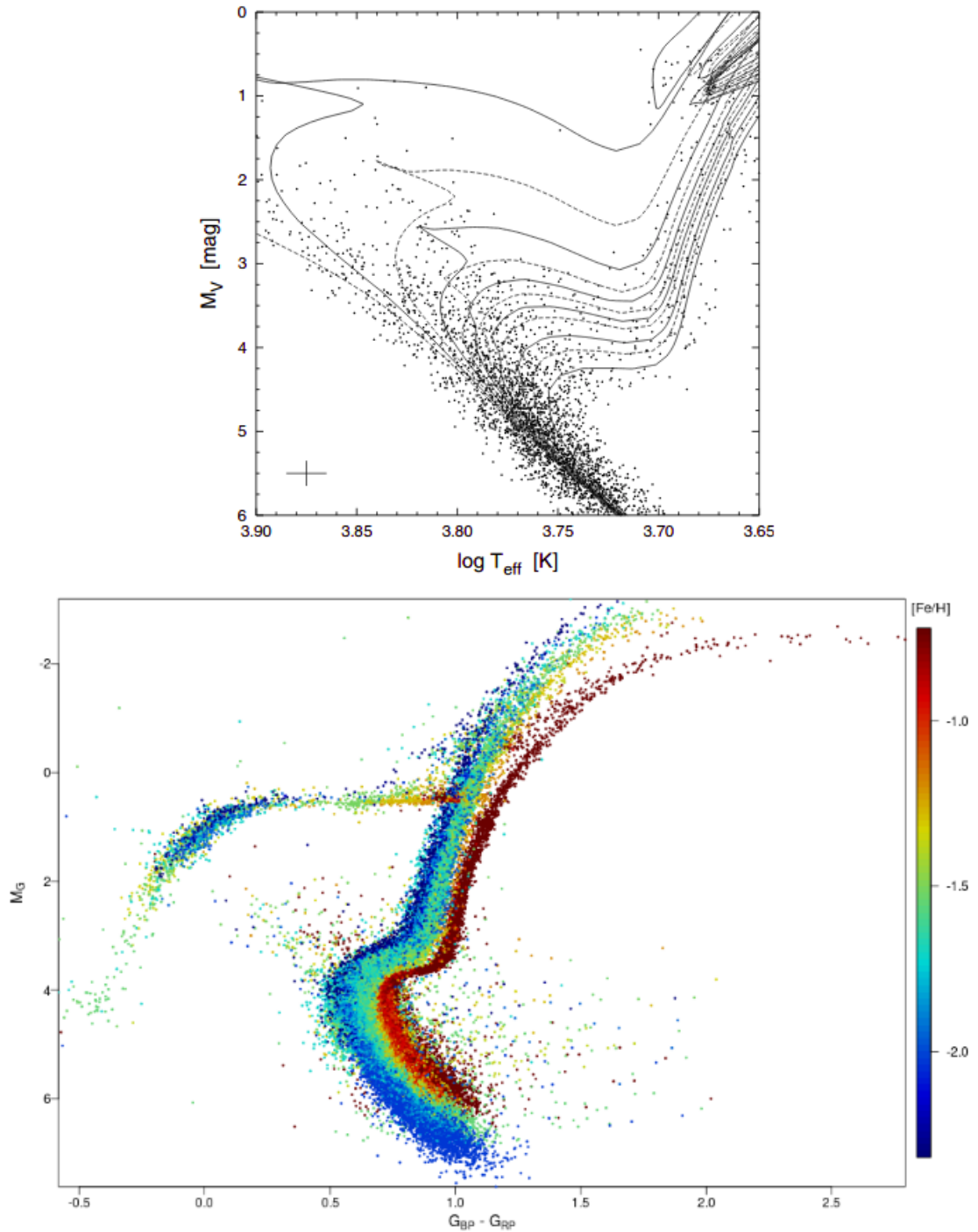


FIGURE 1.7: **Top:** Hertzsprung-Russel (HR) diagram for a generated sample of 2968 stars. The assumed observational uncertainties in $\log(T_{\text{eff}})$ and M_V are indicated in the lower-left corner (in addition there is a ± 0.1 dex uncertainty in metallicity). The isochrones are for ages = 0, 1, 2, ..., 8, 10, 12 and 15 Gyr. (Source: [Jørgensen & Lindegren, 2005](#)). **Bottom:** HR diagram for 14 globular clusters, coloured according to metallicity, using the extinction and distance moduli as determined from the *Gaia* data. (Source: [Gaia Collaboration et al., 2018b](#)).

addition, this technique is particularly useful for estimate the age and the distance of stars clusters, which populate the color-magnitude plane, and the isochrone can be fitted to the main sequence, turn-off region and the red-giant branch (RGB). The average relative precision are often around 20–50% (Jørgensen & Lindegren, 2005, Soderblom, 2010).

To obtain a precise age estimate, accurate parallaxes (to provide the absolute luminosity/magnitude after an extinction correction) and high-resolution spectroscopy or broad-band photometry (to derive T_{eff} and $\log g$ ¹⁹) are required. With the advent of the *Gaia* mission (Sect. 1.3), a huge increase in accurate parallaxes has been achieved, and hence in the precision of the age determination.

Asteroseismology

Asteroseismology is a direct age estimate technique via the knowledge of the internal structure of a star. The stellar oscillation frequencies, measured by photometric or radial velocity variations, depend on the density distribution in the stellar interior, that is, on the stellar mass, effective temperature global metallicity, and radius of the star. The frequency spectrum of stellar oscillations, together with stellar evolution models, can be used to estimate the mass of the star, which changes with the stellar age for main-sequence and giant stars. The main source of uncertainties comes from the problems in modelling the stellar interior (e.g. transport equation, atmosphere pulsations, near-surface convection area).

The space missions COROT (COnvection, ROtation and planetary Transits, Auvergne et al., 2009), Kepler (Gilliland et al., 2010), and the ongoing TESS mission (Transiting Exoplanet Survey Satellite, Ricker et al., 2015), have recently improved the age determination via asteroseismology in their respective explorations of the structure and diversity of planetary systems in the Milky Way. They monitor the changes in a star’s brightness that comes from a planet transit. They are able to detect acoustical waves generated deep inside a star that send ripples across a star’s surface, altering its brightness. The exact nature of the ripples allows to calculate the star’s precise mass, age and chemical composition.

Other techniques: gyrochronology and nucleo-cosmochronology

There are few other techniques for deriving ages of individual stars based on stellar rotation (gyrochronology), chromospheric activity, and radioactive elements decay (nucleo-cosmochronology); see pioneer work by Skumanich (1972).

For main-sequence stars, the rotation period (typically measured via photometric surveys, e.g. COROT, Kepler) can be used to estimate the stellar age: the stars spin down with age. In addition, for the same stellar type, a decrease of chromospheric activity with age has been reported by analysing the stellar chromospheric Calcium-K emission (Ca K; pair of Fraunhofer lines in the violet, associated with ionised calcium). The same can be said for the Lithium abundance. Both techniques require a previous calibration on star clusters and the Sun, and have shown a good agreement between each other (Barnes, 2007, Bland-Hawthorn et al., 2014).

Finally, nucleo-cosmochronology is a direct method based on the aging of the element through radioactive decay, widely used to date meteorites in solar-system geophysics. It consists in a high-precision method on the spectroscopic abundances of heavy radioactive isotopes of uranium (²³⁸U) and thorium (²³²Th) (Fowler & Hoyle, 1960, Hill et al., 2002). It can be effectively applied to old metal-poor stars in the Galaxy. The main limitation is the poor presence of uranium and thorium lines in the stellar spectra.

¹⁹Surface gravity of the star, corresponds to: $g = G M_{\star}/R_{\star}^2$, where G is the gravitational constant ($G = 6.67 \times 10^{-8} \text{ cm}^{-3} \text{ g}^{-1} \text{ s}^{-2}$), and M and R are the mass and the radius of the star, respectively.

1.3 The Gaia mission

*Gaia*²⁰ is the first astrometric and spectroscopic space mission, being the cornerstone of the ESA's (European Space Agency) science programme since 2000 (Perryman et al., 2001). The *Gaia* satellite was launched the 19th December 2013, and currently orbits the Lagrangian point L2 of the Sun-Earth-Moon system, performing an autonomous and unbiased on-board observing detection programme. Following the legacy of the pioneer astrometric spatial mission *Hipparcos* (HIGH Precision PARallax COLlecting Satellite, Perryman et al., 1997), *Gaia* provides accurate astrometry (parallaxes²¹, positions and proper motions²²) and spectrophotometry for more than one billion objects in the Milky Way (complete catalogue up to $G = 20.7$ mag, i.e. $V = 20-22$), and radial velocities²³ for one hundred million brighter sources ($G \lesssim 17$ mag).

Compared to *Hipparcos* astrometry (errors around 10^{-3} arcseconds, *mas*), precision in parallaxes and proper motions have been reduced by three orders of magnitude with *Gaia* ($\sim 10^{-6}$ arcseconds, *μas*). As a consequence, *Gaia* is providing a precise 6-D view (radial velocity + five astrometric parameters: parallax (distance), two-coordinate positions and proper motions) of our Galaxy in unprecedented detail.

A large pan-European team of expert scientists and software developers known as DPAC (Data Processing and Analysis Consortium, Mignard et al., 2008) is responsible for the processing of *Gaia*'s data with the final objective of producing the *Gaia* Catalogue. Coordinated by the DPAC Executive, the consortium is sub-divided into nine Coordination Units (CU), with each unit being assigned to a unique set of data processing tasks. The nominal *Gaia* mission supposed to end on mid-2019 after 5 years of measurements, although the ESA Science Programme Committee (SPC) confirmed the *Gaia* mission extension for mid-2019 to end of 2020, and has given an indicative extension up to end of 2022²⁴.

Gaia instruments

The satellite has two telescopes (1.45×0.5 m²) with an angular separation of $\sim 106.5^\circ$ (basic angle), both orientated perpendicularly to the spin axis. As the spacecraft slowly rotates, the object image transits the focal plane along the scan direction (see a full description of the *Gaia* spacecraft in Gaia Collaboration et al., 2016). In this way, *Gaia* steadily scans the whole sky, observing each part around 70 times in the course of the operational lifetime (~ 5 years). The focal-plane assembly is common to both telescopes, containing 106 charge-coupled devices (CCDs), and serves five main functions (see Fig. 1.8):

- The wave-front sensor (WF, Vosteen et al., 2009) and the basic-angle monitor (BAM, Meijer et al., 2009), covering 2+2 CCDs, for re-aligning the telescopes in orbit.
- The sky mapper (SM, Gai et al., 2005), 7 x 2 CCDs (seven per telescope), which autonomously detects objects with $G \lesssim 20$ mag entering the fields of view and communicates the transit's details to the subsequent CCDs.

²⁰Initially was the acronym of Global Astrometric Interferometer for Astrophysics (Lindegren & Perryman, 1996). The posterior abandon of the interferometric approach during the evolution of the project did not change the global name of the mission.

²¹Measured semi-angle corresponding to the apparent displacement of a star from two different line of sight (Earth on opposite sides of the Sun in its orbit) with respect to the stellar background. Nearby stars show larger parallax values than farther stars.

²²Time derivative of the position.

²³Line-of-sight velocities.

²⁴At the present time of this manuscript, an additional extension up to 2025 is close to being approved.

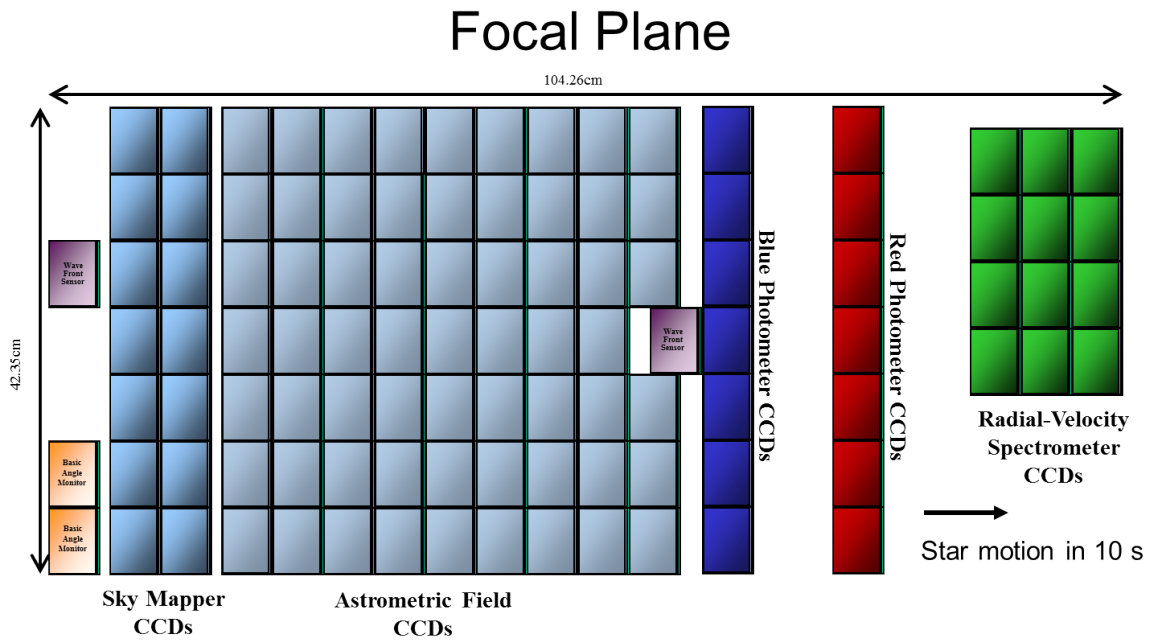


FIGURE 1.8: Schematic view of the *Gaia* focal-plane assembly. (Source: ESA).

- The astrometric field (AF), covering 62 CCDs (7 x 9, in the middle of the last column is placed one WF), provides the five astrometric parameters.
- The blue (BP, 330-680 nm) and red (RP, 640-1050 nm) photometers (7 x 1 CCDs), providing low-resolution spectro-photometric measurements for each observed object (Jordi et al., 2010, Evans et al., 2018, see Fig. 1.9).
- The radial velocity spectrometer (RVS, Cropper et al., 2018), uses the last 12 CCDs in a 3 x 4 arrangement, collecting medium-resolution ($R = \lambda/\Delta\lambda^{25} \sim 11500$) spectra of all objects brighter than 17th magnitude, and only stars in the temperature range [3550,6900] K. The instrument is a near-infrared (845-872 nm) integral-field spectrograph. It allows the derivation of radial velocities and stellar atmospheric parameters. In addition, it provides astrophysical information (e.g. extinction, stellar rotation) to $G_{RVS} \lesssim 14-15$, and some individual chemical abundances (Mg, Si, S, Ca, Ti, Cr, Fe, Ni) for the brightest sample up to $G_{RVS} \lesssim 11$. The magnitude limit varies depending on the observed number of transits and the need of a minimum signal-to-noise, which are different for each parameter and data release.

Gaia data releases

For the Milky Way stellar components (halo, disc(s), and bulge), *Gaia* is providing precise and accurate observations of tracers of the Galactic structure, kinematics, star formation and chemical evolution across the whole HR diagram (Gaia Collaboration et al., 2018b, e.g. *Gaia* DR2 contains 4 276 690 stars with $E(B - V)^{26} < 0.015$, filtered on parallax and photometry quality prescriptions, see an example in Fig. 1.7), including variable stars (e.g. Cepheids, RR Lyrae) and white dwarfs.

²⁵Where $\Delta\lambda$ is the FWHM (Full Width Half Maximum) of the instrumental profile.

²⁶The colour excess $E(B - V)$ is the difference between the observed color index of a star and the intrinsic color index predicted from its spectral type: $E(B - V) = (B - V)_{\text{observed}} - (B - V)_{\text{intrinsic}}$

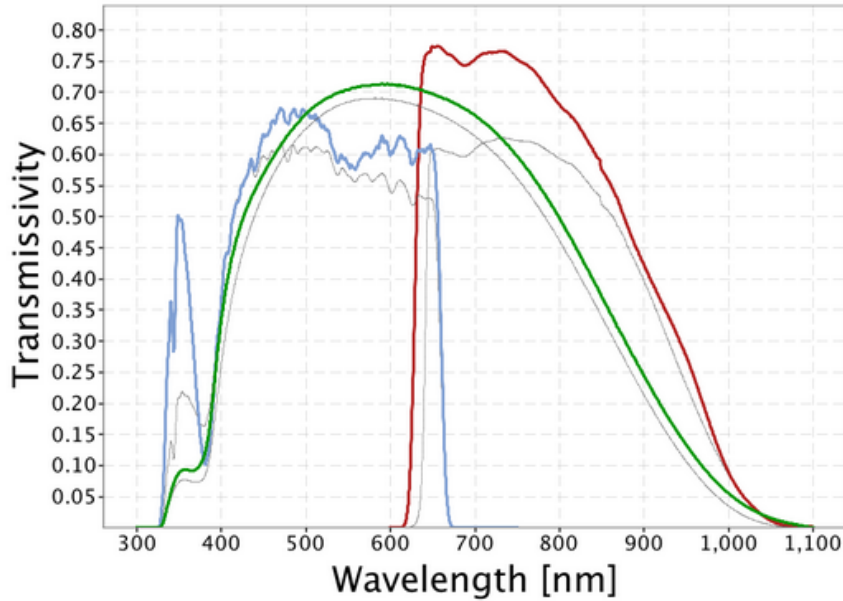


FIGURE 1.9: Passbands of the *Gaia* revised photometric filters (Evans et al., 2018): G_{BP} (blue), G (green) and G_{RP} (red), defining the *Gaia* DR2 photometric system. Grey lines represent the nominal pre-launch passbands (Jordi et al., 2010) used for *Gaia* DR1. (Source: ESA).

Figure 1.10 illustrates an overview of the public catalogues to date. The second *Gaia* data release (*Gaia* DR2²⁷) was published on 25th April 2018, based on data taken during less than half of the mission’s nominal lifetime (22 months out of 60), and containing the full astrometric solution and photometric values for more than 1.3 billion stars, with a limiting magnitude of $G = 21$. For more than 360 million extra sources, a two-parameter astrometric solution (position in the sky) is also reported with the mean G magnitude. The third *Gaia* Data Release (*Gaia* DR3) will be split into two releases: the early release called *Gaia* Early Data Release 3 (*Gaia* EDR3) and the full *Gaia* DR3. *Gaia* EDR3 was recently released on 3th December 2020. The full *Gaia* DR3 is planned for the first half of 2022, providing an updated and extended catalogues of variable stars and solar system objects, along with BP/RP and RVS spectra for sources with astrophysical parameters. Finally, a complete data release for the nominal mission (*Gaia* DR4) will be released with the epoch and transit data for all sources, including all BP/RP/RVS spectra.

Regarding the *Gaia* DR2 data, I first show in Fig. 1.11 the uncertainty in parallax versus the G magnitude for sources with a five-parameter astrometric solution: 0.03 mas for sources at $G \lesssim 15$, 0.1 mas for sources with $G = 17$, 0.7 mas at $G = 20$, and 2.0 mas at $G = 21$ mag. In addition, the uncertainties in the proper motion components are around 0.06 mas yr^{-1} for $G \lesssim 15$, 0.2 mas yr^{-1} for $G = 17$, and 1.2 mas yr^{-1} for $G = 20$ mag. The G_{BP} and G_{RP} magnitudes present uncertainties from few milli-mag for $G \leq 13$ to around 200 milli-mag at $G = 20$. Moreover, radial velocities for more than 7.2 million sources brighter than $G \lesssim 13$ mag are provided, with uncertainties between 200 m s^{-1} and 2.5 km s^{-1} . During this thesis, we will analyse bright stars from the more precise astrometric regime observed by *Gaia*.

Furthermore, *Gaia* DR2 contains the effective temperature parameter for more than 160 million sources with $G \lesssim 17$ mag. For a sub-sample of 76 million stars, the radius and the luminosity values were also reported in the catalogue. Also the line-of-sight extinction (A_G) and the reddening estimate ($E(G_{BP} - G_{RP})$) were measured for 76 million sources.

²⁷*Gaia* DR1 came out on 14th September 2016.

	# sources in Gaia EDR3	# sources in Gaia DR2	# sources in Gaia DR1
Total number of sources	$\approx 1,800,000,000$	1,692,919,135	1,142,679,769
Number of 5-parameter sources	$\approx 1,500,000,000$	1,331,909,727	2,057,050
Number of 2-parameter sources	$\approx 300,000,000$	361,009,408	1,140,622,719
Sources with mean G magnitude	$\approx 1,800,000,000$	1,692,919,135	1,142,679,769
Sources with mean G_{BP} -band photometry	$\approx 1,500,000,000$	1,381,964,755	-
Sources with mean G_{RP} -band photometry	$\approx 1,500,000,000$	1,383,551,713	-
Gaia-CRF sources	$\approx 1,500,000$	556,869	2,191
Sources with radial velocities	expected with Gaia DR3 / $\approx 7,210,000$ from Gaia DR2 in Gaia EDR3	7,224,631	-
Variable sources	expected with Gaia DR3 / see Gaia DR2	550,737	3,194
Known asteroids with epoch data	expected with Gaia DR3 / see Gaia DR2	14,099	-
Effective temperatures (T_{eff})	expected with Gaia DR3 / see Gaia DR2	161,497,595	-
Extinction (A_G) and reddening ($E(G_{BP}-G_{RP})$)	expected with Gaia DR3 / see Gaia DR2	87,733,672	-
Sources with radius and luminosity	expected with Gaia DR3 / see Gaia DR2	76,956,778	-

FIGURE 1.10: Overview of the observed sources' progress in *Gaia* DR1&DR2, and the recent *Gaia* Early Data Release 3 (EDR3). For user convenience, *Gaia* DR2 radial velocities are provided for Gaia EDR3 sources along with the *Gaia* EDR3 data. *Gaia* EDR3 does not contain other data: no variables, no solar system objects, and no astrophysical parameters. (Source: ESA).

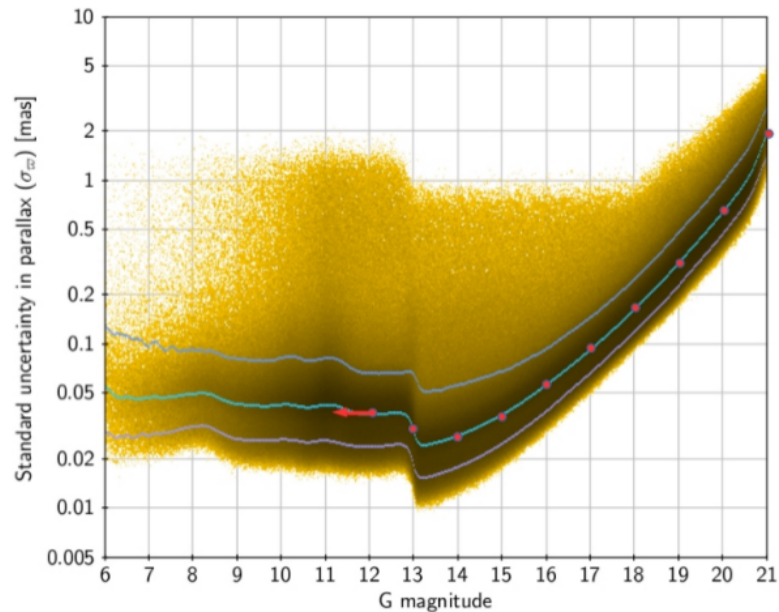


FIGURE 1.11: Standard deviation in parallax as a function of the G magnitude for sources with five-parameter astrometric solution in *Gaia* DR2. (Source: [Lindgren et al., 2018](#)).

1.4 Galactic spectroscopic surveys

Galactic archaeology demands high-quality data to detect stellar populations that differ in their abundances/kinematics/dynamics from each other (Lindegren & Feltzing, 2013). In addition, statistically significant stellar samples (at least several hundreds of targets) are required to study, interpret and distinguish among the different formation and evolution scenarios of the Galaxy, and also to minimize the biases from stellar selection effects. For that reason, there are several ongoing and forthcoming ground-based spectroscopic surveys (with different stellar and spectral domains, targets, and spectral resolutions) that, complementing the ESA *Gaia* mission, are revolutionizing the empirical information about Galactic stellar populations.

In this section, I will briefly describe the main on-going and future spectroscopic surveys (see an schematic overview in Fig. 1.12):

Gaia-ESO Survey

The Gaia-ESO survey (GES, Gilmore et al., 2012) comprises $\sim 10^5$ FGK-type stars for different populations of the Milky Way, covering the major components of the Galaxy (bulge, halo, and disc), and a large sample of observed open clusters. For the observations (between 2011 and 2018), GES used the Fibre Large Array Multi Element Spectrograph (FLAMES, Pasquini et al., 2002) on the Very Large Telescope array (VLT, 8m) in Cerro Paranal, Chile. As illustrated in Fig. 1.12, GES targets stars in a broad spectral range through two different spectrographs: GIRAFFE ($R \sim 20000$, Pasquini et al., 2000), and UVES ($R \sim 47000$, Dekker et al., 2000).

RAVE

The RAdial Velocity Experiment (RAVE, Steinmetz et al., 2006) is a multi-fibre spectroscopic survey ($R \sim 7500$) designed to study the chemical and dynamical evolution of the Galaxy through the analysis of more than 400 000 local dwarfs and giant stars. The observations were performed between 2003 to 2013 on the 1.2 m UK Schmidt Telescope of the Anglo-Australian Observatory (AAO) in Siding Spring, Australia. Figure 1.12 shows the overlap between the RAVE wavelength range (around the CaII triplet, 848-874 nm) and the one from *Gaia* RVS (845-872 nm, described before in Sect. 1.3). As a consequence, RAVE works as a good complement for the astrometric surveys, providing radial velocities, stellar parameters and individual abundances.

APOGEE

The Apache Point Observatory Galactic Evolution Experiment (APOGEE, Majewski et al., 2017) is one of the SDSS surveys, starting in 2011 with the 2.5 m Sloan Telescope, at New Mexico, and covering the near-infrared H-band regime ($1.5 \mu\text{m} - 1.7 \mu\text{m}$, see Fig. 1.12) to explore the dust-hidden populations in the Galaxy. The observed stars ($\sim 10^5$) at high spectral resolution ($R \sim 22500$) are predominantly red giants and other post-main-sequence stars from the Galactic mid-plane and inner Galactic regions.

GALAH

The Galactic Archaeology with HERMES (GALAH, De Silva et al., 2015) is a large-scale high-resolution ($R \sim 28000$) Milky Way stellar spectroscopic survey, using the High Efficiency and

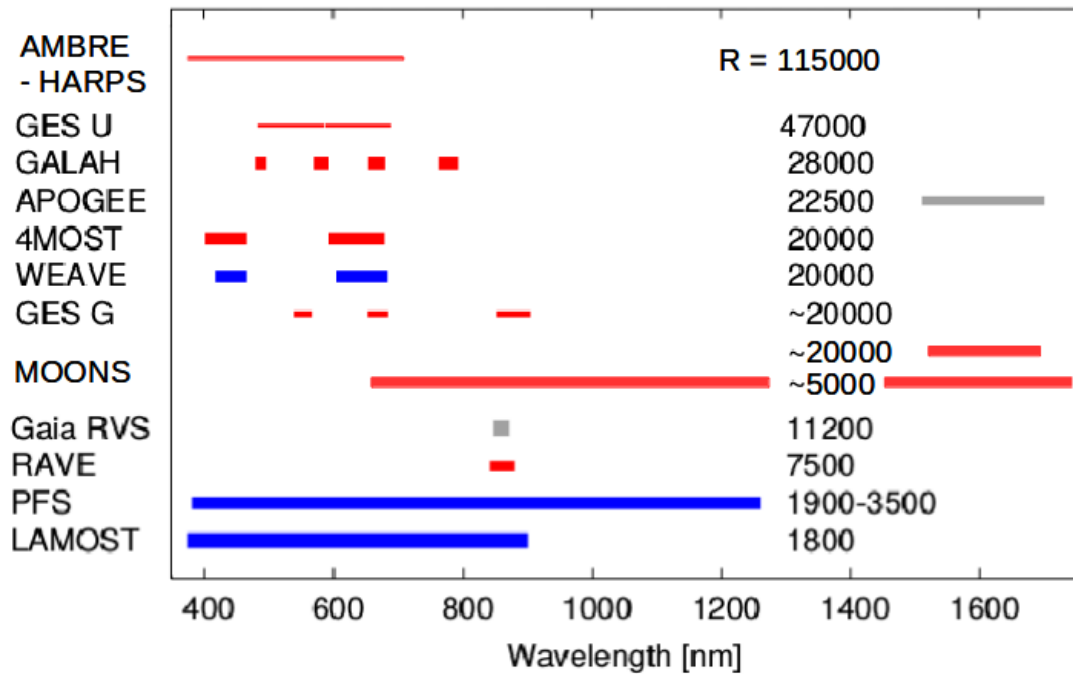


FIGURE 1.12: Overview of on-going and future spectroscopic surveys, sorted by spectral resolution (see labels to the right). In particular, GES U / G correspond to the Gaia-ESO UVES / GIRAFFE spectrographs, respectively. Horizontal lines show the covered wavelength intervals. Northern, southern, and all-sky surveys are represented by blue, red, and grey colours, respectively. Broader lines indicate larger numbers of target stars. Adapted from [Jofré et al. \(2019\)](#).

Resolution Multi-Element Spectrograph (HERMES) at the 3.9 m Anglo-Australian Telescope. The survey aims to observe 10^6 stars, observing dwarf and red giant branch stars. GALAH is highly complementary to the existing spectroscopic surveys like APOGEE and GES, and *Gaia* targets.

LAMOST

The Large Sky Area Multi-Object Fiber Spectroscopic Telescope (LAMOST, [Zhao et al., 2012](#)) is a low-resolution ($R \sim 2000$) ground-based spectroscopic survey performed at the 4m Guo Shou-jing reflecting Schmidt Telescope in China. The survey contains the LAMOST Experiment for Galactic Understanding and Exploration (LEGUE, [Deng et al., 2012](#)). It aims at observing 10^6 stars of the Galactic discs and halo in a multi-dimensional phase space, providing radial velocities, stellar parameters, and chemical abundances.

SEGUE

The Sloan Extension for Galactic Understanding and Exploration (SEGUE, [Yanny et al., 2009](#)), and its extension SEGUE-2 ([Rockosi et al., 2009](#)) observed more than 350 000 faint stars ($14.0 < g < 20.3$) at low spectral resolution $R \sim 2000$ in the optical range (3900-9000 Å). The aim was studying the kinematics and stellar atmospheric parameters of dwarfs and giant stars in the Galactic halo.

WEAVE

The WHT Enhanced Area Velocity Explorer (WEAVE, [Dalton et al., 2012](#)) is a multi-object spectroscopic survey that will be carried out on the 4.2 m William Herschel Telescope (WHT) at the Observatorio del Roque de los Muchachos, on La Palma (Canary Islands). The WEAVE spectrograph presents two optimised arms, red and blue, with $R \sim 5000$ and $R \sim 20000$, respectively. WEAVE started operations in 2019. It will provide the kinematics and abundances for 10^6 bright stars in the northern hemisphere to complement the *Gaia* mission from the ground and study the Galactic structures in more detail.

4MOST

The 4-metre Multi-Object Spectroscopic Telescope project (4MOST, [de Jong et al., 2016](#)) is a new fibre-fed spectroscopic survey facility on the VISTA telescope (4.1 metre mirror, located at the Paranal Observatory in Chile, ESO), scheduled to start observations in 2022. The fibers will consist of one high-resolution ($R \sim 20,000$) and two low resolution ($R \sim 5000$) spectrographs.

4MOST will be followed by the Multi-Object Optical and Near-infrared Spectrograph (MOONS, [Cirasuolo et al., 2014](#)), at the 8m VLT, which will also provide a low-resolution ($R \sim 5000$) and a high-resolution ($R \sim 20000$) mode for the observed spectra. It will provide accurate radial velocities, metallicities and chemical abundances for bulge stars.

1.4.1 The AMBRE Project

The AMBRE Project (Archéologie avec Matisse Basée sur les aRchives de l'ESO, [de Laverny et al., 2013](#)), is a collaboration between the Observatoire de la Côte d'Azur (OCA) and the European Southern Observatory (ESO) to automatically and homogeneously parametrise archived stellar spectra from ESO spectrographs: FEROS ($R = 48000$, [Kaufer et al., 1999](#)), HARPS ($R = 115000$, [Mayor et al., 2003](#)) and UVES ($R \sim 47000$, [Dekker et al., 2000](#)). The AMBRE parametrisation analysis for each ESO spectrograph database are fully described in [Worley et al. \(2012, 2016, FEROS and UVES, respectively\)](#) and [De Pascale et al. \(2014, HARPS\)](#).

The stellar atmospheric parameters (T_{eff} , $\log(g)$, $[M/H]$, $[\alpha/Fe]$) were derived by the multi-linear regression algorithm MATISSE (MATrix Inversion for Spectrum SynthEsis, [Recio-Blanco et al., 2006](#)), developed at OCA and used in the *Gaia* RVS analysis pipeline (see [Recio-Blanco et al., 2016](#)), using the AMBRE grid of synthetic spectra ([de Laverny et al., 2012](#)). The radial velocity (v_{rad}) is estimated by a cross-correlation function between the observed spectra and the used synthetic templates.

In the framework of this thesis, we analyse a large sample of the AMBRE:HARPS²⁸ optical stellar spectra (see Chapter 4), from which we determine individual $[Mg/Fe]$ chemical abundances. As illustrated in Fig. 1.12, the HARPS ESO spectrograph offers a very high spectral resolution dataset ($R = 115000$) for a broad spectral range in the optical (378 - 691 nm). These high-quality observations allow to measure atmospheric parameters, radial velocities and chemical abundances with high precision. Concretely, the full AMBRE:HARPS catalogue is comprised of 126688 spectra corresponding to ~ 17218 different stars in the solar neighbourhood ([De Pascale et al., 2014](#)).

²⁸The AMBRE analysis of the HARPS spectra comprises the observations collected from October 2003 to October 2010 with the HARPS spectrograph at the 3.6m telescope at the La Silla Paranal Observatory, ESO (Chile).

1.5 Chemical evolution of the Galactic disc

The formation of the Galactic disc and, in particular, the origin and existence of the thin-thick disc bimodality (see description in Sect. 1.1.3), are currently a matter of debate. As a consequence, disentangling the chemodynamical signatures present in the disc's stellar populations is essential to unveiling the formation and evolution of the Milky Way.

Following the initial thick disc identification from stellar density distributions (Yoshii, 1982, Gilmore & Reid, 1983) and the first attempts to classify kinematically the stars to either the thin or the thick disc (Bensby et al., 2003, 2005, Reddy et al., 2006), chemical signatures (preserved in FGK-type stars' atmospheres, see Sect. 1.2.1) have been suggested as the best criteria to differentiate between both Galactic disc stellar populations. Numerous studies (e.g. Soubiran & Girard, 2005, Adibekyan et al., 2012, Recio-Blanco et al., 2014, Bensby et al., 2014, Kordopatis et al., 2015a, Wojno et al., 2016, Fuhrmann et al., 2017, Hayden et al., 2017, Minchev et al., 2018, Buder et al., 2019, Haywood et al., 2019) have distinguished the two Galactic disc populations, in the solar neighbourhood and beyond, based on their α -elements abundance (e.g. Mg, Si, Ti), relative to iron.

The $[\alpha/\text{Fe}]$ vs. $[\text{M}/\text{H}]$ plane provides some hints regarding the disc stellar populations evolution. For most metallicities, the thick disc is often reported to be $[\alpha/\text{Fe}]$ -enhanced relative to the thin disc, suggesting distinct chemical evolution histories (see Fig. 1.13, observational results from Hayden et al., 2017). As mentioned in Sect. 1.2.1, the observed flat trend at low metallicities and the subsequent decline of $[\alpha/\text{Fe}]$ abundance with increasing $[\text{M}/\text{H}]$ are caused by the timescale delay between the core-collapse supernovae (Type II SNe) of massive stars, main source of α -elements to the ISM, and the supernovae Type Ia, mostly iron-peak elements supplier (Matteucci & Greggio, 1986). However, both high- and low- α sequences seem to overlap at supersolar metallicities, showing a flat trend for most α -process elements (not expected by chemical evolution models) being impossible to chemically identify to which stellar population they belong. Furthermore, the observed bimodal chemical distribution suggests that the thick disc stellar population was formed on a short timescale before the epoch of the thin disc formation, in agreement with other literature studies (Soubiran & Girard, 2005, Haywood et al., 2013, Kordopatis et al., 2015a, Fuhrmann et al., 2017, Silva Aguirre et al., 2018, Delgado Mena et al., 2019, Ciucă et al., 2021). This scenario is supported by two-infall chemical evolution models (Chiappini et al., 1997, Grisoni et al., 2017).

In particular, magnesium is often used as an α -elements tracer (e.g. Mikolaitis et al., 2014, Bergemann et al., 2014, Carrera et al., 2019) since $[\text{Mg}/\text{Fe}]$ abundance shows a clear separation of the Galactic thick-thin disc populations. In addition, magnesium is known to have a significant number of measurable spectral lines in optical spectra, along with a smaller scatter and a shallower trend with temperature and metallicity (Brewer et al., 2016, Bergemann et al., 2017, Ivanyuk et al., 2017, Buder et al., 2019). Moreover, due to the strength of some magnesium lines, its abundance can be measured even for distant metal-poor stars (e.g. Fernández-Alvar et al., 2015). For these reasons, a well-defined scale of Mg abundances is very important for stellar spectroscopy as well as Galactic science (Jofré et al., 2019).

1.5.1 Models vs. Observations

The comparison between chemical evolution models (CEM) and observational data allows to put more constraints on the star formation history, stellar nucleosynthesis and timescales for the formation and evolution of the Galaxy.

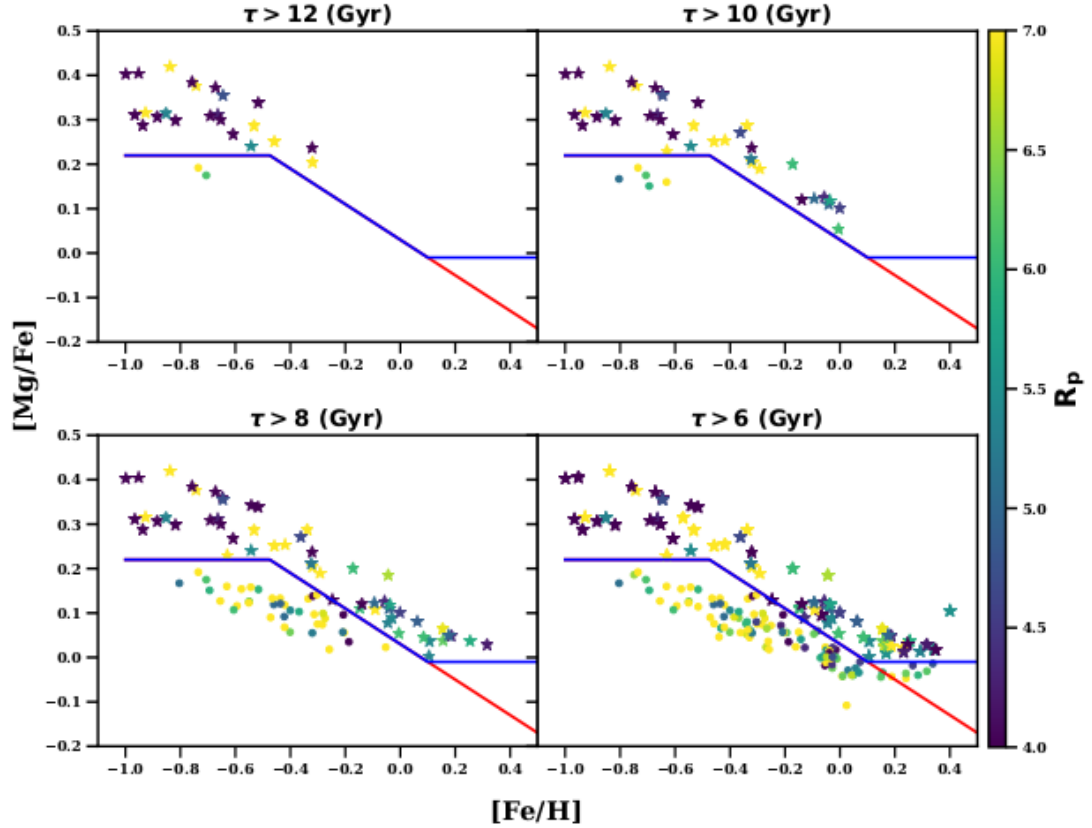


FIGURE 1.13: $[\text{Mg}/\text{Fe}]$ vs. $[\text{Fe}/\text{H}]$ plane as a function of different age ranges, from oldest to younger stellar populations. Stars are color coded by their orbital pericentres R_p in kpc. The blue lines denotes our chemical separation between thin and thick discs, where the thick disc stars (star symbol) are shown above the line and thin disk stars (circle symbol) below the line. The sequence separation becomes unclear for the most metal-rich stars ($[\text{M}/\text{H}] > 0$ dex), where the red line is shown for a different potential split between each stellar population group. (Source: Hayden et al., 2017).

As described in Sect. 1.4, several spectroscopic stellar surveys have provided valuable chemical information and constraints in the solar neighbourhood and beyond. Nevertheless, the flattening of the $[\alpha/\text{Fe}]$ abundances at supersolar metallicities is a common feature of many different studies. For instance, Anders et al. (2014) and Hayden et al. (2015) showed the $[\alpha/\text{Fe}]$ vs $[\text{Fe}/\text{H}]$ plane across the Milky Way for a large sample of giant stars from APOGEE. They find that both low- and high- $[\alpha/\text{Fe}]$ sequences decrease with $[\text{Fe}/\text{H}]$, merging and showing a flattened trend at supersolar metallicities. Recently, Buder et al. (2019) found similar signatures over the sample of dwarfs and turn-off stars from GALAH DR2, showing a remarkable agreement with the results of Adibekyan et al. (2012). Similarly, Mikolaitis et al. (2017) defined both Galactic discs chemically finding the flattening trend in the $[\text{Mg}/\text{Fe}]$ ratio for stars with metallicity $[\text{Fe}/\text{H}] > -0.2$ dex in a dwarf star sample from AMBRE data.

Theoretically, two-infall chemical evolution models (Chiappini et al., 1997, Romano et al., 2010) predict a steeper slope in the metal-rich regime ($[\text{Fe}/\text{H}] > 0.0$ dex), underestimating the measurement of Mg abundances with respect to the observed flat trend. More recent models (e.g. Kubryk et al., 2015) seem to reproduce this flattening including stellar radial migration, introduced by Schönrich & Binney (2009), through churning and blurring. Updated chemical evolution models developed by Grisoni et al. (2017, 2018) conclude also that other mechanisms are needed, in addition to the inside-out formation scenario, to reproduce the flattened trend in the Galactic disc at supersolar metallicities.

On the basis of these apparent discrepancies, the study of chemical signatures requires the best possible precision and accuracy in the abundance measurement.

1.5.2 Radial abundance gradients & radial migration

The observed stellar radial abundance distribution and the age-abundance relations in the Galactic disc are interesting signatures for studying the chemical enrichment history. They contain information about the star formation efficiency at different Galactocentric distances and timescales (Magrini et al., 2009, Minchev et al., 2014, Anders et al., 2014), radial migration of stars (Sellwood & Binney, 2002, Schönrich & Binney, 2009, Minchev et al., 2018), and infall of gas (Oort, 1970, Schönrich & McMillan, 2017, Grisoni et al., 2017).

The inside-out formation scenario (Matteucci & Francois, 1989), combined with a higher star formation efficiency in the inner regions of the Galaxy, seems to reproduce the present-day local abundance gradients (Grisoni et al., 2018), where metallicity decreases with the Galactocentric radius. In addition, a tight correlation between [Mg/Fe]-enhancement and age has been found for the old thick disc population (e.g. Haywood et al., 2013, Hayden et al., 2017, Delgado Mena et al., 2019, Nissen et al., 2017, 2020), but without global consensus (e.g. Silva Aguirre et al., 2018). However, the stellar thin disc component shows a larger dispersion, along with a significant scatter in the age-metallicity relation (AMR). This signature has been noticed as a sign of superposition of different stellar populations in the thin disc, with different enrichment histories and birth radii (Carlberg et al., 1985, Friel, 1995, Nordström et al., 2004, Schönrich & Binney, 2009, Wojno et al., 2016).

Furthermore, the radial migration of stars in the Galaxy, through churning and blurring, has theoretical (Sellwood & Binney, 2002, Schönrich & Binney, 2009, Di Matteo et al., 2013) and observational evidences, using data from different spectroscopic stellar surveys such as RAVE (Kordopatis et al., 2015b), ESO spectrograph HARPS (Hayden et al., 2017, Minchev et al., 2018) or APOGEE (Kordopatis et al., 2017, Feltzing et al., 2020). Theoretically, stars can be scattered by transient spiral arm perturbations and star-cloud encounters, provoking substantial variations in their angular momentum that allow the star to migrate in the integral space (Bland-Hawthorn et al., 2014). From an observational point of view, the presence of supersolar metallicity stars (e.g. super-metal-rich stars: $[M/H] \geq +0.1$ dex) with circular orbits at solar galactocentric distances has been interpreted as a clear evidence of stellar migration from inner birth regions in the Galaxy. Migrated stars are expected to cause a flattening of the radial abundance gradients with time (Boissier & Prantzos, 1999, Hou et al., 2000, Roškar et al., 2008, Schönrich & Binney, 2009, Pilkington et al., 2012, Minchev et al., 2018, Magrini et al., 2017, Vincenzo & Kobayashi, 2020). The temporal and spatial dimensions are therefore crucial to interpreting and clarifying the present-day chemodynamical relations in order to disentangle the formation and evolution of the Galactic disc.

One of the aims of this manuscript has been the exploration of possible error sources concerning the determination of high-precision Mg abundances (see Chapters 2, 3, and 5), and its impact on the interpretation of the observed chemical signatures in the Galactic disc stellar populations, together with the resulting implications on the reported chemodynamical relations (Chapter 7).

1.5.3 Gaia mission impact on Milky Way disc studies

Thanks to the *Gaia* mission (see general description in Sect. 1.3), a vast space over which accurate 6D phase space information is currently available, allowing to study the kinematic substructure in the solar neighbourhood and beyond with unprecedented accuracy, precision, and spatial

resolution (e.g. [Gaia Collaboration et al., 2018a](#)). The maps show the complexity and richness of the velocity field of the Galactic disc: e.g. observing for the first time some spiral patterns, ridges and wrinkles in the position-velocity space ([Antoja et al., 2018](#)), or the evidence of a dynamically evolving Galactic warp ([Poggio et al., 2020](#)).

The modelling of the rich phase structure unveiled by *Gaia* DR2 points to a Milky Way disc in the process of phase mixing from an out equilibrium state, with a strong influence of bar/spiral arms and the effects of recent perturbations. This has led to discussions about the origin of the reported coupled perturbations in vertical and in-plane directions in the disc: due to the interaction of the Sgr dwarf galaxy with the MW disc ([Antoja et al., 2018](#), [Bland-Hawthorn et al., 2019](#), [Laporte et al., 2019](#)), or by vertical bending oscillations in disc ([Darling & Widrow, 2019](#)), or simple analytical models ([Binney & Schönrich, 2018](#)).

According to *Gaia* DR2 data, one of the most influential discoveries has been the clear signatures of a major accretion event by a massive satellite in the Milky Way's history, approximately 10 Gyr ago, so-called *Gaia*-Enceladus/Sausage ([Helmi et al., 2018](#), [Belokurov et al., 2018](#), [Di Matteo et al., 2019b](#), [Gallart et al., 2019](#), [Belokurov et al., 2020](#)). A double sequence in the halo HR diagram is observed ([Gaia Collaboration et al., 2018b](#)), where this population lies on the blue sequence, with estimated ages from 10 to 13 Gyr old from isochrone fitting. Additionally, this metal-poor population ($-2.5 \leq [\text{Fe}/\text{H}] \leq -0.5$ dex) shows a very broad tangential velocity distribution. On the one hand, [Helmi et al. \(2018\)](#) revealed a sequence consistent with a population that was formed over ~ 2 Gyr time span at $\sim 0.3 M_{\odot}/\text{yr}$ in a different system from the thick disc. They estimated a mass comparable to the present-day SMC, and suggested that it might have fallen in when the progenitor of the Milky Way thick disc was already in place. On the other hand, [Belokurov et al. \(2018\)](#) measured a halo kinematic anisotropy due to radialisation of the progenitors orbit, and inferred that the *Gaia*-Sausage stellar debris were deposited by a major satellite with $M_{\text{vir}} > 10^{10} M_{\odot}$ about ~ 8 -11 Gyr ago.

This event seems to be a key piece of the puzzle for the Galactic disc formation and evolution scenarios, and it will be discussed in the context of the obtained results in this thesis, along with the potential improvement that this work could have in a precise chemical characterisation of the *Gaia*-Enceladus population in the near future.

1.6 Goals of this thesis

The described impressive collection of observed stellar spectra needs the implementation of automated methods and algorithms to be able to explore the Milky Way in unprecedented detail. The adequate optimisation of the automatic procedures is crucial to constrain chemical evolution models and improve our understanding of the observed chemodynamical trends in the Galactic disc.

This thesis project aims at unveiling the Milky Way disc formation and evolution process from an in-depth perspective of the present-day solar neighbourhood population. To this purpose, the goals of the thesis are:

- To explore in detail the different sources of uncertainties affecting the determination of high-precision abundances from observed spectra of metal-rich stars, for which the measurement of abundances is still challenging due to the high presence of molecular and blended lines.
- To establish the existent chemodynamical correlations in the Galactic disc using the high-quality astrometric data provided by the *Gaia* space mission.

-
- To estimate stellar ages for the stars with spectroscopic measurements.
 - To analyse the evolution of the Milky Way disc characteristics and to conclude on the possible scenarios of the Galaxy formation.

During this thesis, I optimise the spectral normalisation procedure for different stellar types. To this purpose, I analyse a large sample of the AMBRE:HARPS high resolution optical stellar spectra ($R = 115000$), from which I determine individual $[\text{Mg}/\text{Fe}]$ chemical abundances using the GAUGUIN automated abundance estimation algorithm (used for the Gaia RVS spectra analysis, [Bijaoui et al., 2012](#), [Recio-Blanco et al., 2014, 2016](#)). Subsequently, I take advantage of the accurate astrometric and photometric data from the *Gaia* DR2 catalogue to determine precise stellar ages and orbital parameters, and build a time evolving chemodynamical picture of the Milky Way disc from the solar neighbourhood perspective. The combination of both surveys, along with detailed comparisons with up-to-date Galactic model predictions, will shed new light on the exploration and interpretation of the present chemodynamical trends in the disc (radial chemical abundance gradients, role of radial migration/churning, age-abundance relations), and on the experienced formation and evolving processes in the Milky Way history.

The structure of this manuscript is described as follows. In Chapter 2 we introduce the automatic stellar parametrisation methods used in the literature to characterise Galactic stellar populations, and highlight the current challenges and difficulties on deriving precise and accurate chemical abundances from observed spectral lines. The employed normalisation algorithm and the abundance estimate code GAUGUIN are described in Chapter 3, together with the used synthetic spectra grid. The observational data sample used in this thesis is presented in Chapter 4. In Chapter 5 we detail the abundance determination analysis and the optimisation of the spectral continuum placement procedure as a function of the stellar type and the studied line. The determination of ages and orbital parameters for a local stellar sample is explained in Chapter 6. Chapter 7 is devoted to the study of the observed chemodynamical trends and the discussion of the proposed scenario for the formation and evolution of the Galactic disc. The conclusions and future work is summarized in the final Chapter 8. An appendix with the list of publications is also included.

Chapter 2

Determination of chemical abundances from stellar atmospheres

Contents

2.1 Spectral continuum and line formation	30
2.1.1 Parameter dependence	32
2.2 Automated abundance analysis	35
2.2.1 Measurement of equivalent widths	35
2.2.2 Spectrum synthesis	37
2.3 Automatic parametrisation algorithms	37
2.3.1 Optimisation methods	38
2.3.2 Projection methods	38
2.3.3 Classification methods	39
2.4 Challenges for high-precise and accurate abundance measurements	39

The Solar spectrum was first observed by the physicist Joseph von Fraunhofer in the early 19th century, discovering the presence of some dark absorption lines. At the present day, more than 50 different atoms and molecules have been identified in it.

An accurate analysis of the stellar spectra provides the most valuable information to characterise its upper atmosphere: effective temperature (T_{eff}), surface gravity ($\log g$), chemical abundances or microturbulence (v_{mic})¹. The derived spectral information allows to infer the stellar formation and evolution mechanisms, to estimate other stellar properties as their distance or radial velocity, and to develop Galactic chemical evolution models with the combination of stellar dynamics and ages.

As mentioned in the previous chapter, one of the main goals of this thesis consisted in deriving precise and accurate stellar chemical abundances from observed spectra, in particular the [Mg/Fe] abundance. Figure 2 illustrates every aspect and step for deriving chemical abundances in stars. According to the scientific goal and the analysed stellar type, the treatment of the observed spectra needs to be optimised differently. This is fundamental for current studies of the Milky

¹ v_{mic} : considered as a thermal velocity, it corresponds to the small-scale turbulent motions of the particles in the stellar photosphere, and contributes to the absorption coefficient of the line, leading to an excess in the line-broadening.

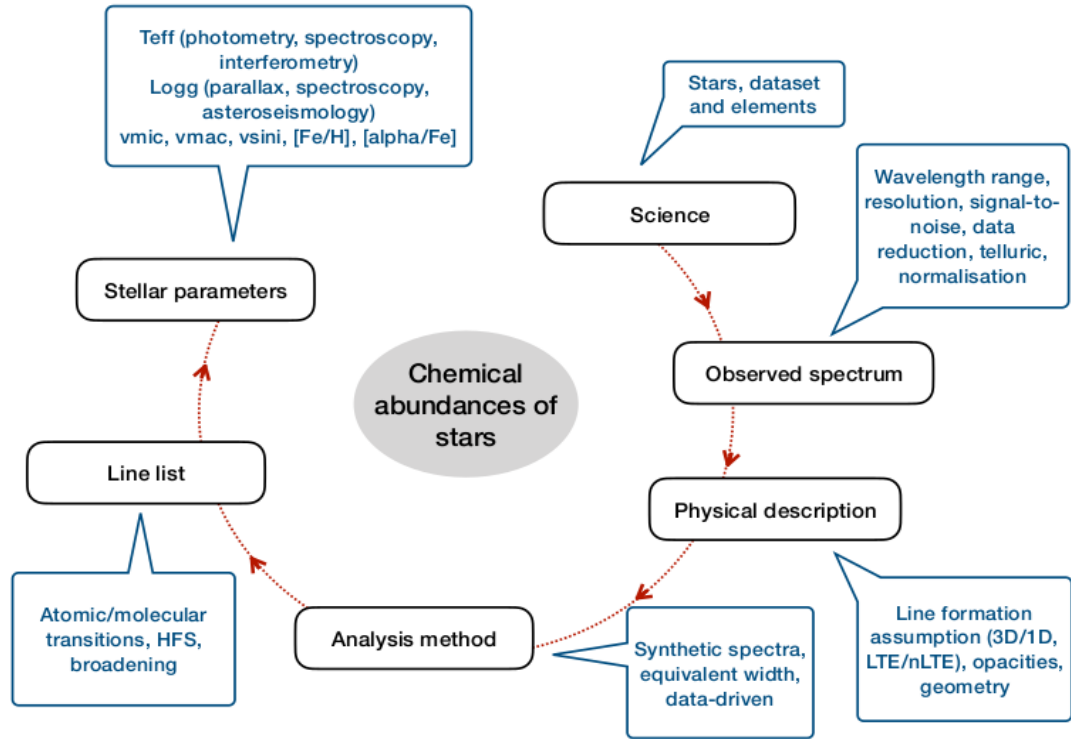


FIGURE 2.1: Illustration of the steps needed for obtaining abundances of chemical elements in stars. (Source: Jofré et al., 2019).

Way to carefully interpret its formation and evolution, especially for the ongoing large-scale spectroscopic surveys in the Galaxy that have increased the size of the observational databases, relying on automated techniques to perform a rapid and homogeneous processing of the data.

2.1 Spectral continuum and line formation

The measurement of the main stellar properties (effective temperature, surface gravity, and chemical abundances) relies on the knowledge of the stellar atmosphere. During the stars' lifetime, the energy is produced in their cores via thermonuclear reactions (as described in Sect. 1.2.1), transferred to the outer layers, and finally emitted from the photosphere. The interaction of the photon radiation with the gas relatively colder (or hotter) of the stellar atmosphere produces the absorption (or emission) lines in the observed spectrum, since the atoms and molecules absorb the photons in a particular wavelength or energy regime (see Fig. 2.2). In addition, for each atom or molecule there is an optimal temperature range for which their different transitions appear. As a consequence, the resulting spectrum of a star consists of a continuum distribution of energy with emission and absorption lines superimposed, and it is different from one star to another.

The final observed spectral lines pattern can be directly linked with the effective temperature, the surface gravity, and the chemical composition of the star. For this purpose, a spectral line is generally analysed with the help of a radiative transfer equation (to describe the transport of the energy flux inside the atmosphere of the star) and an atmosphere model (to describe its chemical and physical properties: geometry, molecular balance, or the thermodynamic equilibrium). There are some general assumptions that are commonly considered to reproduce the photospheric spectrum in great detail:

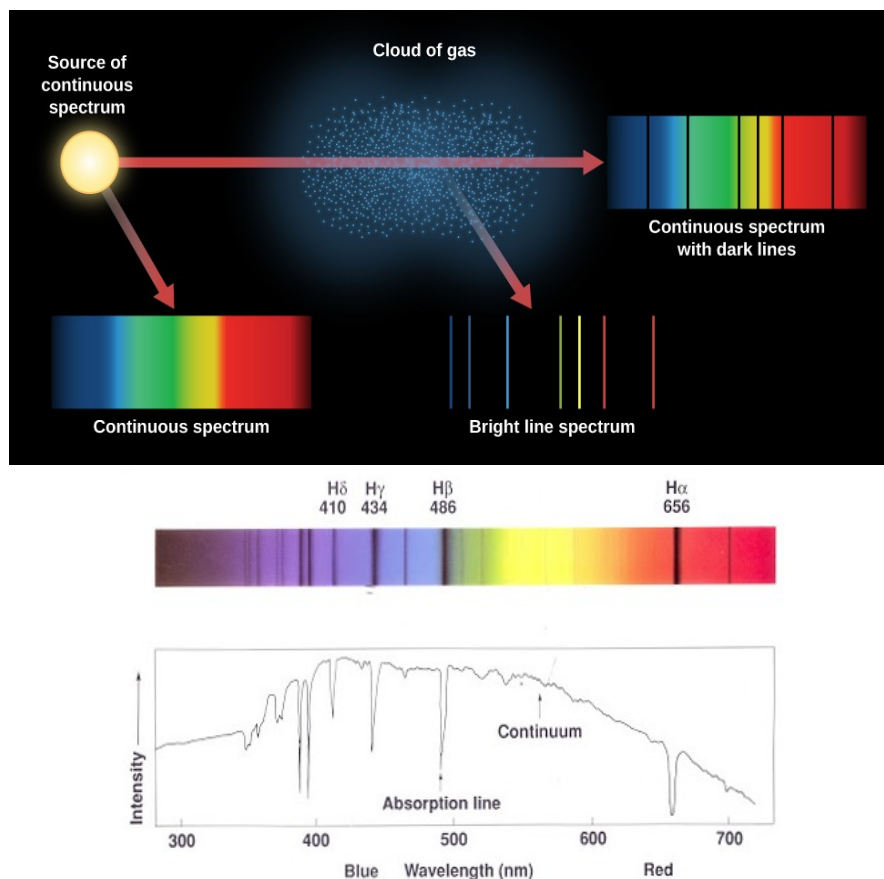


FIGURE 2.2: Schematic illustration of the lines absorption in the stellar atmospheres (top, Source: Lumen Learning astronomy courses), and the resulting observed spectrum of a star (bottom, Source: astro.princeton.edu.)

- Hydrostatic equilibrium: the gravity and the pressure forces of the star are balanced, the stellar atmosphere does not lose any mass and does not expand or contract.
- In the stellar photosphere, the different layers are really narrow in comparison with the radius of the star. This implies that the curvature of the stellar surface can be neglected, and a stationary one-dimensional (1D) plane-parallel geometry is assumed.
- Radiative equilibrium: by energy conservation, the incoming energy into an atmosphere layer is equally transferred to the next layer.
- To reproduce the spectral lines formation for each chemical element, it is usually assumed the Local Thermodynamic Equilibrium (LTE): Maxwell equations + Plack function (source function: the ratio between the emission and absorption coefficients) + laws of Boltzmann (relative atoms population in excited states) and Saha (fraction of atoms in an ionised state)

In particular, we can infer the chemical abundance of each element by the analysis of their spectral lines profile. The line strength (i.e. intensity) or equivalent width (EW^2) are correlated with the chemical abundance of the element since they mostly depend on the absorption coefficient

²The area of a spectral line measured below the continuum level is related to a rectangular line profile, with the same area, that has unit height and a certain equivalent width.

and the number of absorbers (derived from the Boltzmann and Saha equations under the LTE assumption described above).

Additionally, the structure of the stellar photospheres can be strongly affected by some line-broadening parameters. In particular for 1D-LTE models, one of the most significant contributors is the microturbulence (v_{mic}), which commonly needs to be included in spectral synthesis calculations by an *ad hoc* calibrated function with the rest of the stellar atmospheric parameters. Other examples are the projected rotational velocity ($v \sin(i)$, where i is the inclination angle with respect to the line-of-sight) and the macroturbulence (v_{mac}), that corresponds to the large-scale turbulent motions in the atmospheres. Both parameters have a similar impact on the spectrum shape, and are generally either ignored or embedded in a synthetic global broadening parameter determination (Jofré et al., 2019).

In the last decade, a remarkable progress has been achieved in the modelling of stellar atmospheres to describe their nature with a more realistic description. On the one hand, 3D models have allowed to perform a full hydrodynamical simulation of the atmospheres (Magic et al., 2013, Amarsi, 2015, Bergemann et al., 2017) although it requires a significant increase in calculations ($> 10^6$) with respect to 1D models. On the other hand, an increase in accuracy has been reported by the abandon of the LTE in the radiation transfer, including more atomic data to describe the non-local radiative effects on the excitation of each atomic level, and on the ionisation and recombination of each ionisation stage (Nissen & Gustafsson, 2018). The non-Local Thermodynamic Equilibrium (NLTE) is highly recommended for late type stars whose convective flows in the atmosphere affect the shape and the strength of spectral lines (Bergemann et al., 2017). Applying NLTE corrections is computationally expensive, but they significantly improve the absolute chemical abundance accuracy, particularly for certain elements and stellar types (e.g. Amarsi et al., 2016, Nordlander et al., 2017).

2.1.1 Parameter dependence

To illustrate the stellar spectrum dependence on the atmospheric parameters³, I first employed the high-resolution synthetic reference grid ($R \gtrsim 300000$, 13784 spectra; further descriptions in de Laverny et al., 2012) computed for the Gaia-ESO Survey (GES) pipeline (Gilmore et al., 2012) in the context of the AMBRE Project (de Laverny et al., 2013). For each stellar parameters combination in the computed spectra grid, five different values of the enrichment in α -elements were considered around the standard values ($[\Delta\alpha/\text{Fe}] = 0.0, \pm 0.2$ dex and ± 0.4 dex). Hereafter, the plotted synthetic spectra are colour coded according to the $[\Delta\alpha/\text{Fe}]$ value.

Effective temperature

The effective temperature is the temperature at the stellar photosphere (the temperature increases towards inside the star), that corresponds to a blackbody emitting energy from its surface: $\text{Flux} = \sigma T_{\text{eff}}^4$, where σ is the Stefan-Boltzmann constant ($\sigma = 5.67 \times 10^{-5} \text{ erg cm}^{-2} \text{ s}^{-1} \text{ K}^{-4}$).

The effective temperature is the most important stellar parameter, which determines the presence (or the absence) of the spectral lines and their strength. Not only there is a strong dependence with the effective temperature in the excitation and ionization processes (exponential and power dependence in laws of Boltzmann and Saha, respectively), but also in the atomic absorption coefficient, that should be carefully taken into account for the weak spectral lines (where the

³We use the following nomenclature:

$[\text{M}/\text{H}] \lesssim -0.2$ dex (metal-poor); $T_{\text{eff}} < 5400$ K (cool); $\log g < 3.5 \text{ cm s}^{-2}$ (giant).
 $[\text{M}/\text{H}] > -0.2$ dex (metal-rich); $T_{\text{eff}} \gtrsim 5400$ K (hot); $\log g \gtrsim 3.5 \text{ cm s}^{-2}$ (dwarf).

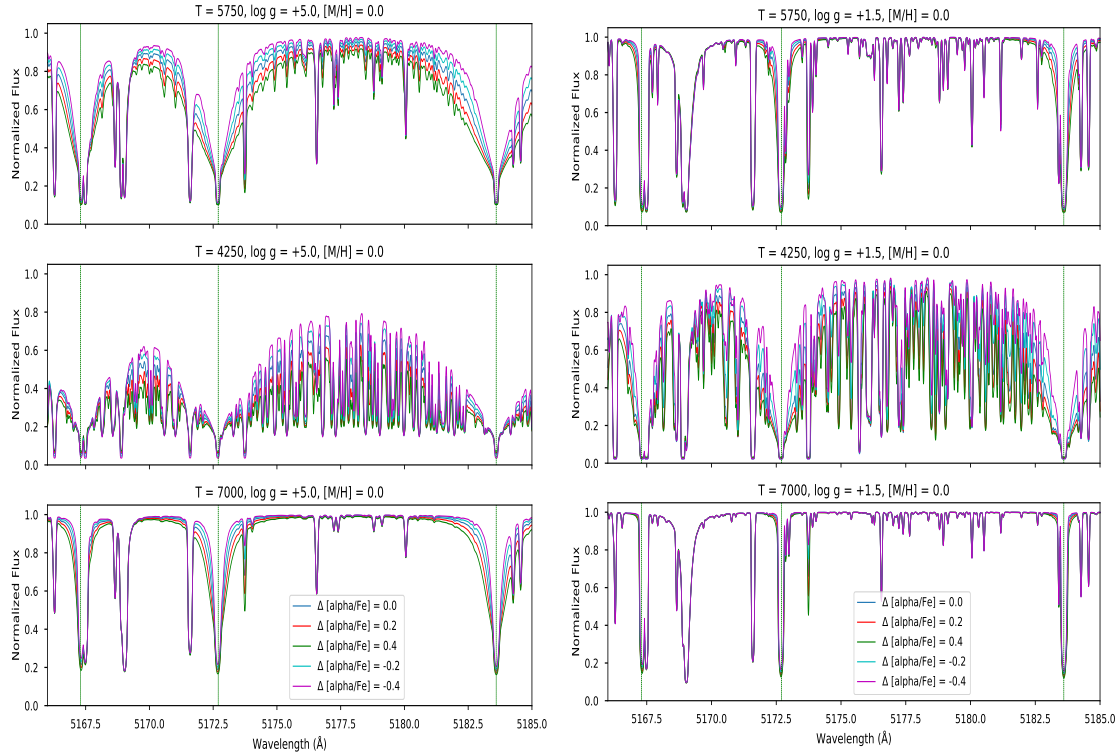


FIGURE 2.3: Spectral comparison between a dwarf ($\log g = 5.0$; left panel) and a giant ($\log g = 1.5$; right panel) star. The global metallicity is fixed at $[M/H] = 0.0$, and at each panel five different α - enhancements have been computed. Green vertical lines correspond to the Mg Ib triplet lines: 5167.3, 5172.7 and 5183.6 Å (from left to right). From top to bottom, the computed synthetic spectra are shown for three different effective temperatures: 5750 (solar), 4250 and 7000 K. The increased on the effective temperature reduces the presence of absorption lines and leads to narrower and lower intensity lines.

wings do not dominate the line profile). How a spectral line grows or weakens depends directly on the gas temperature in the line-forming layers in the stellar photosphere and the excitation potential of the line. Therefore, large differences are expected across identical spectra with different effective temperature values.

We observed that the increased on the effective temperature reduces the presence of metallic absorption lines in the spectrum and leads to narrower and lower intensity lines (see Fig. 2.3).

Surface gravity

The surface gravity corresponds to: $g = G M_{\star}/R_{\star}^2$, where G is the gravitational constant ($G = 6.67 \times 10^{-8} \text{ cm}^{-3} \text{ g}^{-1} \text{ s}^{-2}$), and M and R are the mass and the radius of the star, respectively. For cool stars, the gas and the electron pressure can be approximately related by $P_g \approx P_e^2/\text{constant}$, and pressure can be written in term of surface gravity as $P_g \approx \text{constant} \cdot g^{2/3} \Leftrightarrow P_e \approx \text{constant} \cdot g^{1/3}$. For the FGK-type stars, where these relations are hold, pressure dependences can be translated into gravity dependences. These relations between pressure and surface gravity changes rapidly with the effective temperature for hotter stars.

Pressure effects in the observed stellar spectra are much weaker than the effective temperature effects (i.e. a variation of few tens of per cent in the effective temperature provokes a similar change in the line profile than a variation of several hundred per cent in the surface gravity value). Theoretically, at a given effective temperature, narrower equivalent widths are predicted

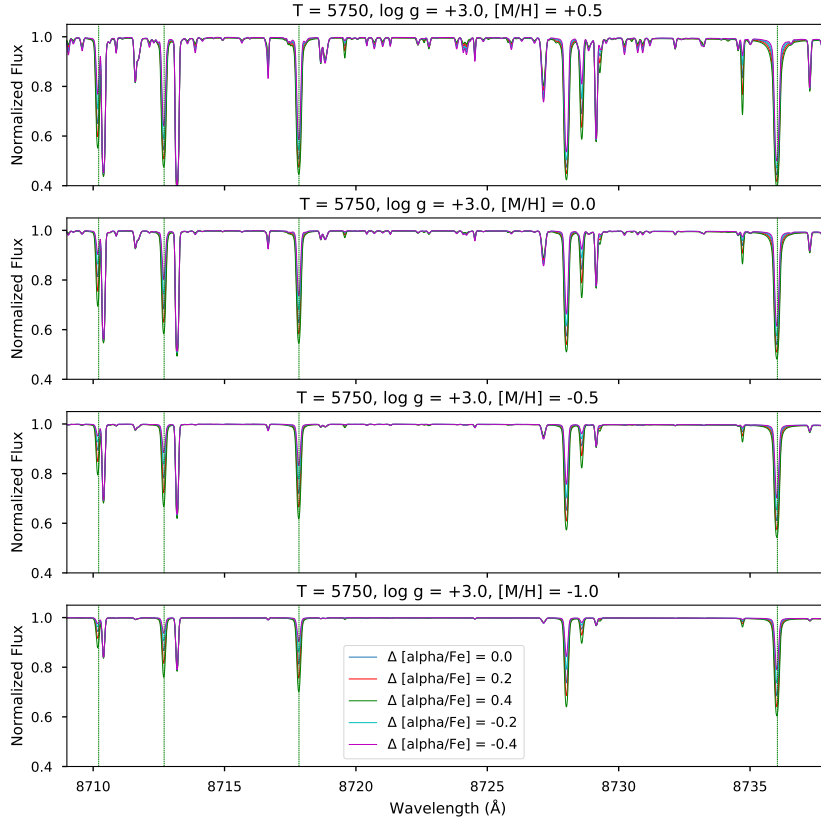


FIGURE 2.4: Spectral comparison for a hot sub-giant star ($T_{\text{eff}} = 5750$ K, $\log g = +3.0$) at different global metallicity values: $[M/H] = +0.5, 0.0, -0.5, -1.0$ dex (from top to bottom). At each panel five different α -enhancements have been computed. Green vertical lines correspond to the weak Mg lines: 8710.21, 8712.70, 8717.83, and 8736.04 Å (from left to right).

by decreasing the surface gravity of star (low pressure implies a lower collisional broadening). Therefore, the spectral lines become more saturated towards dwarf stars ($\log g > 3.5$).

This behaviour is illustrated in Fig. 2.3 for the Mg triplet. We observe that the equivalent widths of the selected Mg lines decrease with decreasing the surface gravity value, being more saturated towards dwarf stars. Also the $[\Delta\alpha/Fe]$ dependence becomes less significant. In conclusion, for higher $\log g$ values, we find stronger lines but may be saturated, which implies that $[\Delta\alpha/Fe]$ differences can only be found in the wings of the line profile, not in the core.

Global metallicity $[M/H]$ and the $[\alpha/Fe]$ abundance

The global metallicity includes every element heavier than helium (including α -elements), expressed as a fraction of hydrogen ($[M/H]$). The notation for the global stellar metallicity can be expressed by $[M/H]$ (considering all the metal lines as M) or $[Fe/H]$ (since iron lines are the most numerous ones in the optical). The chemical abundance values are always expressed with respect to the Sun in a logarithmic scale (e.g. $[Fe/H] = \log[N(\text{Fe})/N(\text{H})]_{\star} - \log[N(\text{Fe})/N(\text{H})]_{\odot}$, where $N(X)$ is the density of the number of atoms for the element X). Figure 2.4 shows how an increase of the global metallicity implies stronger or more intense lines.

On the other hand, in all the previous figures and stellar cases, we find that a higher $[\Delta\alpha/\text{Fe}]$ value increases the intensity of the Mg spectral lines, as expected. Furthermore, we observe that $[\Delta\alpha/\text{Fe}]$ has a lower impact on the synthetic spectra when we work at higher effective temperatures and lower surface gravity values. An increase of α - elements causes larger amounts of electrons which, in turn, increases the continuum opacity in the photosphere, especially for lower effective temperature values.

In addition, the $[\Delta\alpha/\text{Fe}]$ dependence varies with the spectral line type. We first showed the saturated lines (Mg Ib triplet) behaviour in Fig. 2.3, for which the variation in $[\alpha/\text{Fe}]$ only affects the wings of the line profile. However, Fig. 2.4 illustrates the opposite behavior for weak non-saturated lines, for which a clear variation in the intensity is observed, not only in the wings, and directly affects the measured $[\text{Mg}/\text{Fe}]$ abundance. As described later in Chapter 5, the optimisation of an automatic analysis procedure should be different depending on the strength of the studied line.

2.2 Automated abundance analysis

For deriving chemical abundances from observed spectra, automated stellar abundance analysis are based on data mining methodologies that use different parametrisation approaches.

For a given element, the measured equivalent width (EW) of the spectral line describes a curve of growth with respect to the chemical abundance. Figure 2.5 illustrates this behaviour, showing two different regimes for the spectral lines, separated by a knee: weak lines (non-saturated, linear correlation), and strong lines (core saturated, only the wings are sensitive to the abundance). The strong lines do not show a linear correlation of the abundance with the measured EW. The known curve of growth, which differs from one element to another and also among lines of same chemical element, has been widely analysed in the literature to obtain the different chemical abundances of a star.

Automatic methods to determine abundances from observed spectra are generally based on two main techniques: the measurement of equivalent widths, or the computation of synthetic spectra by reproducing the absorption lines shape of the analysed chemical element for different stellar atmospheric parameters. For a particular chemical element, the derived abundance value from each individual line in the spectrum should be consistent among each other. In addition, automated abundance analysis need to carefully identify the continuum of the spectrum and the presence of blends, in order not to overestimate the final abundance measurement.

2.2.1 Measurement of equivalent widths

The equivalent width of the spectral lines can be measured by fitting a Gaussian profile or by a direct integration over the line profile. This method is particularly used for weak non-saturated lines. As shown in previous Fig. 2.5, the linear increase of the abundance with the EW for weak lines allows to automatically derive precise chemical abundances in this regime (the corresponding internal error in logarithmic abundance is ~ 0.01 dex, Nissen & Gustafsson, 2018).

The spectral continuum placement comprises the main source of error for this technique, which has a direct impact on the measurement of the spectral line's area. For that reason, some works in the literature have measured the EW by hand, using the IRAF `plot task` by fitting Gaussian profiles to the observed lines profile one by one (e.g. Bensby et al., 2014, Nissen et al., 2017), although this methodology is limited for small samples of stars (mainly for the sake of the

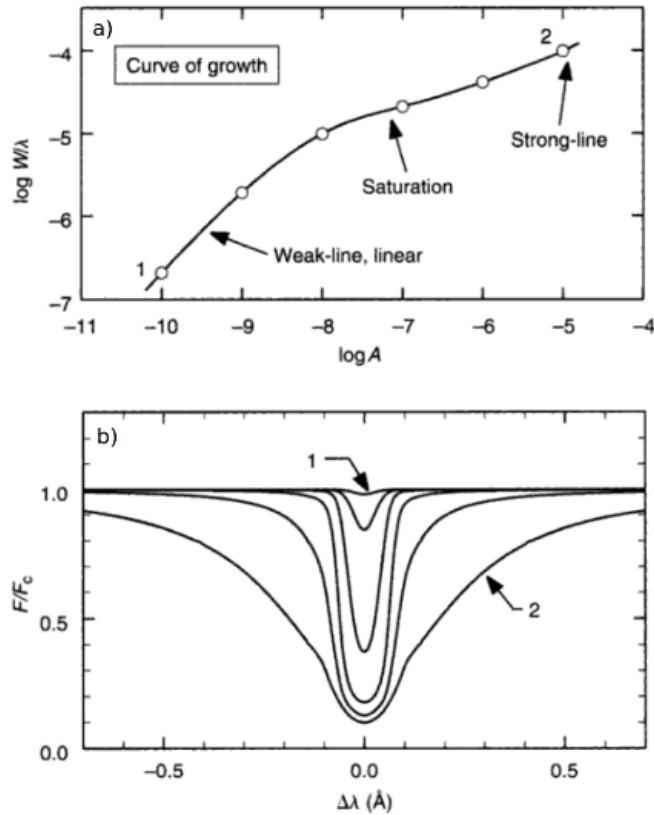


FIGURE 2.5: a) Curve of growth for a chemical element: equivalent width increases as a function of the abundance. For weak lines (non-saturated), there is a linear correlation. The curve describe a knee when the line becomes saturated, and larger equivalent widths correspond to the strong lines regime. b) Normalized flux for the different abundance values illustrated in a) (Source: [Gray, 2005](#)).

health and limited lifetime of the researcher). In this era of large spectroscopic surveys, some automatic pipelines have been developed, such as ARES ([Sousa et al., 2007](#), [Adibekyan et al., 2012](#)), GAUFRE⁴ ([Valentini et al., 2013](#)), or GALA ([Mucciarelli et al., 2013](#)), which is based on the WIDTH9 code ([Kurucz, 2005](#)). The automatic procedures use radiative transfer codes and atmosphere models to reproduce the curve of growth and estimate the chemical abundances.

The measurement of equivalent widths has been successful for weak ‘isolated’ lines observed at high-spectral resolution and high signal-to-noise. The main constraints of this methodology consists of the need of an ‘isolated’ line (i.e. no blended with neighboring lines). If lines are blended, the abundance will be overestimated (the measured EW will be larger). Therefore, crowded regions of the spectrum needs to be discarded in the analysis. Additionally, intrinsic broadening of the line (e.g. due to stellar rotation or macroturbulence) will contribute in the same way. Thus, the measurement of equivalent widths will be more accurate for slow-rotating FGK-type stars.

⁴Both ARES code and GAUFRE procedure were used as a part of the Gaia-ESO Survey pipeline in the analysis framework of the UVES spectrograph ([Smiljanic et al., 2014](#)).

2.2.2 Spectrum synthesis

This method consists of deriving stellar abundances by comparing the observed spectra with synthetic model-atmosphere spectra generated for different abundance values and stellar parameters. To reduce the computing time, some automatic pipelines use pre-computed grids of synthetic spectra. Currently, spectrum synthesis codes are an useful and common tool for large spectroscopic surveys: SME (Spectroscopy Made Easy, Valenti & Piskunov, 1996, Buder et al., 2019, used for GALAH survey calibration), ASPCAP (APOGEE Stellar Parameter and Chemical Abundances Pipeline, García Pérez et al., 2016), or GAUGUIN (Bijaoui et al., 2012, Recio-Blanco et al., 2014, 2016, part of the analysis pipeline of the Gaia-ESO Survey for the GIRAFFE spectra and also used for Gaia RVS spectra). The stellar parameters and the chemical abundances (for the selected lines of the element) are commonly obtained by the minimum quadratic distance (e.g. χ^2 fitting; or more sophisticated optimisation methods, e.g. Gauss-Newton algorithm) between the observed and the synthetic spectra in certain selected spectral windows (a full description about parametrisation algorithms can be found in Sect. 2.3). The spectrum synthesis code converge when the best final fit is found.

Spectral synthesis is the only way to determine precise abundances for crowded spectral regions and blended lines (e.g. cool stars and molecules). In addition, the inclusion of broadening mechanisms in the synthetic spectra (e.g. by microturbulence empirical function in the model atmospheres) avoid their direct effects on the determined parameters and abundances with respect to the equivalent widths estimates. However, uncertainties from the continuum placement still need to be considered. Moreover, this methodology also requires enough high spectral resolution to properly identify the spectral lines, since it is quite sensitive to the wavelength calibration (Hinkel et al., 2016, Jofré et al., 2017, 2019).

The first part of this thesis project has been to analyse in detail the different sources of uncertainties affecting the magnesium abundance estimations from optical spectra of metal-rich stars, for which a precise chemical abundance determination is still challenging due to the high presence of molecular and blended lines. To this purpose, I employed the automated spectrum synthesis code GAUGUIN. Further detailed discussions about the optimisation of spectrum synthesis methods will be addressed throughout this manuscript (Chapters 3 and 5).

2.3 Automatic parametrisation algorithms

In this section, I will describe the different stellar parametrisation techniques implemented in the automatic exploration of the Milky Way by large observational surveys (e.g. see complete review by Recio-Blanco, 2014).

Depending on the physical knowledge of the studied objects, theoretical models (with more or less number of variables) are used as a reference to map the observed targets. Those models constitute a N-dimensional grid, where N is the number of parameters to determine (e.g. atmospheric parameters, chemical abundances, radial velocity, stellar rotation).

The main goal of a parametrisation algorithm is to minimize the distance between the observations and models, defined by:

$$D = \sum_{i=1}^I [O(i) - M(i)]^2 \quad (2.1)$$

where $O(i)$ and $M(i)$ are the observed and the reference one, respectively. They are defined through I variables (e.g. the spectrum pixels, further details in Chapter 3, or equivalent widths values). Each reference model with a distance value smaller than the adopted noise threshold can be considered as a potential solution.

The more common applied mathematical approaches in the literature, to find the absolute minimum of the distance function, are: optimisation, projection, and classification methods.

2.3.1 Optimisation methods

The simplest optimisation method in the discrete plane consists in a complete and detail exploration of the reference models grid, by individually calculating the distance between the observed target and each reference, finally finding the absolute minimum (i.e. the nearest neighbour).

To reduce the computing time of this method, gradient descent algorithms have been widely developed. These algorithms search for the direction in the parameter space that has the highest negative gradient as a function of the distance. Once this direction is found, the parameters are modified and the algorithm proceeds in an iterative way by re-calculating the gradient again, until convergence of the parameter solution. Two representative methods of this type of algorithms are the Gauss-Newton (e.g. [Bijaoui et al., 2012](#), implemented in our code GAUGUIN, see Sect. 3.2) or the Levenberg-Marquadt ([Moré, 1978](#)).

In addition, the precision of the optimised result is always limited by the step of the used reference grid. This problem is currently solved by the interpolation in the parameter space. Besides GAUGUIN, another example of an optimisation code is FERRE (publicly available⁵, [Allende Prieto et al., 2006](#), [Allende-Prieto & Apogee Team, 2015](#)), used at the core of the APOGEE Stellar Parameters and Chemical Abundances Pipeline ([García Pérez et al., 2016](#)). The FERRE code performs a distance minimisation between the full input spectrum and the reference spectra grid, by using the Nelder-Mead (1965) algorithm. The model evaluation is based on a linear interpolation in a pre-computed grid, forcing the observed and (interpolated) model spectra to have the same mean value.

Some other optimisation algorithm examples in the literature are: SME ([Valenti & Piskunov, 1996](#)), GALA ([Mucciarelli et al., 2013](#)), iSpec ([Blanco-Cuaresma et al., 2014](#), two different pipelines, based on synthetic spectral fitting technique and equivalent width method, to derive atmospheric parameters and individual chemical abundances), SP_Ace (Stellar Parameters And Chemical abundances Estimator, [Boeche & Grebel, 2016](#), which search the synthetic spectrum or the line's EWs that match the observed ones), FAMA (Fast Automatic MOOG Analysis, [Magrini et al., 2013](#), automatic iterative spectral analysis using EWs for the determination of atmospheric parameters), SPADES ([Posbic et al., 2012](#), stellar parameter determination by a line-by-line analysis on synthetic spectra modeling), MyGIsFOS ([Sbordone et al., 2014](#), which use a precomputed grid of synthetic spectra to derive atmospheric parameters and chemical abundances from high-resolution spectra of cool stars), or FASMA ([Tsantaki et al., 2018](#), spectral synthesis technique to estimate the stellar atmospheric parameters for FGK-type stars in medium and high resolution).

2.3.2 Projection methods

Another mathematical parametrisation algorithm is the projection approach, for which it is first necessary to go through a training phase before the application for the final parameter estimate.

⁵<http://hebe.as.utexas.edu/ferre>

During the training phase, a set of projection vectors is calculated, containing the most important signatures to allow the derivation of a given physical parameter. In other words, the projection methods comprise the information of the reference model grid in vectors, which result as a linear combination of the models. Once the training phase is successfully performed, the final estimate is obtained through a simple scalar product between the vectors and the observations.

Some projection examples with recent astrophysics applications are the methods MATISSE (MATrix Inversion for Spectrum Synthesis, [Recio-Blanco et al., 2006](#)), MOPED (Massively Optimized Parameter Estimation and Data compression method, [Heavens et al., 2000](#)), the penalized χ^2 algorithm ([Zwitter et al., 2008](#)), or The Cannon ([Ness et al., 2015](#), a data-driven approach for determining stellar labels from spectroscopic data).

In this manuscript, MATISSE is part of the AMBRE Project pipeline (see description of the observational database in Chapter 4) to automatically and homogeneously derive the stellar atmospheric parameters (T_{eff} , $\log(g)$, $[M/H]$, $[\alpha/Fe]$), and the radial velocity (v_{rad}), of the archived stellar spectra from ESO spectrographs: FEROS, HARPS and UVES. It was developed at the Observatoire de la Côte d’Azur (OCA), and also used in the Gaia RVS analysis pipeline (Radial Velocity Spectrometer, see [Recio-Blanco et al., 2016](#)). It consists of an automatic parametrisation approach that use all the included information in a spectrum. The vectorial space is defined by the pixels of the spectrum. For each region in the reference grid, MATISSE indicates the directions that allow to determine the parameter values by projection.

2.3.3 Classification methods

The classification algorithms to parametrise the stellar spectra consider each model of the reference grid as a different class. In the same way as the projection methods, a previous training phase has to be performed over the reference models. However, the classification methods perform a more global application of the distance function over the parameter space. They are based on pattern recognition, taking decisions at each step of the algorithm as a function of the selected class and the identified property.

At the present time, the advent of large-scale spectroscopic surveys has triggered a formidable spectral modelling challenge to provide stellar parameters and abundances for hundreds of thousands of stars. For that reason, the classification methods are quite popular in astrophysics. Decision trees (e.g. DEGAS, [Kordopatis et al., 2011a](#)), artificial neural networks (ANNs, [Bailer-Jones, 2000](#), [Snider et al., 2001](#), [Leung & Bovy, 2019](#)), and support vector machines are examples of classification algorithms used for stellar parametrisation. These methods seem to be the only way to determine precise stellar abundances from low-resolution spectral surveys such as SEGUE ([Yanny et al., 2009](#), $R \sim 1800$) or LAMOST ([Zhao et al., 2012](#), $R \sim 1800$). As an application example, [Leung & Bovy \(2019\)](#) derived abundances from APOGEE spectra using ANNs.

2.4 Challenges for high-precise and accurate abundance measurements

A detailed exploration of possible error sources is crucial to interpreting the reality of the observed chemical signatures in the Galactic stellar populations and the resulting implications on chemodynamical relations (such as the contribution of radial migration in the solar neighbourhood or the use of $[Mg/Fe]$ as a good chronological proxy for the Milky Way disc), which are mainly constrained by the abundance precision. The main issues concerning the determination of high-precision abundances are characterised by the need for both high signal-to-noise

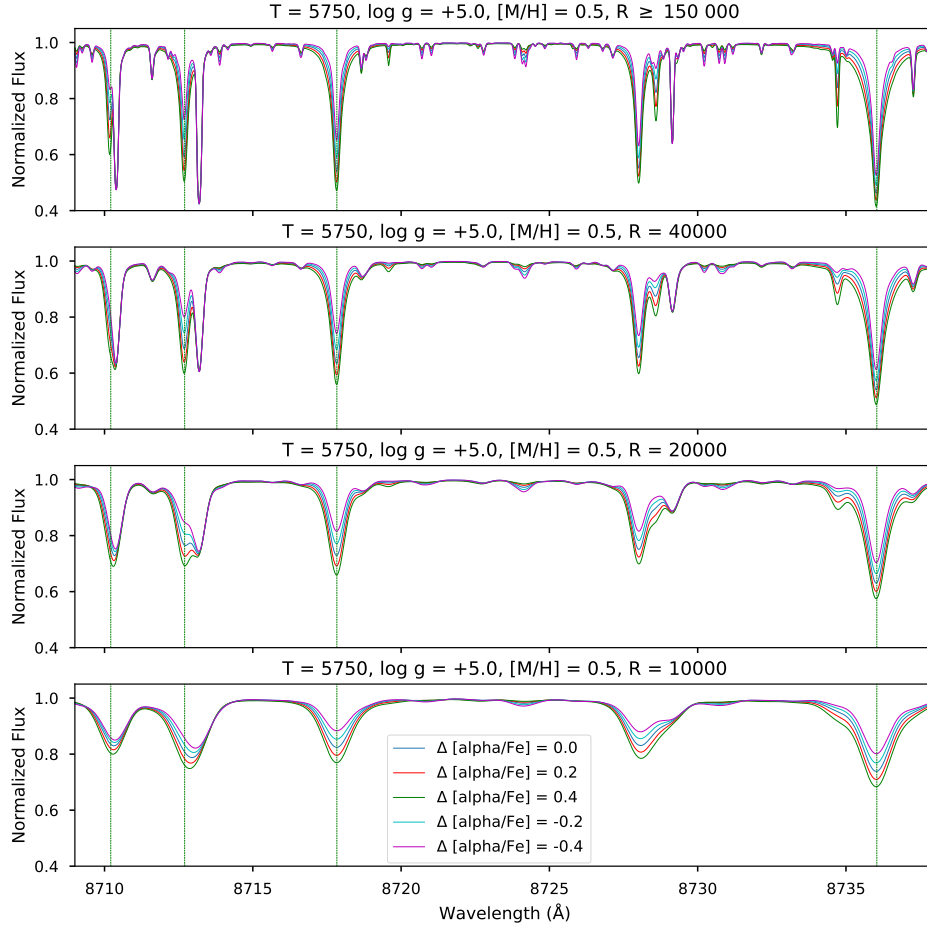


FIGURE 2.6: Spectrum comparison of a hot metal-rich dwarf star ($T_{\text{eff}} = 5750$ K, $\log g = +5.0$ dex, $[M/H] = +0.5$ dex), computed for five different α -enhancements. Green vertical lines correspond to the redder Magnesium lines (8710.21, 8712.70, 8717.83, and 8736.04 Å). From top to bottom, the synthetic spectra is plotted at resolution: $R \gtrsim 150000$, $R = 40000$, $R = 20000$ and $R = 10000$.

ratio (S/N) and spectral resolution⁶, and predominantly by the definition of continuum to normalise the observed spectral data. The latter issue can be responsible for the largest fraction of the uncertainty in the abundance estimations, which is still complex for cool metal-rich stars due to the high presence of blended and molecular lines (as reviewed by [Nissen & Gustafsson, 2018](#), [Jofré et al., 2019](#)). In particular, the continuum normalisation is not fully optimised for different stellar types in large spectroscopic stellar surveys.

In large spectroscopic stellar surveys, an automatic adjustment of the continuum is performed over the observed spectrum, generally via few iterations, searching for possible line-free regions ([Valenti & Piskunov, 1996](#), [Sousa et al., 2007](#), [García Pérez et al., 2016](#)). Most of the spectral analysis pipelines for determining chemical abundances and stellar atmospheric parameters carry out the same normalisation procedure for all stellar types, applying a constant continuum interval around the considered spectral feature. For instance, [Mikolaitis et al. \(2014\)](#) used a spectral fitting method to correct the local continuum in regions of $\pm 5\text{Å}$ and $\pm 15\text{Å}$ for weak and strong

⁶The spectral resolution, or resolving power, is defined as the ratio $R = \lambda/\Delta\lambda_{\text{instr}}$, where $\Delta\lambda_{\text{instr}}$ is the FWHM (Full Width Half Maximum) of the instrumental profile.

lines, respectively. In addition, [Adibekyan et al. \(2012\)](#) applied similar normalisation intervals on the measurement of equivalent widths (private communication). The width of the constant normalisation window is assumed to find continuum information around the analysed line for any stellar type. As a consequence, the methodology is not optimised to the difficulty of identifying the continuum, which depends on the spectral type. Cool metal-rich stars are a particularly difficult case due to the presence of blended and molecular lines. For instance, in the case of the APOGEE survey, [Holtzman et al. \(2015\)](#) remark how challenging it is to identify a true continuum in the observed spectra of these stellar types, leading to a ‘pseudo-continuum’ normalisation. Similarly, after an analysis of systematic errors using six different methods, [Jofré et al. \(2017\)](#) concluded that the definition of continuum may be responsible for the largest fraction of the uncertainty in abundance estimations.

Furthermore, [Nissen & Gustafsson \(2018\)](#) claimed that, in order to avoid a significant additional instrumental broadening of spectral lines, one needs a spectrograph with at least $R \gtrsim 50000$, which allows to disentangle blended lines and define a reliable continuum. As an illustrative example, [Fig. 2.6](#) shows how the stellar spectrum profile dramatically changes for different spectral resolutions values (keeping constant the stellar atmospheric parameters). We observe how the spectrum becomes significantly worse towards lower resolutions, i.e. more line blending and lower intensity of the lines. On the other hand, abundances from observed spectra with $S/N < 20 \text{ pixel}^{-1}$ are usually considered to be unreliable (e.g. [Smiljanic et al., 2014](#), [Heiter et al., 2015](#), [Jofré et al., 2019](#)). In conclusion, for planning large observational spectroscopic surveys, it is extremely important to carefully balance the necessary power resolution and signal-to-noise to derive accurate chemical abundances for the aimed stellar targets.

Chapter 3

Automated normalisation and abundance estimation procedures

Contents

3.1 Normalisation procedure	42
3.2 The GAUGUIN automated abundance estimation algorithm	43
3.3 Synthetic spectra grid	44
3.4 Line list	45
3.5 Sensitivity to spectral resolution and signal-to-noise	47

The aim of this chapter is to describe our normalisation procedure and the automated abundance estimation code GAUGUIN, i.e. our implemented spectrum synthesis algorithm for deriving precise [Mg/Fe] abundances. GAUGUIN is part of the analysis pipeline of the Gaia-ESO Survey and is also used for *Gaia* RVS spectra (Bijaoui et al., 2012, Recio-Blanco et al., 2014, 2016). Figure 3.1 illustrates the main steps of the pipeline. From the known atmospheric parameters of an observed star (T_{eff}^* , $\log g^*$, $[M/H]^*$, and $[\alpha/Fe]^*$), the code interpolates at the input atmospheric parameters in order to create a specific-reference synthetic spectra grid that covers a large range of the element abundance dimension (A_X). Then, a minimum quadratic distance is calculated, providing a first guess of the abundance estimate (A_0). Finally, a Gauss-Newton algorithm (developed by Bijaoui et al., 2012, described in Sect. 2.3.1) is applied in order to optimise the first guess solution, through a linearisation correction around the value, and provide the final measured abundance: A_X^* .

3.1 Normalisation procedure

The details regarding the normalisation algorithm are described hereafter.

The observed spectrum flux is normalised over a given wavelength interval centred on the analysed spectral line. For this purpose, the observed spectrum (O) is compared to an interpolated synthetic one (S) with the same atmospheric parameters. First, the most appropriate pixels of the residual ($R = S/O$) are selected using an iterative procedure that implements a linear fit to R followed by a σ -clipping. The clipping values vary from the first to the final iteration, starting with $\sigma_{-0.5}^{+5}$ and ending with σ_{-1}^{+2} . Then, a final residual is calculated ($R_{\text{final}} = S^*_{\text{norm}}/O^*_{\text{norm}}$), where S^*_{norm} and O^*_{norm} are the synthetic and observed flux values in the previously selected

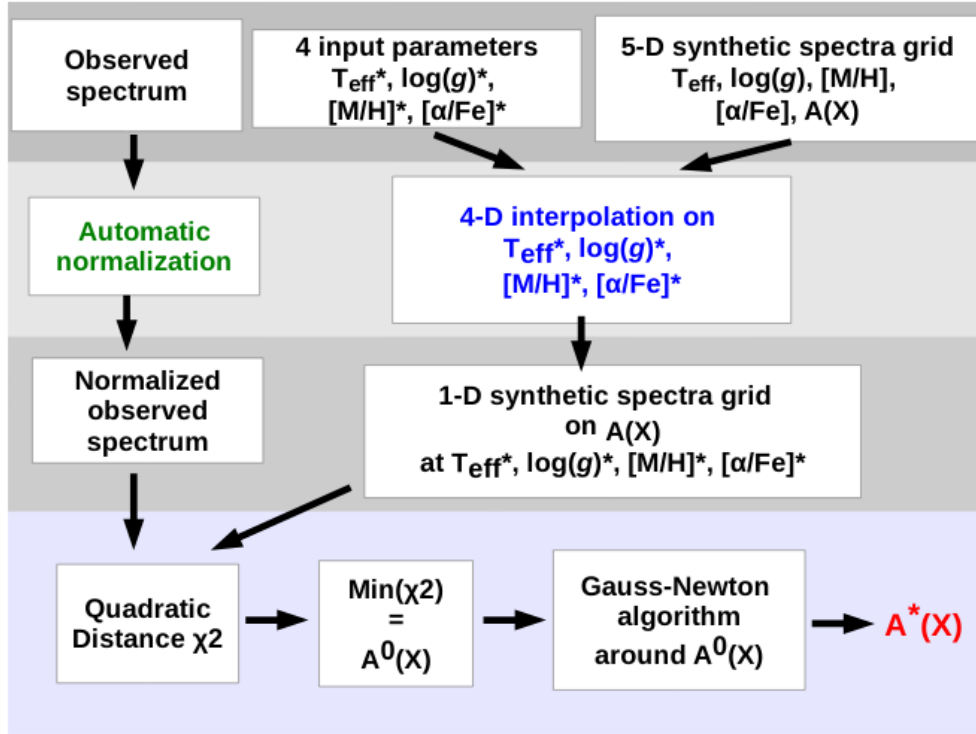


FIGURE 3.1: Schematic representation of the steps carried out by the implemented automatic procedure GAUGUIN. (Source: Guiglion, 2015).

pixels, applying an additional 0.2σ -clipping. Finally, the normalised spectrum is obtained after dividing the observed spectrum by a linear function resulting by the fit of R_{final} . No convolution is carried out during the normalisation procedure, so the original spectral resolution is conserved. As an example, Fig. 3.2 shows the normalised observed solar spectrum around the Mg line 5711.09 \AA .

It is worth noting that the local normalisation interval does not need to be perfectly symmetric around the analysed line. For some cases, due to contiguous strong absorption lines present on a particular side of the line, an asymmetric window can be chosen in order to maximise the number of pixels close to the continuum level (see next Sect. 5.1 for further details). For those particular configurations, where the abundance estimation window although included in the normalisation interval would be off centre, the observed chemical abundance trends were consistent with the results obtained from symmetrically selected windows.

3.2 The GAUGUIN automated abundance estimation algorithm

The GAUGUIN code is a classical optimisation method based on a local linearisation around a given set of parameters from the reference synthetic spectrum, via linear interpolation of the derivatives. The abundance estimate is performed considering the spectral flux in a predefined wavelength window, which is always inside the defined local normalisation one.

In our particular [Mg/Fe] abundance analysis, the abundance estimation window ($\Delta\lambda_{\text{Abund}}$, c.f. Fig. 3.2) was set around 0.5\AA for non-saturated lines, and 2.5\AA for strong saturated ones (see classification in Sect. 3.4 below). The abundance window's width is around ~ 1.5 -2 times

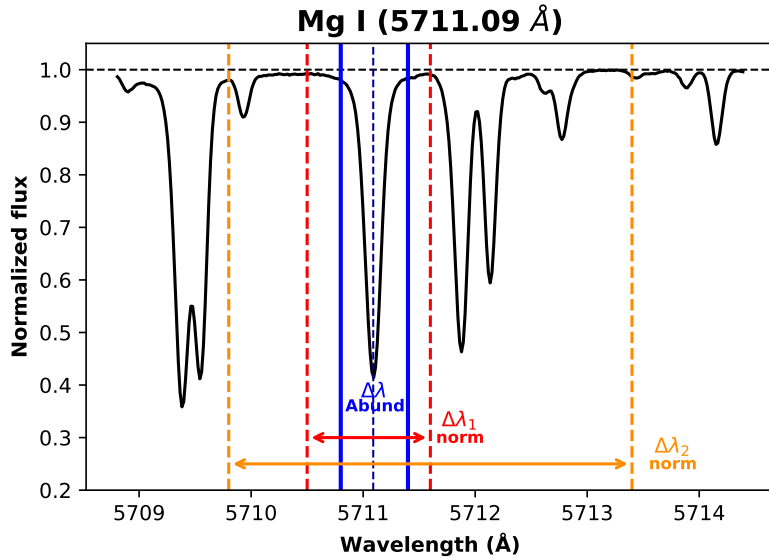


FIGURE 3.2: Observed solar spectrum from HARPS spectrograph ($R = 115\,000$, asteroid reflection) around the line 5711.09 \AA . The adopted wavelength domain where the abundance is measured is delimited by blue vertical lines ($\Delta\lambda_{\text{Abund}} \sim 0.5\text{ \AA}$; ~ 1.5 -2 times the FWHM of line in a solar-type star). Two different used normalisation intervals of 1 \AA ($\Delta\lambda_1$) and 4 \AA ($\Delta\lambda_2$) are shown with red and orange dashed vertical lines, respectively.

the FWHM of each line in a solar-type star. We tested different local continuum intervals, always larger than these abundance estimation windows, to study the normalisation influence on the derived abundances for each type of line (full analysis in Chapter 5).

Once the observed spectrum is normalised, a new specific-reference synthetic spectra grid is interpolated at the input atmospheric parameters in order to measure the abundance from the analysed spectral line. This grid now includes a large range of the element abundance dimension (A_X). For the α -elements abundance determination, the grid covers different $[\alpha/\text{Fe}]$ values. As previously illustrated in Fig. 3.1, a minimum quadratic distance is then calculated between the reference grid and the observed spectrum¹, providing a first guess of the abundance estimate (A_0). Then, this first guess is optimised via a Gauss-Newton algorithm, carrying out iterations through linearisation around the new solutions. The algorithm stops when the relative difference between two consecutive iterations is less than $\Delta A_X^2/100$. Figure 3.3 shows, for the observed solar spectrum, the final obtained fit for the Mg line 5711.09 \AA .

3.3 Synthetic spectra grid

A high-resolution optical synthetic grid (4200 - 6900 \AA ; $R \sim 300\,000$, $18\,452$ spectra) of non-rotating FGKM type spectra was used as a reference for the GAUGUIN procedure. One-dimensional LTE MARCS atmosphere models (Gustafsson et al., 2008) and the spectrum synthesis code TURBOSPECTRUM for radiative transfer (Alvarez & Plez, 1998) were adopted, together with the solar chemical abundances of Grevesse et al. (2007). The covered atmospheric parameter ranges are shown in Fig. 3.4: $3750 \leq T_{\text{eff}} \leq 8000\text{ K}$ (in steps of 250 K), $0.0 \leq \log(g) \leq 5.5\text{ cm s}^{-2}$ (in steps of 0.5 cm s^{-2}), $-3.5 \leq [M/H] \leq +1\text{ dex}$ (in steps of 0.25 dex), whereas the variation

¹Calculated over the wavelength domain, centred on the line, where GAUGUIN derives the abundance: $\chi^2 = \sum_{i=1}^N [O(i) - S(i)]^2$, where O and S are the observed and the synthetic spectrum, respectively.

² $\Delta A_X = 0.20\text{ dex}$ in the AMBRE grid.

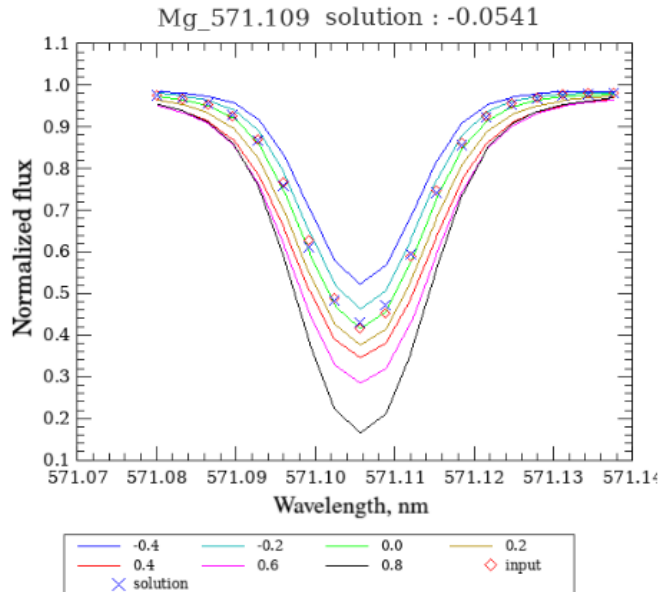


FIGURE 3.3: Example of the fit carried out by the optimisation code GAUGUIN for the line 5711.09 Å of the observed solar spectrum. The normalised observed spectrum is shown with red open diamonds, while the solution is indicated by blue crosses. The reference synthetic spectra grid is colour-coded according to $[\alpha/\text{Fe}]$ value.

in $[\alpha/\text{Fe}]$ is $-0.4 \leq [\alpha/\text{Fe}] \leq 0.8$ dex (for $[\text{M}/\text{H}] \geq 0.0$ dex), $-0.2 \leq [\alpha/\text{Fe}] \leq 0.8$ dex (for $-0.5 \leq [\text{M}/\text{H}] < 0.0$ dex), and $0.0 \leq [\alpha/\text{Fe}] \leq 0.8$ (for $[\text{M}/\text{H}] < -0.5$ dex), with steps of 0.2 dex.

This grid was computed in a similar way to the original AMBRE grid (de Laverny et al., 2012), which was adopted for the stellar parameter estimation (T_{eff}^* , $\log g^*$, $[\text{M}/\text{H}]^*$, $[\alpha/\text{Fe}]^*$, and v_{rad}^*). It does however contain some more recent specificities. First, we adopted the Gaia-ESO Survey atomic and molecular line lists (Heiter et al., 2015, 2020). Next, we considered more realistic values of the microturbulent velocity for the spectra computation by adopting a polynomial relation between v_{mic} and the main atmospheric parameters (M. Bergemann, private communication). Finally, we always considered perfectly consistent $[\alpha/\text{Fe}]$ enrichments between the selected MARCS models and the calculated emerging spectra. To be in agreement with the observational spectra data set (see next Chapter 4), we reduced the resolution of the synthetic spectra to the observed resolving power ($R = 115000$) by convolving with a Gaussian kernel.

It is worth noting that the $[\text{M}/\text{H}]$ notation comes from the atmosphere models. However, in the computation of the synthetic grid (where the models are used) we imposed that the $[\text{M}/\text{H}]$ parameter must be equal to the iron abundance value ($[\text{Fe}/\text{H}]$) of the star. Therefore, in the following results, and the corresponding interpretation with the time-delay model of the $[\text{Mg}/\text{Fe}]$ vs. $[\text{M}/\text{H}]$ plane (see Sect. 1.2.1), we can assume that $[\text{M}/\text{H}]$ actually behaves as $[\text{Fe}/\text{H}]$ since it does not take into account the α -elements enrichment.

3.4 Line list

The abundance analysis was performed using nine magnesium spectral lines in the optical range (shown in Table 3.1), adopting the atomic data of Heiter et al. (2015).

We performed an in-depth analysis of each line separately in order to test their reliability at different metallicity regimes. For a solar-type star, the selected lines could be classified in two

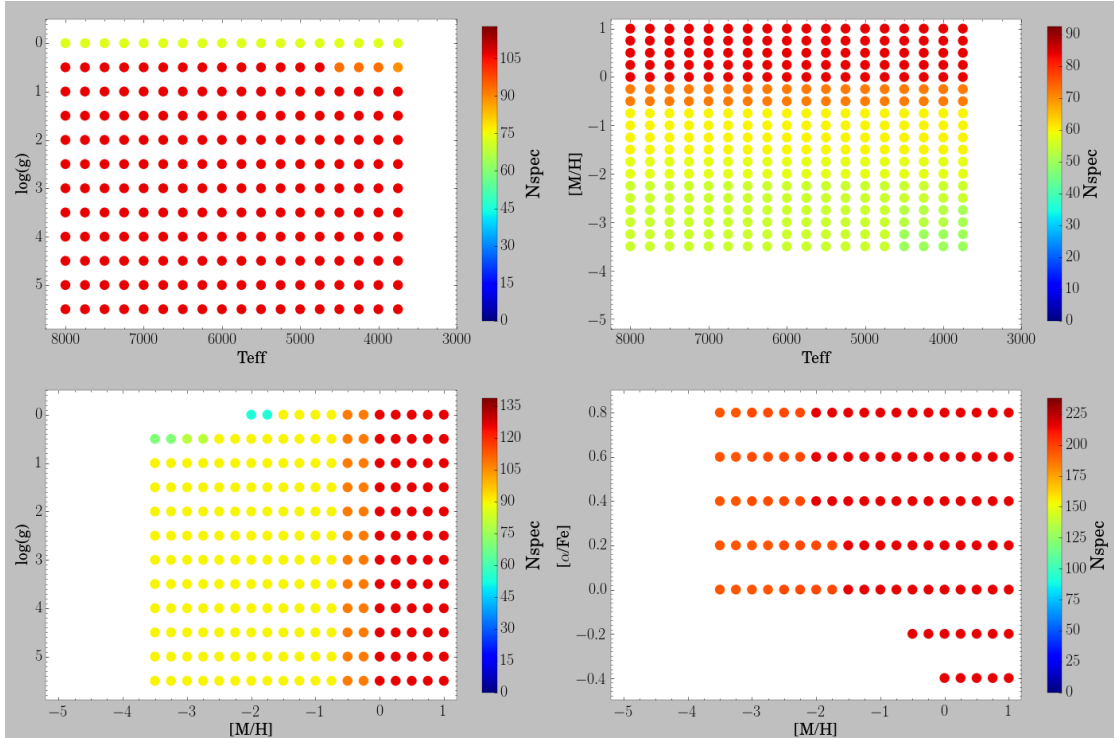


FIGURE 3.4: Stellar atmospheric parameters of the employed synthetic spectra grid in the $[\text{Mg}/\text{Fe}]$ abundance analysis with the automated code GAUGUIN.

categories: non-saturated (4730.04, 5711.09, and triplet: 6318.7, 6319.24, 6319.49 Å) and strong saturated lines (Mg Ib triplet: 5167.3, 5172.7 & 5183.6, and the line 5528.4 Å). Both cases are illustrated in Fig. 3.5. The number of pixels available for strong lines are approximately five times higher than for non-saturated lines. We only considered non-saturated lines for spectra with $\text{FWHM}_{\text{CCF}} \leq 7 \text{ km s}^{-1}$ to avoid possible uncertainties from line-broadening sources (see Sect. 5.2 for further details).

The selected lines in Table 3.1 have been widely used in the literature to determine both $[\text{Mg}/\text{Fe}]$ and $[\alpha/\text{Fe}]$ abundances. Bergemann et al. (2014, 2017) analysed different approximations for radiative transfer and spectral line formation in model atmospheres, focused on their effect on Mg abundance determination using lines in the optical and infrared, among which there are four lines used in our analysis (5172, 5183, 5528, and 5711 Å). They find no significant differences between 1D LTE and 1D NLTE abundances, and for the lines in common with ours, they present a quite robust behaviour with respect to the full 3D NLTE calculations in cool FGK stars. Small NLTE effects on Mg I line formation were also found by Zhao et al. (2016) and Alexeeva et al. (2018). In conclusion, 1D LTE Mg abundances are accurate enough for our selected sample and computationally cheaper than applying NLTE corrections. The results and discussions presented in this manuscript are therefore based on 1D LTE Mg abundances.

The methodology to calculate the final stellar $[\text{Mg}/\text{Fe}]$ abundance from all the Mg lines information is described as follows. For a given spectrum, a weighted average of the individual lines results was calculated following Adibekyan et al. (2016), where the distance from the median abundance was considered as a weight. This method allows us to avoid the combined random uncertainties of the different lines, minimising the error when more lines are considered. Next, as at least four spectra were available for each star in the sample, the final $[\text{Mg}/\text{Fe}]$ abundance of each object was calculated from the median value of the repeats.

Mg I (Å):				
<i>Non-saturated lines:</i>				
4730.04	5711.09	6318.7	6319.24	6319.49
<i>Saturated lines:</i>				
5167.3	5172.7	5183.6	5528.4	

TABLE 3.1: Optical magnesium lines selected in the present analysis.

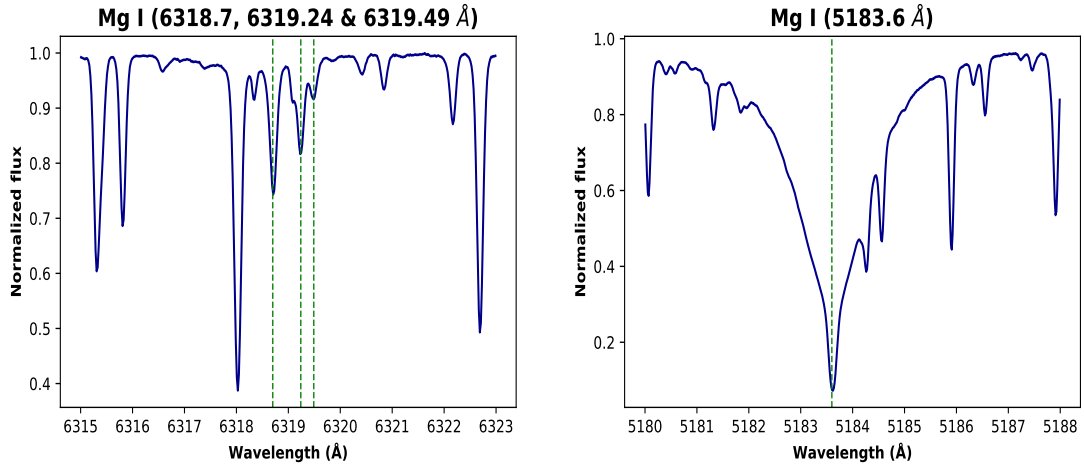


FIGURE 3.5: Non-saturated triplet lines around 6319 Å (left panel) and the strong saturated line 5183.6 Å (right panel), identified by green dashed vertical lines, in the normalised observed solar spectrum.

3.5 Sensitivity to spectral resolution and signal-to-noise

First of all, we implemented a test with theoretical spectra to evaluate the internal error sources in our method of $[\text{Mg}/\text{Fe}]$ estimation, focusing on the strong lines of the Mg Ib triplet (5167.3, 5172.7, 5183.6 Å). This error assessment leaves out the error sources restricted to real data, like the uncertainties in the line-broadening or the continuum normalisation, discussed in Chapter 5. In particular, the theoretical internal error analysis allows us to identify possible internal biases inside the automated procedure GAUGUIN.

We built statistically significant sets of interpolated spectra from the high-resolution synthetic spectra grid, convolving to six different spectral resolutions, in the range from $R \sim 2000$ to $R \sim 110000$ (\sim the HARPS resolution), and artificially adding five different random Gaussian noise (SNR = 10, 25, 50, 75, and 100). We defined four different stellar types:

- cool dwarf ($4000 \leq T_{\text{eff}} \leq 5000\text{K}$, $4.4 \leq \log(g) \leq 5.0 \text{ cm s}^{-2}$)
- turn-off ($5800 \leq T_{\text{eff}} \leq 6200\text{K}$, $3.5 \leq \log(g) \leq 4.1 \text{ cm s}^{-2}$)
- solar-type ($5500 \leq T_{\text{eff}} \leq 6000\text{K}$, $4.2 \leq \log(g) \leq 4.7 \text{ cm s}^{-2}$)
- red clump ($4000 \leq T_{\text{eff}} \leq 4700\text{K}$, $2.0 \leq \log(g) \leq 3.0 \text{ cm s}^{-2}$).

For each case, at a given spectral resolution, we generated 250000 spectra (50000 per bin of SNR) for three different metallicity bins: $-1.0 \leq [\text{M}/\text{H}] \leq -0.5$, $-0.2 \leq [\text{M}/\text{H}] \leq +0.2$ (\sim solar metallicity regime), and $+0.2 \leq [\text{M}/\text{H}] \leq +0.6$ dex, performing the abundance estimation with GAUGUIN.

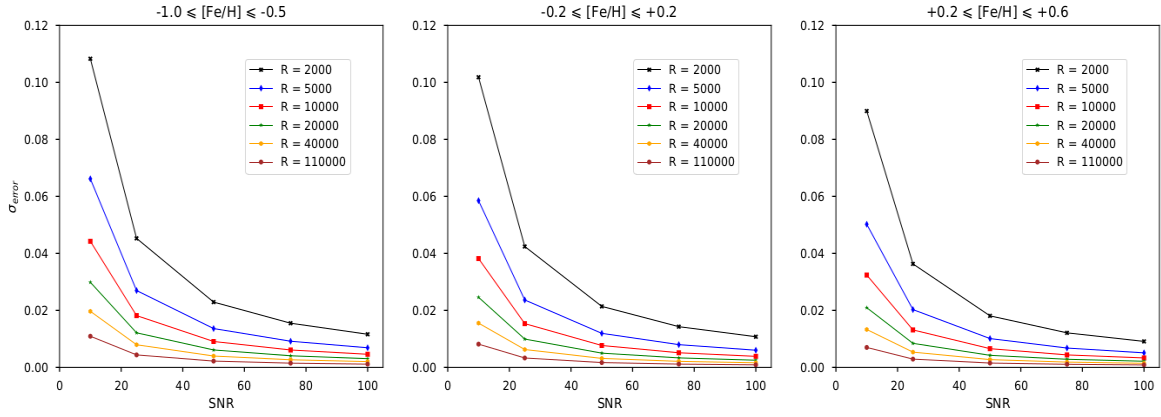


FIGURE 3.6: Internal error, in the MgIb triplet lines, given as the standard deviation of the mean of the abundances difference ($[\text{Mg}/\text{Fe}]_{\text{measured}} - [\text{Mg}/\text{Fe}]_{\text{input}}$) obtained from all measurements at a certain SNR and spectral resolution R , for a particular stellar type from the metal-poor (left) to the metal-rich (right) regime.

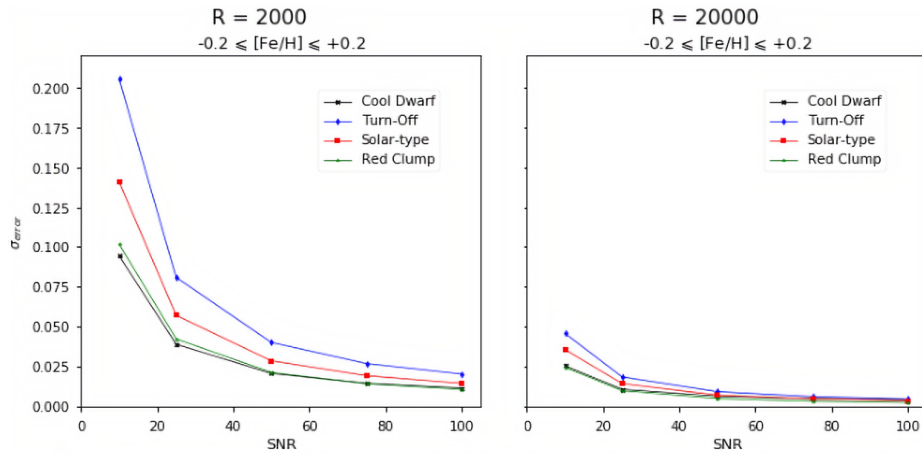


FIGURE 3.7: Same as Fig. 3.6 for different stellar types at low (left: $R = 2000$) and high (right: $R = 20000$) spectral resolution and solar metallicity.

First, no biases with stellar parameters are present in the results regardless of the resolution or the signal-to-noise ratio of the data. Secondly, it appears that working at high resolution always leads to better results, independently of the stellar type and the metallicity range. In Fig. 3.6, the errors in the average $[\text{Mg}/\text{Fe}]$ estimate (among the three Mg Ib lines) are given as a function of the SNR and for different resolutions. The three panels correspond to the three analysed metallicity intervals. In Fig. 3.7, the abundance error is shown for the four considered stellar types (cool dwarf, turn-off, solar-type and red clump), at the solar metallicity regime, and changing the spectral resolution from 2000 (left) to 20000 (right).

These two figures (Fig. 3.6 and Fig. 3.7) illustrate that the abundance estimation precision depends principally on the spectral resolution and secondly on the target's effective temperature and metallicity. On the one hand, despite the fact that the considered lines are very large, the uncertainty increases critically when the spectral resolution is degraded. Although, as expected, this effect is more significant at low signal-to-noise values, increasing the SNR does not always compensate a resolution loss. Working at large spectral resolutions always leads to better results than at lower ones. In addition, even at high signal-to-noise values, significant dependences of the uncertainty with the stellar type appear, if the spectral resolution is not high enough. In fact, the abundance uncertainties observed at low resolution are more dependent on

the stellar type than those obtained at high resolution. This behaviour highlights the importance of working at high resolution for spectroscopic surveys targeting a variety of stellar types and metallicity ranges, in order to achieve more precise and homogeneous results, even when strong lines are used. Moreover, the pseudo-continuum is expected to become more significant (fewer pixels close to the continuum level) at lower spectral resolutions.

These results are in agreement with the analysis of [Nissen & Gustafsson \(2018\)](#) (see previous Sect. 2.4) regarding high-precision stellar abundances, underlining the relevance of carefully balancing the need for a large sample of stars against the spectral resolution and the signal-to-noise necessary to achieve a good precision in abundances.

Chapter 4

Observational data sample

Contents

4.1 The AMBRE:HARPS spectra	50
4.2 Gaia DR2: photometry, astrometry and distances	52

In this chapter, we present the used observational data in the course of this thesis project. In particular, we make use of a large sample of AMBRE:HARPS optical stellar spectra (parametrised archived spectra at high spectral resolution $R \sim 115000$, see Sect. 1.4.1), for which we carry out the automatic determination analysis of high-precision Mg abundances with the GAUGUIN algorithm. In addition, we take advantage of the precise astrometric and photometric data from the *Gaia* DR2 catalogue to estimate accurate stellar ages and orbital parameters. As later explained, the combination of both surveys will shed new light on the exploration and interpretation of the present chemodynamical trend in the Milky Way disc.

4.1 The AMBRE:HARPS spectra

As described in Sect. 1.4.1, the AMBRE Project (de Laverny et al., 2013) is a collaboration between the Observatoire de la Côte d’Azur (OCA) and the European Southern Observatory (ESO) to automatically and homogeneously parametrise archived stellar spectra from ESO spectrographs: FEROS, HARPS and UVES. The stellar atmospheric parameters (T_{eff} , $\log(g)$, $[M/H]$, $[\alpha/Fe]$) were derived by the multi-linear regression algorithm MATISSE (Recio-Blanco et al., 2006, see Sect. 2.3.2), using the AMBRE grid of synthetic spectra (de Laverny et al., 2012, see Sect. 3.3). The AMBRE Project estimates the radial velocity (v_{rad}) by a cross-correlation function between the observed spectra and the used synthetic templates.

During this thesis, we derived $[Mg/Fe]$ abundances over a sample of 87522 HARPS spectra, corresponding to 2210 stars in the solar neighbourhood. These spectra sample was selected according to the goodness of fit between the synthetic and the observed spectrum, keeping those that present a quality label of 0 or 1 (see Table 3 of De Pascale et al., 2014). The signal-to-noise ratio (S/N) distribution of the sample is shown in Fig. 4.1. We only considered the HARPS spectra sample due to the high spectral resolution ($R \sim 115000$, Mayor et al., 2003) and to avoid biases among the different spectrographs included in the AMBRE Project. The external uncertainties of our database (estimated by comparison with external catalogues, see De Pascale et al., 2014) on T_{eff} , $\log(g)$, $[M/H]$, $[\alpha/Fe]$ and v_{rad} are 93K, 0.26 cm s^{-2} , 0.08 dex, 0.04 dex and 1 km s^{-1} , respectively. Moreover, the radial velocity correction was performed using the accurate

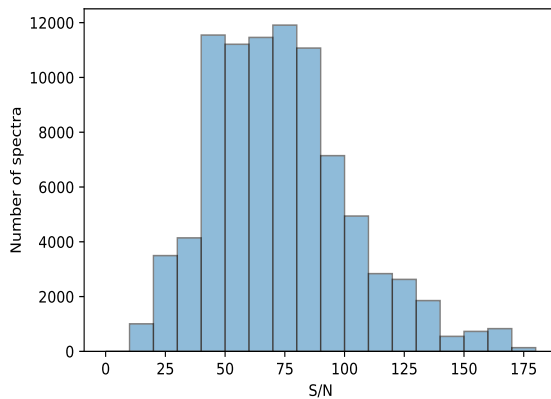


FIGURE 4.1: Signal-to-noise ratio (S/N) for the spectra in our AMBRE:HARPS sample.

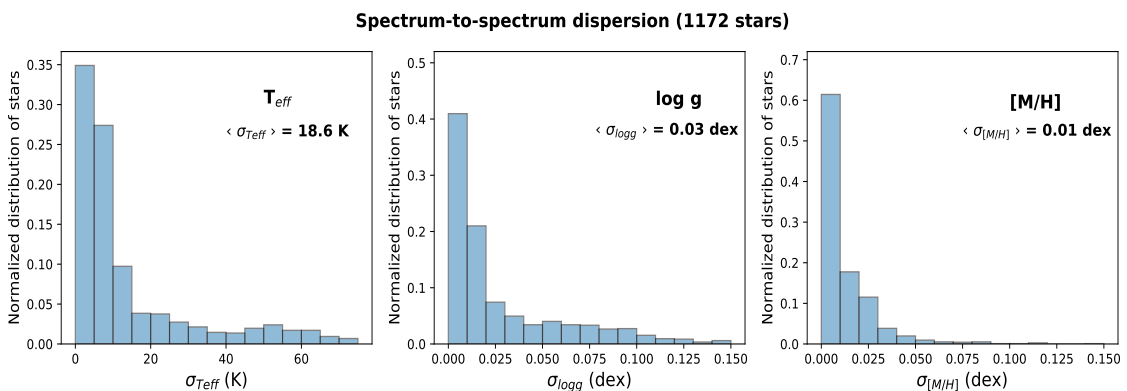


FIGURE 4.2: Estimated dispersion of the selected stars (> 4 repeats) on the effective temperature (left), the surface gravity (middle), and the global metallicity (right).

estimate provided by the ESO:HARPS reduction pipeline, except for a small proportion of the spectra with no HARPS radial velocity available, for which it was estimated by the AMBRE analysis procedure with similar precision (see [Worley et al., 2012](#), [De Pascale et al., 2014](#)).

The HARPS sample contains a large number of repeated observations for some stars. A cross-match with the *Gaia* DR2 catalogue ([Gaia Collaboration et al., 2018c](#)) allowed us to assign a *Gaia* ID to each spectrum, identifying the different spectra of the same star. In order to be statistically significant and avoid spurious effects in single spectra, we analysed the stars with more than four observed spectra (> 4 repeats), only selecting stars with $T_{\text{eff}} > 4700$ K, as cooler stars could have larger errors in the parameters (c.f. Fig. 12 in [De Pascale et al., 2014](#), where the cool main sequence flattens for metal-rich targets). In addition, for each star we excluded spectra whose atmospheric parameters differ by more than two sigma from the mean value of said star. This allows us to discard possible mismatches and avoid the propagation of uncertainties on the atmospheric parameters to the stellar abundances. These different quality selections lead to a total of 76502 spectra, corresponding to 1172 stars. The estimated dispersion on the stellar atmospheric parameters from the different spectra of the same star are shown in Fig. 4.2. The average dispersion on T_{eff} , $\log(g)$ and $[M/H]$ are 18.6 K, 0.03 dex and 0.01 dex, respectively.

To avoid any possible source of uncertainties from line-broadening, we only kept spectra with

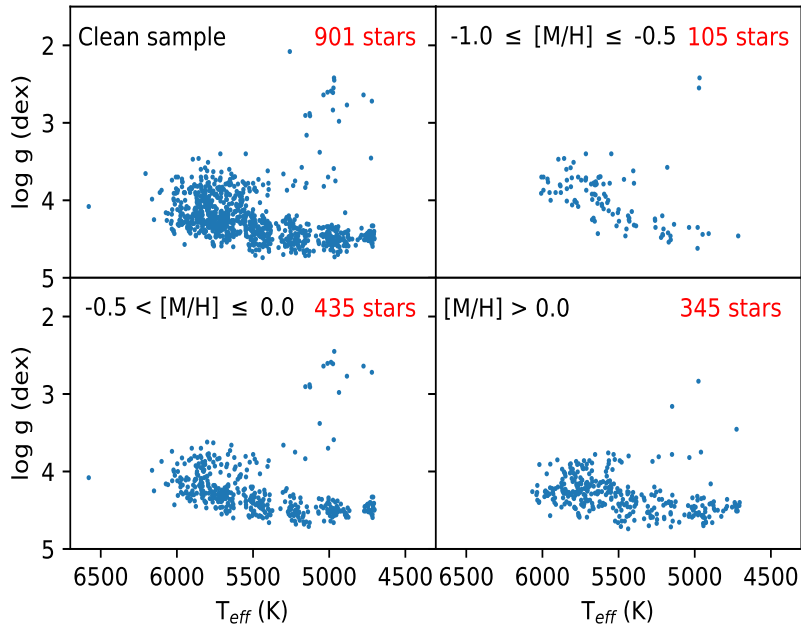


FIGURE 4.3: Hertzsprung-Russel diagram (in metallicity bins) of the selected AMBRE:HARPS stellar sample with $\text{FWHM}_{\text{CCF}} \leq 8 \text{ km s}^{-1}$ and more than four observed spectra (> 4 repeats).

$\text{FWHM}_{\text{CCF}}^1 \leq 8 \text{ km s}^{-1}$ (see further details in Sect. 5.2). As a consequence, the selected AMBRE:HARPS sample is restricted to the stellar atmospheric parameters shown in Fig. 4.3, mostly dwarf stars cooler than 6200K.

Secondly, after a deeply $[\text{Mg}/\text{Fe}]$ abundance estimation analysis (discussed in the following Chapter 5), we selected an AMBRE:HARPS spectra sub-sample that correspond to 494 main sequence turn-off (MSTO) stars. We restricted our sample to only MSTO stars in order to estimate reliable ages using an isochrone fitting method (see review in Sect. 1.2.3, and a full description of our method in Chapter 6). This stellar sample is identical to the one selected and presented by Hayden et al. (2017, see Fig. 1.13). In addition, those stars with more than four observed spectra (> 4 repeats) that present $\sigma_{\text{vrad}} > 5 \text{ km s}^{-1}$ were ruled out as binary system candidates. The remaining stellar sample in the analysis present $\sigma_{\text{vrad}} < 1 \text{ km s}^{-1}$. For this stellar sub-sample, we used the previously derived stellar $[\text{Mg}/\text{Fe}]$ abundances, and the accurate information from the *Gaia* DR2 catalogue to determine stellar ages and dynamics, and establish the existent chemodynamical correlations in the Milky Way disc.

4.2 Gaia DR2: photometry, astrometry and distances

We used astrometric (Lindgren et al., 2018) and photometric data (Evans et al., 2018, full passband information for BP and RP) from the *Gaia* DR2 catalogue (Gaia Collaboration et al., 2018c), along with distances calculated by Bailer-Jones et al. (2018) from *Gaia* DR2 parallaxes using a bayesian approach.

For this purpose, a cross-match was performed over the whole AMBRE:HARPS database with the *Gaia* DR2 catalogue through the CDS interface, looking for a match in a radius of 5 arcsec.

¹Cross-correlation function between the observed spectra and the corresponding templates used for the radial velocity estimation.

This allowed us to assign a *Gaia* ID to each spectrum, identifying the different spectra of the same star. In order to verify the goodness of the cross-match, we compared the spectroscopically derived T_{eff} and radial velocities with those provided by *Gaia* DR2. Since the number of sources with T_{eff} determinations in *Gaia* DR2 is not very large for the AMBRE:HARPS sample, we also estimated T_{eff} values from 2MASS (Skrutskie et al., 2006) and APASS (Henden et al., 2018) photometry, following González Hernández & Bonifacio (2009) (after performing the subsequent cross-match in the same way as we did with *Gaia*), to compare with the spectroscopic ones. As an additional check, we also estimated the corresponding 2MASS and APASS photometric magnitudes from *Gaia* photometry. Thus, we verified the right identification of stars in the cross-match by comparing the T_{eff} , the photometric magnitudes and the radial velocities for the each spectrum separately. We found that the median differences among AMBRE:HARPS, 2MASS, APASS, and *Gaia* data are lower than 150 K in T_{eff} , and around 0.1 for the photometric magnitudes J, H, and K. As far as the radial velocities are concerned, we only were able to compare AMBRE:HARPS and *Gaia* measurements, and found a median difference about 0.02 km s^{-1} . All these checks confirmed that the AMBRE / *Gaia* cross-match can be used with confidence.

As fully described in Chapter 6, we will estimate the ages and the orbital parameters with the *Gaia* DR2 astrometric positions and proper motions, also using the photometric information (Evans et al., 2018, full passband information for BP and RP), the calculated distances by Bailer-Jones et al. (2018) from *Gaia* DR2 parallaxes, and the spectroscopic stellar parameters determined by the AMBRE analysis procedure (see Worley et al., 2012, De Pascale et al., 2014).

Chapter 5

Optimisation of the automatic normalisation procedure: influence on the magnesium abundances in the Galactic disc

Contents

5.1	Analysed local normalisation intervals	55
5.2	Sensitivity to spectral line-broadening	55
5.3	Continuum placement optimisation for different lines and stellar types	58
5.3.1	Non-saturated lines	58
5.3.2	Strong saturated lines	58
5.3.3	Mg abundances line-to-line scatter	63
5.4	Disentangling the low- and high-[Mg/Fe] sequences in the disc . .	65
5.5	Summary	68

From the high-resolution observational AMBRE:HARPS spectra sample described in previous Chapter 4, we automatically derived and analysed the [Mg/Fe] abundances using 9 Mg I spectral lines in the optical range (see Table 3.1 in Sect. 3.4), via the optimisation method GAUGUIN (Bijaoui et al., 2012, Guiglion et al., 2016, Recio-Blanco et al., 2016), and using a reference synthetic spectra grid produced in the framework of the Gaia-ESO Survey (GES) project (Gilmore et al., 2012). As mentioned in previous chapters, GAUGUIN was part of the analysis pipeline of GES for the GIRAFFE spectra (Recio-Blanco et al., 2014), and is also used for Gaia RVS spectra (Recio-Blanco et al., 2016).

We derived [Mg/Fe] abundances for 87522 high-resolution spectra of 2210 solar neighbourhood stars from the AMBRE Project, and selected the 1172 best parametrised stars with more than four observed spectra (> 4 repeats). The atmospheric parameters (T_{eff} , $\log(g)$, $[M/H]$, $[\alpha/Fe]$) were used as an input in the abundance estimate analysis (independently determined within the AMBRE Project). A first global normalisation procedure was iteratively attached to the parameter estimation. This iteration is described in Worley et al. (2012) and was performed by De Pascale et al. (2014).

TABLE 5.1: Selected local normalisation windows (\AA) around each Mg I spectral line.

4730.04	5167.3	5172.7	5183.6	5528.4	5711.09	6319 triplet
[4729.5,4730.6]	[5166.0,5168.5]	[5170.8,5175.0]	[5180.3,5185.7]	[5527.6,5529.5]	[5710.7,5711.5]	[6318.3,6319.8]
[4728.2,4732.6]	[5162.5,5168.5]	[5169.5,5176.3]	[5177.6,5188.0]	[5527.1,5529.5]	[5710.5,5711.6]	[6318.3,6320.2]
	[5159.5,5168.5]	[5169.5,5181.5]	[5177.6,5191.0]	[5525.7,5530.4]	[5709.8,5713.4]	[6316.0,6321.9]
	[5156.5,5168.5]		[5174.0,5197.0]	[5522.7,5532.4]	[5709.8,5714.4]	
	[5151.5,5168.5]				[5709.8,5717.4]	
	[5148.5,5168.5]					
[4696 - 4764]	[5140 - 5210]	[5140 - 5210]	[5140 - 5210]	[5492 - 5564]	[5676 - 5746]	[6284 - 6354]

For the present abundance analysis, an initial global normalisation was applied, considering a large wavelength domain of 70\AA . In addition, an iterative local normalisation around the considered spectral line was performed to optimise the continuum placement. For this purpose, different widths of the local normalisation window were explored for each Mg spectral line.

5.1 Analysed local normalisation intervals

Different local continuum intervals were defined around each Mg I spectral line to explore their impact in the abundance analysis. By a spectral visualisation for different stellar types, the selection of the normalisation windows was adjusted to avoid the presence of strong absorption lines in the limits of the spanned region and chosen to have enough continuum points at the ends of the intervals. Figure 5.1 shows, for the observed solar spectrum, the different local normalisation intervals, along with the abundance estimation window, applied around each Mg line individually. In addition to the wavelength intervals plotted in this figure, we also tested a very large wavelength range around each analysed line of $\Delta\lambda_{\text{norm}} \sim 70\text{\AA}$. The complete list of the defined normalisation windows around each line is shown in Table 5.1.

As previously mentioned in Sect. 3.2, the abundance estimation window ($\Delta\lambda_{\text{Abund}}$) was set around 0.5\AA for non-saturated lines, and 2.5\AA for strong saturated ones (classification shown in Sect. 3.4), which corresponds to ~ 1.5 -2 times the FWHM of each spectral line in a solar-type star. We tested different local continuum intervals, always larger than these abundance estimation windows, to study the normalisation influence on the derived abundances for each type of line. As can be clearly seen in Fig. 5.1, denoted by red dashed vertical lines, the local normalisation interval is not always perfectly symmetric around the analysed line. For some cases, due to contiguous strong absorption lines present on a particular side of the line, an asymmetric window is chosen in order to maximise the number of pixels close to the continuum level. For those particular configurations (only a few among the total analysed cases), the abundance window although included in the normalisation interval would be off centre. However, the observed abundance trends for these cases were consistent with the results obtained from symmetrically selected windows.

5.2 Sensitivity to spectral line-broadening

First of all, we analysed the possible impact of line-broadening sources in the abundance estimate (see description in previous Sect. 2.1).

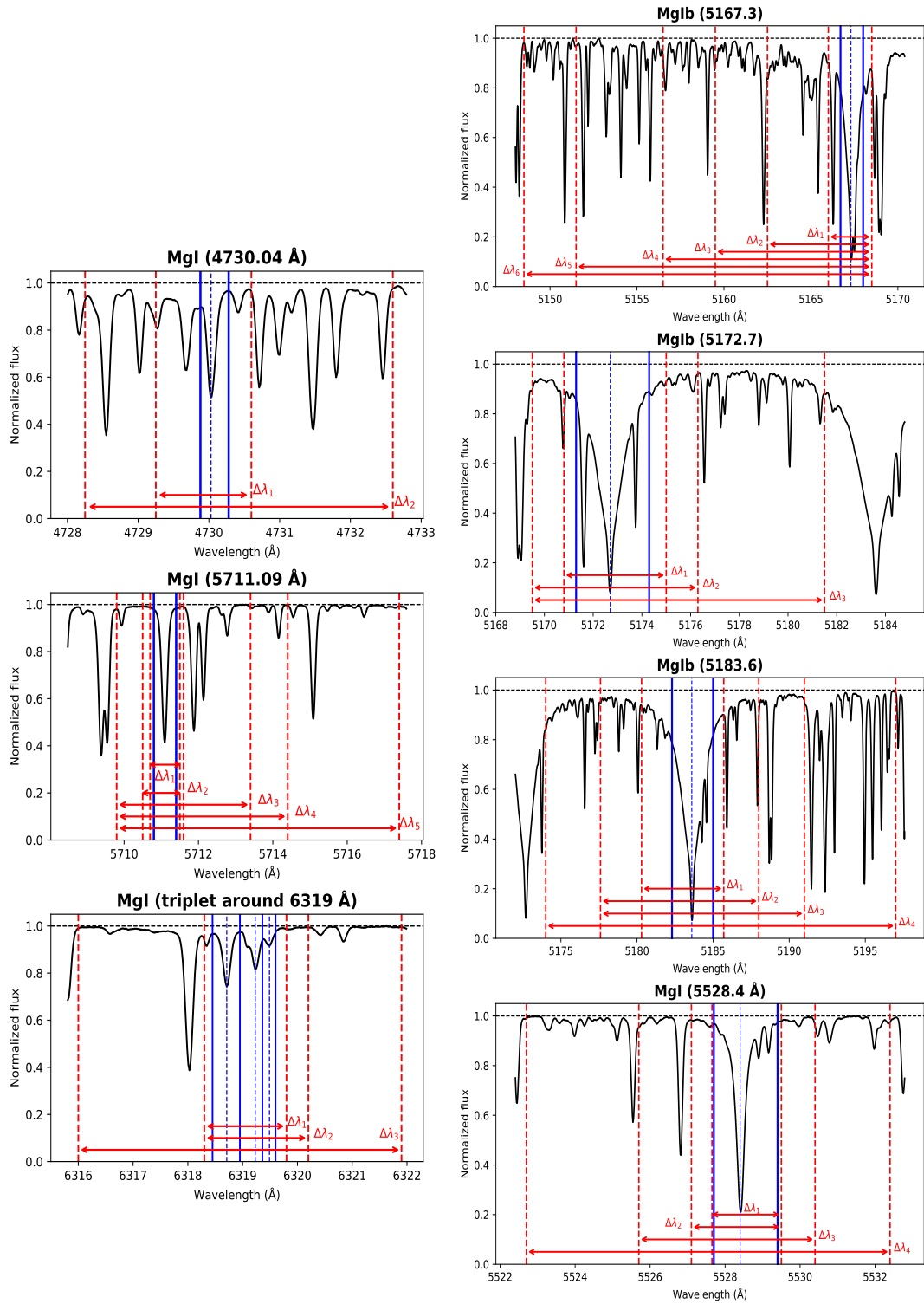


FIGURE 5.1: Observed solar spectrum from HARPS around each Mg I spectral lines. The abundance estimation window is delimited by blue vertical lines ($\Delta\lambda_{\text{Abund}} \sim 0.5 \text{ \AA}$ for non-saturated lines and $\Delta\lambda_{\text{Abund}} \sim 2.5 \text{ \AA}$ for strong saturated ones). The different local normalisation intervals applied in the analysis are shown with red dashed vertical lines. **Left:** non-saturated lines: 4730.04, 5711.09, 6318.7, 6319.24, and 6319.49 Å. **Right:** strong saturated lines: 5167.3, 5172.7, 5183.6, and 5528.4 Å (from top to bottom).

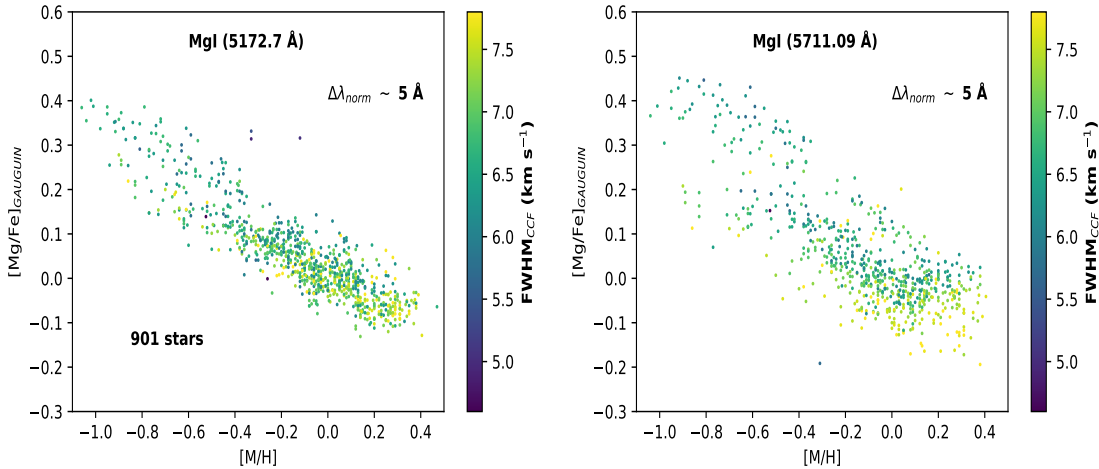


FIGURE 5.2: Abundance ratio $[\text{Mg}/\text{Fe}]$ as a function of $[\text{M}/\text{H}]$, colour-coded by the FWHM_{CCF} of the cross-correlation function. Both panels contain the same number of stars. Strong saturated lines (left, with less dispersed sequences) are less sensitive to spectral line-broadening than non-saturated lines (right). The $[\text{Mg}/\text{Fe}]$ abundances were derived by performing the continuum placement around a local wavelength interval of 5\AA .

On the one hand, our pre-computed synthetic spectra grid consisted of non-rotating spectra ($v\text{-sin}(i) = 0.0 \text{ km s}^{-1}$; projected rotational velocity), where the only considered line-broadening source is the microturbulence v_{mic} , for which a calibrated empirical relation with respect to the atmospheric parameters was adopted (M.Bergemann, private communication). The typical errors are around 0.3 km s^{-1} , having a negligible effect on the final abundance estimate.

On the other hand, the AMBRE Project provides the FWHM of the cross-correlation function between the observed spectra and the corresponding templates used for the radial velocity estimation. This parameter, denoted as FWHM_{CCF} , can be used as a global broadening measurement in order to study the sensitivity of the abundance precision to the main line-broadening sources (e.g. stellar rotation $v\text{-sin}(i)$, and macroturbulence v_{mac}).

Figure 5.2 shows the derived $[\text{Mg}/\text{Fe}]$ vs. $[\text{M}/\text{H}]$ abundances from two different spectral lines: a saturated one (5172.7\AA , left panel) and a non-saturated one (5711.09\AA , right panel). For each line, the continuum placement has been performed over a local window of the same width. We conclude that the dispersion on the $[\text{Mg}/\text{Fe}]$ abundance measurement, with respect to $[\text{M}/\text{H}]$, is dominated by the spectral line-broadening for non-saturated lines, although not for strong saturated lines. This is expected since the larger natural broadening of strong lines makes them less sensitive to the line-broadening. Similarly, high-resolution spectra are more sensitive to this effect than low-resolution data. This result highlights the relevance of a correct treatment when using weak non-saturated lines. Otherwise, choosing stronger lines or restricting the analysis to cool stars (for which the $v\text{-sin}(i)$ is lower) would minimise the effects.

We only kept spectra with $\text{FWHM}_{\text{CCF}} \leq 8 \text{ km s}^{-1}$ for strong saturated lines, but only spectra with $\text{FWHM}_{\text{CCF}} \leq 7 \text{ km s}^{-1}$ for non-saturated lines. As we do not have any $v\text{-sin}(i)$ determinations for these stars, we applied this cut based on the minimisation of the observed dispersion from each particular type of line.

5.3 Continuum placement optimisation for different lines and stellar types

As described in Chapter 3, GAUGUIN carries out an iterative procedure over a local window around the analysed line to normalise the spectrum. For that reason, we studied the normalisation influence on the derived abundances applying (for each Mg I line; see Table 3.1) different local continuum intervals (from narrow, $\Delta\lambda_{\text{norm}} \sim 1\text{\AA}$, to very large ranges, $\Delta\lambda_{\text{norm}} \sim 70\text{\AA}$. See Fig. 5.1). For this purpose, we evaluated the quality of the resulting normalisation, using a goodness of fit (χ^2 ; minimum quadratic distance) between the interpolated synthetic spectrum (with the corresponding atmospheric parameters of the star) and the normalised observed one (shown in previous Fig. 3.3). This was performed over the abundance estimation window, as it is constant for each line (c.f. blue lines in Fig. 3.2 and Fig. 5.1).

5.3.1 Non-saturated lines

Figure 5.3 shows, for the non-saturated line 4730.04 Å, the difference in the line χ^2 fitting in logarithmic scale (top-left panel) and the corresponding derived abundance values (bottom-left panel) between different local normalisation intervals. The resulting comparison reveals a more precise fit applying the narrowest interval ($\Delta\chi^2 < 0$) for all the metallicities. We find that this improvement of the fit has a larger impact on the derived abundances for the metal-rich stars, leading to lower [Mg/Fe] abundances at supersolar metallicities, with differences as high as ~ 0.3 dex at $[M/H] = +0.2$ dex in comparison with the largest wavelength domain. The right panel of Fig. 5.3, showing the [Mg/Fe] vs. [M/H] plane, highlights the influence of the normalisation procedure on the behaviour of the α -elements in the metal-rich regime of the disc.

In addition, Fig. 5.4 illustrates the effect of the different normalisation windows in the flux of the Mg line at 4730.04 Å, for a particular metal-rich star ($[M/H] = +0.31$ dex). The observed flux variations are responsible for the abundance differences observed in Fig. 5.3. The use of a larger normalisation interval can drop artificially the observed flux, leading to higher abundance estimates. More difficult pseudo-continuum placements due to contiguous absorption lines can explain this continuum drop, and the poorer goodness-of-fit values observed in Fig. 5.3.

As for the 4730.04 Å line, the weak triplet lines around 6319 Å are better fitted by applying a narrow normalisation interval. For the Mg line 5711.09 Å, which is stronger than the other non-saturated lines, the optimal local normalisation window is larger for cool metal-rich stars, for which the line is more intense although still not saturated.

In conclusion, for non-saturated lines, there is generally enough continuum information around and close to the line. As a consequence, it is convenient to optimise the normalisation interval, close to the considered spectral feature.

5.3.2 Strong saturated lines

For strong saturated lines like the Mg Ib triplet (5167.3, 5172.7, and 5183.6 Å) and the line 5528.4 Å, no pixels are available close to the continuum level for most of the stellar types in the analysed region (see e.g. right panel in Fig. 3.5 or right column in Fig. 5.1), and a pseudo-continuum normalisation has to be performed for the automatic fit, including part of the line wings.

However, two main difficulties affect the procedure. On the one hand, due to the line saturation, only the wings are sensitive to the abundance. As a consequence, an important degeneracy

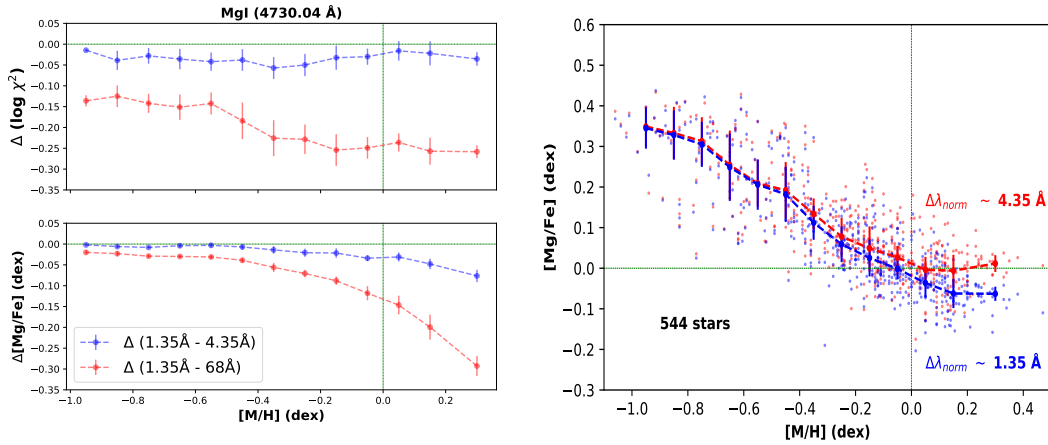


FIGURE 5.3: Analysis of the non-saturated line 4730.04 Å. **Left:** comparison, averaged in metallicity bins of 0.1 dex, of the line χ^2 fitting in logarithmic scale (top) and the derived abundance (bottom) values from different local normalisation intervals ($\Delta\lambda_{\text{norm}} = 1.35, 4.35, 68\text{ Å}$; taking the shortest interval as a reference, which corresponds to around four times the FWHM of the line in a solar-type star). **Right:** stellar abundance ratios $[Mg/Fe]$ vs. $[M/H]$ for the local normalisation window $\Delta\lambda_{\text{norm}} = 1.35\text{ Å}$ (blue points) and $\Delta\lambda_{\text{norm}} = 4.35\text{ Å}$ (red points). Their respective behaviours were calculated by the mean $[Mg/Fe]$ abundance value per metallicity bin. The reduced number of stars is due to the cut in FWHM_{CCF} for the non-saturated lines.

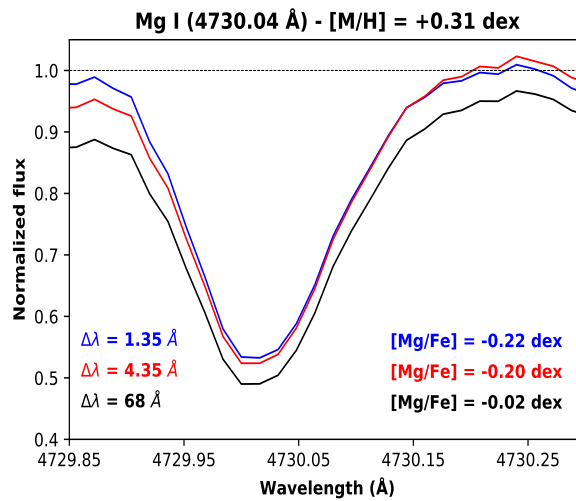


FIGURE 5.4: Normalised observed spectrum of a metal-rich star ($[M/H] = +0.31\text{ dex}$) in the abundance estimation window of the non-saturated line 4730.04 Å. Different line profile depending on the applied local continuum intervals ($\Delta\lambda_{\text{norm}} = 1.35$ (blue), 4.35 (red), 68 Å (black)), along with the derived $[Mg/Fe]$ abundance for each case.

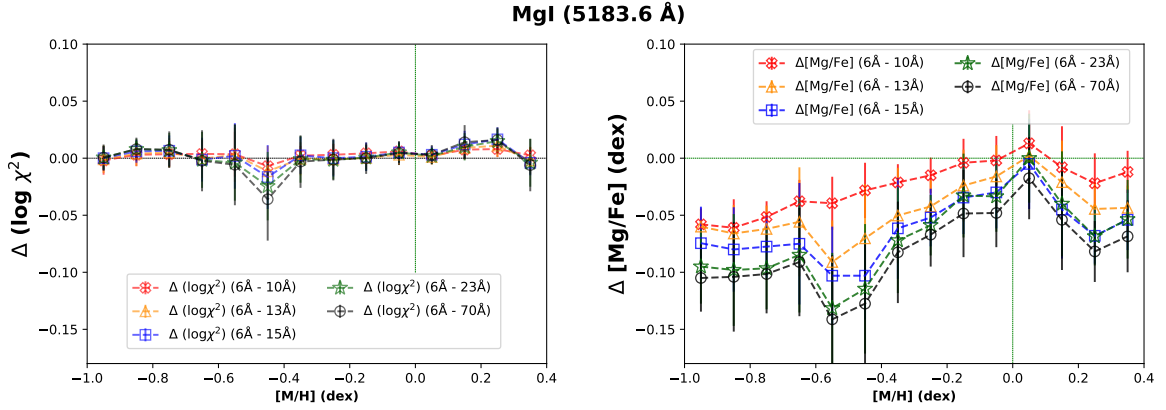


FIGURE 5.5: Analysis of strong saturated line 5183.6 Å. **Left:** comparison, averaged in metallicity bins of 0.1 dex, of the line χ^2 fitting values (in logarithmic scale) for the different applied local normalisation intervals ($\Delta\lambda_{\text{norm}} \sim 6\text{\AA}, 10\text{\AA}, 13\text{\AA}, 15\text{\AA}, 70\text{\AA}$; taking the shortest interval as a reference, which corresponds to two times the FWHM of the line in a solar-type star, approximately). **Right:** same analysis comparing the derived abundance values.

between the continuum placement and the derived $[\text{Mg}/\text{Fe}]$ abundance appears. In other words, large changes in the continuum placement, like those induced by the use of different normalisation windows, can be compensated by a change in the abundance without degrading the line fitting quality. Figure 5.5 illustrates, for the different local normalisation intervals analysed around the 5183.6 Å line, the comparison of the line χ^2 fitting values (left panel), and the corresponding derived abundance values (right panel). A negligible difference in the goodness of fit from the studied continuum intervals is observed, although, as shown on the right-hand side, it corresponds to notorious differences in the abundance estimations. Therefore, the χ^2 quality criterion, reliable to carry out an appropriate normalisation interval selection for the non-saturated lines (previous Sect. 5.3.1), is usually not discriminating enough in saturated lines.

On the other hand, the larger the local normalisation window, the larger the dependencies of the abundance results on the parameters and, as a consequence, the larger the dispersion on the $[\text{Mg}/\text{Fe}]$ abundance with respect to $[\text{M}/\text{H}]$. This is illustrated in Fig. 5.6, where the resulting $[\text{Mg}/\text{Fe}]$ vs. $[\text{M}/\text{H}]$ abundances are shown for the same line and most representative normalisation intervals of Fig. 5.5, colour-coded with the star's effective temperature and surface gravity. Clearly, the results obtained with the largest normalisation window (left panels) have a significant T_{eff} dependence and even a $\log g$ dependence, inducing a higher dispersion. Those effects are alleviated when the normalisation window is narrowed to 10 Å (middle panels), and they practically disappear for the narrowest window of 6 Å (right panels). In addition, broader windows tend to have lower $[\text{Mg}/\text{Fe}]$ values for cooler and higher gravity stars. These trends do not disappear even if an iterative procedure involving local normalisation and abundance estimation is implemented. In addition, the parameter dependence is also observed when larger normalisation intervals are explored (going beyond the MgI triplet wings, up to $\Delta\lambda_{\text{norm}} \sim 70\text{\AA}$; 5140 - 5210 Å). In the following, we analyse in detail the reason for this observed pattern of strong saturated lines.

To better illustrate this behaviour, Fig. 5.7 shows the synthetic spectra for a hot star ($T_{\text{eff}} = 6000\text{ K}$, left panel) and a cool star ($T_{\text{eff}} = 5000\text{ K}$, right panel), keeping the other atmospheric parameters constant to the following values: 4.5 dex in $\log g$, + 0.25 dex for metallicity, and 0.0 dex in $[\alpha/\text{Fe}]$ abundance. The blue synthetic spectra consider all the absorption sources (atomic and molecular lines), while the red ones present only the Mg lines absorption source for comparison purposes. As illustrated in the right panel, the pseudo-continuum level is essentially

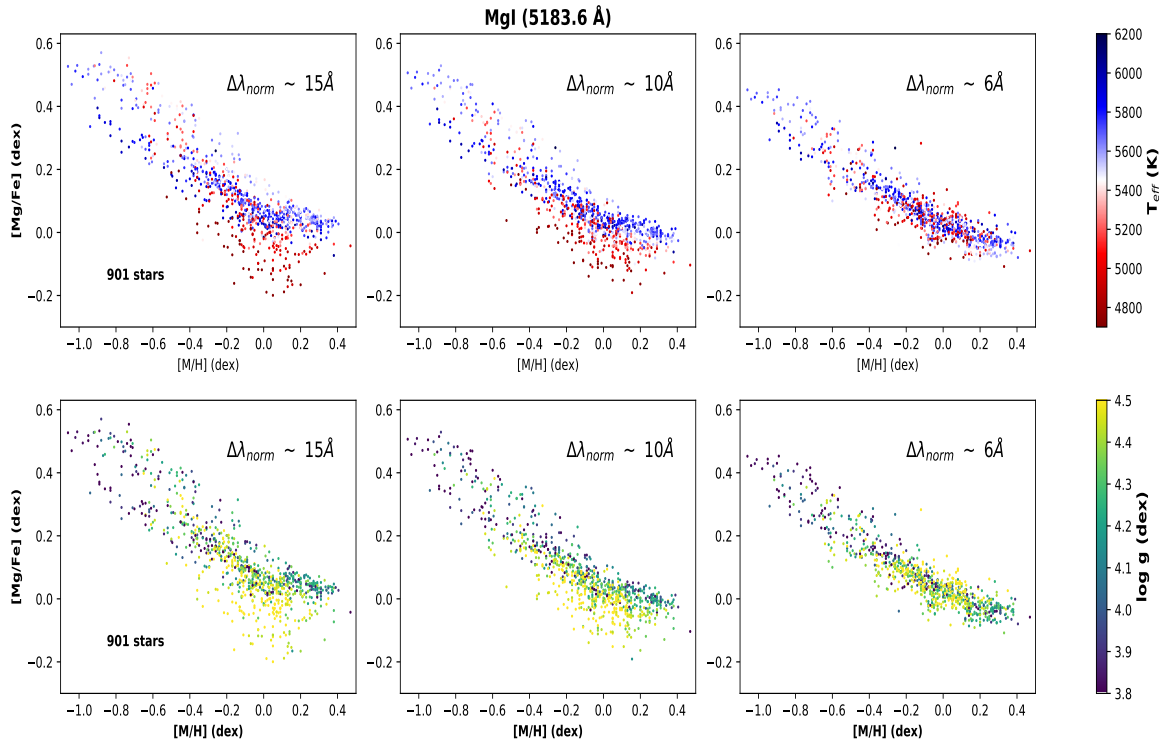


FIGURE 5.6: Comparison of stellar abundance ratios $[Mg/Fe]$ vs. $[M/H]$ derived for the strong saturated line 5183.6 \AA , colour-coded by stellar effective temperature (top row) and surface gravity (bottom row), after carrying out the continuum placement in three different local normalisation intervals around the line. **Left:** $\Delta\lambda_{norm} \sim 15 \text{ \AA}$, typical local continuum interval applied in the literature for strong lines. **Middle:** $\Delta\lambda_{norm} \sim 10 \text{ \AA}$. **Right:** $\Delta\lambda_{norm} \sim 6 \text{ \AA}$, narrow normalisation interval (\sim twice the FWHM of the line in solar-type stars).

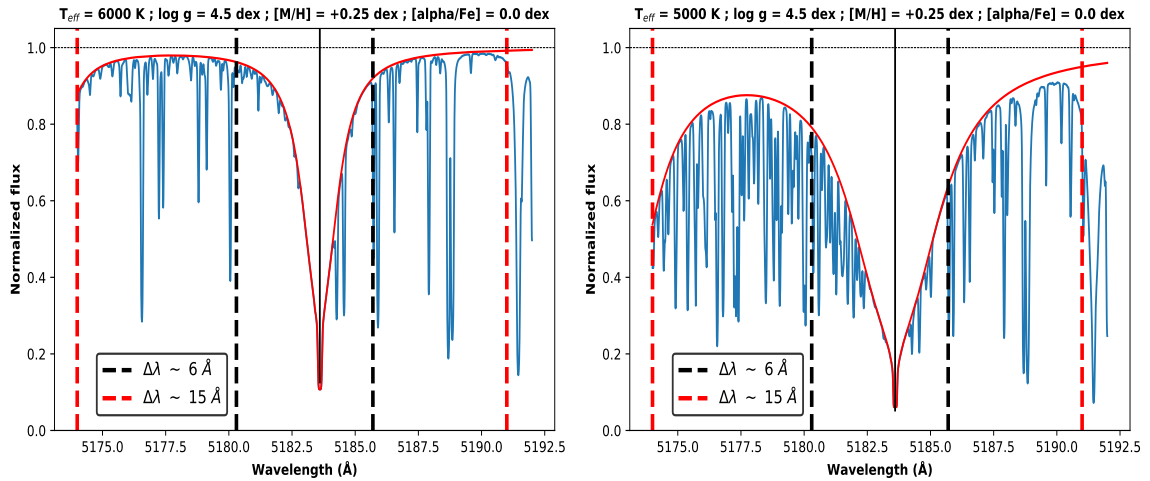


FIGURE 5.7: Comparison of synthetic spectra around the saturated line 5183.6 \AA (black solid vertical line), considering all the absorption lines (blue spectra) and only the Mg line absorption (red spectra). The black and red dashed vertical lines present the limits of the 6 \AA and 15 \AA normalisation windows, respectively. **Left:** hot star ($T_{eff} = 6000 \text{ K}$). **Right:** cool star ($T_{eff} = 5000 \text{ K}$). The other atmospheric parameters are constant ($\log g = 4.5 \text{ dex}$, $[M/H] = +0.25 \text{ dex}$, $[\alpha/Fe] = 0.0 \text{ dex}$).

driven by the Mg line absorption. As a consequence, when no pixels at the continuum are available (e.g. cool and metal-rich stars), the first Mg abundance guess has a strong influence in the pseudo-continuum placement. In our procedure, the normalisation step, taking as a reference a synthetic spectrum with the star's atmospheric parameters, assumes as a first guess that $[\text{Mg}/\text{Fe}]$ is equal to the input $[\alpha/\text{Fe}]$ parameter (see Sect. 3.1).

To explore the dependence of the normalisation, and therefore of the resulting $[\text{Mg}/\text{Fe}]$ estimates, on the initial abundance guess, we artificially subtracted 0.2 dex to the corresponding $[\alpha/\text{Fe}]$ initial value of each star ($[\alpha/\text{Fe}]_{\text{input}}^* = [\alpha/\text{Fe}]_{\text{input}} - 0.2$ dex) without modifying the observed spectra sample, simulating a difference between the $[\alpha/\text{Fe}]$ and the $[\text{Mg}/\text{Fe}]$ abundance. Figure 5.8 shows the difference in the resulting $[\text{Mg}/\text{Fe}]$ estimate for two local normalisation windows of 6 and 15 Å around the saturated line 5183.6 Å (illustrated in Fig. 5.7). On the left panel, the temperature dependence of the differences is plotted only for the metal-rich sample. On the right panel, the metallicity dependence of the differences is only plotted for the cool sample. This allows us to isolate the impact of the $[\alpha/\text{Fe}]$ - $[\text{Mg}/\text{Fe}]$ bias for the typical cases of spectra with pseudo-continuum. The normalisation procedure is independent on the initial $[\alpha/\text{Fe}]$ when the derived $[\text{Mg}/\text{Fe}]$ abundance has not been shifted ($\Delta[\text{Mg}/\text{Fe}]_{\text{measured}} = 0.0$ dex). For the large normalisation window (red curve), we observe that the derived $[\text{Mg}/\text{Fe}]$ abundance depends highly on the assumed parameters (temperature on the right panel and metallicity on the left one). Indeed, as the number of pixels at the real continuum used to normalise varies from nearly 100% (hot, metal-poor stars) to 0% (cool, metal-rich stars), the parameter dependence of the result will vary from no impact ($\Delta[\text{Mg}/\text{Fe}]_{\text{measured}} = 0$) to an almost completely dependent situation ($\Delta[\text{Mg}/\text{Fe}]_{\text{measured}} = +0.2$ dex, that is the introduced bias). In the narrow normalisation window (black curve), all the stellar types have a very low number of pixels at the continuum, implying only small adjustments with respect to the initial implicit guess given by the assumed $[\alpha/\text{Fe}]$. Therefore, almost no parameter dependence is observed around a $\Delta[\text{Mg}/\text{Fe}]_{\text{measured}} = +0.2$ dex.

This result is in close agreement with the synthetic analysis showed in Fig. 5.7. The induced bias in the continuum-level estimation, and therefore in the derived $[\text{Mg}/\text{Fe}]$ abundances, is always present but constant with the stellar atmospheric parameters if the narrow normalisation interval is applied around the strong saturated lines. This is not the case for the 15 Å window, for which this induced bias is partially corrected but only to an extent that depends on the stellar parameters.

The application of a large local continuum interval is only convenient for the stellar types with pixels reaching the continuum level. In those cases, as described before, the normalisation procedure is independent on the initial guess of the $[\alpha/\text{Fe}]$ value. In our sample, this condition only occurs for stars with $5500 \leq T_{\text{eff}} \leq 5750$ K and $3.5 \leq \log g \leq 4.5$ dex. The corresponding $[\text{Mg}/\text{Fe}]$ vs. $[\text{M}/\text{H}]$ for these stars, using the large normalisation window (15 Å), is shown in Fig. 5.9. It can be appreciated that the thin and thick disc sequences clearly separate up to a metallicity of $\sim +0.1$ dex, and the trends at high metallicity do not flatten. These more accurate results are in agreement with the observed trends for the narrowest (6 Å) normalisation window for all the stellar types (right panels of Fig. 5.6). We therefore conclude that our procedure, through narrow normalisation windows using the global $[\alpha/\text{Fe}]$ as an initial abundance guess, is a reliable way of using these strong saturated lines.

In conclusion, the dispersion on the $[\text{Mg}/\text{Fe}]$ abundance estimation from strong saturated lines, with respect to $[\text{M}/\text{H}]$, is dominated by the induced bias in the continuum-level estimation for the stellar types where a pseudo-continuum evaluation around the line is performed. The application of larger normalisation windows results in a parameter dependence of the obtained abundance and a larger line-to-line dispersion, each saturated line having its own level of continuum misplacement for a given star. The amplitude of this continuum placement error is smaller

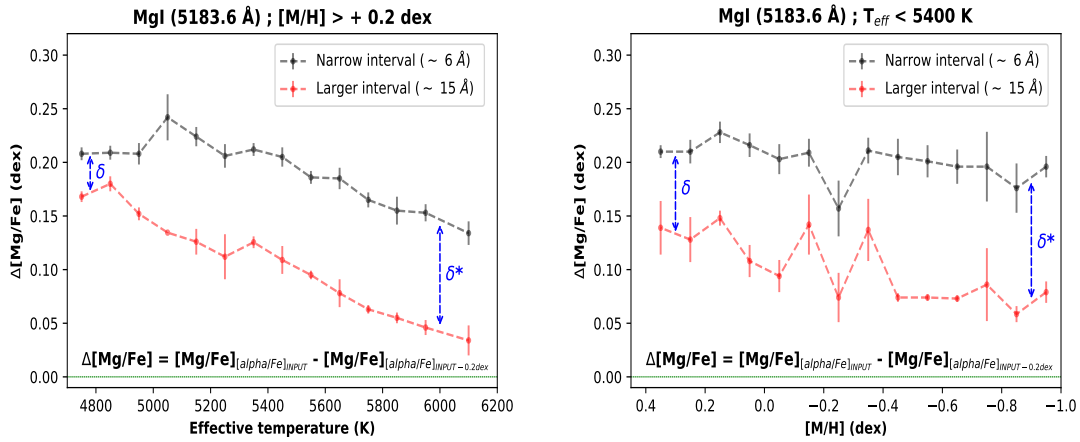


FIGURE 5.8: Analysis of saturated line 5183.6 Å. Comparison of the derived [Mg/Fe] abundances per spectrum after introducing a bias in the input $[\alpha/\text{Fe}]$ value ($[\alpha/\text{Fe}]^* = [\alpha/\text{Fe}] - 0.2$ dex) to simulate a $[\alpha/\text{Fe}]$ -[Mg/Fe] shift. The black and red lines correspond to the normalisation windows of 6 Å and 15 Å, respectively. **Left:** temperature dependence for the metal-rich sample ($[\text{M}/\text{H}] \gtrsim +0.2$ dex). **Right:** metallicity dependence for the cool sample ($T_{\text{eff}} \lesssim 5400$ K).

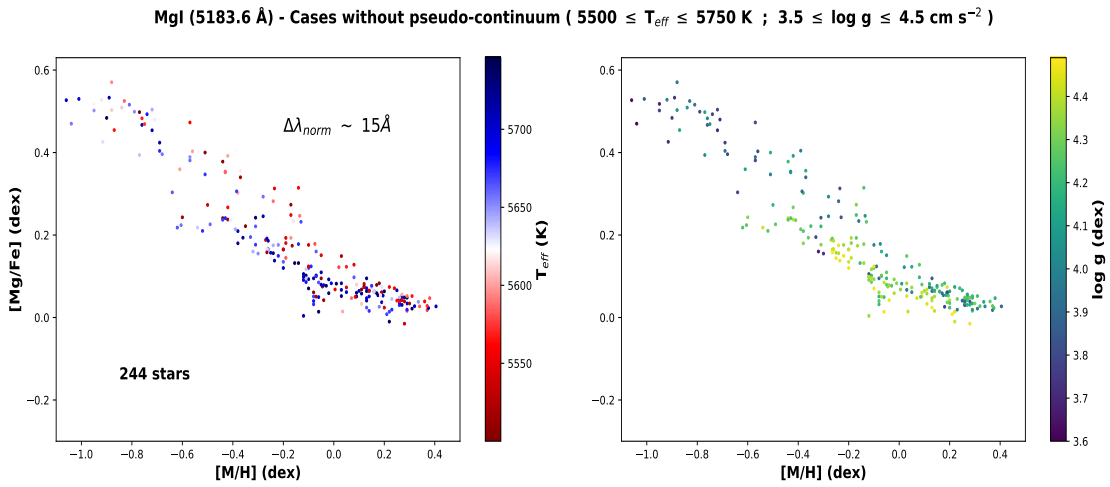


FIGURE 5.9: Stellar abundance ratios [Mg/Fe] vs. [M/H], including only cases without pseudo-continuum, for the large normalisation window of 15 Å around the strong line 5183.6 Å, colour-coded by stellar effective temperature (left panel) and surface gravity (right panel).

applying a narrower normalisation interval, therefore improving the abundance estimation precision. The strong link of the narrow normalisation window to the initial $[\alpha/\text{Fe}]$ guess through the pseudo-continuum reduces the atmospheric parameter dependence.

5.3.3 Mg abundances line-to-line scatter

The previous sections allow us to conclude that: (i) for weak non-saturated lines, the optimal wavelength domain for the local continuum placement has to be evaluated using a goodness-of-fit criterion, allowing a wavelength dependence with the spectral type. Generally, narrow normalisation windows between 1 and 2 Å provide the best line fittings (around two to four times the FWHM of each line in a solar-type star); (ii) for strong saturated lines, a narrow

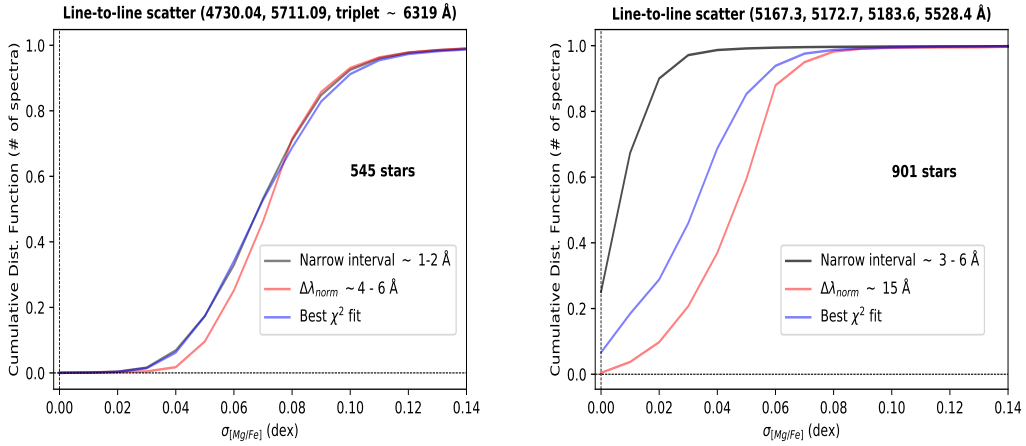


FIGURE 5.10: Cumulative distribution function of the line-to-line scatter estimation of the derived $[\text{Mg}/\text{Fe}]$ abundances per spectrum, for weak non-saturated Mg lines (left-panel; 4730.04, 5711.09, 6318.7, 6319.24, and 6319.49 Å) and strong saturated ones (right-panel; 5167.3, 5172.7, 5183.6, and 5528.4 Å) separately. The blue curve describes the values that correspond to the normalisation interval that presents the lowest χ^2 fitting value, the red one corresponds to the continuum placement performance in the typical wavelength interval used in previous works in the literature, and the black curve corresponds to a narrower local normalisation interval around each line as proposed in this work.

normalisation window allows us to reduce parameter-dependent biases of the abundance estimate, improving the precision (around two to four times the FWHM of each line in a solar-type star).

To evaluate the improvement in precision of the abundance results with our optimised procedure, we analysed the internal error estimation. Figure 5.10 shows the cumulative distribution of the line-to-line scatter per spectrum of the derived $[\text{Mg}/\text{Fe}]$ abundances for non-saturated (left panel) and strong saturated lines (right panel) separately. For non-saturated lines, the improvement in precision is confirmed after the optimisation based on the goodness of fit (blue curve), and applying narrow normalisation windows around each line ($\Delta\lambda_{\text{norm}} \sim 1\text{-}2$ Å) shows the same behaviour in terms of line-to-line scatter (black curve). The reduced number of stars is due to the cut in FWHM_{CCF} (see Sect. 5.2). For strong saturated lines, the application of a narrow normalisation interval ($\Delta\lambda_{\text{norm}} \sim 3\text{-}6$ Å, two to four times their FWHM in a solar-type star) shows a remarkable improvement of the abundance estimation precision. It presents a small scatter of less than 0.03 dex in comparison with the continuum placement performance in the typical wavelength interval used in previous works (red curve) and with the consideration of the goodness of fit as the quality criterion of the resulting normalisation, despite the fact that we showed that it is not discriminating enough for these lines (see Fig. 5.5). In conclusion, our optimised normalisation procedure applies a goodness-of-fit criterion for weak non-saturated lines to choose the appropriate continuum interval, and a fixed narrow normalisation window for the strong saturated ones.

A similar behaviour is observed in Fig. 5.11 when all the Mg lines of different strengths are considered. We compare results for the normalisation windows used in the literature (red) and for our optimised normalisation procedure (blue). In the left panel, we can see the analysis over the whole spectra sample for which all the Mg lines are considered. In addition, 40 % of the sample presents a scatter smaller than 0.05 dex choosing our best value in each case, while this is only the case for 20 % of the sample with the classical normalisation windows. This improvement in precision is even more significant if we focus the analysis on the metal-rich part ($[\text{M}/\text{H}] > 0.0$ dex), as shown in the right panel of Fig. 5.11. In the metal-rich regime, the

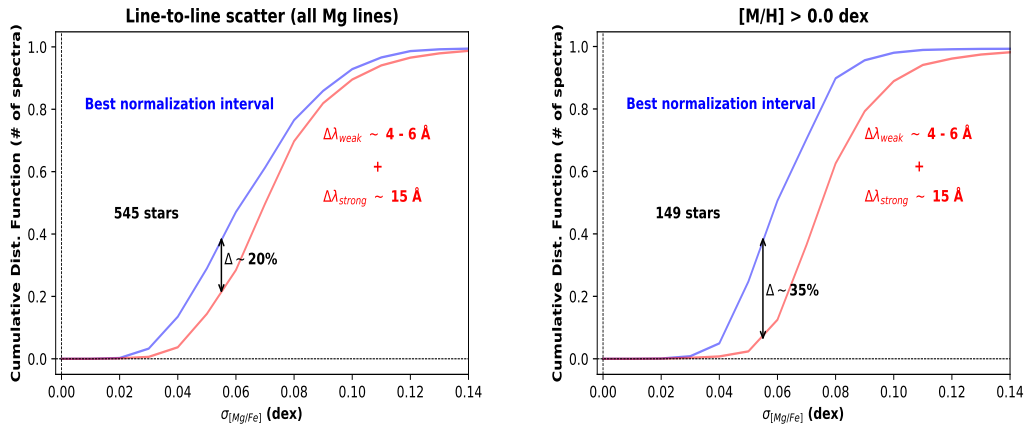


FIGURE 5.11: **Left:** cumulative distribution function of the line-to-line scatter estimation of the derived $[\text{Mg}/\text{Fe}]$ abundance ratio for the spectra sample for which all the Mg lines are taken into account. **Right:** same but for the metal-rich sample ($[\text{M}/\text{H}] > 0.0$ dex). The red curve corresponds to the typical normalisation windows used in the literature, while the blue curve shows the results with our optimised normalisation procedure.

percentage of spectra with a line-to-line scatter lower than 0.05 dex increases from 5 % to 40 %, thanks to our optimised procedure with respect to the classical one.

In conclusion, this reduction of the line-to-line scatter supports an improvement in the abundance estimate’s precision with our procedure. In terms of accuracy, we identified four Gaia-benchmark stars (18 Sco, HD 22879, Sun, and τ Cet) from Jofré et al. (2015) in our sample, finding an excellent agreement with an overall average difference of 0.01 dex. We also tested the derived abundances for those stars applying the normalisation windows used in the literature, finding an average difference within one sigma error from the optimised value. In other words, our normalisation procedure improves the abundance estimation precision, preserving its accuracy.

5.4 Disentangling the low- and high- $[\text{Mg}/\text{Fe}]$ sequences in the disc

In this section, we summarise the final derived $[\text{Mg}/\text{Fe}]$ abundances of our AMBRE:HARPS stellar sample (901 stars, see the Hertzsprung-Russell diagram in Fig. 4.3).

The results for each Mg I line are presented separately in Fig. 5.12. The four saturated lines (MgIb triplet: 5167.3, 5172.7 & 5183.6, and 5528.4 Å) and the intermediate-strength line 5711.09 Å seem to reproduce the thin-thick disc sequences more precisely, also showing a decreasing trend in $[\text{Mg}/\text{Fe}]$ even at supersolar metallicities. This is in agreement with the analysis of NLTE effects on Mg abundances done by Bergemann et al. (2017), where they highlight the robust behaviour of the strong lines 5172, 5183, 5528, and 5711 Å. The higher dispersion present on the abundance results for the weak non-saturated lines with respect to the strong saturated ones is due to different factors. On the one hand, for certain stellar types (towards hot metal-poor stars) and for lower Mg abundances (in terms of $[\text{Mg}/\text{H}]$), weak lines are closer to the spectral noise level. On the other hand, although saturated lines are less sensitive, pixel per pixel, to abundance variations (therefore presenting smaller flux variations per pixel), they span larger wavelength domains than non-saturated lines. As a consequence, the cumulative quantity of information on the abundance through all the considered pixels is very significant for strong lines, favouring a higher precision. This is confirmed by the study of the internal errors, through

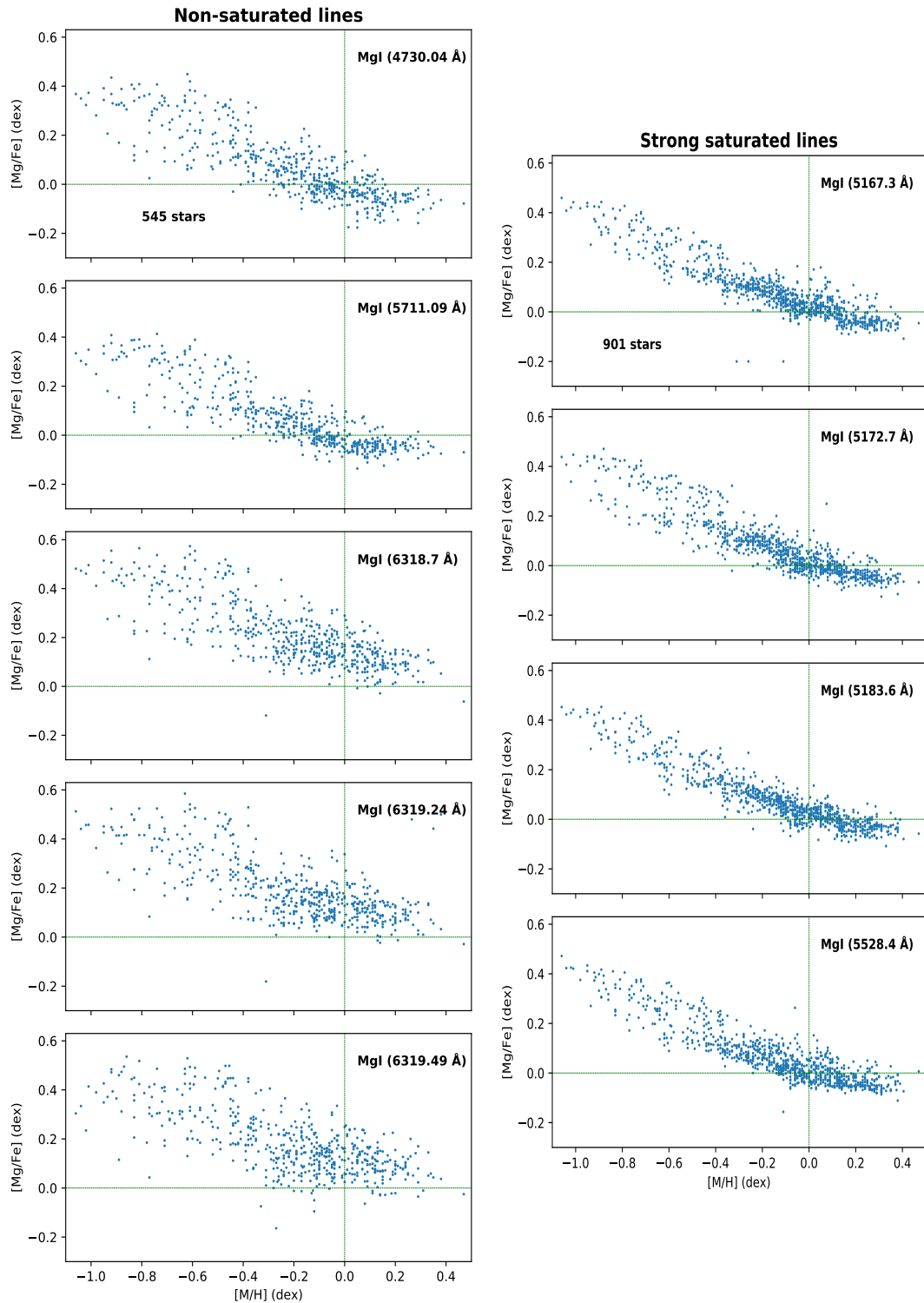


FIGURE 5.12: Most precise stellar abundance ratios $[\text{Mg}/\text{Fe}]$ vs. $[\text{M}/\text{H}]$ following the optimal method for each Mg I spectral line separately. **Left:** non-saturated lines: 4730.04, 5711.09, 6318.7, 6319.24, and 6319.49 Å. **Right:** strong saturated lines: 5167.3, 5172.7, 5183.6, and 5528.4 Å (from top to bottom).

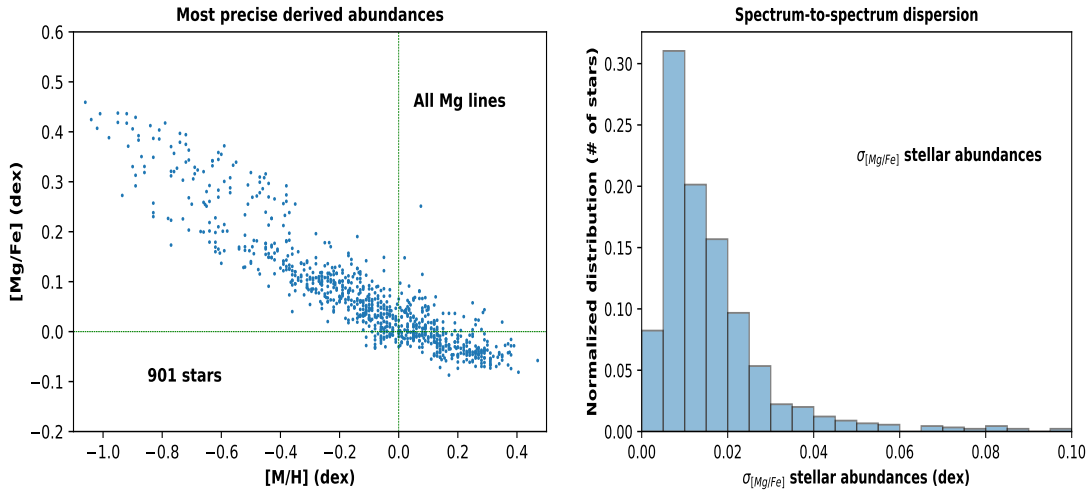


FIGURE 5.13: **Left:** stellar abundance ratios $[\text{Mg}/\text{Fe}]$ vs. $[\text{M}/\text{H}]$ considering the abundance information from all the studied Mg I spectral lines. **Right:** estimated dispersion of the final stellar sample (> 4 repeats) on the derived $[\text{Mg}/\text{Fe}]$ abundances.

simulated noised theoretical spectra (discussed in Sect. 3.5). However, a high spectral resolution is required, even at high signal-to-noise values, to compensate the limited sensitivity of the lines to the abundance (see Fig. 3.6).

Figure 5.13 illustrates the final stellar abundance ratios $[\text{Mg}/\text{Fe}]$ relative to $[\text{M}/\text{H}]$ for our selected stellar sample (left panel), along with their estimated dispersion from the repeated observed spectra (right panel). The chemical distinction between the Galactic thin (low- $[\text{Mg}/\text{Fe}]$)-thick (high- $[\text{Mg}/\text{Fe}]$) disc populations is clearly observed, and the trend in $[\text{Mg}/\text{Fe}]$ abundances at high metallicity ($[\text{M}/\text{H}] > 0$ dex) does not flatten. This result seems to partly solve the apparent discrepancies between the common observed flat trend in the metal-rich disc by observational studies (Adibekyan et al., 2012, Recio-Blanco et al., 2014, Hayden et al., 2015, 2017, Mikolaitis et al., 2017, Buder et al., 2019), and the steeper slope predicted by chemical evolution models of the Milky Way (Chiappini et al., 1997, Romano et al., 2010, Spitoni et al., 2020). In addition, the gap in the $[\text{Mg}/\text{Fe}]$ -enhanced disc stellar population, first observed by Adibekyan et al. (2012) and later confirmed by Mikolaitis et al. (2017), still seems to be present in Fig. 5.12 & Fig. 5.13 around $[\text{M}/\text{H}] \approx -0.3$ dex and $[\text{Mg}/\text{Fe}] \approx +0.2$ dex.

Recent studies analysing dwarf stars in the solar neighbourhood (Mikolaitis et al., 2017, Fuhrmann et al., 2017) present Mg lines that are in common with our work (c.f. Table 1 and Table 2 of Mikolaitis et al. 2017 and Fuhrmann et al. 1997, respectively). Mikolaitis et al. (2017) observed a different trend at high metallicities. However, as described before, Mikolaitis et al. (2017) did not optimise the continuum normalisation for different stellar types, applying a constant local interval depending on the intensity of the line. On the other side, the agreement of our results with those of Fuhrmann et al. (2017) is higher. Nevertheless, the slope of the low- α sequence in Fuhrmann et al. (2017) seems less pronounced than in our work. Fuhrmann et al. (2017) used the Mg I abundance estimate from weak lines as the input parameter to the Mg Ib lines (strong saturated). This first-guess abundance could have an important influence on the pseudo-continuum estimate, and therefore in the derived $[\text{Mg}/\text{Fe}]$ abundance, for saturated lines. For cool or metal-rich dwarf stars, the impact of this first guess in the derived Mg Ib abundances could be stronger than for the other stars in the sample. As a consequence, possible parameter-dependencies in the results could remain.

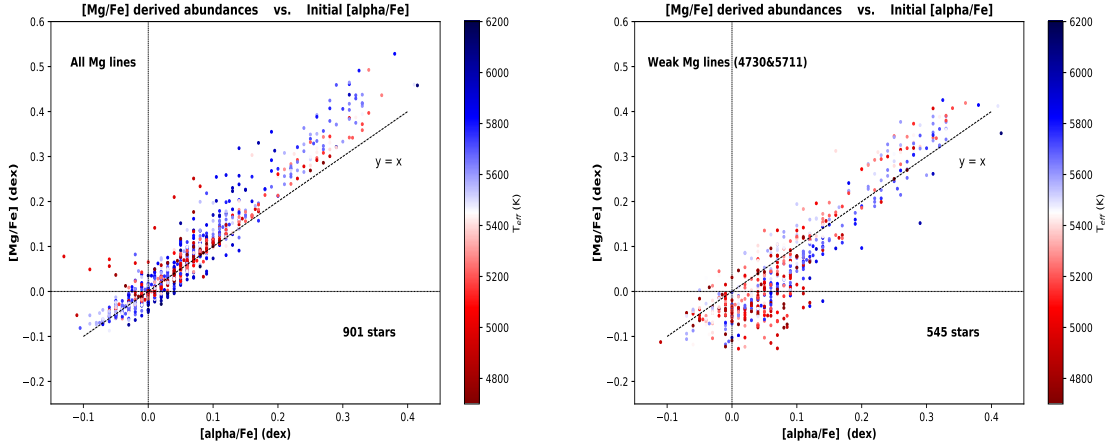


FIGURE 5.14: Derived stellar abundance ratios $[\text{Mg}/\text{Fe}]$ vs. initial stellar parameter $[\alpha/\text{Fe}]$, colour-coded by stellar effective temperature. **Left:** considering the abundance information from all the studied Mg I spectral lines. **Right:** considering only the weak non-saturated lines 4730.04 & 5711.09 Å (used in Fuhrmann et al., 2017, as the input parameter to the strong saturated lines).

Finally, we checked the consistency of our first-guess assumptions by comparing (left panel of Fig. 5.14) our initial abundance guess, coming from the $[\alpha/\text{Fe}]$, and our final derived $[\text{Mg}/\text{Fe}]$ abundances. The very good agreement between both quantities confirms the consistency of the procedure. In addition, the right panel of Fig. 5.14 compares our initial guess with other suggested initial input in the literature, the abundance result from the weak lines (4730.04 and 5711.09 Å) used by Fuhrmann et al. (2017). There is a very good agreement between our initial guess (the global $[\alpha/\text{Fe}]$) and the $[\text{Mg}/\text{Fe}]$ from the weak lines, with only a few cool stars with $[\alpha/\text{Fe}]$ around 0.1 dex with lower $[\text{Mg}/\text{Fe}]_{\text{weak lines}}$ values. Those few cases correspond to cool stars with supersolar metallicities. This suggests that the two weak lines could suffer from blends in the very crowded spectra, affecting the continuum placement and therefore the abundance estimate. As we can indeed see in Fig. 5.12, the results of the two weak lines are more dispersed. On the other hand, the global $[\alpha/\text{Fe}]$ parameter value was derived considering the complete HARPS wavelength domain (De Pascale et al., 2014). Therefore, it is also less affected by continuum placement problems. For this reason, we believe that the global $[\alpha/\text{Fe}]$ determined by the AMBRE pipeline, although very similar to the results of the weak lines, is a more precise initial guess for our application.

Our analysis allows a remarkable improvement with regard to previous efforts to chemically disentangle the Galactic thin(low- $[\text{Mg}/\text{Fe}]$)-thick(high- $[\text{Mg}/\text{Fe}]$) disc populations, and emphasises the importance of the normalisation procedure to properly interpret the chemical evolution of the disc. In conclusion, the feasibility of an optimal treatment on strong saturated lines to derive precise non-parameter-dependent abundances represents a major advancement. It will allow us to appropriately study the chemical signatures in the Galactic stellar populations and the resulting implications on chemodynamical relations, such as the abundance ratio $[\text{Mg}/\text{Fe}]$ as a good age proxy, or the contribution of radial migration in the solar neighbourhood (fully discussed in Chapter 7).

5.5 Summary

We carried out a detailed spectroscopic analysis of the Mg abundance estimation over a sample of 2210 FGK-type stars in the solar neighbourhood observed and parameterised at high spectral

resolution ($R=115000$) within the context of the AMBRE Project. From this sample, we selected 1172 stars that have more than four observed spectra (> 4 repeats).

We explored the possible sources of uncertainties in deriving chemical abundances, focusing on the continuum normalisation. From different stellar populations and nine Mg I spectral lines in the optical range, we observed different behaviours depending on the stellar type and the intensity of the line.

The normalisation procedure has an important impact on the derived abundances, with a strong dependence on the stellar parameters (T_{eff} , $\log g$, $[M/H]$). Contrary to what is currently done in large spectroscopic surveys, the continuum placement procedure therefore has to be optimised for each stellar type and each spectral line. As expected, the intensity of the spectral lines has a drastic influence in the optimal width of the normalisation interval:

- **Non-saturated lines:** the optimal wavelength domain for the local continuum placement could be evaluated using a goodness-of-fit criterion, allowing a wavelength dependence with the spectral type. It is generally convenient to optimise the normalisation window close to the considered line (around two to four times their FWHM). For stronger (although not saturated) lines like 5711.09 \AA , a larger interval could be necessary when dealing with cool metal-rich stars ($[M/H] > -0.2 \text{ dex}$; $T_{\text{eff}} < 5400 \text{ K}$).
- **Saturated lines:** no pixels are available at the continuum level for most of the stellar types in the analysed region, and a pseudo-continuum normalisation has to be performed for the automatic fit. The level of the pseudo-continuum depends on the Mg abundance itself, which is at first assumed to be equal to the global α -element abundance (or to another first-guess abundance). The induced bias in the Mg estimate is only partially corrected by the Mg line fitting due to a degeneracy between the fitting quality and the continuum placement (as the line is saturated, only the wings profile changes). In addition, the bias correction depends on the pseudo-continuum level itself. In this situation, one possibility consists in reducing the analysis of the saturated lines to the stellar types presenting continuum in the spectra (hot metal-poor stars). Alternatively, we have demonstrated that using a narrow normalisation window (around two to four times the FWHM of each line in a solar-type star) drastically reduces the parameter-dependence of the abundance estimate, increasing the line-to-line precision. This relies on the assumption that the Mg abundance behaviour is not very different from that of the global $[\alpha/Fe]$ abundance.

The final derived stellar abundance ratios $[Mg/Fe]$, relative to $[M/H]$, present a clear chemical distinction between the Galactic thin-thick disc populations and a decreasing trend in $[Mg/Fe]$ abundances even at supersolar metallicities ($[M/H] > 0 \text{ dex}$). With our analysis, we highlight the importance of carrying out an exploration on the optimisation of the continuum intervals in the preliminary and preparatory stages of any spectroscopic survey (in accordance with the stellar targets, spectral resolution, etc.). We suggest exploring the application of narrow normalisation windows around the studied lines in order to improve the abundance estimation precision.

The optimisation of the normalisation procedure in large spectroscopic stellar surveys would provide a significant improvement to the analysis of the chemical patterns of the different Galactic populations. The improvement in chemical abundance precision is strongly required in the present era of precise kinematical and dynamical data driven by the Gaia mission.

Chapter 6

Determination of stellar ages and orbital properties

Contents

6.1 Estimation of ages	70
6.2 Determination of orbital properties	72

After the abundance determination analysis with GAUGUIN (discussed in previous Chapter 5), we selected a subsample of the AMBRE:HARPS spectral dataset (see Chapter 4) that corresponds to 494 MSTO stars in the local solar neighbourhood ($d < 300$ pc from the Sun), selected and used in [Hayden et al. \(2017\)](#) (they made the sample selection by requiring $M_J < 3.75$ and $3.6 < \log g < 4.4$), for which we estimated accurate ages, kinematical and dynamical parameters.

We used astrometric ([Lindegren et al., 2018](#)) and photometric data ([Evans et al., 2018](#), full passband information for BP and RP) from the *Gaia* DR2 catalogue ([Gaia Collaboration et al., 2018c](#)), along with distances estimated by [Bailer-Jones et al. \(2018\)](#) from *Gaia* DR2 parallaxes using a bayesian approach. As the analysed sample is within 300 pc around the Sun (with $G \leq 11$ mag), the parallax uncertainties ($\sigma_\varpi/\varpi < 3\%$ for our stars) and the choice of prior have little impact on the distance results.

6.1 Estimation of ages

We restricted our sample to MSTO stars in order to estimate reliable ages using the isochrone fitting method described in [Kordopatis et al. \(2016\)](#). For each individual star, we computed the age probability distribution function (PDF) by projecting the stellar parameters (T_{eff} , $\log g$, $[M/H]$), the BP-RP colour, and the G absolute magnitude, on the PARSEC isochrones ([Bressan et al., 2012](#)), linearly scaled in age in steps of 0.1 Gyr from 0 to 15 Gyr, with the [Evans et al. \(2018\)](#) colour transformation. Every parameter and magnitude was weighted by their respective error bars, and each isochrone point was weighted by mass following [Zwitter et al. \(2010\)](#).

We first checked that the relation between the effective temperature (derived spectroscopically) and the colour (from *Gaia* DR2) was on the same scale as the one used by the isochrone models. As shown in the left panel of Fig. 6.1, a metallicity-dependent disagreement was found. The

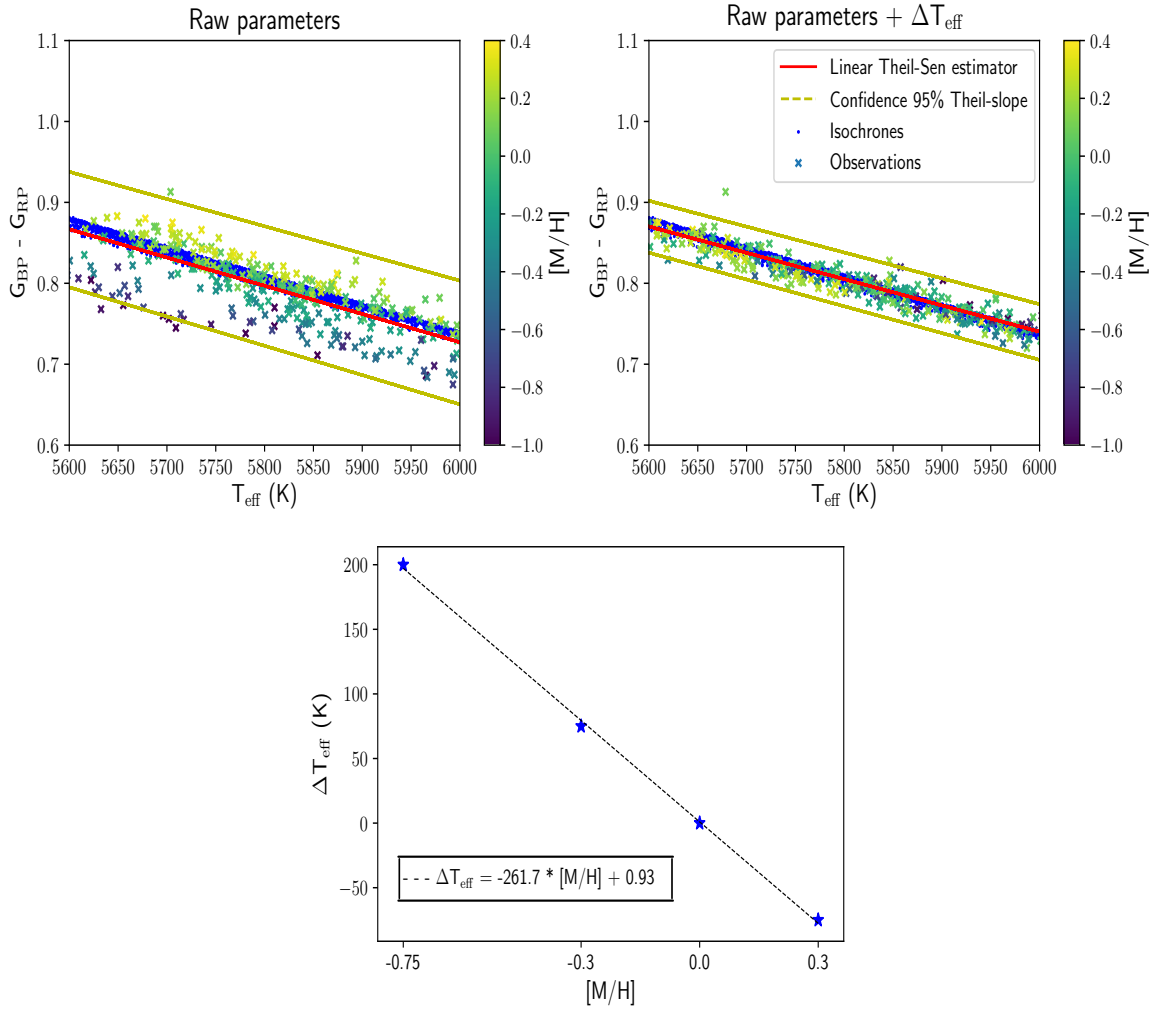


FIGURE 6.1: **Top:** The colour-temperature relation of the MSTO stars in the working sample (colour-coded by the metallicity) and the isochrones models (blue points on a straight line), for the original derived AMBRE effective temperatures (left panel) and after the offset correction in T_{eff} (right panel). The linear Theil-Sen estimator method (red line) was applied to the stellar parameter values. The green lines delimit the lower and upper bound of the 95% confidence interval of the Theil-Sen linear regression method. **Bottom:** The observed linear T_{eff} -offset ($\Delta T_{\text{eff}} = T_{\text{eff, MODEL}} - T_{\text{eff, OBSERVATION}}$) for different metallicity values.

observed offset was evaluated for four different metallicity values¹, showing a linear dependence on the metallicity (bottom panel):

$$\Delta T_{\text{eff}} \text{ (K)} = (-261.7 \pm 5.4) * [\text{M}/\text{H}] \text{ (dex)} + (0.93 \pm 2.32) \quad (6.1)$$

Figure 6.1 shows, for all the metallicities, the colour-temperature relation before (left panel) and after applying the correction in the AMBRE effective temperatures (right panel) in order to put them on the same temperature-scale as the PARSEC isochrones. We determined the dispersion in the colour BP-RP differences between the observations and the models, finding an improvement from $\sigma_{\Delta(\text{BP}-\text{RP})} \approx 0.028$ to $\sigma_{\Delta(\text{BP}-\text{RP})} \approx 0.018$ (before and after applying the T_{eff} -offset, respectively). We therefore used the shifted stellar temperatures (right-panel points) in the projection on the PARSEC isochrones to estimate the final stellar ages.

¹[M/H] = [- 0.75 , - 0.3 , 0.0 , + 0.3].

Moreover, the estimated distance from *Gaia* DR2 parallaxes was taken into account to compute the distance modulus of each star in order to calculate its absolute magnitude. We firstly estimated the Galactic extinction for our sample by implementing the 3D dust maps from [Green et al. \(2018\)](#), and also [Schlegel et al. \(1998\)](#) maps with the proposed correction by [Sharma et al. \(2014, see Equation 24\)](#) in order to not overestimate the reddening. We calculated a negligible extinction ($E(B-V) \lesssim 0.025$ mag) for most of the observed stars, while some cases showed significant values but with uncertainties as high as the estimated correction. The very low derived extinctions are consistent with the fact that our sample is in the solar vicinity ($d < 300$ pc). As a consequence, we decided not to apply any extinction correction, as they have a negligible impact on our results. Furthermore, we did not adopt any prior neither for the Galaxy model nor for the age as a function of other stellar parameters as $[M/H]$ or $[Mg/Fe]$. We assumed a uniform star formation history to avoid prioritising a particular formation epoch.

Finally, we excluded the stars whose mean, median and mode age PDF values differed between them by more than 2 Gyr, leading to a total of 366 stars with a very reliable age estimate. The adopted age for each star was the one derived by the mean of the PDF. The age distribution for our data sample ranges from 2.5 to 13.5 Gyr, with an average relative standard deviation of $\sigma \sim 20$ % around the mean PDF value.

6.2 Determination of orbital properties

We estimated the orbital parameters with the *Gaia* DR2 astrometric positions and proper motions, the calculated distances by [Bailer-Jones et al. \(2018\)](#), and the spectroscopic radial velocities determined by the AMBRE analysis procedure (see [Worley et al., 2012](#), [De Pascale et al., 2014](#)). To this purpose, we used the python code `galpy` ([Bovy, 2015](#)), together with the `MWpotential2014`: a Milky-Way-like gravitational potential that is the sum of a power-law density profile for the bulge (power-law exponent of -1.8 and a cut-off radius of 1.9 kpc), a Miyamoto-Nagai potential for the disc ([Miyamoto & Nagai, 1975](#)) and a Navarro-Frenk-White potential to model the halo ([Navarro et al., 1997](#)). The orbits were integrated over 10 Gyr in order to evaluate the pericentres (R_{per}) and the apocentres (R_{apo}), as well as the maximum heights above the Galactic plane ($|z_{\text{max}}|$). Since we analysed a local stellar sample in the solar neighbourhood (large parallaxes: $3 < \varpi < 50$ mas), the found parallax bias in the *Gaia* DR2 data, e.g. global shift of $\delta_{\varpi} = -0.029$ mas ([Lindegren et al., 2018](#)) or $\delta_{\varpi} = -0.054$ mas by later studies ([Schönrich et al., 2019](#), [Graczyk et al., 2019](#)), has a negligible effect on the estimated kinematic and orbital quantities.

Figure 6.2 shows the distribution of the main stellar properties of our final sample, consisting on 366 MSTO stars. They are Galactic disc stars, describing relatively circular prograde orbits ($0 < e \lesssim 0.4$) close to the Galactic plane ($|z_{\text{max}}| \lesssim 1$ kpc), and they are evenly distributed in age from 2.5 to 13.5 Gyr. We found a significant fraction of stars that seem to be passing through our local limited sample on the present day, with R_{per} values lower than 6 kpc, and also some of them reaching up to R_{apo} larger than 10 kpc from the Galactic centre. We used the guiding centre radius (R_g) as an estimate of the current value of the Galactocentric radius (R_{GC}), since it is an useful tracer for the radial migration of the different stellar populations in the Galactic disc (e.g. [Kordopatis et al., 2017](#)). For this work, it has been calculated as the average between the pericentre and the apocentre of the orbit of the star: $R_g = (R_{\text{per}} + R_{\text{apo}})/2$. The sample is well distributed in Galactocentric R_g from 4 to 11 kpc.

In order to estimate the error in R_g , we re-calculated the orbits using the upper and lower distance limit derived by [Bailer-Jones et al. \(2018\)](#). The comparison shows a negligible uncertainty lower than 1 parsec. We also calculated the orbits using other potentials: the `MWpotential2014` adding

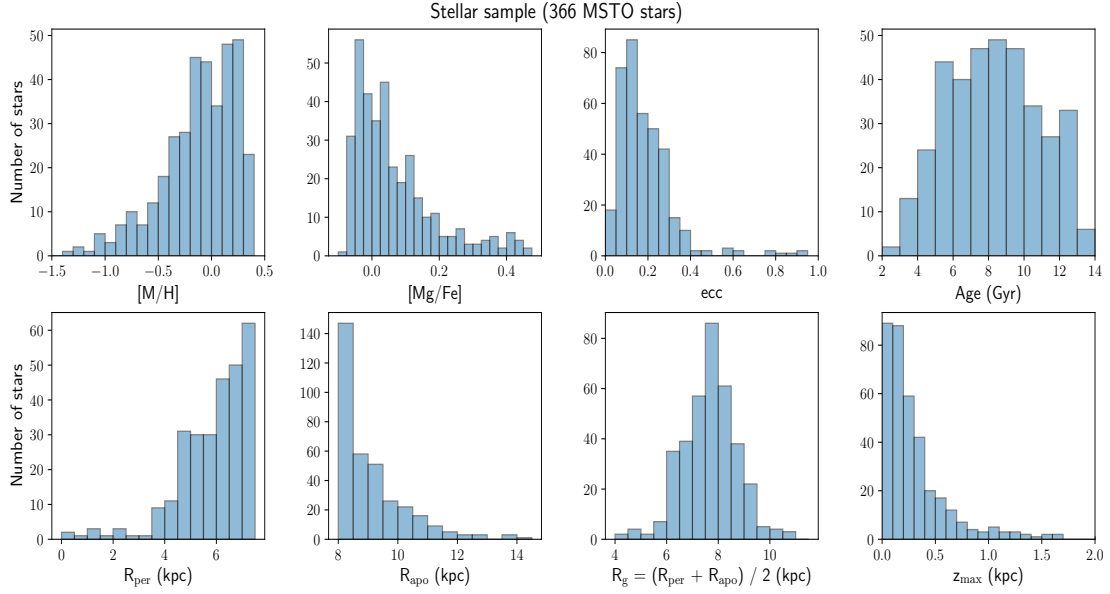


FIGURE 6.2: Distribution of the main properties ($[M/H]$, $[Mg/Fe]$, eccentricity, age, R_{per} , R_{apo} , R_g , z_{max}) of the selected MSTO stars.

a bar (`DehnenBarPotential`) on the one hand, and the potential presented by [McMillan \(2017\)](#) on the other. For both cases, the differences in the R_g value were around 0.2 kpc with respect to the initial calculated ones. Our results are robust against the choice of the Galactic potential model and the uncertainty in the parameters.

Chapter 7

Solar neighbourhood chemodynamical constraints on Galactic disc evolution

Contents

7.1	Radial chemical trends and stellar migration	75
7.1.1	Definition of the thin disc	75
7.1.2	Present-day chemical abundance gradients	76
7.1.3	Radial migration	80
7.2	Age-abundance relations	84
7.2.1	[Mg/Fe] abundance as a chemical clock	84
7.2.2	Temporal evolution in the [Mg/Fe]-[M/H] plane	87
7.2.3	Trends with stellar age: relation to radius	89
7.3	Formation and evolution history of the Galactic disc	91
7.4	Summary	94

In previous Chapter 5, after a deeply [Mg/Fe] abundance estimation analysis, we showed a significant improvement in the precision of the [Mg/Fe] abundance estimate by carrying out an optimisation of the spectral normalisation procedure, in particular for the metal-rich population ($[M/H] > 0$). The followed methodology made it possible to highlight a decreasing trend in the [Mg/Fe] abundance even at supersolar metallicities, partly solving the apparent discrepancies between the common observed flat trend in the metal-rich disc by observational studies (Adibekyan et al., 2012, Recio-Blanco et al., 2014, Hayden et al., 2015, 2017, Mikolaitis et al., 2017, Buder et al., 2019), and the steeper slope predicted by chemical evolution models of the Galaxy (Chiappini et al., 1997, Romano et al., 2010, Spitoni et al., 2019, Palla et al., 2020).

In this chapter, we use the new [Mg/Fe] abundance measurements in order to study their impact on the reported chemodynamical features of the Galactic disc (e.g. radial chemical abundance gradients, role of radial migration/churning, age-abundance relations), and therefore on the interpretation of the Galactic disc evolution.

As introduced in previous Chapter 6 regarding the data analysis, we only considered the AMBRE:HARPS stellar sample that corresponds to 366 main sequence turn-off (MSTO) stars in the local solar neighbourhood ($d < 300$ pc from the Sun), for which we estimated ages, kinematical and dynamical parameters using the accurate astrometric measurements of the *Gaia* space mission.

7.1 Radial chemical trends and stellar migration

In this section, we first explore the present-day distribution of $[\text{Mg}/\text{Fe}]$ and $[\text{M}/\text{H}]$ in the thin disc, as a function of Galactocentric position and age. Then, we analyse the impact of radial migration in the solar neighbourhood.

7.1.1 Definition of the thin disc

We adopt here a chemical definition of the thin disc, based on the $[\text{Mg}/\text{Fe}]$ content in a given $[\text{M}/\text{H}]$ bin.

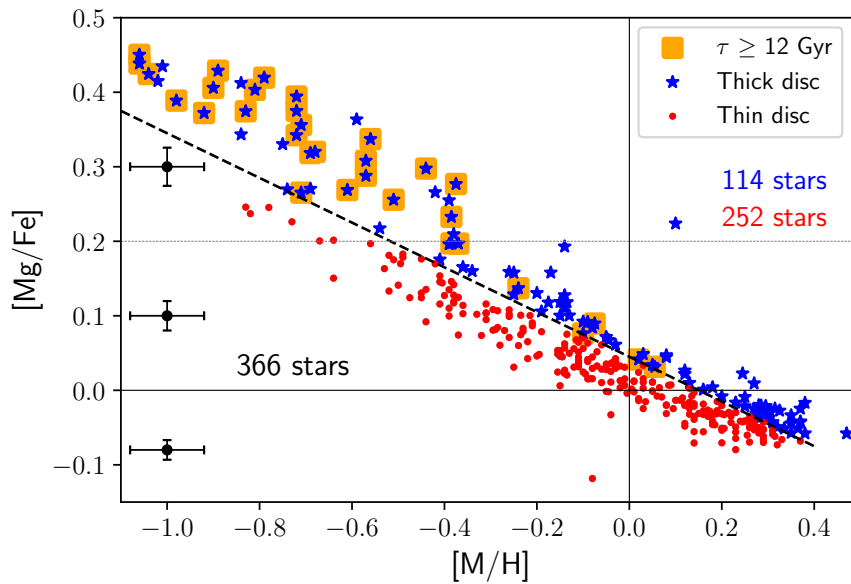


FIGURE 7.1: $[\text{Mg}/\text{Fe}]$ vs. $[\text{M}/\text{H}]$ of our working sample. The stars with ages older than 12 Gyr are shaded by orange squares. The black dashed line defines the thin (red circles)-thick (blue stars) disc chemical separation. The mean estimated errors are represented in the left-hand side for three different intervals in $[\text{Mg}/\text{Fe}]$.

Figure 7.1 illustrates the chemical separation in the $[\text{Mg}/\text{Fe}]$ - $[\text{M}/\text{H}]$ plane for our working sample, classifying the stars into high- and low- $[\text{Mg}/\text{Fe}]$ sequences. First of all, we selected stars older than 12 Gyr. According to previous works in the literature (c.f. Fuhrmann, 2011, Haywood et al., 2013, Hayden et al., 2017), this would trace the old (thick) disc population. These stars, shaded by orange squares in Fig. 7.1, are mostly $[\text{Mg}/\text{Fe}]$ -enhanced ($[\text{Mg}/\text{Fe}] \gtrsim +0.2$ dex), but span a wide range in $[\text{M}/\text{H}]$, reaching the solar values. We used the lower $[\text{Mg}/\text{Fe}]$ -bound fit¹ to these stars to chemically define the thick (blue stars in Fig. 7.1) and the thin disc (red points in Fig. 7.1). This line separates well the two chemical sequences at low metallicities, yet, the extrapolation to the metal-rich tail ($[\text{M}/\text{H}] > -0.3$ dex) is rather arbitrary and the classified thick disc, also called α -rich metal-rich population in previous works (e.g. Adibekyan et al., 2012), has an *ad hoc* assignment that needs to be analysed in detail.

Distinct metal-rich populations?

The difficulty in separating chemically the thin and the thick disc stars at high metallicities is a matter of debate in the literature. On the one hand, Adibekyan et al. (2012) and Mikolaitis et al.

¹ $[\text{Mg}/\text{Fe}] = -0.3 \cdot [\text{M}/\text{H}] + 0.045$ (dex).

(2017) found a gap in metallicity ($[\text{Fe}/\text{H}] \approx -0.2$ dex) for the thick disc population in a dwarf stars sample from HARPS data. They used this gap to chemically define the thick disc and the α -rich metal-rich sequences separately. Adibekyan et al. (2012) showed that high- α metal-rich stars were on average older than thin disc stars, but with similar kinematics and orbits to the thin disc population. On the other hand, Hayden et al. (2015) and Buder et al. (2019) (for two independent samples of giants from APOGEE and dwarfs from GALAH DR2 data, respectively) found a continuous evolution for the thick disc sequence, describing an independent track from the thin disc up to supersolar metallicities.

Moreover, due to possible ignored uncertainties in our abundance estimates (see Chapter 5), each sample is expected to contain a fraction of contamination from the other sample at the metal-rich regime ($[\text{M}/\text{H}] > -0.3$ dex). To evaluate the advantages for a separate treatment of the thick disc metal-rich population with respect to the thin disc one, we have assessed the possible differences between the classified thick and thin disc populations in the metal-rich regime. Figure 7.2 shows the chemodynamical properties of the thick (blue) and thin (brown) disc metal-rich stars (for $[\text{M}/\text{H}] > -0.3$ dex). Some of the thick disc metal-rich stars show low eccentric orbits, young ages, and are close to the plane (low- z_{max}), similarly to the metal-rich thin disc population. The Kolmogorov-Smirnov test between the two samples does not allow to reject that these high metallicity stars are truly different stellar populations. This is particularly true for the z_{max} and the eccentricity distributions, while for the radial and age distribution the p-value is smaller.

For comparison purposes, Fig. 7.3 illustrates the same analysis over the metal-poor stellar sub-sample ($[\text{M}/\text{H}] \leq -0.3$ dex). Besides the clear $[\text{Mg}/\text{Fe}]$ distinction observed in Fig. 7.1 at this metallicity regime, it seems reasonable to interpret the reported p-values as a hint towards two different stellar populations (p-values $< 10^{-3}$ for the orbital parameter distributions: ecc , R_{per} , R_{apo} , and R_{g}). The thick disc metal-poor population clearly shows a more centrally concentrated distribution (reaching the innermost regions: $R_{\text{per}} \sim 0.7$ kpc and R_{g} down to 4 kpc from the Galactic centre) and present a higher eccentricity tail. On the contrary, the thin disc metal-poor population reaches the outer parts of the Galactic disc (up to $R_{\text{apo}} \sim 14$ kpc and $R_{\text{g}} \sim 10$ kpc) and only describe circular orbits ($e \lesssim 0.3$).

In conclusion, we decided to apply the chemical criterion described in Fig. 7.1 in order to minimise the thick disc contamination in the study of the thin disc properties. Nevertheless, the similarities observed in the metal-rich regime do not support a thin-thick disc separation at high metallicities. As a consequence, a global consideration of the entire disc population will be adopted for the disc evolution analysis in Section 7.2.

7.1.2 Present-day chemical abundance gradients

Table 7.1 shows the radial gradients of $[\text{M}/\text{H}]$ and $[\text{Mg}/\text{Fe}]$ for the thin disc stars, assuming R_{g} as their true position in the Galaxy. The values of the slope and the uncertainties are reported in Table 7.1, and come from a Theil-Sen regression model.

We find a negative gradient of -0.097 ± 0.033 dex kpc^{-1} for $[\text{M}/\text{H}]$ and a positive gradient of $+0.025 \pm 0.009$ dex kpc^{-1} for the $[\text{Mg}/\text{Fe}]$ abundance. Both chemical gradients are flatter for young stars (≤ 6 Gyr), although the differences are within the slope uncertainties. In contrast, for the same stellar sub-sample, the Mikolaitis et al. (2017) $[\text{Mg}/\text{Fe}]$ abundances lead to a shallower gradient: $+0.008 \pm 0.007$ dex kpc^{-1} .

As described before, our $[\text{Mg}/\text{Fe}]$ abundances show a decreasing trend even at supersolar metallicities, reaching negative values. In contrast, previous observational studies of the solar neighbourhood observed a flattened trend (e.g. Adibekyan et al., 2012, Mikolaitis et al., 2017). As a consequence, it seems that the reported improvement in the $[\text{Mg}/\text{Fe}]$ abundance precision for the

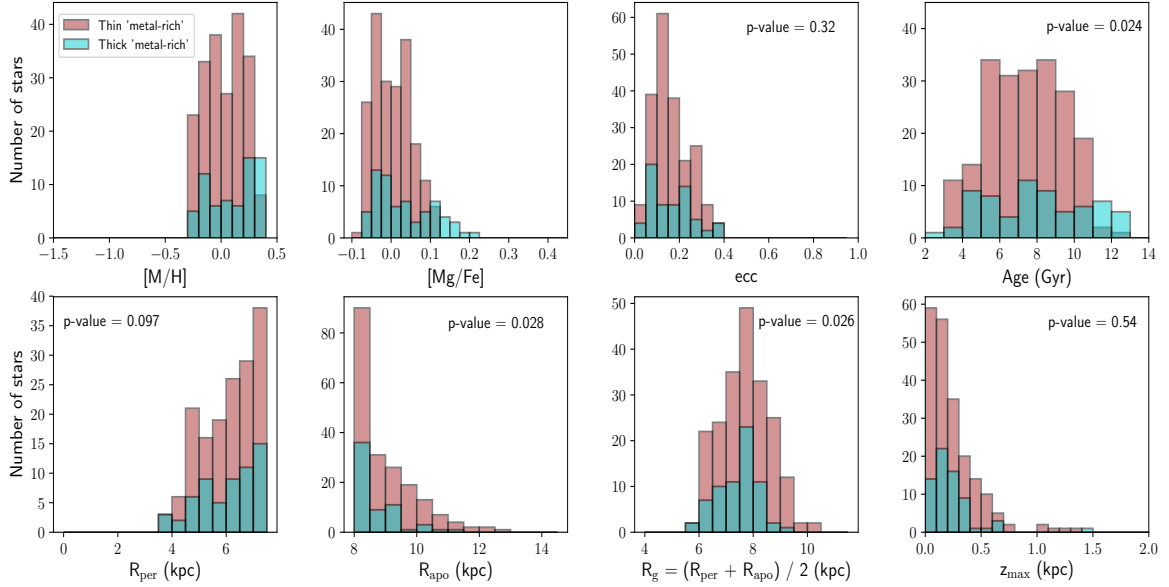


FIGURE 7.2: Same stellar properties as Fig. 6.2, separated into the chemically defined thin (brown) and thick (blue) disc populations for the metal-rich sub-sample ($[M/H] > -0.3$ dex). The p-values of the two-sample Kolmogorov-Smirnov tests are reported for each parameter distribution.

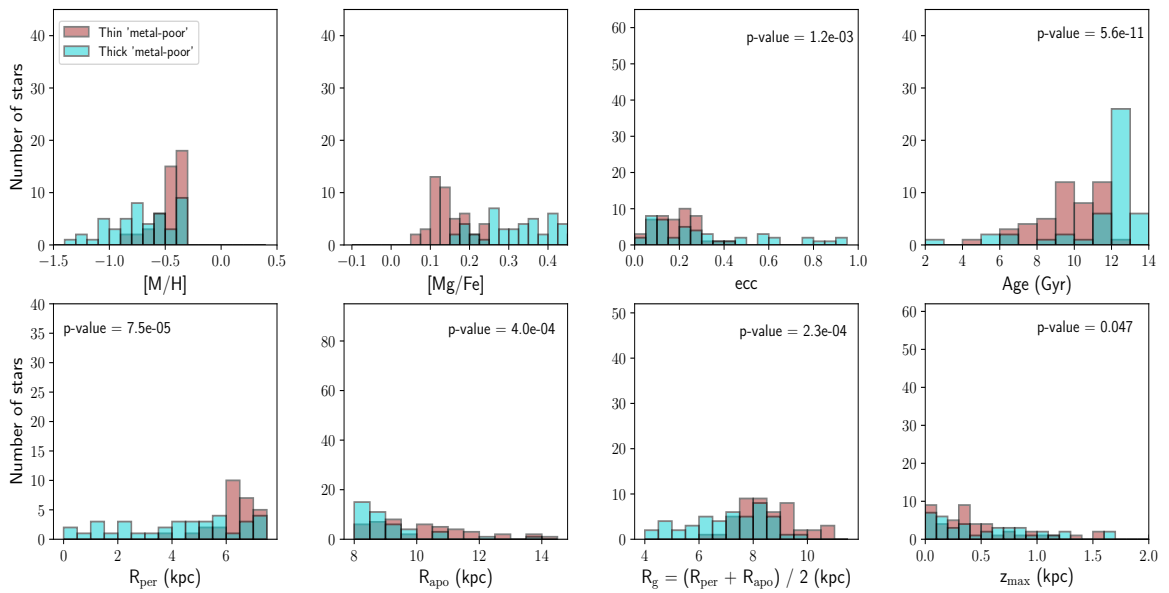


FIGURE 7.3: Same as Fig. 7.2 for the metal-poor sub-sample ($[M/H] \leq -0.3$ dex), with the respective p-values of the two-sample Kolmogorov-Smirnov tests.

TABLE 7.1: Radial abundance gradients (dex kpc^{-1}) in the range $6 \leq R_g \leq 11$ kpc for Galactic thin disc stars.

	$\frac{d[\text{M}/\text{H}]}{dR_g}$	$\frac{d[\text{Mg}/\text{Fe}]}{dR_g}$	$\frac{d[\text{Mg}/\text{Fe}]^\dagger}{dR_g}$
Whole sample	-0.097 ± 0.033	$+0.025 \pm 0.009$	$+0.008 \pm 0.007$
Young (≤ 6 Gyr)	-0.071 ± 0.061	$+0.020 \pm 0.015$	-0.003 ± 0.013
Old (> 6 Gyr)	-0.106 ± 0.037	$+0.028 \pm 0.010$	$+0.013 \pm 0.008$

† Abundances from Mikolaitis et al. (2017)

metal-rich disc implies a significant change in the radial gradient measurement, showing steeper slopes. As an additional test, we also explored the possible influence of a thin-thick disc misclassification (see Sect. 7.1.1) by including in our thin disc radial gradient the measurements of all our metal-rich thick disc stars, finding similar results: $d[\text{Mg}/\text{Fe}]/dR_g = +0.023 \pm 0.009 \text{ dex kpc}^{-1}$ (whole sample), $+0.021 \pm 0.015 \text{ dex kpc}^{-1}$ (young stars), and $+0.025 \pm 0.010 \text{ dex kpc}^{-1}$ (old stars). Therefore, the observed steeper $[\text{Mg}/\text{Fe}]$ gradient is not affected by the possible thin-thick disc contamination, and it seems to be a direct result from the newly derived $[\text{Mg}/\text{Fe}]$ abundances.

Comparison with literature studies

The radial metallicity gradient value in the Galactic disc (and its evolution with time) is still a matter of debate within the literature, with negative slopes ranging from -0.04 to $-0.1 \text{ dex kpc}^{-1}$ for the analysis of different Galactic populations: planetary nebulae (PNe), HII regions, open clusters, variable (Cepheids) and field stars. Our measured value is therefore in agreement within the literature range (see Table 7.2). It is worth noting that the shown gradients correspond to works with different target selections and implemented methodologies to estimate abundances and distances. Depending on the work, the metallicity value was measured globally ($[\text{M}/\text{H}]$) or considering only iron lines ($[\text{Fe}/\text{H}]$), and the radial distance estimate comes from either the guiding centre radius of the stellar orbit (R_g) or the Galactocentric radius of the star (R_{GC}).

First, Table 7.2 shows how our metallicity gradient estimation is qualitatively in good agreement with previous analysis of field stars from different Galactic surveys. Compatible results were obtained using data from SEGUE ($R \sim 2000$, Cheng et al., 2012), RAVE ($R \sim 7500$, Boechi et al., 2013a), APOGEE ($R \sim 22500$, Hayden et al., 2014, Anders et al., 2014), and Gaia-ESO Survey (GES) GIRAFFE ($R \sim 20000$, Mikolaitis et al., 2014, Recio-Blanco et al., 2014) and UVES data ($R \sim 47000$, Bergemann et al., 2014).

Additionally, stellar open clusters (OCs) are considered a unique tool to study the time evolution of the radial metallicity gradients, due to their accurate derived ages and Galactocentric distances, covering wide ranges along the Galactic disc (c.f. Magrini et al., 2009, OCs ages from ~ 30 Myr to 11 Gyr). Our measurement shows a good agreement with the one presented by Magrini et al. (2009) for OCs older than 0.8 Gyr, and also with the overall gradient found by Frinchaboy et al. (2013) from the OCCAM survey using APOGEE data, recently updated by Donor et al. (2020).

Furthermore, Cepheid variable stars provide the present-day abundance gradients of the Galactic disc since they are massive stars younger than 300 Myr, and are commonly used as good distance indicators and as chemical tracers for the interstellar medium (ISM) abundance (c.f. Genovali et al., 2014, and references therein). For an homogeneous Galactic Cepheids sample, observed at high spectral resolution ($R \sim 38000$), Genovali et al. (2014) derived a consistent estimate for the present-time ISM abundance gradient.

TABLE 7.2: Radial abundance gradients (dex kpc⁻¹) in the Galactic thin disc from literature.

Abundance	Value	Work	Tracer	Thin disc definition	Database
$\frac{d[\text{Fe}/\text{H}]}{dR_{\text{GC}}}$	-0.066 ± 0.037	Cheng et al. (2012)	Field dwarf stars	$0.15 < z < 0.25$ kpc ($6 < R_{\text{GC}} < 16$ kpc)	SEGUE
$\frac{d[\text{Fe}/\text{H}]}{dR_{\text{g}}}$	-0.065 ± 0.003	Boeche et al. (2013a)	Field dwarf stars	$ z_{\text{max}} < 0.4$ kpc ($4.5 < R_{\text{g}} < 9.5$ kpc)	RAVE
$\frac{d[\text{M}/\text{H}]}{dR_{\text{GC}}}$	-0.090 ± 0.002	Hayden et al. (2014)	Field giant stars	Chemical + $ z < 0.25$ kpc ($5 < R_{\text{GC}} < 15$ kpc)	APOGEE
$\frac{d[\text{Fe}/\text{H}]}{dR_{\text{g}}}$	-0.074 ± 0.010	Anders et al. (2014)	Field giant stars	$ z_{\text{max}} < 0.4$ kpc ($6 < R_{\text{g}} < 11$ kpc)	APOGEE Gold
$\frac{d[\text{Fe}/\text{H}]}{dR_{\text{GC}}}$	-0.068 ± 0.016	Bergemann et al. (2014)	Field stars	$ z < 0.3$ kpc ($6 < R_{\text{GC}} < 9.5$ kpc)	GES UVES
$\frac{d[\text{Fe}/\text{H}]}{dR_{\text{GC}}}$	-0.045 ± 0.012	Mikolaitis et al. (2014)	Field stars	Chemical + $ z < 0.61$ kpc ($4 < R_{\text{GC}} < 12$ kpc)	GES GIRAFFE
$\frac{d[\text{Fe}/\text{H}]}{dR_{\text{GC}}}$	-0.058 ± 0.008	Recio-Blanco et al. (2014)	Field stars	Chemical + $ z < 0.7$ kpc ($5 < R_{\text{GC}} < 11$ kpc)	GES GIRAFFE
$\frac{d[\text{Fe}/\text{H}]}{dR_{\text{GC}}}$	-0.053 ± 0.029		≤ 0.8 Gyr		
$\frac{d[\text{Fe}/\text{H}]}{dR_{\text{GC}}}$	-0.094 ± 0.008	Magrini et al. (2009)	OCs: 0.8 - 4 Gyr	($7 < R_{\text{GC}} < 12$ kpc)	
$\frac{d[\text{Fe}/\text{H}]}{dR_{\text{GC}}}$	-0.091 ± 0.060		4 - 11 Gyr		
$\frac{d[\text{Fe}/\text{H}]}{dR_{\text{GC}}}$	-0.090 ± 0.030	Frinchaboy et al. (2013)	OCs	($7.9 < R_{\text{GC}} < 14$ kpc)	OCCAM-APOGEE
$\frac{d[\text{Fe}/\text{H}]}{dR_{\text{GC}}}$	-0.068 ± 0.004	Donor et al. (2020)	OCs	($6 < R_{\text{GC}} < 13.9$ kpc)	OCCAM-APOGEE
$\frac{d[\text{Fe}/\text{H}]}{dR_{\text{GC}}}$	-0.060 ± 0.002	Genovali et al. (2014)	Cepheids	($5 < R_{\text{GC}} < 19$ kpc)	
$\frac{d[\text{Mg}/\text{Fe}]}{dR_{\text{g}}}$	-0.009 ± 0.002	Boeche et al. (2013a)	Field dwarf stars	$ z_{\text{max}} < 0.4$ kpc ($4.5 < R_{\text{g}} < 9.5$ kpc)	RAVE
$\frac{d[\text{Mg}/\text{Fe}]}{dR_{\text{GC}}}$	$+0.021 \pm 0.016$	Bergemann et al. (2014)	Field stars	$ z < 0.3$ kpc ($6 < R_{\text{GC}} < 9.5$ kpc)	GES UVES
$\frac{d[\text{Mg}/\text{M}]}{dR_{\text{GC}}}$	$+0.009 \pm 0.003$	Mikolaitis et al. (2014)	Field stars	Chemical + $ z < 0.61$ kpc ($4 < R_{\text{GC}} < 12$ kpc)	GES GIRAFFE
$\frac{d[\text{Mg}/\text{Fe}]}{dR_{\text{GC}}}$	$+0.012 \pm 0.002$	Recio-Blanco et al. (2014)	Field stars	Chemical + $ z < 0.7$ kpc ($5 < R_{\text{GC}} < 11$ kpc)	GES GIRAFFE
$\frac{d[\text{Mg}/\text{Fe}]}{dR_{\text{GC}}}$	$+0.013 \pm 0.006$	Mikolaitis et al. (2019)	Field dwarf stars	Kinematical ($6 < R_{\text{GC}} < 10$ kpc)	VUES
$\frac{d[\text{Mg}/\text{Fe}]}{dR_{\text{GC}}}$	$+0.013 \pm 0.003$	Genovali et al. (2015)	Cepheids	($4.1 < R_{\text{GC}} < 18.4$ kpc)	UVES
$\frac{d[\text{Mg}/\text{Fe}]}{dR_{\text{GC}}}$	$+0.009 \pm 0.001$	Donor et al. (2020)	OCs	($6 < R_{\text{GC}} < 13.9$ kpc)	OCCAM-APOGEE

On the other hand, the observed positive gradient in the $[\text{Mg}/\text{Fe}]$ abundance with radius is in close agreement with the results from Bergemann et al. (2014). However, shallower positive gradients in $[\text{Mg}/\text{Fe}]$ are commonly reported within the literature (e.g. Mikolaitis et al., 2014, Recio-Blanco et al., 2014, Mikolaitis et al., 2019, recent analysis using high-resolution VUES spectrograph, $R \sim 60000$), even finding negative values (Boeche et al., 2013a). Additionally, Genovali et al. (2015) and Donor et al. (2020) reported a similar slope by analysing Galactic Cepheids and open clusters, respectively, over the Galactic disc.

As a consequence, our radial $[\text{Mg}/\text{Fe}]$ gradient is not only steeper than the one estimated from Mikolaitis et al. (2017) abundances (see Table 7.1), it is also steeper than other previous measures in the literature. Once again, this is a major consequence of the Santos-Peral et al. (2020) improvement of the metal-rich star data. We however point out that Perdigon et al. (2021)

report a flatter radial gradient for sulphur (another α -element) equal to $+0.012 \text{ dex kpc}^{-1}$ for AMBRE stars and adopting a similar methodology as ours (further details in Sect. 7.2.1).

7.1.3 Radial migration

The stars in the Galactic disc are very likely to be scattered by resonances with the spiral arms or by giant molecular clouds that could increase the radial oscillation amplitudes around their R_g (blurring), or change the angular momentum of the orbit (churning) (Lynden-Bell & Kalnajs, 1972, Lacey, 1984, Grenon, 1989, 1999, Sellwood & Binney, 2002, Schönrich & Binney, 2009, Minchev et al., 2014, Kordopatis et al., 2015a). On the one hand, stars with more eccentric and inclined orbits can belong to galactic regions far from the Sun but reach the solar neighbourhood via blurring. However, as shown in Fig. 6.2, 50 % of our selected sample is on very circular orbits with $e < 0.15$. Therefore, the observed stars are either expected to have been born locally or to have increased (decreased) their angular momentum via churning, increasing (decreasing) their guiding centre radius (R_g) without changing their orbit eccentricity.

The impact of radial migration over a whole observed stellar sample is a complex, unsolved problem. In particular, its final effect on the chemical evolution and the metallicity distribution function in the solar vicinity is very uncertain, also suggested to be negligible (Spitoni et al., 2015, Vincenzo & Kobayashi, 2020). The unique observational constraint consists in the presence of too metal-rich stars in the solar annulus that cannot be justified by chemical evolution models without an exchange of matter between different radial annuli in the Galactic disc (Grisoni et al., 2017). Under the assumption that a negative radial metallicity gradient has been present in the Galaxy since the thin disc formation epoch (Roškar et al., 2008, Magrini et al., 2009, Schönrich & McMillan, 2017, Minchev et al., 2018), and given a present-day ISM abundance at the solar vicinity of around $[M/H] \sim 0.0 \text{ dex}$, the observed super-metal-rich stars (SMR; $[M/H] \gtrsim +0.1 \text{ dex}$) should have been formed in the inner disc regions (Minchev et al., 2013, Kordopatis et al., 2015a).

Following the procedure described in Hayden et al. (2020), we estimated the minimum required eccentricity of a star, at a given metallicity, to reach the solar neighbourhood exclusively due to blurring. To this purpose, we assumed that the orbit's apocentre is the measured present-day's position. Additionally, assuming a given radial ISM metallicity gradient and fixing the local ISM abundance at $(R_\odot, [M/H]) = (8.0 \text{ kpc}, 0.0 \text{ dex})$, it is possible to estimate the birth radius of the star from its observed present-day $[M/H]$. In this framework, we selected the churned candidates through the following required minimum eccentricity relation:

$$\text{ecc}^*([M/H]) \geq \frac{R}{R_{\text{birth}}([M/H])} - 1 \quad (7.1)$$

In this relation, R is the present-day's position star, which is assumed to lie between 7.7 and 8.3 kpc since our sample is located within 300 pc of the Sun, and R_{birth} is the estimated birth radius of the star given its metallicity $[M/H]$, but also assuming an ISM gradient.

The evolution with time of the ISM radial metallicity gradient is a current source of discussion for Galactic chemical evolution models and cosmological simulations: some models predict a time invariant gradient (e.g. Magrini et al., 2009, Gibson et al., 2013), while others predict a steepening of the ISM metallicity gradient with time (e.g. Chiappini et al., 2001, Schönrich & McMillan, 2017), or a flattening with time (e.g. Boissier & Prantzos, 1999, Hou et al., 2000, Roškar et al., 2008, Pilkington et al., 2012, Minchev et al., 2018). For that reason, we decided to consider different ISM gradient values in the R_{birth} estimate for the SMR stars, and study the influence of these assumptions on the conclusions.

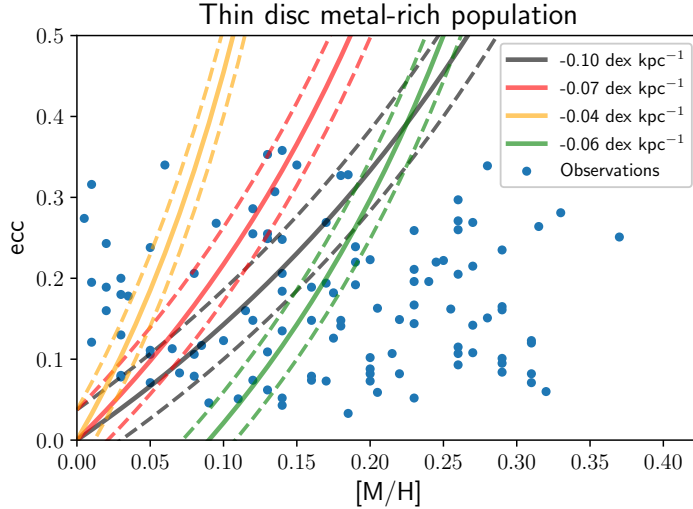


FIGURE 7.4: Distribution of the orbital eccentricities as a function of $[M/H]$ for the thin disc metal-rich sample. The solid (dashed) lines indicate the required eccentricity to reach $R = 8$ kpc (± 300 pc) without the need of churning (see Eq. 7.1). For a fixed zero-point, $ISM_{[M/H]}(R_{\odot}) = 0.0$, we studied three different ISM gradients (black, red, and orange). The green one corresponds to the one from [Genovali et al. \(2014\)](#). The stars to the right require churning to reach the solar neighbourhood.

Figure 7.4 shows the orbital eccentricities as a function of $[M/H]$ for the thin disc metal-rich sample. The solid lines correspond to the required eccentricity (see Equation (7.1)) for different values of ISM radial metallicity gradients: -0.10 dex kpc^{-1} (black), -0.07 dex kpc^{-1} (our measured gradient for young stars in Table 7.1, see also [Minchev et al., 2018](#), red), -0.04 dex kpc^{-1} (orange), and -0.06 dex kpc^{-1} (Cepheids analysis from [Genovali et al., 2014](#), green). For the three first cases, we assumed $ISM_{[M/H]}(R_{\odot}) = 0.0$ to estimate R_{birth} from the stellar metallicity. However, [Genovali et al. \(2014\)](#) have their own zero point, defined as: $[Fe/H] = -0.06 * R_g + 0.57$, with a clear shift in the relation compared to the other ones assumed in this work. The impact of the ISM gradient value and the zero-point assumption in the derived R_{birth} , and thus in the required eccentricity to reach the solar vicinity without the need of churning, is clearly observed. As described in [Hayden et al. \(2020\)](#), given the measured $[M/H]$ and eccentricity, stars lying to the left are able to reach the solar neighbourhood through blurring, while the presence of stars to the right of the line cannot be explained by blurring alone and are solid candidates to have been migrated through churning. This is the case for most of the SMR stars (70% of the SMR stars lie below the line that corresponds to the Cepheids analysis), they are thus likely to have been brought to the solar neighbourhood by churning, which is in close agreement with previous studies (e.g. [Kordopatis et al., 2015a](#), [Wojno et al., 2016](#)). In absolute terms, our churned candidates with $[M/H] > +0.1$ comprise around the 17 % of the whole stellar sample. If we constraint the number of migrators to only stars with $[M/H] > +0.25$, the global percentage decreases to an 8 % of the sample.

In particular, we analysed the possible age trends in the radial changes ($\Delta R_g = R_g - R_{\text{birth}}$) associated to churning. For each assumed ISM abundance gradient separately, Fig. 7.5 shows the ΔR_g as a function of stellar age for the churned candidates (see Fig. 7.4). The migrated SMR stars cover a wide range of ages from ~ 4 to 12 Gyr. As a consequence of the R_{birth} estimation proxy (zero-point fixed at $ISM_{[M/H]}(R_{\odot}) = 0.0$ dex), the flatter the applied ISM gradient, the larger the ΔR_g . The respective slopes and errors were derived by the Theil-Sen linear regression estimator. We observe that the general trend is slightly negative with stellar age, becoming steeper as the assumed ISM gradient flattens (see right-hand panel). In addition, we obtain different ΔR_g values based on the [Genovali et al. \(2014\)](#) analysis, but showing as well a shallow

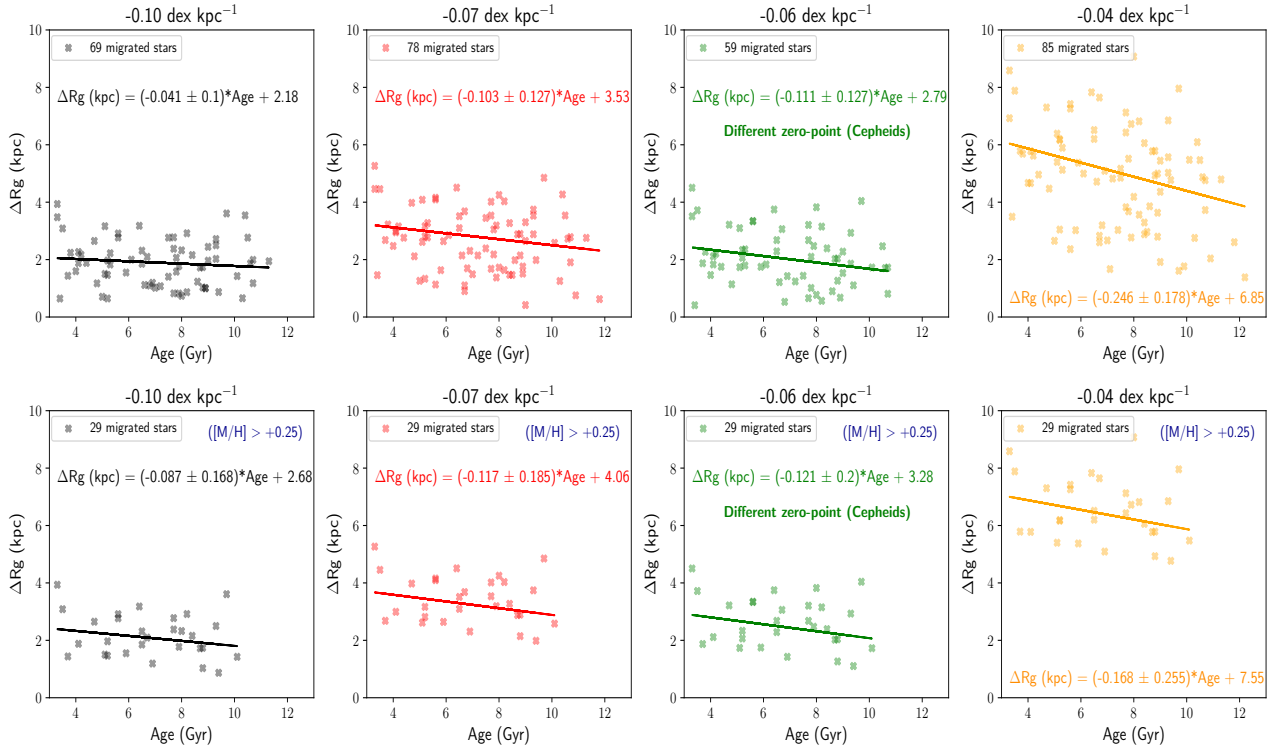


FIGURE 7.5: The estimated covered distance ΔR_g ($R_g - R_{\text{birth}}$) vs. stellar age for the selected churned SMR stars for different ISM metallicity gradients (see Fig. 7.4 and titles of the plots). **Top:** churned candidates with $[M/H] > 0.1$. **Bottom:** only migrators with $[M/H] > 0.25$.

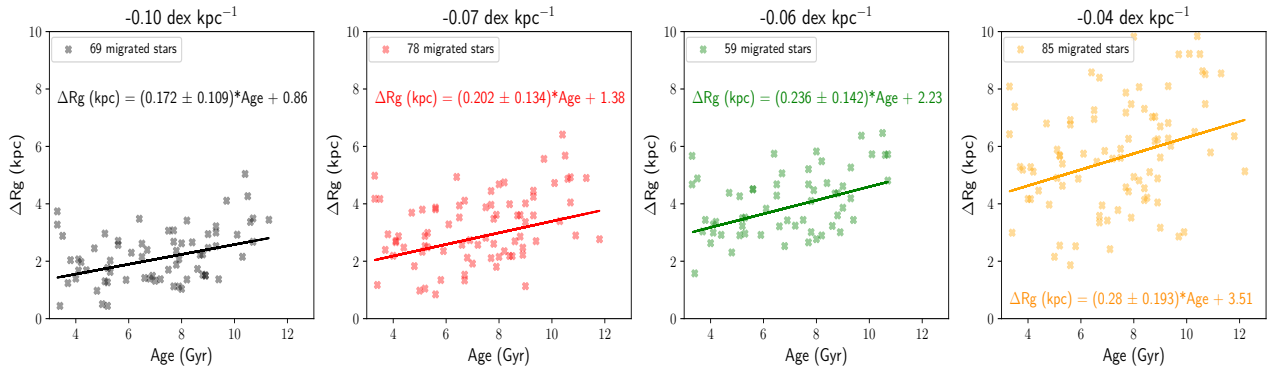


FIGURE 7.6: Same as top row of Fig. 7.5, but applying a different zero-point as a function of the stellar age ($\text{ISM}_{[M/H]}(R_{\odot}, \tau)$) in the R_{birth} estimate (see Sect 7.1.3).

negative gradient with stellar age. We observe the same behaviour when we restrict the analysis to stars with $[M/H] > +0.25$ (bottom-row panels). From now on, we will show the analysis for the churned candidates with $[M/H] > +0.1$ due to the larger statistical sample.

However, the application of a fixed zero-point for every star may introduce a bias in the ΔR_g estimate, in particular for old stars, since $\text{ISM}_{[M/H]}(R_{\odot})$ is expected to have been chemically enriched with time to reach the used present-time value. To explore the dependence on the zero-point assumption, we applied a more appropriate value for each star, according to their age. To this purpose, we selected the observed stars in our sample that lie on the solar annulus ($7.5 \leq R_g < 8.5$ kpc), and calculated the average metallicity ($[M/H] = 0.02, -0.03, -0.05,$ and -0.15 dex) at different age bins ($[2-6], [6-8], [8-10],$ and $[10-12]$ Gyr). Then, we assumed these values as a proxy of the $\text{ISM}_{[M/H]}(R_{\odot})$ evolution with time. The adopted trend is consistent with

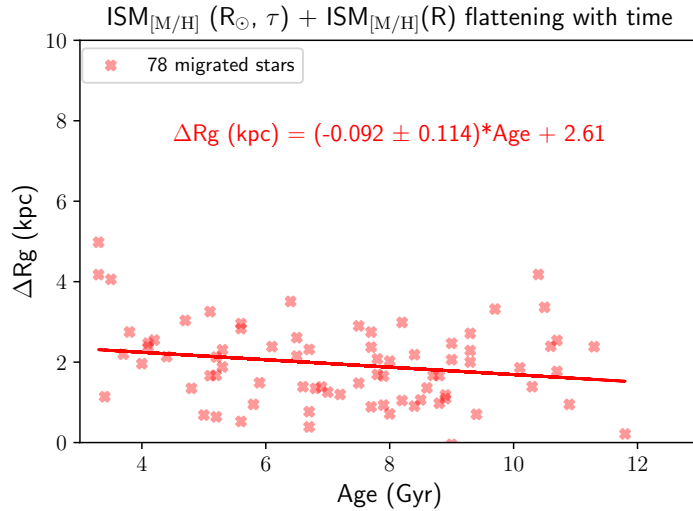


FIGURE 7.7: The estimated covered distance ΔR_g ($R_g - R_{\text{birth}}$) vs. stellar age for the selected churned SMR stars, applying a different zero-point ($\text{ISM}_{[M/H]}(R_{\odot}, \tau)$), and a different ISM metallicity gradient as a function of the stellar age (linearly flattening with time from -0.15 to -0.07 dex kpc^{-1} between 11.8 Gyr and 3.3 Gyr, respectively) in the R_{birth} estimate.

the ISM enrichment of the solar neighbourhood found by Galactic chemical evolution models (e.g. Hou et al., 2000, Schönrich & McMillan, 2017, Minchev et al., 2018), although an accurate $\text{ISM}_{[M/H]}(R_{\odot}, \tau)$ estimate is outside the scope of this paper. Figure 7.6 shows the observed trend by applying the estimated zero-point as a function of the SMR stellar age. For each analysed ISM abundance gradient, we obtained significantly higher ΔR_g values for old SMR stars up to inverting to a positive trend with stellar age. We stress that the selected stars in the solar annulus are likely to be originally born far from their present location. In that case, a more accurate $\text{ISM}_{[M/H]}(R_{\odot}, \tau)$ estimate might present lower values than the ones shown here, and therefore the impact on the ΔR_g value could be larger than the illustrated one.

Moreover, we have explored the influence in the R_{birth} estimate of a time evolution of the ISM gradient, combined with an evolving $\text{ISM}_{[M/H]}(R_{\odot})$ zero-point. To this purpose, we decided to apply a simple toy model based on the assumptions of Minchev et al. (2018): a thin disc formed with an initial metallicity gradient of ~ -0.15 dex kpc^{-1} , flattening with time to a present-day ISM profile of ~ -0.07 dex kpc^{-1} (which is equal to our measured gradient for young stars, shown in Table 7.1). Our toy model simply assigns these limit ISM gradient values to the youngest (3.3 Gyr) and the oldest (11.8 Gyr) SMR stars in our selected sample. Then, a linear interpolation was performed to estimate the corresponding ISM metallicity gradient as a function of each SMR stellar age. Figure 7.7 shows the resulting trend of ΔR_g with stellar age, which has now changed sign compared to the one derived in Fig. 7.6, but similar to the observed trend in our first simple approach shown in Fig. 7.5. It is worth noting that the aim of this analysis is to visualise the strong dependence on the assumptions of the observed radial migration trend with age. An accurate $\text{ISM}_{[M/H]}(R)$ determination at any epoch is outside the scope of this paper.

In conclusion, our local analysis hints towards a possible clear, although not necessary predominant, presence of radially migrated stars in the Galactic disc via churning, in agreement with Kordopatis et al. (2015a). The large variety of ages and ΔR_g values observed for the churned SMR stars in every case (e.g. $3.3 \leq \tau \leq 11.8$ Gyr and $0 \leq \Delta R_g \leq 6$ kpc for the steepest ISM gradient, which shows lower ΔR_g estimates), allows us to think that an important fraction of stars in the Galactic disc could have been also sensitive to radial changes associated to churning. Unfortunately, from an observational point of view, only high metallicity stars in the solar vicinity can be certainly assumed as radial migrators. We again remark how complicate it is to

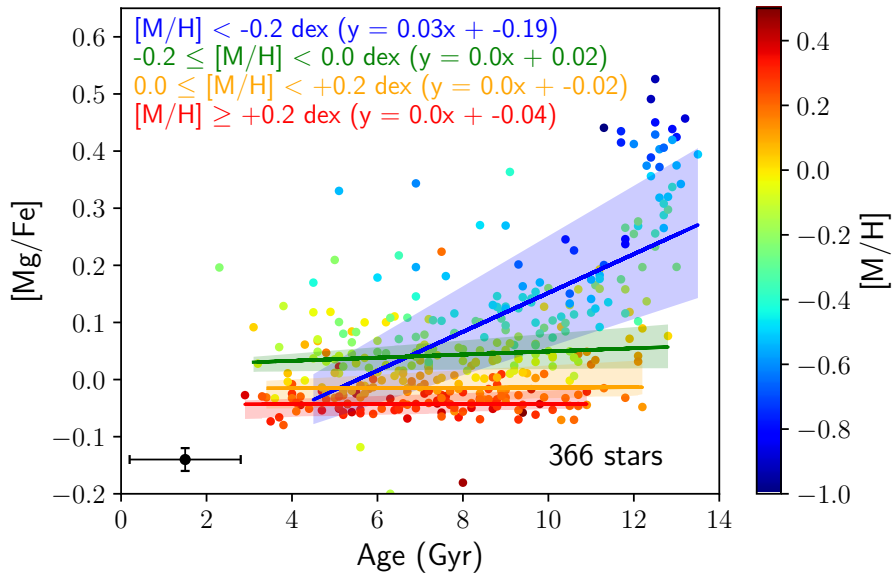


FIGURE 7.8: $[\text{Mg}/\text{Fe}]$ as a function of age for the working sample. The colour lines correspond to the Theil-Sen linear regression over different metallicity ranges, from metal-rich to metal-poor (from bottom to top). The respective shadow area spans the lower-upper bound of the 95% confidence interval of the fit. The mean estimated uncertainties for each star values are shown in the bottom-left corner.

accurately measure the radial migration efficiency, and how the interpretation of the reported signatures strongly rely on the model assumptions.

7.2 Age-abundance relations

In this section, we analyse the Galactic disc as a whole, without considering a thin/thick disc dichotomy, to allow a general, parametrised view of the disc evolution with time.

7.2.1 $[\text{Mg}/\text{Fe}]$ abundance as a chemical clock

Fig. 7.8 shows the $[\text{Mg}/\text{Fe}]$ vs. age relation, colour-coded by the stellar metallicity. The figure clearly shows a significant spread of stellar ages at any given $[\text{Mg}/\text{Fe}]$ value, particularly for $[\text{Mg}/\text{Fe}]$ lower than 0.2 dex. The covered age range at a fixed $[\text{Mg}/\text{Fe}]$ is generally wider in comparison with the Hayden et al. (2017) analysis of the same sample of stars (see their Fig. 2) using Gaia DR1 data and abundances from Mikolaitis et al. (2017). On the other hand, our result is in good agreement with Silva Aguirre et al. (2018), who studied a sample of red giants with asteroseismic ages noticing a similar $[\alpha/\text{Fe}]$ -age behaviour (c.f. their Fig. 10). Furthermore, for stars younger than about 11 Gyr, we observe a larger dispersion in the $[\text{Mg}/\text{Fe}]$ abundance ($\sigma_{[\text{Mg}/\text{Fe}]} \sim 0.1$ dex at a given age) with respect to previous studies (e.g. Delgado Mena et al., 2019, Nissen et al., 2017, 2020). This dispersion is correlated with the stellar metallicity and appears more clearly thanks to the unveiled slope of $[\text{Mg}/\text{Fe}]$ with $[\text{M}/\text{H}]$ in Santos-Peral et al. (2020) for metal-rich stars. Indeed, in close agreement with Haywood et al. (2013), the lower envelope is occupied by metal-rich stars, while the upper envelope is occupied mainly by more metal-poor stars.

As a consequence, we have studied the $[\text{Mg}/\text{Fe}]$ -age trends in different metallicity bins. For $[\text{M}/\text{H}] \geq -0.2$, we find stars with ages from ~ 3 up to 12 Gyr, describing a flat trend in the $[\text{Mg}/\text{Fe}]$ -age plane, without a change of the slope in the different metallicity bins. This observed pattern could only be explained by chemical evolution models if an important co-existence of different stellar populations in the solar neighbourhood is assumed, with different enrichment histories and birth origins in the Galactic disc (as previously suggested by several studies, e.g. Sellwood & Binney, 2002, Nordström et al., 2004, Fuhrmann, 2011, Boeche et al., 2013b, Kor-dopatis et al., 2015a, Wojno et al., 2016).

For more metal-poor stars ($[\text{M}/\text{H}] < -0.2$ dex), we find a linear correlation of $[\text{Mg}/\text{Fe}]$ with age, showing a consistent positive slope value with the results of Delgado Mena et al. (2019) (~ 0.02 dex Gyr^{-1} , see their Fig. 7 for a dwarf thin disc stars sample in the solar neighbourhood), and Ness et al. (2019) (~ 0.03 dex Gyr^{-1} , see their Fig. 7 over a sample of red clump stars across a wide range of Galactocentric distances). However, these works do not find a clear trend of $[\text{Mg}/\text{Fe}]$ abundances with metallicity in the metal-rich regime, as we reported in our sample.

Finally, we remark the presence of young, metal-poor and high- $[\text{Mg}/\text{Fe}]$ stars, also reported within the literature (Martig et al., 2015, Chiappini et al., 2015, Silva Aguirre et al., 2018, Delgado Mena et al., 2019, Ciucă et al., 2021). The origin of this type of stars has been suggested to be radial migrated candidates expelled outwards by the Galactic bar (Chiappini et al., 2015), or blue stragglers stars as products of mass transfer in binary systems (Jofré et al., 2016, Wyse et al., 2020) that may lead to an underestimation of their age.

Comparison with sulfur abundances

In a parallel work within the AMBRE Project context, Perdigon et al. (2021) derived sulfur abundances (another α -element) for a large collection of HARPS, UVES and FEROS spectra. They adopted narrow normalisation intervals around each line, following our optimised methodology for a correct continuum placement (fully described in Chapter 5). They independently clearly seen the same negative trend on the supersolar metallicity regime for the $[\text{S}/\text{M}]$ abundance, as we reported before for our measurements of $[\text{Mg}/\text{Fe}]$.

Due to different selection criteria, they present 89 stars in common with our working sample. Figure 7.9 illustrates the comparison between AMBRE/sulfur and AMBRE/magnesium abundances. The two α -elements show the same global behaviour with metallicity, which confirms that sulfur is predominantly produced by the same nucleosynthesis channel (SNe II). The shifted $[\text{S}/\text{Mg}]$ ratios could be caused by different calibrations adopted for the abundance derivation analysis. The variation with metallicity (slightly larger at higher $[\text{M}/\text{H}]$) suggests possible differences in their enrichment timescales during the Galactic evolution.

In addition, Perdigon et al. (2021) also adopted our precise estimated ages (see Chapter 6) for a common sub-sample of MSTO stars. Figure 7.10 shows the variation of $[\text{S}/\text{M}]$ and $[\text{S}/\text{Mg}]$ abundances as a function of age. They found a slope for the $[\text{S}/\text{M}]$ (~ 0.02 dex Gyr^{-1}) very consistent with the one reported in Fig. 7.8 for the more metal-poor stars, which points that sulfur can be considered as a good chemical clock, although some dispersion is also present. Furthermore, the bottom panel shows a similar sulfur and magnesium content for all the stellar ages, revealing no important differences in the production rate (yields) of both elements with time. This trend could confirm their common origin from SNe II.

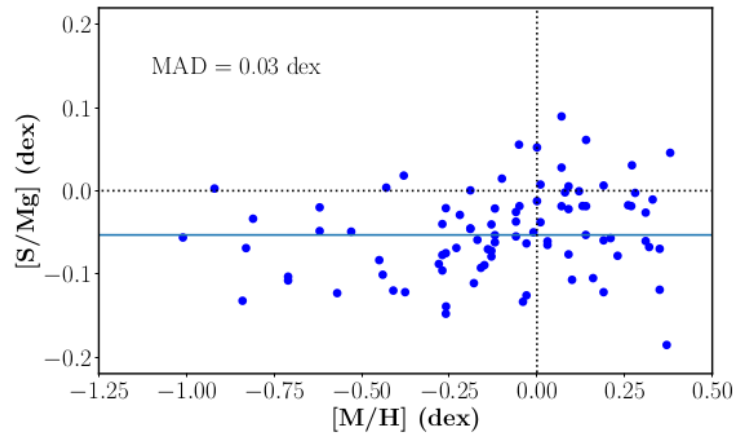


FIGURE 7.9: Sulfur over magnesium abundances as a function of the mean stellar metallicity $[M/H]$ for stars in common with [Perdigon et al. \(2021\)](#). The blue horizontal line indicates the median of this $[S/Mg]$ ratio (-0.05 dex) over the whole metallicity domain and the associated Median Absolute Deviation is reported in the upper left corner. (Source: [Perdigon et al., 2021](#)).

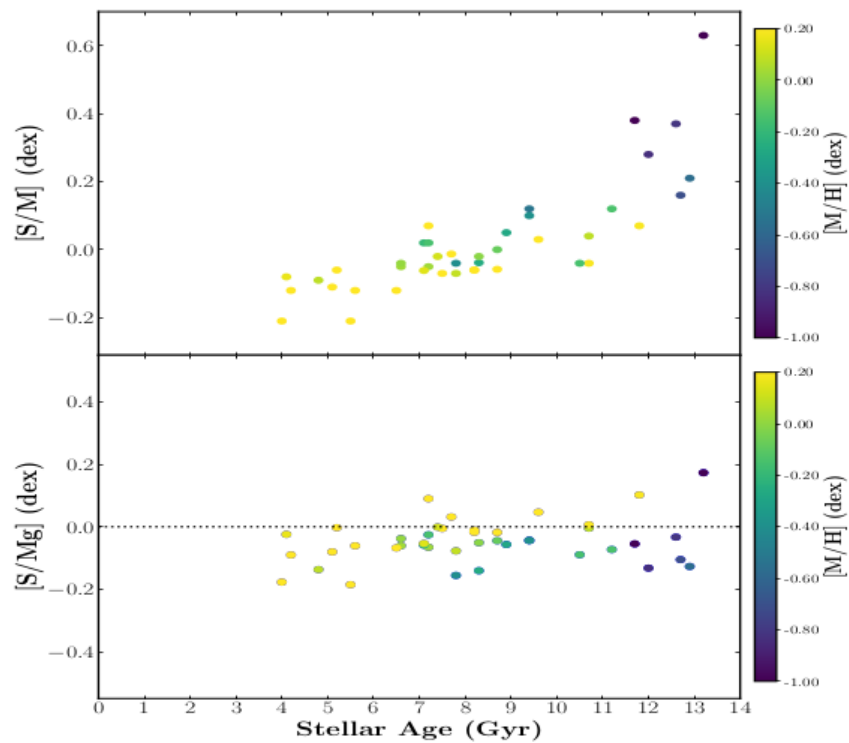


FIGURE 7.10: Sulfur over mean metallicity $[S/M]$ (top panel) and over magnesium abundance $[S/Mg]$ (bottom panel) as a function of the stellar ages for the main sequence turn-off stars in common with [Perdigon et al. \(2021\)](#). The color code corresponds to the mean stellar metallicity. (Source: [Perdigon et al., 2021](#)).

7.2.2 Temporal evolution in the [Mg/Fe]-[M/H] plane

Figure 7.11 and Figure 7.12 illustrate the [Mg/Fe] abundance ratios relative to [M/H] for our sample stars, in different age intervals and Galactic disc locations (top row: inner Galactic disc $R_g \leq 7.5$ kpc; bottom row: outer disc $R_g > 7.5$ kpc). The bin selection was optimised to allow a significant statistical sample of stars at different radii.

Figure 7.11 shows that the oldest stellar population ($\tau \geq 12$ Gyr) at every radius is located in what has been classically called the thick disc, i.e. an α -enhanced population (see Sect. 7.1.1). During this early epoch, we observe a rapid chemical enrichment, reaching solar metallicities. In addition, the stars are more centrally concentrated (see Sect. 7.1.1). Interestingly, 11-12 Gyr ago, a second chemical sequence appears in the outer regions of the Galactic disc, populating the metal-poor low-[Mg/Fe] tail and starting at $[M/H] \sim -0.8$ dex and $[Mg/Fe] \sim 0.2$ dex. This corresponds to the classically called thin disc or low- α population and it is highlighted in the figure by red points. Based on the radial extension of the thick disc sample (see Figs. 7.2 and 7.3 in Sect. 7.1.1), the averaged R_g of this second chemical sequence seems to be significantly larger than the Galactic disc extension at that time ($R_g < 8.5$ kpc), reaching the outer parts up to $R_g \sim 11$ kpc. Furthermore, those stars are shown to be significantly more metal-poor ($[M/H] \lesssim -0.4$ dex) with respect to the coexisting stellar population in the inner parts of the disc. They also show lower [Mg/Fe] abundances than the previous external disc (lower left panel), although presenting a similar metallicity distribution. This implies a chemical discontinuity in the disc around 11 Gyr ago, suggesting that the new sequence might have followed a different chemical evolution pathway than the previous formed component, possibly triggered by accretion of metal-poor external gas (e.g. Grisoni et al., 2017, Noguchi, 2018, Spitoni et al., 2019, Buck, 2020, Palla et al., 2020).

Figure 7.12 illustrates the chemical evolution history in the last 10 Gyr. During this long period of time, the Galactic disc seems to have experienced a slower and continuous chemical evolution towards more metal-rich and lower [Mg/Fe] regimes, compared to the more primitive epochs described in Fig. 7.11. In addition, the averaged z_{\max} seems to decrease with age, regardless the chosen chemical sequence and space location, which could be a signature of a disc settling with time. However, a larger statistical sample would be needed to justify this assumption. Finally, the difference in z_{\max} between both chemical sequences does not allow any relevant conclusion, given the low number of stars and the same followed z_{\max} distribution (the present similarities do not support two distinct disc populations, see Sect. 7.1.1).

Comparison with chemical evolution models

In a previous work within the AMBRE Project, Grisoni et al. (2017) adopted two different approaches to model the chemical evolution of thick and thin discs and interpret the AMBRE data presented in Mikolaitis et al. (2017). On the one hand, they adopted a two-infall model where the Galaxy is formed as a result of two separated infall episodes: the first forms the thick disc in a short timescale of mass accretion, followed by a second one which gives rise to the thin disc in a much slower infall of gas. On the other hand, they adopted a parallel approach by considering two distinct one-infall episodes that started at the same time but evolved in a completely independent way. In both cases, the origin of the gas in the infall episodes is extragalactic with a primordial composition, and there is no exchange of matter between different Galactic disc regions.

In a more recent study, Palla et al. (2020) revisited and applied new updated models from the two-infall paradigm to reproduce new observational data from the APOGEE survey: e.g. implementing a possible exchange of gas due to radial inflows (Spitoni & Matteucci, 2011),

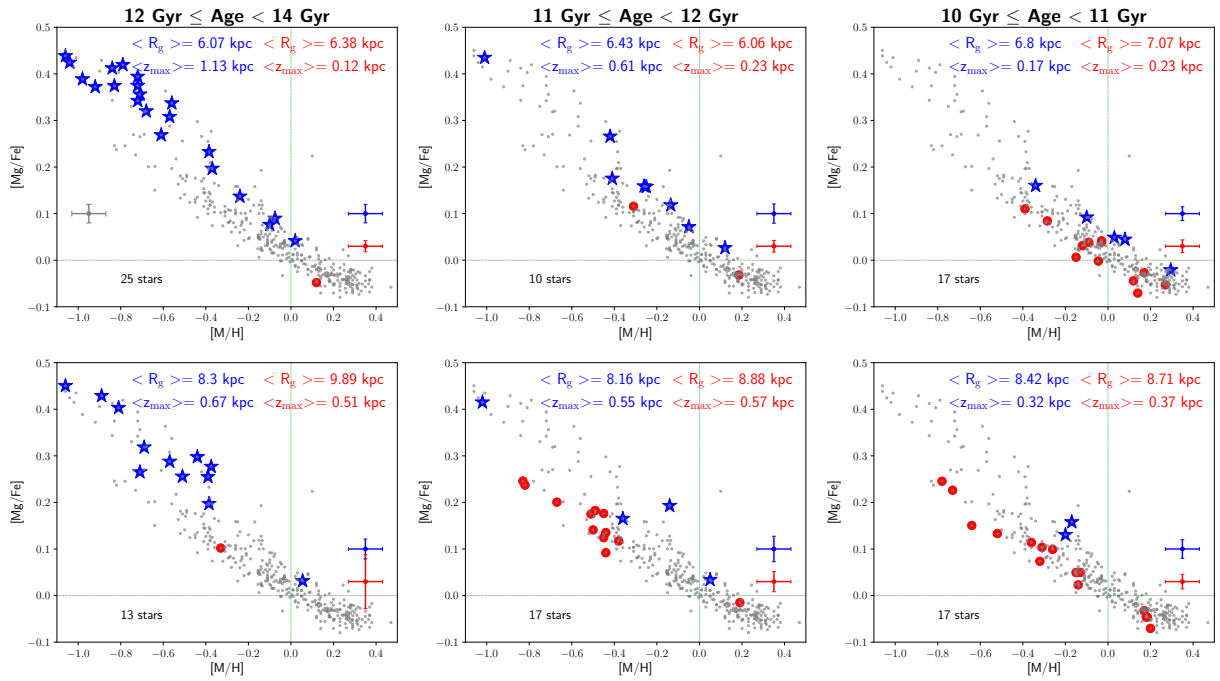


FIGURE 7.11: Distribution of the selected sample in the $([M/H], [Mg/Fe])$ plane at different ages and locations in the Galaxy (R_g). Two chemical sequences appear for ages younger than ~ 11 -12 Gyr, corresponding to the classical thick (blue stars) and thin (red circles) disc components. Each panel corresponds to a bin in the (age, R_g) space, dividing the Galactic disc in two regions: inner ($R_g \leq 7.5$ kpc; top row) and outer ($R_g > 7.5$ kpc; bottom row). The blue and red crosses in the bottom-right corner of each panel represent the mean estimated errors in $[Mg/Fe]$ and $[M/H]$ for the thick and thin disc population at that particular radius and time. The averaged R_g and z_{\max} for each population are given in the top of the respective panel. The whole working sample is shown by the dotted grey points.

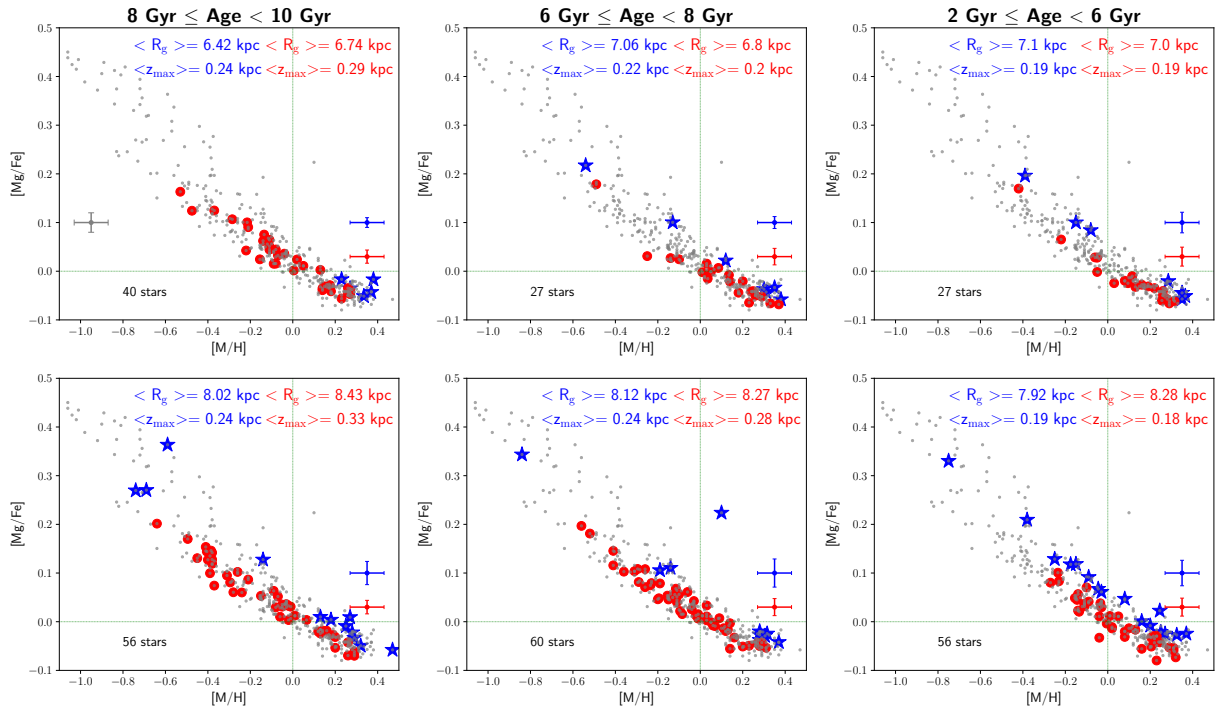


FIGURE 7.12: Same as Fig. 7.11 for the younger age intervals.

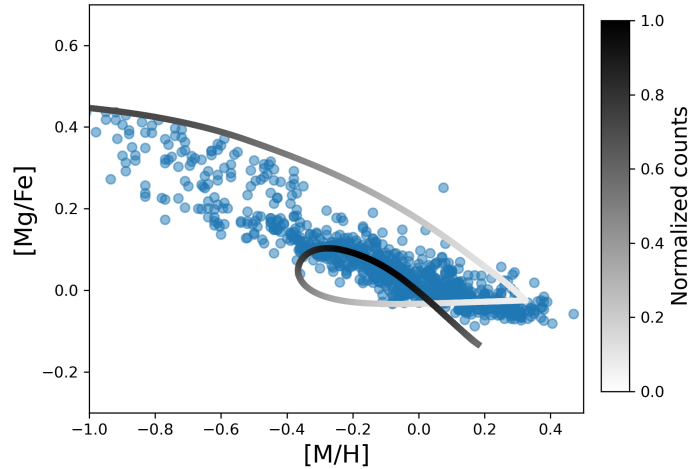


FIGURE 7.13: Observed $[Mg/Fe]$ vs. $[M/H]$ abundance ratios presented in Chapter 5, compared with the delayed (3.25 Gyr) two-infall model from Palla et al. (2020). The colorbar indicates the normalised star formation rate (SFR) in the model at a certain time (and hence at certain $[Mg/Fe]$ and $[M/H]$).

or assuming that the mass accretion in the Galactic thin disc follows the inside-out scenario (Matteucci & Francois, 1989, Chiappini et al., 2001). Their best model suggests a delayed two-infall model (gap of around ~ 3.25 Gyr between the formation of the two discs), in agreement with the previous work by Spitoni et al. (2019, delay of ~ 4.3 Gyr), and a variable star formation efficiency and the presence of radial gas flows with constant speed during the Galactic disc evolution.

A comparison with models and simulations is missing in the interpretation of our observational results. The next step will consist in performing a detailed comparison in order to draw more robust conclusions. At the present time, a preliminary result is illustrated in Fig. 7.13 from a paper in preparation within the work developed by Palla et al. (2020). Since a direct comparison does not require our estimated ages, we have overplotted the delayed two-infall model over the whole AMBRE:HARPS sample (see Chapter 5). We find that the model could reproduce satisfactorily the data, although further analysis needs to be done.

7.2.3 Trends with stellar age: relation to radius

Figure 7.14 represents the $[Mg/Fe]$ vs. age (left panel) and the age-metallicity relation (AMR; right panel), in two bins of guiding centre radius: the inner regions ($R_g \leq 7.5$ kpc) and the outer regions ($R_g > 7.5$ kpc). The points correspond to the average abundance estimate for each bin in the (age, R_g) space, shown as individual panels in Figs. 7.11 and 7.12.

In order to propagate the uncertainties on the $[M/H]$, $[Mg/Fe]$, and age for each star, we performed 1000 Gaussian Monte Carlo realisations, within the corresponding error bars of each object. In addition, to include the effect of possible statistical fluctuations in the sampled population, we have randomly selected 80 % of the stars for each Monte Carlo realisation, and estimated the average values in age, $[M/H]$ and $[Mg/Fe]$ for the different bins in age. Finally, the plotted errors correspond to the 16th and 84th percentile values ($\pm 1\sigma$) of the resulting distributions of the average age, $[M/H]$, and $[Mg/Fe]$ abundances. We did not consider the uncertainties in the R_g estimation since they are negligible (smaller than 0.2 kpc, see Sect. 6.2).

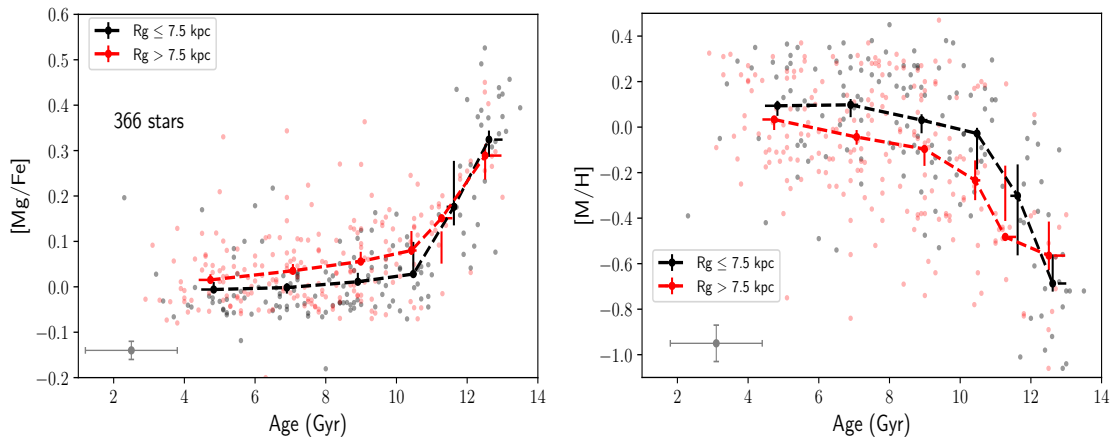


FIGURE 7.14: Stellar distribution in the $[Mg/Fe]$ vs. age (left panel) and the $[M/H]$ vs. age relation (right panel) for the inner ($R_g \leq 7.5$ kpc) and the outer ($R_g > 7.5$ kpc) regions of the Galactic disc. Their respective trends are indicated by the average abundance value per age bin ($[2-6]$, $[6-8]$, $[8-10]$, $[10-11]$, $[11-12]$ and $[12-14]$ Gyr), together with the error bars in $[Mg/Fe]$, $[M/H]$, and age. The overall mean estimated errors are shown in the bottom-left corner.

At early epochs (10-14 Gyr), Fig. 7.14 shows a rapid chemical enrichment, with a sharp increase in metallicity and decrease in $[Mg/Fe]$ to solar abundance values. No significant differences between the inner and outer regions seem to exist earlier than 12 Gyr, i.e. the population seems to be chemically homogeneous, although in our local sample the outer disc population does not extend farther than ~ 8.5 kpc earlier than $\sim 11-12$ Gyr.

Afterwards, the appearance of the second Galactic disc sequence separates the averaged values of the inner and outer disc bins. In particular, the outer bin, seems to move away from the initial tracks, with a flatter behaviour in $[M/H]$ vs. age around 11 Gyr. From that epoch, we find two approximately parallel and well-defined patterns for the inner and outer disc, flattening in a same way with time for the last 10 Gyr of evolution. The measured $[M/H]$ ($[Mg/Fe]$) abundance is shifted towards lower (higher) values for the outer disc at any age, which corresponds to the measured negative (positive) radial gradient in Sect. 7.1.2. The inside-out scenario for the disc build-up (Matteucci & Francois, 1989, Chiappini et al., 2001), i.e. larger timescales for larger radii, reproduce the observed radial gradients in the disc and the higher surface gas density for star formation in the inner regions, which agrees with our result. Although our limited sample does not allowed to interpret the result at different galactocentric distances or smaller bins in R_g , it is worth noting the similar slopes of the $[Mg/Fe]$ and $[M/H]$ trends with age point to a similar chemical evolution at all radii for ages younger than 10 Gyr, without a spatial discontinuity of the chemical evolution in Galactic radius. In fact, a continuous, radially dependent zero point shift in chemistry cannot be excluded.

Finally, the shift in the abundance space is particularly visible in the outer disc bin and the age interval 11-12 Gyr (right panel of Fig. 7.14), caused by the appearance of the thin disc sequence, leading to a misalignment between the average abundance value and the error bar for this bin. We found that the Monte Carlo realisations introduced a bias in this particular bin due to the random contamination of younger and older stars in the propagation of the stellar age uncertainties. Based on the original sample shown in Fig. 7.11, the inclusion of stars younger than 11 Gyr shifts the metallicity distribution to significantly higher values than the original one, while stars older than 12 Gyr do not compensate this bias due to their similar metallicity composition ($[M/H] \lesssim -0.4$ dex).

7.3 Formation and evolution history of the Galactic disc

Different formation and evolution scenarios for the Milky Way disc have been proposed in order to interpret/reproduce the present-day observed chemodynamical trends in the disc. In particular, the chemical bimodality identified in the $([\alpha/\text{Fe}], [\text{M}/\text{H}])$ plane as the thin and thick disc components, and the observed radial abundance gradients, encode information on how discs have evolved. The main ingredients of disc evolution (mass accretion and radial migration) will be examined in the light of our results.

Our results are purely observational and the described interpretation hereafter is based on a revision of literature studies, with a lack of direct comparison with models or simulations. We are aware of this limitation in our interpretation, and a detailed comparison between our data and models results will be performed in a future work, aiming at drawing more robust conclusions.

Importance of internal evolutionary processes

One of the main model assumptions influencing disc evolution is the importance of the Milky Way environment. It is a known fact that the Milky Way is not evolving in isolation, however, the role of internal secular processes in the shapening of the α -elements bimodality is difficult to evaluate. To tackle this point, some studies have tested the reproducibility of the disc chemodynamical features involving minor quantities of mass accretion and mass loss. In particular, the importance of the following internal processes has been explored: (i) radial flows of gas and radial migration of stars playing a significant role in the stellar distribution (e.g. Schönrich & Binney, 2009, Bovy et al., 2016, Mackereth et al., 2017, Sharma et al., 2020), and (ii) inflow of metal-poor left over gas from the outskirts of the disc (Haywood et al., 2019, Khoperskov et al., 2020), triggered by the formation of the bar and the establishment of the Outer Lindblad Resonance.

Our results present a clear $[\text{Mg}/\text{Fe}]$ chemical distinction between both Galactic disc sequences in the metallicity regime $[\text{M}/\text{H}] \leq -0.3$ dex, and a general decreasing trend even at supersolar metallicities ($[\text{M}/\text{H}] > 0$). We found that the oldest observed population ($\tau > 12$ Gyr) constitutes the majority of the more metal-poor high- $[\text{Mg}/\text{Fe}]$ stars, in agreement with previous observational works on the local disc (e.g. Fuhrmann, 2011, Haywood et al., 2013, Hayden et al., 2017), who reported a temporal transition between the high- and low- $[\text{Mg}/\text{Fe}]$ populations due to two different star formation epochs. Furthermore, we identified the presence of the metal-poor low- $[\text{Mg}/\text{Fe}]$ stellar population in the outer regions of the Galactic disc (up to $R_g \sim 11$ kpc) around 10-12 Gyr ago. These stars look significantly more metal-poor ($[\text{M}/\text{H}] \lesssim -0.4$ dex) with respect to the coexisting stellar population in the inner parts of the disc. For the next 10 Gyr of evolution up to the present-time, we do not observe significant differences in the chemical enrichment of the inner and outer regions, both presenting similar slopes with respect to the stellar age.

We have evaluated our results considering the above mentioned works that test dominant internal evolution processes. First, regarding radial migration, our estimates in Sect. 7.1.3 suggest an important efficiency of the churning process, although the actual amplitude of the induced radial changes remains uncertain. Second, the outer origin of the metal-poor thin disc stars by an inflow of gas from the outskirts of the disc (Haywood et al., 2013, 2019) could be challenged by the similar continuous behaviour of the chemical tracks with radius, not showing enrichment discontinuities between the internal and the external regions. Indeed, as mentioned above, after the appearance of low- $[\text{Mg}/\text{Fe}]$ sequence around 10-12 Gyr ago, our results show similar chemical evolution trends ($[\text{Mg}/\text{Fe}]$ vs. age, and AMR) for the inner and the outer Galactic disc. They

describe well-defined separated patterns, where the measured metallicity is always higher in the inner regions at any age, describing a negative radial gradient. The observed behaviour may indicate that the stellar Galactic disc has likely followed the same chemical evolution path at different radius, without any apparent radial discontinuity. This does not preclude a separate evolution of the external disc before this secondary phase, 10-12 Gyr ago, but it would imply a change in the radial dependencies of the chemical evolution that needs to be explained. Further analysis with a larger disc stellar sample, beyond the solar vicinity region, needs to be done to draw more robust conclusions.

Mass accretion

Recent analysis based on *Gaia* DR2 data have revealed that the Galaxy is perturbed from equilibrium, finding evidence that the Galactic disc can be strongly perturbed by external interactions with satellite galaxies (Antoja et al., 2018, Laporte et al., 2019, Gaia Collaboration et al., 2020, latter work with current EDR3 data), affecting its dynamics and star formation history. In line with this findings, Helmi et al. (2018) and Belokurov et al. (2018) found clear signatures of a major accretion event by a massive satellite approximately 10 Gyr ago, so-called *Gaia*-Enceladus/Sausage, that seems to be considered as a key piece of the puzzle. In this context, models invoking a steady Galaxy's star formation history seem to neglect a very important ingredient of Milky Way history: mass accretion events.

A variety of disc evolution scenarios allows an infall of mass from the Milky Way environment. This includes chemical evolution models predicting infall of gas in long timescales (Chiappini et al., 1997, Spitoni et al., 2020), and cosmological Λ CDM simulations (Buck, 2020, Agertz et al., 2020) describing mass accretion through mergers of satellites and gas. In these models, the disc formation goes through two separated star formation epochs, driven by two main gas accretion episodes of extragalactic pristine gas triggering two different chemical evolution pathways (e.g. Chiappini et al., 1997, Grisoni et al., 2017, 2018, Noguchi, 2018, Spitoni et al., 2019, Montalbán et al., 2020, Buck, 2020, Palla et al., 2020).

Recent cosmological hydrodynamical simulations developed by Buck (2020) reproduce the bimodal sequences in the $[\text{Fe}/\text{H}]$ vs. $[\alpha/\text{Fe}]$ plane as a consequence of a gas-rich merger during the Galaxy's evolution. In agreement with our results, their models recreate a formation scenario where the high- α sequence evolves first in the early galaxy, pre-enriching the ISM to high metallicities before the appearance of the low- α sequence. The second low- α sequence is formed after the gas-rich merger, that provides metal-poor gas, diluting the ISM metallicity. In all simulations, they observed an old (younger), more radially concentrated (extended) high (low)- α disc, compatible with our results. Additionally, the recent work by Agertz et al. (2020), using cosmological zoom-in simulations of a Milky Way-mass disc galaxy, found a similar connection between a last major merger at $z \sim 1.5$ and the formation of an outer, metal-poor, low- α gas disc around the inner, in-situ metal-rich galaxy containing the old high- α stars.

There is an apparent overlap in time and metallicity between the reported formation of the outer metal-poor low- $[\text{Mg}/\text{Fe}]$ disc in our results and the signature of a major merger by a massive satellite found in the literature (Helmi et al., 2018, Belokurov et al., 2018, Myeong et al., 2018, Di Matteo et al., 2019b, Gallart et al., 2019, Fernández-Alvar et al., 2019, Belokurov et al., 2020, Feuillet et al., 2020, Naidu et al., 2020, Kordopatis et al., 2020). Therefore, our results support the arrival of a pristine gas-rich merger, after the formation of the pre-existing old high- $[\text{Mg}/\text{Fe}]$ population, that may have been diluted at different Galactic radii and lead to the formation of the second $[\text{Mg}/\text{Fe}]$ sequence on longer timescales. In other words, we find that the Galaxy could have already formed a significant population of thick disc stars before the infall of the satellite galaxy *Gaia*-Enceladus/Sausage (Montalbán et al., 2020), which could have triggered

the formation of the thin disc sequence more than 10 Gyr ago. However, this suggestion should be proven by comparing with chemical evolution models. For instance, the recent work by [Palla et al. \(2020\)](#), following a comparison between two-infall models and APOGEE data, discuss several cases where the thick and the thin disc are formed by enriched infall episodes including the chemical composition of *Gaia*-Enceladus/Sausage, finding that this satellite merger can have only contributed to the formation of the thick disc.

From our observational interpretation, a pre-existing old high-[Mg/Fe] population set the initial chemical conditions in the inner regions ($R_g < 8.5$ kpc). Since a higher surface density towards the Galactic centre is expected already at early epochs, the pristine accreted gas from *Gaia*-Enceladus/Sausage could have been diluted with a progressively increasing amount of in-situ enriched ISM gas towards the disc inner regions. Beyond the limiting radius of the more compact early disc, the infalling gas could have triggered the formation of stars with a chemical composition equal to the accreted one. This scenario would be consistent with the observed chemical similarities between the more metal-rich *Gaia*-Enceladus/Sausage stars and the metal-poor thin disc population, which are located in neighbouring regions of the [Mg/Fe] vs. [M/H] plane (see e.g. [Helmi et al., 2018](#), [Myeong et al., 2019](#), [Feuillet et al., 2020](#)). In addition, this scenario would reproduce the observed chemical radial gradients and the similar observed evolution with age in the inner and outer regions.

Radial mixing of stars or gas

The interpretation of the abundance gradient evolution with time might be misleading if an undetermined fraction of stars were actually born far from their present location ([Magrini et al., 2009](#)). Radial stellar migration can decouple the observed evolution of stellar chemical gradients from that of the ISM ones ([Roškar et al., 2008](#), [Pilkington et al., 2012](#), [Schönrich & McMillan, 2017](#)).

To account for this uncertainty, our analysis of Sect. 7.1.3 has considered the impact of different zero-points and metallicity gradients in the estimates of stellar migration via churning. All the considered radial distributions imply a clear presence of churned stars in the solar neighbourhood, even considering a slightly super-solar metallicity for the present day abundance (e.g. [Genovali et al., 2014](#)). Nevertheless, an important uncertainty remains in the amplitude of the induced radial changes. Indeed, some of the explored scenarios in Figures 7.5, 7.6 and 7.7 imply R_g variations smaller than 1-2 kpc through the entire disc evolution history. We can therefore not rule out the possibility that the observed evolution of stellar radial gradients with age is a good first approximation of the actual ISM time evolution. The possibility, from the dynamical point of view, of an intense radial migration inducing only small R_g changes on the stellar distribution is out of the scope of the present paper. A similar analysis by [Feltzing et al. \(2020\)](#) also shows an effective radial migration where some fraction of stars have not moved radially since they formed. It is also worth noting that its effect on the $[\alpha/\text{Fe}]$ versus [M/H] plane deserves further investigation.

Finally, regarding radial gas flows could occur in a scenario invoking gas accretion to explain the low- α sequence formation. It is indeed physically plausible that the infalling gas could have had lower angular momentum than the circular motions in the disc, inducing a radial gas inflow towards the inner parts ([Spitoni & Matteucci, 2011](#), [Schönrich & McMillan, 2017](#)). This would contribute to the dilution of the pre-enriched ISM abundance, shaping the radial gradient 10-12 Gyrs ago.

Chemical enrichment efficiency and star formation rate

At early times ($10 \leq \tau < 14$ Gyr), the observed high-[Mg/Fe] population in our analysis presents a steep age-metallicity correlation, showing an active chemical enrichment, pre-enriching the ISM up to the metal-rich regime before the second low-[Mg/Fe] sequence started to form. These observations are consistent with chemical evolution models predicting an early and fast thick disc formation from a massive gaseous disc, mainly supported by turbulence, with a strong star formation rate (SFR) and well-mixed ISM, likely triggered by numerous mergers and accretion events (Haywood et al., 2013, Snaith et al., 2014, Nidever et al., 2014) or due to the rapid collapse of the halo (e.g. Boissier & Prantzos, 1999, Pilkington et al., 2012, Kordopatis et al., 2017).

In the last 10 Gyrs, our analysis shows a flattening with time of the chemical enrichment (c.f. Fig. 7.14), with a similar slope for the inner and outer regions. This suggests a lower star formation rate with no major radial dependencies, in the absence of an efficient radial migration. If a radial dependent SFR was at play, with an increasing SFR with decreasing radius (as expected if the gas density decreases outwards), the radial migration should compensate its effects to mimic a similar chemical enrichment with age at all radii. Indeed, as the stellar density is higher at the inner galaxy, there are more stars migrating outwards than inwards. Therefore, in the presence of active radial migration a radial dependent SFR is compatible with our observations. In this framework, the evolution of radial gradients with time will be also affected, inducing a progressive flattening.

7.4 Summary

We carried out a detailed chemodynamic analysis over a sample of 494 MSTO stars in the solar neighbourhood ($d < 300$ pc with respect to the Sun), observed at high spectral resolution ($R = 115000$) and parametrised within the context of the AMBRE Project. From this sample, we selected 366 stars for which we have estimated accurate ages, kinematical and dynamical parameters using the accurate astrometric measurements from the *Gaia* DR2 catalogue.

For the analysis, we used the derived [Mg/Fe] abundances in Chapter 5, where we showed a significant improvement in the abundance precision for the metal-rich population ($[M/H] > 0$ dex), observing a decreasing trend in the [Mg/Fe] abundance even at supersolar metallicities. In contrast, previous observational studies of the solar neighbourhood observed a flattened trend. Therefore, we have studied their impact on the reported chemodynamical features (radial chemical abundance gradients, role of radial migration/churning, age-abundance relations), and hence on the interpretation of the Galactic disc evolution.

First of all, we explored the present-day chemical abundance distribution ($[Mg/Fe]$, $[M/H]$) in the thin disc, at different Galactic radii and ages, after applying a chemical definition to avoid possible thick disc contamination:

- **Radial chemical trends:** we adopted the guiding centre radius (R_g) as an estimate of the current stellar Galactocentric radius (R_{GC}) to derive the radial abundance gradients. We find a consistent negative gradient of -0.097 ± 0.033 dex kpc^{-1} for $[M/H]$ and a slightly positive gradient of $+0.025 \pm 0.009$ dex kpc^{-1} for the [Mg/Fe] abundance. The observed steeper [Mg/Fe] gradient, compared to literature values, is a major consequence of the improvement of the metal-rich spectral analysis shown in Chapter 5. In the framework of the time-delay model, this result for the thin disc could be explained by an inside-out formation with a steeper decrease of the star formation efficiency with radius, enhancing the chemical enrichment in the inner regions relative to outer ones.

- **Stellar migration:** under the assumptions of a set of ISM gradients, we estimated the birth radius (R_{birth}) of the stars in our sample, given their $[M/H]$, and selected the super-metal-rich stars (SMR; $[M/H] \gtrsim +0.1$ dex) whose presence in the solar neighbourhood cannot be explained by blurring alone. These stars comprise the 17% of the whole sample (8 % when we constraint to $[M/H] > +0.25$), and cover a wide range of ages from ~ 4 to 12 Gyr.

In particular, we analysed the possible age trends in the radial changes ($\Delta R_g = R_g - R_{\text{birth}}$) associated to stellar migration via churning. First, we fixed the zero-point at the present-day value ($\text{ISM}_{[M/H]}(R_\odot) = 0.0$ dex), observing a slightly negative trend of ΔR_g with age, becoming steeper as the assumed ISM gradient flattens. Secondly, we applied an approach to estimate a more appropriate $\text{ISM}_{[M/H]}(R_\odot)$ value, that is expected to be chemically enriched with time (Hou et al., 2000, Schönrich & McMillan, 2017). For each analysed ISM abundance gradient, we obtained significantly higher ΔR_g values for old SMR stars up to inverting to a positive trend with stellar age. Finally, we also considered a time evolution of the ISM gradient by applying a simple linear toy model, based on an initial metallicity gradient flattening with time (Minchev et al., 2018). The resulting slightly negative trend with stellar age is similar to the observed trend in our first simple approach.

Our analysis showed that regardless the chosen ISM model, there is a large variety of ages and ΔR_g values for the selected churned stars. This trend points that different stars in the Galactic disc could have radially migrated during their lives. The radial migration efficiency is, however, very dependent on the adopted ISM gradient (Feltzing et al., 2020).

Secondly, in order to shed light into the history of the Milky Way disc, we explored the time evolution of the observed chemodynamical relations. After a previous exploration of the thin-thick disc distinction at high metallicities ($[M/H] > -0.3$ dex), we concluded that given the similarity between both subsamples, we cannot ensure that these high metallicity stars are truly different stellar populations. As a consequence, we considered the Galactic disc as a whole for the evolution analysis:

- **[Mg/Fe] abundance as a chemical clock:** we found a significant spread of stellar ages at any given $[Mg/Fe]$ value, particularly for $[Mg/Fe]$ higher than -0.2 dex, while for more metal-poor stars we find a linear correlation of $[Mg/Fe]$ with age. Furthermore, for stars younger than about 11 Gyr, we observe a large dispersion in the $[Mg/Fe]$ abundance ($\sigma_{[Mg/Fe]} \sim 0.1$ dex at a given age), which is directly correlated with the stellar metallicity. For $[M/H] \geq -0.2$ dex, we find stars with ages from ~ 3 up to 12 Gyr old, describing an almost flat trend in the $[Mg/Fe]$ -age relation without significant changes of slope among the different metallicity bins.
- **Chemical discontinuity in the $[Mg/Fe]$ vs. $[M/H]$ plane:** we studied the chemical evolution of the $[Mg/Fe]$ abundance relative to $[M/H]$, at different age intervals and Galactic disc locations: inner ($R_g \leq 7.5$ kpc), and outer ($R_g > 7.5$ kpc). At early epochs (10-14 Gyr), we observed a rapid chemical enrichment, with a sharp increase in metallicity and decrease in $[Mg/Fe]$ to solar abundance values, without showing differences between the inner and outer regions, pointing towards a chemically well-mixed population (Haywood et al., 2013, Nidever et al., 2014, Kordopatis et al., 2017).

Interestingly, around 10-12 Gyr ago, a second sequence appears in the outer regions of the Galactic disc, populating the metal-poor low- $[Mg/Fe]$ tail. The averaged R_g of this second sequence is significantly larger than the Galactic disc extension at that epoch ($R_g < 8.5$ kpc), reaching the outer parts up to $R_g \sim 11$ kpc. Furthermore, these stars are more metal-poor with respect to the coexisting stellar population in the inner parts,

and show lower $[\text{Mg}/\text{Fe}]$ abundances than the prior external disc, although presenting a similar metallicity distribution. This implies a chemical discontinuity in the disc, also observed in the $[\text{Mg}/\text{Fe}]$ and $[\text{M}/\text{H}]$ trends with age, suggesting that the new sequence might have followed a different chemical evolution pathway than the previous formed component (Grisoni et al., 2017, Noguchi, 2018, Spitoni et al., 2019, Buck, 2020). It is worth noting that the present result does not support a spatial discontinuity of the chemical evolution in Galactic radius.

From that epoch, 10 Gyr ago, the Galactic disc seems to have experienced a slower and continuous chemical evolution. The similar slopes of the $[\text{Mg}/\text{Fe}]$ and $[\text{M}/\text{H}]$ trends with age point to a similar chemical evolution at all radii.

Our analysis sheds new light into the disc evolution process from the perspective of the present-day solar neighbourhood population. This has the advantage of a high precision view, but is limited by the absence of unbiased constraints at different galactic radii.

In this framework, our results favour the rapid formation of an early disc, settled in the inner regions ($R < 8.5$ kpc), followed by the accretion of external-metal poor gas, possibly related to a major accretion event such as the Gaia-Enceladus/Sausage one 10-12 Gyrs ago (Helmi et al., 2018, Belokurov et al., 2018, Di Matteo et al., 2019b, Gallart et al., 2019). This would dilute the pre-enriched ISM abundance with a radial dependence, induced by the surface density distribution of the early disc and the possible radial inflows of gas. Beyond the limiting radius of the more compact early disc, the infalling gas could have triggered the formation of stars with a chemical composition similar to the accreted one, as supported by the chemical similarities between the more metal-rich Gaia-Enceladus/Sausage stars and the metal-poor thin disc population (Mackereth et al., 2019, Feuillet et al., 2020).

In addition, our analysis supports the fact that radial migration via churning was at play in the last 10 Gyrs of disc evolution (Kordopatis et al., 2015a), although the actual amplitude of the induced R_g changes remains largely uncertain and could be as low as 1-2 kpc.

Finally, our data support a very fast chemical enrichment at early epochs slowing down about 10 Gyr ago. The observed similar slopes in the chemical enrichment for the inner and outer regions suggest an equilibrium between the radial SFR dependences and the radial migration efficiency.

Chapter 8

Conclusions and future works

Contents

8.1 High-precision estimation of chemical abundances	98
8.2 From surveys to models: Galactic disc formation scenarios	100
8.3 Future works: perspectives in Galactic archaeology	101

The formation and evolution of disc galaxies are a matter of debate and a central theme in astrophysics. In the framework of the Λ CDM (Λ Cold Dark Matter) model, the galaxies are formed following an hierarchical evolution model, by accretion of smaller systems that can be considered as building blocks, providing gas to the formation and evolution of the disc. A detailed examination of our Galaxy, the Milky Way, offers a unique opportunity to add constraints on the early stages of its formation, back to high redshifts and long look-back times.

Galactic archaeology demands high-quality data to detect stellar populations that differ in their abundances/kinematics/dynamics from each other. In the recent years, the combination of several on-going (e.g. Gaia-ESO, RAVE) and forthcoming (e.g. WEAVE, 4MOST) large ground-based spectroscopic surveys (with different stellar and spectral domains, targets, and spectral resolutions), with the ESA *Gaia* space mission, are opening a new era for Galactic archaeology, providing a full dimensional map of the Milky Way (distances, two-coordinate positions and proper motions, velocities, chemical abundances, and stellar ages) that aims at unveiling its history in unprecedented detail.

In particular, the abundance of α -elements, relative to iron ($[\alpha/\text{Fe}]$), is an important fossil signature in Galactic archaeology to trace the chemical evolution of disc stellar populations. The thick disc component is often reported to be $[\alpha/\text{Fe}]$ -enhanced relative to the thin disc, describing a chemical bimodality in the ($[\alpha/\text{Fe}]$, $[\text{M}/\text{H}]$) plane, and suggesting distinct chemical evolution histories. Despite the numerous analysis already published in the literature at that time, most studies obtained discrepant $[\alpha/\text{Fe}]$ estimates with respect to chemical evolution models in the metal-rich regime. This has important consequences on several crucial constraints like radial chemical gradients or stellar radial migration.

As a consequence, high-precision and accurate chemical abundances of large samples of stars are crucial to constrain chemical evolution models and improve our understanding of the present-day observed chemodynamical trends in the disc. The main issues concerning the determination of high-precision abundances are characterised by the need for both high signal-to-noise ratio (S/N) and spectral resolution, and predominantly by the definition of continuum to normalise the observed spectral data. The latter issue can be responsible for the largest fraction of the uncertainty

in the abundance estimations, which is still complex for cool metal-rich stars due to the high presence of blended and molecular lines.

An in-depth state-of-the-art knowledge in the Galactic disc formation and evolution scenarios has been described and explored throughout this manuscript, addressing the scientific questions described above. Specifically, the goals of the project have been:

1. Optimisation of the spectral continuum placement for different stellar types and 9 Mg lines separately. Reanalysis of the ESO:HARPS archived spectra (R=115 000), providing a high precision [Mg/Fe] abundance dataset in the solar neighbourhood (Santos-Peral et al., 2020).
2. Take advantage of the accurate *Gaia* DR2 astrometric data to determine accurate stellar ages and orbital parameters, and build a time evolving chemodynamical picture with the newly derived [Mg/Fe] abundances. Exploration of the observed chemodynamical trends (radial chemical abundance gradients, role of radial migration/churning, age-abundance relations), and to conclude on the possible scenarios of the Galactic disc formation and evolution (Santos-Peral, 2021, submitted).

8.1 High-precision estimation of chemical abundances

In the context of this thesis, I have optimised the spectral normalisation procedure and understood its impact on the derived chemical abundances, that I measured using the GAUGUIN automated abundance estimation algorithm. The GAUGUIN procedure is currently being used in the framework of the *Gaia*/DPAC for the chemical abundances derivation from *Gaia*/RVS spectra (Radial Velocity Spectrometer, Recio-Blanco et al., 2016), and it has also been implemented for several international ground-based surveys as RAVE, the *Gaia*-ESO survey, WEAVE and MOONS.

In particular, I explored the possible sources of uncertainties concerning the determination of high-precision [Mg/Fe] abundances. Indeed, magnesium is often used as an α -elements tracer since it has a high number of measurable spectral lines in optical spectra and, due to the strength of some lines, its abundance can be measured even for distant metal-poor stars. For these reasons, a well-defined scale of Mg abundances is very important for stellar spectroscopy as well as Galactic research.

First, I implemented tests with theoretical spectra to evaluate the internal error, building statistically significant sets by convolving to six different spectral resolutions (from $R \sim 2000$ to $R \sim 110000$), artificially adding five different random Gaussian noise (signal-to-noise: $S/N = 10, 25, 50, 75,$ and 100), and defining four different stellar types (cool dwarfs, turn-off, solar-type, and red-clump stars). We observed that significant dependences of the uncertainty with the stellar type appear if the spectral resolution is not high enough, even at high S/N values. Increasing the S/N does not always compensate a resolution loss.

Secondly, I performed an in-depth analysis of nine magnesium lines in order to test their reliability at different metallicity regimes. For a solar-type star, the selected lines could be classified in two categories: non-saturated (4730.04, 5711.09, and triplet: 6318.7, 6319.24, 6319.49 Å) and strong saturated lines (Mg Ib triplet: 5167.3, 5172.7 & 5183.6, and the line 5528.4 Å). The selected lines have been widely used in the literature to determine both [Mg/Fe] and [α /Fe] abundances.

In the framework of the AMBRE Project (de Laverny et al., 2013), in which observed spectra from ESO spectrographs (FEROS, HARPS and UVES) are automatically and homogeneously parametrised (T_{eff} , $\log g$, [M/H], [α /Fe], and v_{rad}), I analysed 87522 high-resolution spectra

($R \sim 115000$) of 2210 solar neighbourhood stars from the AMBRE:HARPS database, and selected the 1172 best parametrised stars with more than four observed spectra (> 4 repeats).

Optimisation of the continuum normalisation procedure

Different local continuum intervals were defined around each Mg I spectral line to explore their impact in the abundance analysis. By a spectral visualisation for different stellar types, the selection of the normalisation windows was adjusted to avoid the presence of strong absorption lines in the limits of the spanned region and chosen to have enough continuum points at the ends of the intervals.

We found that the normalisation procedure has an important impact on the derived abundances, with a strong dependence on the stellar parameters (T_{eff} , $\log g$, $[M/H]$) and the intensity of the spectral line, which have a drastic influence in the optimal width of the normalisation interval. As a consequence, if a constant wavelength interval is chosen, different biases appear depending on the stellar parameters, especially in the metal-rich regime ($[M/H] \geq 0$ dex), blurring the chemical features of the studied population.

For non-saturated lines, the optimal wavelength domain for the local continuum placement should be evaluated using a goodness-of-fit criterion, allowing mask-size dependence with the spectral type. For strong saturated lines, applying a narrow normalisation window drastically reduces the parameter-dependent biases of the abundance estimate, increasing the line-to-line abundance precision.

The final optimised methodology does not depend on the stellar type and shows a significant improvement in the $[Mg/Fe]$ abundance precision (with an overall internal error around 0.01 dex), in particular for the metal-rich population ($[M/H] > 0$ dex). We observe a decreasing trend in the $[Mg/Fe]$ abundance even at supersolar metallicities, reaching negative values, partly solving the apparent discrepancies between the common observed flat trend in the metal-rich disc by observational studies (e.g. [Adibekyan et al., 2012](#), [Hayden et al., 2017](#)), and the steeper slope predicted by chemical evolution models of the Galaxy (e.g. [Chiappini et al., 1997](#), [Romano et al., 2010](#)).

Application to spectroscopic stellar surveys

In particular, the continuum normalisation is not fully optimised for different stellar types in large spectroscopic stellar surveys. Most of the spectral analysis pipelines for determining chemical abundances and stellar atmospheric parameters carry out the same normalisation procedure for all stellar types, assuming a constant normalisation window to find continuum information around the analysed line. With our analysis, we encourage to explore the optimisation of the continuum intervals in the preliminary and preparatory stages (in accordance with the stellar targets, spectral resolution, etc.). We suggest the application of narrow normalisation windows in order to improve the abundance estimation precision and avoid potential parameter-dependent biases.

The optimisation of the normalisation procedure in large spectroscopic stellar surveys would provide a significant improvement to the analysis of the chemodynamical trends of the different Galactic populations. The improvement in chemical abundance precision is strongly required in the present era of precise kinematical and dynamical data driven by the *Gaia* space mission.

The full *Gaia* DR3 catalogue is planned for the first half of 2022, providing BP/RP and RVS spectra for sources with astrophysical parameters. The RVS allows the derivation of radial velocities and stellar atmospheric parameters, and it will provide some individual chemical abundances (Mg, Si, S, Ca, Ti, Cr, Fe, Ni), taking into account the carried out developments during this thesis, especially concerning the normalisation issues.

8.2 From surveys to models: Galactic disc formation scenarios

Different formation and evolution scenarios for the Milky Way disc have been proposed in order to interpret/reproduce the present-day observed chemodynamical trends in the disc. In particular, the chemical bimodality identified in the ($[\alpha/\text{Fe}]$, $[\text{M}/\text{H}]$) plane as the thin (low- α) and thick (high- α) disc components, and the observed radial abundance gradients, encode information on how the disc has evolved.

In order to constraint the Galactic disc evolution with the new $[\text{Mg}/\text{Fe}]$ abundance measurements, we analysed a subsample of the AMBRE:HARPS spectral dataset that corresponds to 494 MSTO stars, selected and used in [Hayden et al. \(2017\)](#), for which we estimated accurate ages, kinematical and dynamical parameters. We used astrometric and photometric data from the *Gaia* DR2 catalogue, along with distances estimated from parallaxes using a bayesian approach. For the analysis, we adopted the guiding centre radius (R_g) as an estimate of the current stellar Galactocentric radius (R_{GC}). In addition, we estimated reliable ages using an isochrone fitting method ([Kordopatis et al., 2016](#)). We assembled all of the elements above to a coherent interpretation of the time-dependent chemodynamical relations in the solar neighbourhood ($d < 300$ pc from the Sun).

We find a consistent negative gradient of -0.097 ± 0.033 dex kpc^{-1} for $[\text{M}/\text{H}]$ and a positive gradient of $+0.025 \pm 0.009$ dex kpc^{-1} for the $[\text{Mg}/\text{Fe}]$ abundance. The observed steeper $[\text{Mg}/\text{Fe}]$ gradient, compared to literature values, is a major consequence of the achieved improvement of the metal-rich spectral analysis.

We also report the presence of radially migrated/churned stars for a wide range of stellar ages (from ~ 4 to 12 Gyr). We analysed the amplitude of the inferred change in orbital guiding radii ($\Delta R_g = R_g - R_{\text{birth}}$) for a selection of super-metal-rich stars (SMR; $[\text{M}/\text{H}] \gtrsim +0.1$ dex) whose presence in the solar neighbourhood cannot be explained by blurring alone. We estimated the birth radius under the assumptions of a set of ISM gradients, and applying different approaches regarding the abundance at solar radius ($\text{ISM}_{[\text{M}/\text{H}]}(R_{\odot}, \tau)$) and the time evolution of the ISM gradient. We observe a slightly negative trend of ΔR_g with age, although the actual amplitude of the induced R_g changes remains largely uncertain and could be as low as 1-2 kpc, being very dependent on the adopted ISM model.

In addition, we find a significant spread of stellar ages at any given $[\text{Mg}/\text{Fe}]$ value, particularly for $[\text{Mg}/\text{Fe}]$ higher than -0.2 dex, while for more metal-poor stars we find a linear correlation of $[\text{Mg}/\text{Fe}]$ with age. Furthermore, for stars younger than about 11 Gyr, we observe a large dispersion in the $[\text{Mg}/\text{Fe}]$ abundance ($\sigma_{[\text{Mg}/\text{Fe}]} \sim 0.1$ dex at a given age), which it is directly correlated with the stellar metallicity. For $[\text{M}/\text{H}] \geq -0.2$ dex, we find stars with ages from ~ 3 up to 12 Gyr old, describing an almost flat trend in the $[\text{Mg}/\text{Fe}]$ -age relation without significant changes of slope among different metallicity bins. This trend could only be explained by chemical evolution models if an important co-existence of different stellar populations in the solar neighbourhood is assumed, with different enrichment histories and birth origins in the

Galactic disc (as previously suggested by several studies, e.g. [Sellwood & Binney, 2002](#), [Nordström et al., 2004](#), [Kordopatis et al., 2015a](#), [Wojno et al., 2016](#)).

Our results present a clear [Mg/Fe] chemical distinction between both Galactic disc sequences in the metallicity regime $[M/H] \leq -0.3$ dex. The oldest observed population ($\tau > 12$ Gyr) constitutes the majority of the more metal-poor high-[Mg/Fe] stars, in agreement with previous observational works on the local disc (e.g. [Fuhrmann, 2011](#), [Haywood et al., 2013](#), [Hayden et al., 2017](#)), who reported a temporal transition between the high- and low-[Mg/Fe] populations due to two different star formation epochs. At early epochs (10-14 Gyr), we observed a rapid chemical enrichment, with a sharp increase in metallicity and decrease in [Mg/Fe] to solar abundance values, without showing differences between the inner and outer regions, pointing towards a chemically homogeneous population ([Haywood et al., 2013](#), [Nidever et al., 2014](#), [Kordopatis et al., 2017](#)).

Moreover, we identified the presence of the low-[Mg/Fe] stellar population in the outer regions of the Galactic disc (up to $R_g \sim 11$ kpc) around 10-12 Gyr ago. These stars look significantly more metal-poor ($[M/H] \lesssim -0.4$ dex) with respect to the coexisting stellar population in the inner parts of the disc, and show lower [Mg/Fe] abundances than the prior external disc, although presenting a similar metallicity distribution. This implies a chemical discontinuity in the disc.

For the next 10 Gyr of evolution up to the present-time, we do not observe significant differences in the chemical enrichment of the inner and outer regions, presenting similar [Mg/Fe] and [M/H] trends with age. This may suggest an equilibrium between the radial SFR dependences and the radial migration efficiency.

In this framework, our results favour the rapid formation of an early disc, settled in the inner regions ($R < 8.5$ kpc), followed by the accretion of external-metal poor gas, possibly related to a major accretion event such as the Gaia-Enceladus/Sausage one 10-12 Gyrs ago ([Helmi et al., 2018](#), [Belokurov et al., 2018](#), [Di Matteo et al., 2019b](#), [Gallart et al., 2019](#)). This would dilute the pre-enriched ISM abundance with a radial dependence, induced by the surface density distribution of the early disc and the possible radial inflows of gas. Beyond the limiting radius of the more compact early disc, the infalling gas could have triggered the formation of stars with a chemical composition similar to the accreted one, as supported by the chemical similarities between the more metal-rich Gaia-Enceladus/Sausage stars and the metal-poor thin disc population ([Mackereth et al., 2019](#), [Feillet et al., 2020](#)).

8.3 Future works: perspectives in Galactic archaeology

Recent analysis using data from the second *Gaia* data release have revealed that the Milky Way is out of equilibrium, finding evidence that the Galactic disc can be strongly perturbed by internal (e.g. bar or spiral arms) and external (e.g. satellite galaxies or stellar systems) dynamical interactions ([Antoja et al., 2018](#), [Laporte et al., 2019](#)), which affect its dynamics, star formation history, morphology, structure, and chemical enrichment. Concretely, exploring the Galactic disc lies at the core of understanding the complex processes involved in the formation and evolution of the Milky Way (e.g. star formation at different Galactocentric distances and timescales, radial mixing, infall of gas).

Since the nominal *Gaia* mission got an indicative extension up to end of 2022 (with a possible additional extension up to 2025), and a complete final data release (*Gaia* DR4/DR5) will be released including all BP/RP/RVS spectra, the future perspectives of the accomplished work in this thesis need to be discussed looking towards these releases and the forthcoming large

spectroscopic surveys that will be the perfect complement, providing kinematics and chemical abundances from the ground: WEAVE (Dalton et al., 2012) and 4MOST (de Jong et al., 2016).

On a short-term basis, I plan to extend the optimised normalisation procedure to the ESO:UVES ($R \sim 47000$) and FEROS ($R = 48000$) spectra databases (within the AMBRE Project, making possible to extend our analysis beyond the solar neighbourhood and also develop a project centred on heavy element abundances (e.g. r-/s- process elements as Y or Eu) to test their use as chemical clocks or as signatures of accreted populations. In particular, I will try to perform a precise chemical characterisation of the Gaia-Enceladus population with the AMBRE catalogue. In addition, since this thesis work has been focused on local stellar samples in the solar neighbourhood, I would be really interested in combining AMBRE with extensive surveys, such as *Gaia*, WEAVE, or MOONS, in order to explore the chemical analysis farther away the solar vicinity. Moreover, a detailed comparison between our data and chemical evolution models results (e.g. Palla et al., 2020) will be performed in a future work, aiming at drawing more robust conclusions and interpretations of the Galactic disc formation scenario.

On a long-term basis, the extensive work carried out on spectral treatment analysis, together with their stellar parameter dependence and its implementation on different spectroscopic surveys and spectral resolutions in the near future (already considered in the on-going optimisation of the *Gaia* RVS pipeline, and over the UVES/FEROS catalogues), could contribute qualitatively to the improvement of the automatic chemical abundance analysis from the future WEAVE and 4MOST spectra (both offers two spectroscopic resolutions: low $R \sim 5000$, and high $R \sim 20000$).

The synergy between ground-based surveys and the *Gaia* Early Data Release 3 (*Gaia* EDR3, recently released on 3th December 2020) and the full *Gaia* DR3 (planned for the first half of 2022) opens an exciting window in the next years for further exploring the Galactic disc. High-precise and accurate abundance determination, with the help of a dynamical model and the ages of the stars, could shed new light in quantifying the stellar birth-places, their cluster membership, or identifying discrete substructures from the chemical abundance space.

In particular, an interesting area would be the detailed analysis of open stellar clusters (OCs) to deepen the knowledge in the dynamics and chemical evolution of the disc: rotation curve, orbits and spatial structure, or the use of precise derived abundances to detect signs of the existence of multiple stellar populations.

Furthermore, a deeper analysis on the kinematical and dynamical stellar signatures is missing in the results shown in this manuscript. For instance, the addition of a kinematical selection for thin and thick disc components, or further explorations could be performed concerning moving groups in the disc, stellar streams in the halo, or dynamical perturbation signatures towards the Galactic anticentre, in order to examine the impact of external interactions on the Galactic evolution.

A robust picture of the formation and evolution of the Milky Way, with a clear defined history of the chemodynamical processes experienced by the the different structures (halo/disc(s)/bulge), still needs to be built. On the one hand, the interconnection between Galactic halo and the disc is a current central debate, where recent works have found (i) stellar halo populations with ages and chemical abundances typical of disc's stars, probably heated from the thick disc (e.g. Di Matteo et al., 2019b), (ii) how accretion events could have significantly contributed to the growth of the disc 10 Gyr ago (e.g. Belokurov et al., 2018, 2020, Vincenzo et al., 2019, Montalbán et al., 2020, Buck, 2020), but also (iii) the most metal-poor stars ($[\text{Fe}/\text{H}] \leq -2.5$ dex) seem to be confined and formed in the disc (Sestito et al., 2020), challenging theoretical and cosmological models. On the other side, the interaction between the bulge and the formation of a bar with the disc evolution has also played an important role, driving radial migration of matter in the Galaxy. The observed peanut-shaped bulge and the surrounding inner thin disc shed light on the early times population in the disc galaxies (Di Matteo et al., 2019a, Matteucci et al., 2019). The

next ESO MOONS spectrograph will provide metallicities and chemical abundances for several millions stars from the more obscured regions of the Galactic bulge, following-up for the *Gaia* mission, in order to trace the assembly history the Milky Way.

Appendix A

Publications

Non-refereed:

1. **Precise magnesium abundances in the metal-rich disc**

P. Santos-Peral, A. Recio-Blanco, P. de Laverny & E. Fernández-Alvar

Published in *SF2A-2019: Proceedings of the Annual meeting of the French Society of Astronomy and Astrophysics* (pp. 151-152)

Refereed:

2. **The AMBRE Project: Spectrum normalisation influence on Mg abundances in the metal-rich Galactic disc**

P. Santos-Peral, A. Recio-Blanco, P. de Laverny, E. Fernández-Alvar & C. Ordenovic

Paper published in the journal *Astronomy & Astrophysics* (*A&A*, 639, A140)

3. **The AMBRE Project: Solar neighbourhood chemodynamical constraints on Galactic disc evolution**

P. Santos-Peral, A. Recio-Blanco, G. Kordopatis, E. Fernández-Alvar & P. de Laverny

Paper submitted in the journal *Astronomy & Astrophysics* (*A&A*)

4. **The AMBRE Project: Origin and evolution of sulphur in the Milky Way**

J. Perdigon, P. de Laverny, A. Recio-Blanco, E. Fernández-Alvar, P. Santos-Peral, G. Kordopatis, & M.A. Álvarez

Paper published in the journal *Astronomy & Astrophysics* (*A&A*, 647, A162)

Bibliography

- Abel, T., Bryan, G. L., & Norman, M. L. 2002, *Science*, 295, 93
- Adibekyan, V., Delgado-Mena, E., Figueira, P., et al. 2016, *A&A*, 591, A34
- Adibekyan, V. Z., Santos, N. C., Sousa, S. G., & Israelian, G. 2011, *A&A*, 535, L11
- Adibekyan, V. Z., Sousa, S. G., Santos, N. C., et al. 2012, *A&A*, 545, A32
- Adibekyan, V. Z., Figueira, P., Santos, N. C., et al. 2013, *A&A*, 554, A44
- Agertz, O., Renaud, F., Feltzing, S., et al. 2020, arXiv e-prints, arXiv:2006.06008
- Alexeeva, S., Ryabchikova, T., Mashonkina, L., & Hu, S. 2018, *ApJ*, 866, 153
- Allende-Prieto, C., & Apogee Team. 2015, in *American Astronomical Society Meeting Abstracts*, Vol. 225, *American Astronomical Society Meeting Abstracts #225*, 422.07
- Allende Prieto, C., Beers, T. C., Wilhelm, R., et al. 2006, *ApJ*, 636, 804
- Alvarez, R., & Plez, B. 1998, *A&A*, 330, 1109
- Amarsi, A. M. 2015, *MNRAS*, 452, 1612
- Amarsi, A. M., Lind, K., Asplund, M., Barklem, P. S., & Collet, R. 2016, *MNRAS*, 463, 1518
- Anders, F., Chiappini, C., Santiago, B. X., et al. 2014, *A&A*, 564, A115
- Antoja, T., Helmi, A., Romero-Gómez, M., et al. 2018, *Nature*, 561, 360
- Auvergne, M., Bodin, P., Boissard, L., et al. 2009, *A&A*, 506, 411
- Baganoff, F. K., Maeda, Y., Morris, M., et al. 2003, *ApJ*, 591, 891
- Bailer-Jones, C. A. L. 2000, *A&A*, 357, 197
- Bailer-Jones, C. A. L., Rybizki, J., Foesneau, M., Mantelet, G., & Andrae, R. 2018, *AJ*, 156, 58
- Barbuy, B., Chiappini, C., & Gerhard, O. 2018, *ARA&A*, 56, 223
- Barnes, S. A. 2007, *ApJ*, 669, 1167
- Belokurov, V., Erkal, D., Evans, N. W., Koposov, S. E., & Deason, A. J. 2018, *MNRAS*, 478, 611
- Belokurov, V., Sanders, J. L., Fattahi, A., et al. 2020, *MNRAS*, 494, 3880
- Bennett, C. L., Halpern, M., Hinshaw, G., et al. 2003, *ApJS*, 148, 1
- Bensby, T., & Feltzing, S. 2006, *MNRAS*, 367, 1181
- Bensby, T., Feltzing, S., & Lundström, I. 2003, *A&A*, 410, 527
- Bensby, T., Feltzing, S., Lundström, I., & Ilyin, I. 2005, *A&A*, 433, 185

- Bensby, T., Feltzing, S., & Oey, M. S. 2014, *A&A*, 562, A71
- Bensby, T., Yee, J. C., Feltzing, S., et al. 2013, *A&A*, 549, A147
- Bergemann, M., Collet, R., Schönrich, R., et al. 2017, *ApJ*, 847, 16
- Bergemann, M., Ruchti, G. R., Serenelli, A., et al. 2014, *A&A*, 565, A89
- Bijaoui, A., Recio-Blanco, A., de Laverny, P., & Ordenovic, C. 2012, *Statistical Methodology*, 9, 55
- Binney, J., Gerhard, O., & Spergel, D. 1997, *MNRAS*, 288, 365
- Binney, J., & Schönrich, R. 2018, *MNRAS*, 481, 1501
- Binney, J., & Tremaine, S. 2008, *Galactic Dynamics: Second Edition*
- Blanco-Cuaresma, S., Soubiran, C., Heiter, U., & Jofré, P. 2014, *A&A*, 569, A111
- Bland-Hawthorn, J., Freeman, K., & Matteucci, F. 2014, *The Origin of the Galaxy and Local Group*, Saas-Fee Advanced Course, doi:10.1007/978-3-642-41720-7
- Bland-Hawthorn, J., & Gerhard, O. 2016, *ARA&A*, 54, 529
- Bland-Hawthorn, J., Sharma, S., Tepper-Garcia, T., et al. 2019, *MNRAS*, 486, 1167
- Boeche, C., & Grebel, E. K. 2016, *A&A*, 587, A2
- Boeche, C., Siebert, A., Piffl, T., et al. 2013a, *A&A*, 559, A59
- Boeche, C., Chiappini, C., Minchev, I., et al. 2013b, *A&A*, 553, A19
- Boissier, S., & Prantzos, N. 1999, *MNRAS*, 307, 857
- Bovy, J. 2015, *ApJS*, 216, 29
- Bovy, J., Rix, H.-W., Schlafly, E. F., et al. 2016, *ApJ*, 823, 30
- Bressan, A., Marigo, P., Girardi, L., et al. 2012, *MNRAS*, 427, 127
- Brewer, J. M., Fischer, D. A., Valenti, J. A., & Piskunov, N. 2016, *ApJS*, 225, 32
- Buck, T. 2020, *MNRAS*, 491, 5435
- Buder, S., Lind, K., Ness, M. K., et al. 2019, *A&A*, 624, A19
- Bullock, J. S., Stewart, K. R., Kaplinghat, M., Tollerud, E. J., & Wolf, J. 2010, *ApJ*, 717, 1043
- Burbidge, E. M., Burbidge, G. R., Fowler, W. A., & Hoyle, F. 1957, *Reviews of Modern Physics*, 29, 547
- Carlberg, R. G., Dawson, P. C., Hsu, T., & Vandenberg, D. A. 1985, *ApJ*, 294, 674
- Carollo, D., Beers, T. C., Lee, Y. S., et al. 2007, *Nature*, 450, 1020
- Carrera, R., Bragaglia, A., Cantat-Gaudin, T., et al. 2019, *A&A*, 623, A80
- Cheng, J. Y., Rockosi, C. M., Morrison, H. L., et al. 2012, *ApJ*, 746, 149
- Chiappini, C., Matteucci, F., & Gratton, R. 1997, *ApJ*, 477, 765
- Chiappini, C., Matteucci, F., & Romano, D. 2001, *ApJ*, 554, 1044
- Chiappini, C., Anders, F., Rodrigues, T. S., et al. 2015, *A&A*, 576, L12
- Cirasuolo, M., Afonso, J., Carollo, M., et al. 2014, in *Society of Photo-Optical Instrumentation Engineers (SPIE) Conference Series*, Vol. 9147, *Ground-based and Airborne Instrumentation for Astronomy V*, ed. S. K. Ramsay, I. S. McLean, & H. Takami, 91470N

- Ciucă, I., Kawata, D., Miglio, A., Davies, G. R., & Grand, R. J. J. 2021, MNRAS, arXiv:2003.03316
- Conroy, C., Naidu, R. P., Zaritsky, D., et al. 2019, ApJ, 887, 237
- Cropper, M., Katz, D., Sartoretti, P., et al. 2018, A&A, 616, A5
- Dalton, G., Trager, S. C., Abrams, D. C., et al. 2012, in Society of Photo-Optical Instrumentation Engineers (SPIE) Conference Series, Vol. 8446, Ground-based and Airborne Instrumentation for Astronomy IV, ed. I. S. McLean, S. K. Ramsay, & H. Takami, 84460P
- Darling, K., & Widrow, L. M. 2019, MNRAS, 484, 1050
- de Jong, R. S., Barden, S. C., Bellido-Tirado, O., et al. 2016, in Society of Photo-Optical Instrumentation Engineers (SPIE) Conference Series, Vol. 9908, Ground-based and Airborne Instrumentation for Astronomy VI, ed. C. J. Evans, L. Simard, & H. Takami, 99081O
- de Laverny, P., Recio-Blanco, A., Worley, C. C., et al. 2013, The Messenger, 153, 18
- de Laverny, P., Recio-Blanco, A., Worley, C. C., & Plez, B. 2012, A&A, 544, A126
- De Pascale, M., Worley, C. C., de Laverny, P., et al. 2014, A&A, 570, A68
- De Silva, G. M., Freeman, K. C., Bland-Hawthorn, J., et al. 2015, MNRAS, 449, 2604
- Deason, A. J., Belokurov, V., & Sanders, J. L. 2019, MNRAS, 490, 3426
- Dekker, H., D’Odorico, S., Kaufer, A., Delabre, B., & Kotzlowski, H. 2000, in Society of Photo-Optical Instrumentation Engineers (SPIE) Conference Series, Vol. 4008, Optical and IR Telescope Instrumentation and Detectors, ed. M. Iye & A. F. Moorwood, 534–545
- Delgado Mena, E., Moya, A., Adibekyan, V., et al. 2019, A&A, 624, A78
- Deng, L.-C., Newberg, H. J., Liu, C., et al. 2012, Research in Astronomy and Astrophysics, 12, 735
- Di Matteo, P., Fragkoudi, F., Khoperskov, S., et al. 2019a, A&A, 628, A11
- Di Matteo, P., Haywood, M., Combes, F., Semelin, B., & Snaith, O. N. 2013, A&A, 553, A102
- Di Matteo, P., Haywood, M., Lehnert, M. D., et al. 2019b, A&A, 632, A4
- Donor, J., Frinchaboy, P. M., Cunha, K., et al. 2020, AJ, 159, 199
- Edvardsson, B., Andersen, J., Gustafsson, B., et al. 1993, A&A, 500, 391
- Eggen, O. J., Lynden-Bell, D., & Sandage, A. R. 1962, ApJ, 136, 748
- Eisenhauer, F., Schödel, R., Genzel, R., et al. 2003, ApJ, 597, L121
- Evans, D. W., Riello, M., De Angeli, F., et al. 2018, A&A, 616, A4
- Feltzing, S., Bowers, J. B., & Agertz, O. 2020, MNRAS, 493, 1419
- Feltzing, S., & Gilmore, G. 2000, A&A, 355, 949
- Fernández-Alvar, E., Tissera, P. B., Carigi, L., et al. 2019, MNRAS, 485, 1745
- Fernández-Alvar, E., Allende Prieto, C., Schlesinger, K. J., et al. 2015, A&A, 577, A81
- Fernández-Alvar, E., Carigi, L., Schuster, W. J., et al. 2018, ApJ, 852, 50
- Feuillet, D. K., Feltzing, S., Sahlholdt, C. L., & Casagrande, L. 2020, MNRAS, 497, 109
- Fowler, W. A., & Hoyle, F. 1960, Annals of Physics, 10, 280
- Freeman, K., & Bland-Hawthorn, J. 2002, ARA&A, 40, 487

- Frenk, C. S., & White, S. D. M. 2012, *Annalen der Physik*, 524, 507
- Friel, E. D. 1995, *ARA&A*, 33, 381
- Frinchaboy, P. M., Thompson, B., Jackson, K. M., et al. 2013, *ApJ*, 777, L1
- Fuhrmann, K. 2011, *MNRAS*, 414, 2893
- Fuhrmann, K., Chini, R., Kaderhandt, L., & Chen, Z. 2017, *MNRAS*, 464, 2610
- Fuhrmann, K., Pfeiffer, M., Frank, C., Reetz, J., & Gehren, T. 1997, *A&A*, 323, 909
- Gai, M., Busonero, D., Gardiol, D., & Loreggia, D. 2005, in *ESA Special Publication*, Vol. 576, *The Three-Dimensional Universe with Gaia*, ed. C. Turon, K. S. O’Flaherty, & M. A. C. Perryman, 433
- Gaia Collaboration, Prusti, T., de Bruijne, J. H. J., et al. 2016, *A&A*, 595, A1
- Gaia Collaboration, Katz, D., Antoja, T., et al. 2018a, *A&A*, 616, A11
- Gaia Collaboration, Babusiaux, C., van Leeuwen, F., et al. 2018b, *A&A*, 616, A10
- Gaia Collaboration, Brown, A. G. A., Vallenari, A., et al. 2018c, *A&A*, 616, A1
- Gaia Collaboration, Antoja, T., McMillan, P., et al. 2020, *A&A*, submitted
- Gallart, C., Bernard, E. J., Brook, C. B., et al. 2019, *Nature Astronomy*, 3, 932
- García Pérez, A. E., Allende Prieto, C., Holtzman, J. A., et al. 2016, *AJ*, 151, 144
- Genovali, K., Lemasle, B., Bono, G., et al. 2014, *A&A*, 566, A37
- Genovali, K., Lemasle, B., da Silva, R., et al. 2015, *A&A*, 580, A17
- Gerhard, O. 2006, in *EAS Publications Series*, Vol. 20, *EAS Publications Series*, ed. G. A. Mamon, F. Combes, C. Deffayet, & B. Fort, 89–96
- Ghez, A. M., Salim, S., Weinberg, N. N., et al. 2008, *ApJ*, 689, 1044
- Gibson, B. K., Pilkington, K., Brook, C. B., Stinson, G. S., & Bailin, J. 2013, *A&A*, 554, A47
- Gilliland, R. L., Brown, T. M., Christensen-Dalsgaard, J., et al. 2010, *PASP*, 122, 131
- Gilmore, G., & Reid, N. 1983, *MNRAS*, 202, 1025
- Gilmore, G., Randich, S., Asplund, M., et al. 2012, *The Messenger*, 147, 25
- González Hernández, J. I., & Bonifacio, P. 2009, *A&A*, 497, 497
- Graczyk, D., Pietrzyński, G., Gieren, W., et al. 2019, *ApJ*, 872, 85
- Gray, D. F. 2005, *The Observation and Analysis of Stellar Photospheres*
- Green, G. M., Schlafly, E. F., Finkbeiner, D., et al. 2018, *MNRAS*, 478, 651
- Grenon, M. 1989, *APSS*, 156, 29
- . 1999, *APSS*, 265, 331
- Grevesse, N., Asplund, M., & Sauval, A. J. 2007, *Space Sci. Rev.*, 130, 105
- Grisoni, V., Matteucci, F., Romano, D., & Fu, X. 2019, *MNRAS*, 489, 3539
- Grisoni, V., Spitoni, E., & Matteucci, F. 2018, *MNRAS*, 481, 2570
- Grisoni, V., Spitoni, E., Matteucci, F., et al. 2017, *MNRAS*, 472, 3637
- Guiglion, G. 2015, *Theses*, Université Nice Sophia Antipolis

- Guiglion, G., de Laverny, P., Recio-Blanco, A., et al. 2016, *A&A*, 595, A18
- Gustafsson, B., Edvardsson, B., Eriksson, K., et al. 2008, *A&A*, 486, 951
- Han, Z., & Podsiadlowski, P. 2004, *MNRAS*, 350, 1301
- Hayden, M. R., Recio-Blanco, A., de Laverny, P., Mikolaitis, S., & Worley, C. C. 2017, *A&A*, 608, L1
- Hayden, M. R., Holtzman, J. A., Bovy, J., et al. 2014, *AJ*, 147, 116
- Hayden, M. R., Bovy, J., Holtzman, J. A., et al. 2015, *ApJ*, 808, 132
- Hayden, M. R., Bland-Hawthorn, J., Sharma, S., et al. 2020, *MNRAS*, 493, 2952
- Haywood, M., Di Matteo, P., Lehnert, M. D., Katz, D., & Gómez, A. 2013, *A&A*, 560, A109
- Haywood, M., Snaith, O., Lehnert, M. D., Di Matteo, P., & Khoperskov, S. 2019, *A&A*, 625, A105
- Heavens, A. F., Jimenez, R., & Lahav, O. 2000, *MNRAS*, 317, 965
- Heiter, U., Lind, K., Asplund, M., et al. 2015, *Phys. Scr*, 90, 054010
- Heiter, U., Lind, K., Bergemann, M., et al. 2020, arXiv e-prints, arXiv:2011.02049
- Helmi, A. 2020, arXiv e-prints, arXiv:2002.04340
- Helmi, A., Babusiaux, C., Koppelman, H. H., et al. 2018, *Nature*, 563, 85
- Helmi, A., White, S. D. M., de Zeeuw, P. T., & Zhao, H. 1999, *Nature*, 402, 53
- Henden, A. A., Levine, S., Terrell, D., et al. 2018, in American Astronomical Society Meeting Abstracts, Vol. 232, American Astronomical Society Meeting Abstracts #232, 223.06
- Hill, V., Plez, B., Cayrel, R., et al. 2002, *A&A*, 387, 560
- Hill, V., Lecureur, A., Gómez, A., et al. 2011, *A&A*, 534, A80
- Hinkel, N. R., Young, P. A., Pagano, M. D., et al. 2016, *ApJS*, 226, 4
- Hogg, D. W., Casey, A. R., Ness, M., et al. 2016, *ApJ*, 833, 262
- Holtzman, J. A., Shetrone, M., Johnson, J. A., et al. 2015, *AJ*, 150, 148
- Hou, J. L., Prantzos, N., & Boissier, S. 2000, *A&A*, 362, 921
- Howard, C. D., Rich, R. M., Reitzel, D. B., et al. 2008, *ApJ*, 688, 1060
- Howard, C. D., Rich, R. M., Clarkson, W., et al. 2009, *ApJ*, 702, L153
- Hubble, E. 1929, *Proceedings of the National Academy of Science*, 15, 168
- Ibata, R. A., Gilmore, G., & Irwin, M. J. 1994, *Nature*, 370, 194
- Ivanyuk, O. M., Jenkins, J. S., Pavlenko, Y. V., Jones, H. R. A., & Pinfield, D. J. 2017, *MNRAS*, 468, 4151
- Iwamoto, K., Brachwitz, F., Nomoto, K., et al. 1999, *ApJS*, 125, 439
- Jofré, P., Heiter, U., & Soubiran, C. 2019, *ARA&A*, 57, 571
- Jofré, P., Heiter, U., Soubiran, C., et al. 2015, *A&A*, 582, A81
- Jofré, P., Jorissen, A., Van Eck, S., et al. 2016, *A&A*, 595, A60
- Jofré, P., Heiter, U., Worley, C. C., et al. 2017, *A&A*, 601, A38

- Jönsson, H., Ryde, N., Schultheis, M., & Zoccali, M. 2017, *A&A*, 598, A101
- Jordi, C., Gebran, M., Carrasco, J. M., et al. 2010, *A&A*, 523, A48
- Jørgensen, B. R., & Lindegren, L. 2005, *A&A*, 436, 127
- Jurić, M., Ivezić, Ž., Brooks, A., et al. 2008, *ApJ*, 673, 864
- Katz, D., Soubiran, C., Cayrel, R., et al. 2011, *A&A*, 525, A90
- Kaufer, A., Stahl, O., Tubbesing, S., et al. 1999, *The Messenger*, 95, 8
- Kerr, F. J., & Lynden-Bell, D. 1986, *MNRAS*, 221, 1023
- Khoperskov, S., Haywood, M., Snaith, O., et al. 2020, arXiv e-prints, arXiv:2006.10195
- Klypin, A., Kravtsov, A. V., Valenzuela, O., & Prada, F. 1999, *ApJ*, 522, 82
- Kordopatis, G. 2011, *Theses, Observatoire de Paris*
- Kordopatis, G., Amorisco, N. C., Evans, N. W., Gilmore, G., & Koposov, S. E. 2016, *MNRAS*, 457, 1299
- Kordopatis, G., Recio-Blanco, A., de Laverny, P., et al. 2011a, *A&A*, 535, A106
- Kordopatis, G., Recio-Blanco, A., Schultheis, M., & Hill, V. 2020, *A&A*, 643, A69
- Kordopatis, G., Wyse, R. F. G., Chiappini, C., et al. 2017, *MNRAS*, 467, 469
- Kordopatis, G., Recio-Blanco, A., de Laverny, P., et al. 2011b, *A&A*, 535, A107
- Kordopatis, G., Wyse, R. F. G., Gilmore, G., et al. 2015a, *A&A*, 582, A122
- Kordopatis, G., Binney, J., Gilmore, G., et al. 2015b, *MNRAS*, 447, 3526
- Kroupa, P., Tout, C. A., & Gilmore, G. 1993, *MNRAS*, 262, 545
- Kubryk, M., Prantzos, N., & Athanassoula, E. 2015, *A&A*, 580, A126
- Kurucz, R. L. 2005, *Memorie della Societa Astronomica Italiana Supplementi*, 8, 14
- Lacey, C. G. 1984, *MNRAS*, 208, 687
- Laporte, C. F. P., Minchev, I., Johnston, K. V., & Gómez, F. A. 2019, *MNRAS*, 485, 3134
- Law, D. R., Majewski, S. R., & Johnston, K. V. 2009, *ApJ*, 703, L67
- Leavitt, H. S. 1908, *Annals of Harvard College Observatory*, 60, 87
- Leung, H. W., & Bovy, J. 2019, *MNRAS*, 483, 3255
- Lindegren, L., & Feltzing, S. 2013, *A&A*, 553, A94
- Lindegren, L., & Perryman, M. A. C. 1996, *A&AS*, 116, 579
- Lindegren, L., Hernández, J., Bombrun, A., et al. 2018, *A&A*, 616, A2
- Lynden-Bell, D. 1967, *MNRAS*, 136, 101
- Lynden-Bell, D., & Kalnajs, A. J. 1972, *MNRAS*, 157, 1
- Mackereth, J. T., Bovy, J., Schiavon, R. P., et al. 2017, *MNRAS*, 471, 3057
- Mackereth, J. T., Schiavon, R. P., Pfeffer, J., et al. 2019, *MNRAS*, 482, 3426
- Magic, Z., Collet, R., Asplund, M., et al. 2013, *A&A*, 557, A26
- Magrini, L., Sestito, P., Randich, S., & Galli, D. 2009, *A&A*, 494, 95

- Magrini, L., Randich, S., Friel, E., et al. 2013, *A&A*, 558, A38
- Magrini, L., Randich, S., Kordopatis, G., et al. 2017, *A&A*, 603, A2
- Majewski, S. R., Schiavon, R. P., Frinchaboy, P. M., et al. 2017, *AJ*, 154, 94
- Martig, M., Rix, H.-W., Silva Aguirre, V., et al. 2015, *MNRAS*, 451, 2230
- Mather, J. C., Cheng, E. S., Eplee, R. E., J., et al. 1990, *ApJ*, 354, L37
- Matteucci, F. 2012, *Chemical Evolution of Galaxies*, doi:10.1007/978-3-642-22491-1
- Matteucci, F., & Brocato, E. 1990, *ApJ*, 365, 539
- Matteucci, F., & Francois, P. 1989, *MNRAS*, 239, 885
- Matteucci, F., & Greggio, L. 1986, *A&A*, 154, 279
- Matteucci, F., Grisoni, V., Spitoni, E., et al. 2019, *MNRAS*, 487, 5363
- Matteucci, F., & Recchi, S. 2001, *ApJ*, 558, 351
- Mayor, M., Pepe, F., Queloz, D., et al. 2003, *The Messenger*, 114, 20
- McMillan, P. J. 2017, *MNRAS*, 465, 76
- McMillan, P. J., & Binney, J. J. 2010, *MNRAS*, 402, 934
- Meijer, E. A., Nijenhuis, J. N., Vink, R. J. P., et al. 2009, in *Society of Photo-Optical Instrumentation Engineers (SPIE) Conference Series*, Vol. 7439, *Astronomical and Space Optical Systems*, ed. P. G. Warren, C. J. Marshall, R. K. Tyson, M. Lloyd-Hart, J. B. Heaney, & E. T. Kvamme, 743915
- Meléndez, J., Asplund, M., Alves-Brito, A., et al. 2008, *A&A*, 484, L21
- Mignard, F., Bailer-Jones, C., Bastian, U., et al. 2008, in *A Giant Step: from Milli- to Microarcsecond Astrometry*, ed. W. J. Jin, I. Platais, & M. A. C. Perryman, Vol. 248, 224–230
- Mikolaitis, Š., de Laverny, P., Recio-Blanco, A., et al. 2017, *A&A*, 600, A22
- Mikolaitis, Š., Hill, V., Recio-Blanco, A., et al. 2014, *A&A*, 572, A33
- Mikolaitis, Š., Drazdauskas, A., Minkevičiūtė, R., et al. 2019, *A&A*, 628, A49
- Minchev, I., Chiappini, C., & Martig, M. 2013, *A&A*, 558, A9
- . 2014, *A&A*, 572, A92
- Minchev, I., Anders, F., Recio-Blanco, A., et al. 2018, *MNRAS*, 481, 1645
- Miyamoto, M., & Nagai, R. 1975, *PASJ*, 27, 533
- Mo, H., van den Bosch, F. C., & White, S. 2010, *Galaxy Formation and Evolution*
- Montalbán, J., Mackereth, J. T., Miglio, A., et al. 2020, *arXiv e-prints*, arXiv:2006.01783
- Moré, J. J. 1978, *The Levenberg-Marquardt algorithm: Implementation and theory*, Vol. 630, 105–116
- Mucciarelli, A., Pancino, E., Lovisi, L., Ferraro, F. R., & Lapenna, E. 2013, *ApJ*, 766, 78
- Myeong, G. C., Evans, N. W., Belokurov, V., Sanders, J. L., & Koposov, S. E. 2018, *ApJ*, 863, L28
- Myeong, G. C., Vasiliev, E., Iorio, G., Evans, N. W., & Belokurov, V. 2019, *MNRAS*, 488, 1235
- Naidu, R. P., Conroy, C., Bonaca, A., et al. 2020, *ApJ*, 901, 48

- Nandakumar, G., Ryde, N., Schultheis, M., et al. 2018, *MNRAS*, 478, 4374
- Navarro, J. F., Frenk, C. S., & White, S. D. M. 1997, *ApJ*, 490, 493
- Ness, M., Hogg, D. W., Rix, H. W., Ho, A. Y. Q., & Zasowski, G. 2015, *ApJ*, 808, 16
- Ness, M. K., Johnston, K. V., Blancato, K., et al. 2019, *ApJ*, 883, 177
- Nidever, D. L., Bovy, J., Bird, J. C., et al. 2014, *ApJ*, 796, 38
- Nissen, P. E., Christensen-Dalsgaard, J., Mosumgaard, J. R., et al. 2020, *A&A*, 640, A81
- Nissen, P. E., & Gustafsson, B. 2018, *A&A Rev.*, 26, 6
- Nissen, P. E., & Schuster, W. J. 2010, *A&A*, 511, L10
- Nissen, P. E., Silva Aguirre, V., Christensen-Dalsgaard, J., et al. 2017, *A&A*, 608, A112
- Noguchi, M. 2018, *Nature*, 559, 585
- Nordlander, T., Amarsi, A. M., Lind, K., et al. 2017, *A&A*, 597, A6
- Nordström, B., Mayor, M., Andersen, J., et al. 2004, *A&A*, 418, 989
- Ojha, D. K. 2001, *MNRAS*, 322, 426
- Oort, J. H. 1970, *A&A*, 7, 381
- Palla, M., Matteucci, F., Spitoni, E., Vincenzo, F., & Grisoni, V. 2020, *MNRAS*, 498, 1710
- Pasquini, L., Avila, G., Allaert, E., et al. 2000, in *Society of Photo-Optical Instrumentation Engineers (SPIE) Conference Series*, Vol. 4008, *Optical and IR Telescope Instrumentation and Detectors*, ed. M. Iye & A. F. Moorwood, 129–140
- Pasquini, L., Avila, G., Blecha, A., et al. 2002, *The Messenger*, 110, 1
- Penzias, A. A., & Wilson, R. W. 1965, *ApJ*, 142, 419
- Perdigon, J., de Laverny, P., Recio-Blanco, A., et al. 2021, *A&A*, 647, A162
- Perryman, M. A. C., Lindegren, L., Kovalevsky, J., et al. 1997, *A&A*, 500, 501
- Perryman, M. A. C., de Boer, K. S., Gilmore, G., et al. 2001, *A&A*, 369, 339
- Pilkington, K., Few, C. G., Gibson, B. K., et al. 2012, *A&A*, 540, A56
- Planck Collaboration, Ade, P. A. R., Aghanim, N., et al. 2016, *A&A*, 594, A13
- Poggio, E., Drimmel, R., Andrae, R., et al. 2020, *Nature Astronomy*, 4, 590
- Posbic, H., Katz, D., Caffau, E., et al. 2012, *A&A*, 544, A154
- Recio-Blanco, A. 2014, in *Setting the scene for Gaia and LAMOST*, ed. S. Feltzing, G. Zhao, N. A. Walton, & P. Whitelock, Vol. 298, 366–374
- Recio-Blanco, A., Bijaoui, A., & de Laverny, P. 2006, *MNRAS*, 370, 141
- Recio-Blanco, A., de Laverny, P., Kordopatis, G., et al. 2014, *A&A*, 567, A5
- Recio-Blanco, A., de Laverny, P., Allende Prieto, C., et al. 2016, *A&A*, 585, A93
- Reddy, B. E., Lambert, D. L., & Allende Prieto, C. 2006, *MNRAS*, 367, 1329
- Ricker, G. R., Winn, J. N., Vanderspek, R., et al. 2015, *Journal of Astronomical Telescopes, Instruments, and Systems*, 1, 014003
- Robin, A. C., Haywood, M., Creze, M., Ojha, D. K., & Bienayme, O. 1996, *A&A*, 305, 125

- Rockosi, C., Beers, T. C., Majewski, S., Schiavon, R., & Eisenstein, D. 2009, in *astro2010: The Astronomy and Astrophysics Decadal Survey*, Vol. 2010, 14
- Rojas-Arriagada, A., Recio-Blanco, A., de Laverny, P., et al. 2017, *A&A*, 601, A140
- Romano, D., Karakas, A. I., Tosi, M., & Matteucci, F. 2010, *A&A*, 522, A32
- Roškar, R., Debattista, V. P., Quinn, T. R., Stinson, G. S., & Wadsley, J. 2008, *ApJ*, 684, L79
- Ryde, N., Edvardsson, B., Gustafsson, B., et al. 2009, *A&A*, 496, 701
- Ryde, N., Gustafsson, B., Edvardsson, B., et al. 2010, *A&A*, 509, A20
- Salpeter, E. E. 1955, *ApJ*, 121, 161
- Santos-Peral, P. 2021, *A&A*, submitted
- Santos-Peral, P., Recio-Blanco, A., de Laverny, P., Fernández-Alvar, E., & Ordenovic, C. 2020, *A&A*, 639, A140
- Sbordone, L., Caffau, E., Bonifacio, P., & Duffau, S. 2014, *A&A*, 564, A109
- Scannapieco, C., Wadepuhl, M., Parry, O. H., et al. 2012, *MNRAS*, 423, 1726
- Schlegel, D. J., Finkbeiner, D. P., & Davis, M. 1998, *ApJ*, 500, 525
- Schmidt, M. 1959, *ApJ*, 129, 243
- Schneider, P. 2015, *Extragalactic Astronomy and Cosmology: An Introduction*, doi:10.1007/978-3-642-54083-7
- Schönrich, R., & Binney, J. 2009, *MNRAS*, 396, 203
- Schönrich, R., McMillan, P., & Eyer, L. 2019, *MNRAS*, 487, 3568
- Schönrich, R., & McMillan, P. J. 2017, *MNRAS*, 467, 1154
- Searle, L., & Zinn, R. 1978, *ApJ*, 225, 357
- Sellwood, J. A., & Binney, J. J. 2002, *MNRAS*, 336, 785
- Sestito, F., Martin, N. F., Starkeburg, E., et al. 2020, *MNRAS*, 497, L7
- Sharma, S., Hayden, M. R., & Bland-Hawthorn, J. 2020, *arXiv e-prints*, arXiv:2005.03646
- Sharma, S., Bland-Hawthorn, J., Binney, J., et al. 2014, *ApJ*, 793, 51
- Silva Aguirre, V., Bojsen-Hansen, M., Slumstrup, D., et al. 2018, *MNRAS*, 475, 5487
- Sirko, E., Goodman, J., Knapp, G. R., et al. 2004, *AJ*, 127, 899
- Skrutskie, M. F., Cutri, R. M., Stiening, R., et al. 2006, *AJ*, 131, 1163
- Skumanich, A. 1972, *ApJ*, 171, 565
- Smiljanic, R., Korn, A. J., Bergemann, M., et al. 2014, *A&A*, 570, A122
- Snaith, O. N., Haywood, M., Di Matteo, P., et al. 2014, *ApJ*, 781, L31
- Snider, S., Allende Prieto, C., von Hippel, T., et al. 2001, *ApJ*, 562, 528
- Soderblom, D. R. 2010, *ARA&A*, 48, 581
- Sofue, Y., Honma, M., & Omodaka, T. 2009, *PASJ*, 61, 227
- Soubiran, C. 1993, *A&A*, 274, 181
- Soubiran, C., Bienaymé, O., Mishenina, T. V., & Kovtyukh, V. V. 2008, *A&A*, 480, 91

- Soubiran, C., Bienaymé, O., & Siebert, A. 2003, *A&A*, 398, 141
- Soubiran, C., & Girard, P. 2005, *A&A*, 438, 139
- Sousa, S. G., Santos, N. C., Israelian, G., Mayor, M., & Monteiro, M. J. P. F. G. 2007, *A&A*, 469, 783
- Sparke, L. S., & Gallagher, John S., I. 2006, *Galaxies in the Universe - 2nd Edition*, doi:10.2277/0521855934
- Spergel, D. N., Bean, R., Doré, O., et al. 2007, *ApJS*, 170, 377
- Spitoni, E., & Matteucci, F. 2011, *A&A*, 531, A72
- Spitoni, E., Romano, D., Matteucci, F., & Ciotti, L. 2015, *ApJ*, 802, 129
- Spitoni, E., Silva Aguirre, V., Matteucci, F., Calura, F., & Grisoni, V. 2019, *A&A*, 623, A60
- Spitoni, E., Verma, K., Silva Aguirre, V., & Calura, F. 2020, *A&A*, 635, A58
- Springel, V., Frenk, C. S., & White, S. D. M. 2006, *Nature*, 440, 1137
- Steinmetz, M., Zwitter, T., Siebert, A., et al. 2006, *AJ*, 132, 1645
- Strigari, L. E., Bullock, J. S., Kaplinghat, M., et al. 2007, *ApJ*, 669, 676
- Thorsbro, B., Ryde, N., Rich, R. M., et al. 2020, *ApJ*, 894, 26
- Timmes, F. X., Woosley, S. E., & Weaver, T. A. 1995, *ApJS*, 98, 617
- Tinsley, B. M. 1979, *ApJ*, 229, 1046
- Tolstoy, E., Hill, V., & Tosi, M. 2009, *ARA&A*, 47, 371
- Tsantaki, M., Andreasen, D. T., Teixeira, G. D. C., et al. 2018, *MNRAS*, 473, 5066
- Valenti, J. A., & Piskunov, N. 1996, *A&AS*, 118, 595
- Valentini, M., Morel, T., Miglio, A., Fossati, L., & Munari, U. 2013, in *European Physical Journal Web of Conferences*, Vol. 43, *European Physical Journal Web of Conferences*, 03006
- Vaucouleurs, G. 1959, *Handbuch der Physik*, 11, 275
- Venn, K. A., Irwin, M., Shetrone, M. D., et al. 2004, *AJ*, 128, 1177
- Vincenzo, F., & Kobayashi, C. 2020, *MNRAS*, 496, 80
- Vincenzo, F., Spitoni, E., Calura, F., et al. 2019, *MNRAS*, 487, L47
- Vosteen, L. L. A., Draaisma, F., van Werkhoven, W. P., et al. 2009, in *Society of Photo-Optical Instrumentation Engineers (SPIE) Conference Series*, Vol. 7439, *Astronomical and Space Optical Systems*, ed. P. G. Warren, C. J. Marshall, R. K. Tyson, M. Lloyd-Hart, J. B. Heaney, & E. T. Kvamme, 743914
- Wegg, C., & Gerhard, O. 2013, *MNRAS*, 435, 1874
- Wegg, C., Gerhard, O., & Portail, M. 2015, *MNRAS*, 450, 4050
- Whelan, J., & Iben, Icko, J. 1973, *ApJ*, 186, 1007
- White, S. D. M., & Rees, M. J. 1978, *MNRAS*, 183, 341
- Wojno, J., Kordopatis, G., Steinmetz, M., et al. 2016, *MNRAS*, 461, 4246
- Worley, C. C., de Laverny, P., Recio-Blanco, A., Hill, V., & Bijaoui, A. 2016, *A&A*, 591, A81
- Worley, C. C., de Laverny, P., Recio-Blanco, A., et al. 2012, *A&A*, 542, A48

- Wyse, R. F. G., & Gilmore, G. 1993, in *Astronomical Society of the Pacific Conference Series*, Vol. 48, *The Globular Cluster-Galaxy Connection*, ed. G. H. Smith & J. P. Brodie, 727
- Wyse, R. F. G., Moe, M., & Kratter, K. M. 2020, *MNRAS*, doi:10.1093/mnras/staa731
- Yanny, B., Rockosi, C., Newberg, H. J., et al. 2009, *AJ*, 137, 4377
- York, D. G., Adelman, J., Anderson, John E., J., et al. 2000, *AJ*, 120, 1579
- Yoshii, Y. 1982, *PASJ*, 34, 365
- Zhao, G., Zhao, Y.-H., Chu, Y.-Q., Jing, Y.-P., & Deng, L.-C. 2012, *Research in Astronomy and Astrophysics*, 12, 723
- Zhao, G., Mashonkina, L., Yan, H. L., et al. 2016, *ApJ*, 833, 225
- Zoccali, M., Hill, V., Lecqueur, A., et al. 2008, *A&A*, 486, 177
- Zoccali, M., Renzini, A., Ortolani, S., et al. 2003, *A&A*, 399, 931
- Zoccali, M., Gonzalez, O. A., Vasquez, S., et al. 2014, *A&A*, 562, A66
- Zwitter, T., Siebert, A., Munari, U., et al. 2008, *AJ*, 136, 421
- Zwitter, T., Matijević, G., Breddels, M. A., et al. 2010, *A&A*, 522, A54